Title

Optical Determination of Absolute Membrane Potential in Cellular Physiology

Author

Lazzari-Dean, Julia Rose

Publication Date

2019

Peer reviewed|Thesis/dissertation

Optical Determination of Absolute Membrane Potential in Cellular Physiology

By

Julia R. Lazzari-Dean

A dissertation submitted in partial satisfaction of the

requirements for the degree of

Doctor of Philosophy

in

Chemistry

in the

Graduate Division

of the

University of California, Berkeley

Committee in charge:

Professor Evan W. Miller, Chair
Professor Ke Xu
Professor David Savage

Fall 2019

Optical Determination of Absolute Membrane Potential in Cellular Physiology

By Julia R. Lazzari-Dean

Abstract

Optical Determination of Absolute Membrane Potential in Cellular Physiology

by

Julia R. Lazzari-Dean

Doctor of Philosophy in Chemistry

University of California, Berkeley

Professor Evan W. Miller, Chair

Membrane potential (V_{mem}) is a voltage across the plasma membrane of all cells, arising from differences in ionic concentration. Changes in V_{mem} over milliseconds transmit electrical impulses in neurons, and V_{mem} dynamics over hours to days can modulate differentiation and body patterning. A complete understanding of V_{mem} requires techniques that can measure its absolute value (in millivolts) across a broad range of time and length scales.

In this dissertation, we develop fluorescence lifetime imaging (FLIM) of small molecule voltage sensitive dyes (VoltageFluors, VFs) as a platform for optical recording of absolute V_{mem}. We review strategies for absolute V_{mem} detection, highlighting a need for optical techniques complementary to traditional electrode-based recording. Using the VoltageFluor VF2.1.Cl, we demonstrate that its fluorescence lifetime (τ_{fl}) can report on absolute V_{mem} with biologically relevant V_{mem} resolution (5 mV RMSD for V_{mem} changes, 19 mV RMSD for V_{mem} in single trials). Using FLIM, we studied the slow V_{mem} response following EGF stimulation of A431 carcinoma cells. Because FLIM is robust to motion and photobleaching, we were able to report a 10-15 mV hyperpolarizing response over the course of 15 minutes. Through a combination of pharmacology and absolute V_{mem} recordings, we demonstrate that the Ca^{2+} activated K^+ channel $K_{Ca}3.1$ mediates the observed hyperpolarization. We then investigated the downstream effects of this V_{mem} change on EGF-induced Ca^{2+} signaling and protein phosphorylation.

To broaden the reach of FLIM-based absolute V_{mem} imaging, we characterized the τ_{fl} of 11 additional VoltageFluors. First, we explored the fluorescence lifetime of a library of conformationally restricted VF dyes, revealing that synthetic modifications to the dimethylaniline electron donor can modulate the photoinduced electron transfer V_{mem} sensing trigger of VFs across a wide range. By relating photophysical characterization to VF performance in detection of fast V_{mem} events, we establish mechanism-based guidelines for VF design. We then developed a red-shifted absolute V_{mem} imaging platform with FLIM of a carborhodamine VF, which displays the highest absolute V_{mem} sensitivity of all VFs tested (~4 ps/mV), as well as excellent photostability and low phototoxicity. With red-shifted FLIM, we can make hundreds of sequential V_{mem} recordings on the same field of view and report V_{mem} during cardiomyocyte action potentials at acquisition speeds of 20 Hz. Towards absolute V_{mem} imaging in thick tissue, we characterize V_{mem}-dependent changes in τ_{fl} across a spectrum of VFs under two photon illumination. We observe V_{mem} sensitivity in all cases, and we identify two additional VFs (carboVF and RhoVR(Me)) with

the capability to report absolute V_{mem} with high fidelity. Finally, we test and discuss various models to describe fluorescence lifetimes of VFs. Together, this work demonstrates that FLIM of VF dyes is a broadly useful strategy for absolute V_{mem} measurement, expanding the possible scope of V_{mem} recordings and enabling new biological inquiry into V_{mem} signaling.

For My Parents

Table of Contents

Acknowledgements

I would first like to express my gratitude to my adviser, Evan Miller, for his steadfast support and enthusiasm during my time in the lab. Although there were many of us in a very young lab, Evan took time for everyone and acknowledged everyone's contribution, both on group jobs and with the research effort. When things weren't working or were difficult, having someone notice and say, "I see you are trying, thank you" meant the world. In many ways, Evan and I learned fluorescence lifetime imaging (FLIM) together, as it was a very new topic for me and a somewhat new topic for him. It perhaps wasn't the most "efficient" way to do science, but Evan was very patient and always prioritized me learning over just getting the job done. As I got more experienced, I came up with lots of half-baked and a few "fully baked" project ideas, and Evan gave me the independence and freedom to try new things. The process of working on projects that I designed was humbling, and I am grateful to have had that learning opportunity. When I was looking at graduate schools, I received the advice that 75% of the tone of my Ph.D. experience would depend on my adviser. I would say that's fairly true, although one can perhaps argue about the exact percentage. I have really enjoyed my time at UC Berkeley, and I owe a lot of that to Evan. Thank you.

I am deeply grateful to Holly Aaron, the director of the Molecular Imaging Center (MIC) at UC Berkeley. Holly routinely goes far above and beyond her duties, moving heaven and earth to run the imaging center (especially Deckard, the FLIM microscope) and to obtain a grant to upgrade the FLIM system. I would also like to thank Jen-Yi Lee and Feather Ives, who helped Holly in this gargantuan task. I am particularly grateful for the opportunity to speak twice at the Advanced Imaging Methods workshop that Holly organizes. It was certainly a risk to invite me as a third-year graduate student to speak about my science to a general audience, and I appreciate that Holly was willing to take that leap of faith. These talks, and the subsequent networking opportunities they gave me, made me feel like I belonged in a scientific community for the first time and connected me to invaluable collaborators and resources. Most of all, though, Holly's positive energy and encouragement helped me to push forward when I felt utterly lost and confused. The time we spent working together, taking Deckard apart and putting it back, helped me build a sense of resilience and independence that I can't imagine finding elsewhere. It was frustrating at the time, but these are some of my fondest memories of graduate school.

I would also like to thank Professor Bob Bergman for his mentorship during my time as a graduate student instructor for Physical Organic Chemistry, as well as his continued support and friendship afterwards. I didn't think I was qualified to teach Phys Org, but Bob believed that I would do a good job. I certainly struggled to stay ahead of the course material and incredibly talented students in the class, but successfully teaching that course, as difficult as it was, is one of my proudest achievements from Berkeley. Bob also connected me with other role models, repeatedly working to dispel my imposter syndrome and convince me that I belong in scientific research. I have never met another person so generous with his time and successful at promoting those around him, and I hope to someday help others advance the way Bob has helped me.

The entire Miller lab has provided me with a fun and supportive place to do science, and it was an honor to be a part of setting up the lab and watching it grow. I am grateful to all of you for your friendship, as well as helpful (and sometimes preposterous) scientific discussions over lunch or

leftover group meeting snacks. In particular, I would like to thank Dr. Alison Walker, who taught me most of what I know about tissue culture and was consistently available and patient with my many questions. I would also like to thank Dr. Parker Deal, Dr. Vincent Grenier, and Dr. Rishikesh Kulkarni for blazing a scientific trail in the lab, as well as providing advice and friendship. Thanks also to Dr. Vadim Degtyar, my first mentor in the lab, who introduced me to FLIM and gave me the drive to be independent. The second class of Miller lab students, of which I was a part, was a bit of an adventure. With 5 of us, it felt as though we took the entire lab with us through our phases of graduate school, be it qualifying exams, paper writing, job applications or dissertations. To Steven Boggess, Pei Liu, Gloria Ortiz, and Jenna Franke - I enjoyed riding that wave with all of you, and I look forward to continuing as friends and colleagues in the future.

I am particularly grateful to the students who worked with me on VF-FLIM and who are carrying this work forward, certainly to greater heights than I was able to achieve. I would like to thank Anneliese Gest, for joining the FLIM project even though she didn't rotate with me and probably didn't know what she was getting herself into. Thanks also to Susanna Yaeger-Weiss, for joining the FLIM project even though she knew what she was getting herself into. This dissertation wouldn't have been possible without their efforts, and teaching FLIM to Anneliese and Susanna made me think much more deeply about the work. Their friendship has made the research a lot more fun, and I'm very proud of both of them and their work so far. I also would like to thank Hannah Thorner, who helped me as an undergraduate researcher, and Alex Ramsey, who worked with me as a graduate rotation student. They have all taught me so much, and I am very grateful for their patience with me through my learning process.

I was very lucky to work with and learn from great collaborators at Berkeley, and one of the biggest lessons of my Ph.D. is the value of reaching out to the experts around me. First of all, thanks to my collaborators within the Miller lab, who synthesized VoltageFluors and provided many helpful discussions about VF mechanism. Thanks to Maya Emmons-Bell and Prof. Iswar Hariharan for showing me the wild world of Drosophila development. Thanks to Dr. Sean Peterson and Prof. John Kuriyan for introducing me to EGFR biology. Thanks to Prof. Shai Berlin for helping with electrode-based resting membrane potential measurements and generously sharing electrophysiology equipment. Thanks to Prof. Nicolas Pegard for help with optics and debugging the two-photon illumination setup on Deckard. Thanks to everyone at Becker & Hickl for going above and beyond to help me with our FLIM setup. Thanks to Dr. Alison Killilea at the Berkeley Cell Culture Facility for cell culture advice. Thanks also to the members of my qualifying exam and thesis committees: Prof. Dave Savage, Prof. Ke Xu, Prof. Ming Hammond, and Prof. Rich Kramer. I didn't seek their input as much as I should have, but all of the advice they gave me was thoughtful and helpful.

I wouldn't be here without the support of the faculty mentors who helped me find my way to UC Berkeley for graduate school. In particular, Prof. Moh El-Naggar and Prof. Anna Krylov at USC, who mentored me as an undergraduate researcher in their labs and patiently counseled me as I bounced around among fields trying to find the right match. I also would like to thank my mentors, Dr. Ian McFarlane and Prof. Ksenia Bravaya, who invested incredible amounts of their time into teaching me how to conduct research. Prof. Danielle Tullman-Ercek, along with her student Dr. Sergey Boyarskiy, helped me greatly when I was an Amgen Scholar in their lab. Prof. Hanna Reisler and Prof. Jahan Dawlaty at USC were also instrumental in orienting me to science, assisting with graduate applications, and providing me with well-timed life advice.

I am incredibly lucky to have brilliant and supportive friends who encouraged me along the way. Thanks to Alice Kunin and Kristin Wucherer, my first housemates in the Bay Area and two of my dearest friends. I'm grateful to have happened upon a house with Alice and Kristin – I can't imagine what graduate school would have looked like without it. Thanks to Meaghan Sullivan – we may be on opposite sides of the country but going through graduate school together has been a gift. Thanks also to Steven Boggess for his friendship and support, both inside and outside of lab. Thanks to my other housemates over the years, especially Harneet Rishi; I hope we have many more fried chicken nights to come. I'm grateful to have met many wonderful and supportive people in the Bay Area, including Zach Hallberg, Sophia Tonnu, Eric Sawyer, Robert Nichols, Luke Bertels, and the Adlers.

I owe a particularly emphatic thank you to my partner, Benjamin Adler. He has been an incredible companion and sounding board since the day we met. He has pushed me and enabled me to achieve more as a scientific professional, urging me to automate my data processing, to jump into networking, and to plan projects effectively. He offered me advice where our research overlapped, and he has an eye for good graphic design and good projects, even outside his core area of expertise. Beyond that, Ben patiently listened to my ups and downs in graduate school, despite having a lot on his plate. He has enriched my life and encouraged me to invest in myself beyond science. I look forward to seeing his career unfold, and I am certain he will be successful.

Last but certainly not least, I would like to thank my parents, Margaret Lazzari and Michael Dean, for their unwavering support. They taught me that both women and men can be assertive, intelligent, and kind, and they model those traits every day. They taught me to be inquisitive about how things work, and they believed that I was smart enough to understand any underlying mechanism. I appreciate their daily efforts over so many years – helping with homework, making family dinners, playing board games, cheering at soccer games and track meets, offering advice about life. I appreciate their Skype calls and many road trips to the Bay Area to provide me a welcome reprieve from research. While I've been at Berkeley, they have enthusiastically asked about my work and patiently listened to all of the details. I dedicate this dissertation to my parents, with gratitude and love.

Chapter 1

Absolute Membrane Potential Recordings across Space and Time

Parts of this review were written in collaboration with Anneliese Gest

Abstract

Membrane potential (V_{mem}) is a fundamental biophysical signal present in all cells. Dynamic V_{mem} signals range in time from milliseconds to days, and differences in V_{mem} may span length scales from microns to centimeters. These V_{mem} messages contain information for diverse cellular processes, ranging from neurotransmitter release to cell cycle control to tissue patterning. Characterizing and understanding V_{mem} in both excitable and non-excitable systems is of great interest and potential therapeutic value. However, existing approaches to measuring V_{mem} cannot access the entire span of space and time that is demanded by the underlying biological processes. Here, we outline the diverse arenas where V_{mem} signaling occurs, using this to draft a "wish list" for an absolute V_{mem} sensing platform that could be translatable across biological length- and timescales. In this light, we discuss electrode-based and optical strategies for recording V_{mem}, highlighting recent improvements to access these underexplored biological arenas.

Introduction

Membrane potential, or voltage across a lipid bilayer, is ubiquitous in biology. Excitable cells such as neurons and cardiomyocytes show millisecond-time V_{mem} fluctuations. Many cell types (both excitable and non-excitable) exhibit V_{mem} signals over seconds to days. An estimated 10 to 50% of the cellular energy budget goes to maintain resting V_{mem}, even in non-excitable cells.[1] Given this large energy expenditure, it stands to reason that the functions of V_{mem} span far beyond excitable electrical activity in the brain or heart;[2] recent work has linked V_{mem} to cell proliferation,[3,4] differentiation,[5,6] and tissue patterning.[7]

Membrane potentials result from differences in ion concentration across a semi-permeable membrane. Although this phenomenon is best studied with respect to the plasma membrane of mammalian cells, any selectively permeable membrane can maintain a voltage. For example voltages in bacterial communities [8–10] and across organelle membranes[11,12] also have signaling roles. Unless otherwise indicated, we use the term membrane potential (V_{mem}) to indicate the plasma membrane potential between the cytosol and the extracellular space. In mammalian cells, the primary ions involved in generating V_{mem} are Na^+ and K^+. (**Figure 1.1**), although various other species (including Cl^-, Ca^{2+}, H^+, and organic anions) play a role. Throughout this work, we use the term absolute V_{mem} to indicate the value of the membrane potential in millivolts, rather than a relative measure of changes in V_{mem}.

V_{mem} is inherently a system-level property. It is determined by the expression and activity of an array of ion channels and pumps, and it regulates many downstream pathways. The best documented class of voltage-sensitive proteins is, by far, voltage gated ion channels, which transduce V_{mem} changes into cellular effects. Nevertheless, all membrane proteins experience V_{mem}, and some may even respond to it. Evidence of V_{mem} sensitivity exists for various membrane components,[13] including phosphatases,[14] G protein coupled receptors,[15,16] and the membrane organization itself.[17] For most systems, we have a very incomplete understanding of both the determinants of V_{mem} and the factors respond to V_{mem}.

The gaps in our understanding stem in part from limitations of the existing V_{mem} recording toolkit; improvements must be made to this toolkit to fully characterize V_{mem} signaling. To understand the constraints of current systems, we first examine a range of V_{mem} signals and discuss challenges

associated with recording them. In doing so, we build a "wish list" of characteristics for an optimized V_{mem} reporter. We then turn our focus the primary two approaches for recording membrane potential: electrodes and fluorescent biosensors. We review recent progress in V_{mem} sensing platforms and highlight arenas where development of new tools would facilitate discoveries in V_{mem} biology.

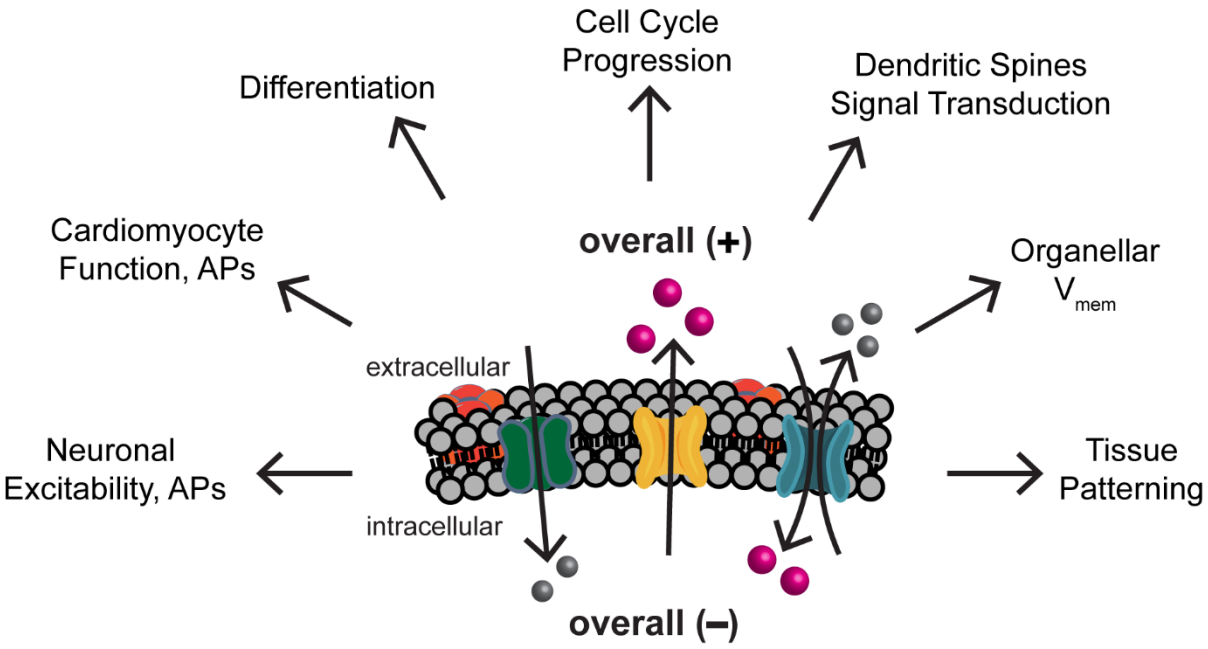

Figure 1.1. Membrane potential is a biophysical signal with broad-reaching implications. Membrane potential (V_{mem}) originates from ionic gradients across the plasma membrane, largely driven by Na^+ (gray spheres) and K^+ (pink spheres) movement. V_{mem} and changes in V_{mem} occur across diverse time and length scales, affecting many aspects of the cell. Some examples of the effects of V_{mem} are highlighted here.

Membrane Potential Signaling Across Space and Time

Membrane potential signaling is most studied in excitable tissue, where rapid changes in cellular V_{mem} initiate cascades of neurotransmitter release or contraction. However, important changes to absolute V_{mem} also occur across minutes, hours, and days.[2] Similarly, as a spatial signal, V_{mem} is canonically treated as cell autonomous and uniform in spherical model cells. Nevertheless, V_{mem} can be compartmentalized subcellularly[18] and delocalized across tissues.[19–21] Here, we break down V_{mem} signals into three length scales: cellular, subcellular, and tissue. From there, we enumerate the unique challenges each brings to V_{mem} measurement.

Cellular Membrane Potentials: Action Potentials and Beyond

The many ion gradients across the plasma membrane create a cellular level-V_{mem}, which is generally uniform across a cell due to free diffusion of ions within the cytosol. One type of dynamic

cellular V_{mem} signal is the action potential (AP) fired by excitable cells. APs in mammalian neurons typically last a few milliseconds in total, involving a rapid depolarization followed by rapid hyperpolarization.[22] Generally, action potentials are triggered when a smaller V_{mem} change known as an excitatory postsynaptic potential (EPSP) brings the cellular V_{mem} above the threshold for firing. EPSPs are small in magnitude (approximately 10 mV) relative to the 100 mV action potentials. The waveform and kinetics of these AP and EPSP signals are determined, in large part, by the identity and expression of ion channels in the cell.[22]

Documentation of fast V_{mem} events in the cell requires high ***temporal resolution*** and ***signal to noise***. These two constraints have been the main focus for development of V_{mem} recording platforms, and modern versions of electrode-based and optical strategies reflect excellent progress toward these hard-to-reach aims (see below). To extend recordings from milliseconds to minutes, hours, or days, two new requirements emerge: the V_{mem} recording technique must be ***absolute*** (stably reporting V_{mem} in mV, not as a relative measure), and ***non-invasive***, as cellular processes must continue normally under chronic observation.

Longer-lasting V_{mem} signals have been described in many contexts, and they present a different set of challenges. The "resting" membrane potential of neurons (i.e. the V_{mem} in between action potentials) affects, among other things, the propensity to fire action potentials. Neuronal resting V_{mem} changes in association with – and perhaps also regulates – many processes, including cellular metabolism,[23] and circadian rhythm.[24] The progression and role of neuronal V_{mem} in differentiation and development is the source of debate, with some conclusions depending on the measurement technique used.[25–27] Furthermore, non-excitable cells also show V_{mem} changes on timescales ranging from minutes to hours, often broadly related to growth. For example, V_{mem} changes associated with progression from G1 to S phase of the cell cycle have been documented in a variety of cell lines,[28–30] and epidermal growth factor receptor activation can be accompanied by a V_{mem} signal.[31–33]

Subcellular Membrane Potential Differences: Organelles and V_{mem} Compartmentalization

To study subcellular V_{mem} differences, a technique requires exquisite ***spatial resolution***, in addition to the other features already discussed. The strategy must be able to access, resolve, and record from the subcellular structure with sufficient signal to noise.

Because V_{mem} originates from ion concentration gradients, subcellular V_{mem} differences can only exist in areas of electrical compartmentalization, where ion diffusion is regionally restricted. Partial compartmentalization produces transient or metastable local differences in V_{mem}. For example, neurons exhibit transient subcellular differences in V_{mem}, as voltage waveforms are transmitted and processed by dendrites[34] and the axon initial segment.[35] Visualization of dendritic computation and action potential propagation pushes the temporal resolution even further, with recording rates often exceeding 10 kHz.[36] For stable subcellular differences to exist, the resistance to ion flow between compartments must be even higher. Dendritic spines in neurons, which are micron-scale structure with high-resistance bottlenecks between the spine and the cell's dendrite, may be electrically distinct from the neuron proper; spine properties are currently of great interest for their potential role in learning and memory.[18] To our knowledge, electrical compartmentalization at the plasma membrane in non-excitable cells has yet to be conclusively shown. Nevertheless, the enrichment of ion channels in particular subcellular regions such as primary cilia[37] and filopodia[38] suggests that non-uniform plasma membrane V_{mem} is plausible.

Organellar membranes also offer an opportunity for ionic, and therefore V_{mem}, compartmentalization. The mitochondrial membrane potential (and H^+ gradient) is required for successful oxidative phosphorylation,[12] the lysosome contains excitable channels,[11] and the endoplasmic reticulum membrane potential has been reported to respond to cellular V_{mem}.[39] Due to technical limitations, much of the evidence for organellar V_{mem} differences is at the level of channel expression, rather than functional recordings. Proteomic and transcriptomic studies of organellar channels and transporters imply complex physiology;[40] our current understanding may be just the tip of the iceberg in this system.

Delocalized Membrane Potentials in Electrically Coupled Tissues

At the other extreme of length scale, membrane potential can be delocalized across tissues via gap junctions, which allow free flow of ions and many small molecules between cells. Such electrical coupling enables transmission of V_{mem} signals across a population of cells; it also precludes "independent" V_{mem} between adjacent and tightly coupled cells. Early studies of electrical coupling were performed in the Drosophila salivary gland, where the resistance to current flow between cells was only slightly higher than the resistance of the cytosol.[19] Since then, gap junctions have been found to be ubiquitous, and other roles for this electrical coupling have been discovered, such as enabling rapid, synchronous electrical signaling in the heart.[20]

Many observations about V_{mem} signaling are made on isolated cells in culture, obviating any delocalized V_{mem} signaling. For epithelial cells that exist in vivo as a tightly coupled tissue, this is an artificial electrical state. It remains unclear how and to what extent observations made on isolated cells will translate into tissues. Is it possible, say, for a cell that is part of an electrically coupled monolayer to experience V_{mem} changes related to its individual cell cycle progression or as a response to a growth factor stimulus? Theoretical studies suggest that, in some conditions, stable and meta-stable electrical patterning is possible, but it is highly dependent on the electrical coupling in the tissue.[41,42] These data suggest that V_{mem} signals are perhaps accompanied – or at least modulated by – dynamic regulation of cell-cell coupling. Direct experimental interrogation of these issues is needed, but it requires ***throughput*** or access to multiple recordings simultaneously, as well as ***the ability to measure in situ***. Although some progress has been made to this end,[21] such measurements are largely unexplored.

Taken together, diverse biological questions necessitate a non-invasive, high throughput, in situ V_{mem} platform with excellent spatiotemporal and voltage resolution measurement. From the array of methods available today, no single approach shows all of these characteristics. Indeed, more realistically, a toolkit of V_{mem} recording strategies will be required to fully interrogate this signal. Below, we discuss the performance of existing V_{mem} strategies, with an eye toward their ability to access signals across a broad range of space and time.

Electrode-based Approaches for Recording Absolute Membrane Potential

Electrode-based techniques are the gold standard for recording membrane potentials, ion channel properties, and currents in cells, and they are the foundation of most knowledge about V_{mem}. We discuss electrode-based strategies for measuring absolute V_{mem} (**Figure 1.2**), along with recent efforts to reduce invasiveness and improve throughput.

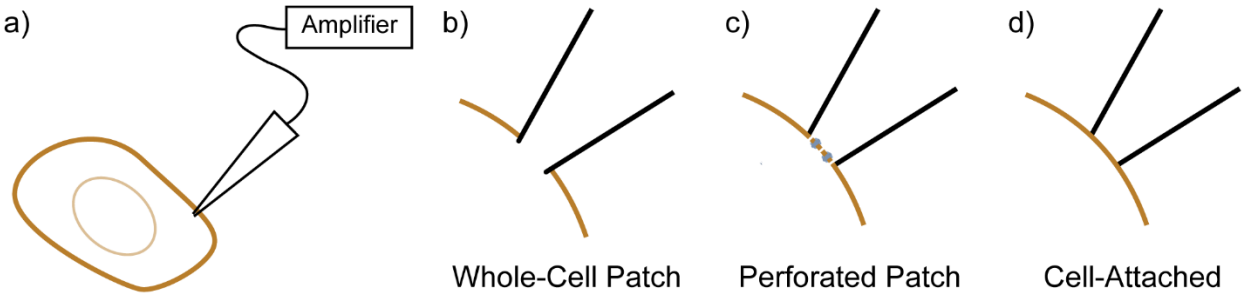

Figure 1.2. Electrode-based configurations for recording absolute V_{mem}.
a) In general, the cell is approached with a microelectrode attached to an amplifier. One the approach to the cell has been made, a variety of configurations are possible; we focus here on those that can report cellular V_{mem}. b) Zoom-in of the interface between the electrode and membrane from (a). In the whole-cell patch configuration, the membrane is ruptured and a path between the electrode tip and the cell is established. c) In perforated patch, introduction of an ionophore allows ionic flow across the plasma membrane, but the membrane is not fully ruptured. d) In the cell attached configuration, the plasma membrane remains intact.

Intracellular Recordings of Absolute V_{mem}

By far the most common strategy for recording V_{mem} is intracellular recording, in which V_{mem} is determined from the difference in potential between a recording electrode in the cytosol and a reference electrode in the extracellular solution. More detailed treatment of the many capabilities of intracellular recording can be found elsewhere;[43] we focus only on V_{mem} measurement. Two main types of intracellular recordings exist: sharp electrode and whole cell recordings. Sharp microelectrodes possess very fine tips and high tip resistances, which produces a variable tip potential and a V_{mem} artifact on the order of tens of millivolts.[43,44] Furthermore, they create a leak in the cell of interest, which can depolarize it artificially.[44] Although sharp electrode recordings are still in use in certain *in vivo* preparations, they have largely been replaced by intracellular recordings in the whole-cell configuration. These "gigaseal" recordings use much larger patch electrodes with lower tip potentials; such electrodes can be sealed onto the cell with less damage than sharp electrodes.[45] Whole cell recordings can also provide higher resolution information about the particular ions and types of channels involved in setting the resting membrane potential.

Intracellular recording is a direct, in situ measure of V_{mem} with sub-mV precision and excellent temporal resolution, but it suffers from a variety of drawbacks. The whole cell patch is highly invasive, creating a large path between the electrode and the cell. This causes the electrode internal solution to dialyze the cytosol, eventually washing out soluble signaling factors.[43,46] The whole cell configuration also can misrepresent membrane potentials due to these disruptions in the cell and leaks in the seal between the recording electrode and the membrane.[25] Furthermore, intracellular recordings are challenging to execute. Attempting each whole cell recording takes an expert researcher or specialized robot approximately 5 minutes, with a 30% success rate for these efforts.[47] Therefore, recording across many cells in the same tissue is nearly impossible, as is cataloguing V_{mem} subpopulations over many cells. More subtly, an electrode has poor spatial resolution, reporting V_{mem} at a point of contact. For tissues with contiguous and partially electrically coupled cells, the effective recording area is unknown. For subcellular recordings,

electrode-based strategies struggle to physically access subcellular compartments, as the size of the electrode tip provides a lower bound on the size of structures that can be interrogated.[48,49]

Reducing Invasiveness: Cell-Attached and Perforated Patch Configurations

To mitigate the washout of soluble factors associated with whole cell recording, it would be useful to measure V_{mem} without disrupting the membrane. This is possible in the "cell attached" configuration, in which an extracellular patch electrode is sealed onto the cell without rupturing the plasma membrane. If the membrane resistance is approximately 100-fold lower than the seal resistance, the voltage across the small membrane region under the pipette will reflect the cellular V_{mem} reasonably accurately.[50] Alternatively, if the channel composition and electrical properties are known in the cells of interest, then the reversal potential of these channels (determined in the cell attached configuration) can also be used to infer V_{mem}. Such techniques have been demonstrated with the K^+ reversal potential in hippocampal interneurons,[51] as well as the NMDA reversal potential in hippocampal CA3 neurons.[25] However, this strategy is difficult to extend, as it requires detailed knowledge of the behavior of channels in the specific system of interest.

Perforated patch recordings offer a more general solution to reduce invasiveness of whole cell recordings.[52,53] With perforated patch, an ionophore placed in the pipette internal solution allows ions to cross the membrane in the cell attached configuration, thereby electrically connecting the cytosol with the pipette solution. Perforated patch recording can last over an hour without run-down of relevant cytosolic factors.[52,54] By providing an alternative to the standard whole cell configuration, it also opened the door for identification of discrepancies in V_{mem} and other passive membrane properties obtained by the two recording approaches.[55]

Engineering Electrodes for Improved Performance: Planar Patch Clamp and Nanopipettes

Efforts to improve electrode-based recordings have also turned to the electrodes themselves. With the development of low-noise arrays of patch electrodes,[56] commercial planar patch clamp systems can now perform simultaneous, automated electrophysiological experiments in 384 or 768 well arrayed format. These systems are increasingly used to screen compound libraries against ion channel targets, expediting the drug discovery process. However, the system requires a suspension of dissociated cells, which precludes recording in situ and over extended time courses. As a result, planar patch clamp is more suited for high throughput screening of ion channel pharmacology than analysis cellular or tissue level voltage signaling.

On the other hand, the development of nanopipettes has enabled electrode-based access to broader length scales, ranging from sub-micron subcellular structures[57] to in vivo recordings during animal behavior.[58] These nanopipettes are a smaller version of sharp microelectrodes; their reduced size brings flexibility and access to small cellular compartments. As with sharp electrodes, the high tip resistances of the nanopipettes filter the signal and create a shunt that changes the observed V_{mem}, so the output signal must be processed to obtain accurate results. Demonstrating the power of this technology, Jayant et al. used nanopipettes to record electrical activity in dendritic spines, providing some of the first direct evidence for functional voltage compartmentalization in these structures.[57] Overall, nanopipettes represent a promising avenue for increasing the spatial reach of electrophysiology.

Calibrated Optical Signals for Recording Absolute Membrane Potential

As an alternative to electrode-based approaches, a variety of optical V_{mem} measurement strategies use fluorescence as a proxy for V_{mem}. These systems rely on small molecule or protein-based probes which have been engineered to display V_{mem}-sensitive fluorescence. Because this is an indirect measure of V_{mem}, calibration is required to interpret the fluorescence signal in units of V_{mem}. Optical platforms generally enjoy excellent spatial resolution, low invasiveness, and medium throughput. However, achieving the requisite temporal resolution, voltage resolution, and signal-to-noise has required more engineering. Below, we broadly group optical strategies into three categories (single color, ratio-based, and spectroscopic), discussing the performance of each with respect to our wish list of features.

Calibration of Optical V_{mem} Reporters

Rigorous calibration is an essential first step for meaningful interpretation of optical V_{mem} recordings. To provide context for the following sections on fluorescent techniques, we first outline strategies for setting V_{mem} to a known value to calibrate the fluorescence signal. As we will discuss, a key difference among the various fluorescence-based strategies is the reproducibility of this calibration, as well as its dependence on V_{mem}-independent artifacts.

The most accurate method for calibrating fluorescence with respect to V_{mem} is whole cell voltage clamp electrophysiology, which uses intracellular recording instrumentation similar to the one described above to inject current until the cell reaches the desired V_{mem}. The response across a range of V_{mem} can be evaluated, determining a calibration with both a slope and y-intercept. However, this approach is best when performed in isolated, single cells, and it suffers from the limitations of electrophysiology discussed above.

If the system is inaccessible to electrode-based strategies, either pharmacology or intrinsic V_{mem} signals can approximate aspects of the V_{mem} calibration. Reference points have been established using ionophores for the primary ion establishing V_{mem},[59–62] high extracellular K^+ (120-150 mM),[59,63] and cell death/fixation with paraformaldehyde (PFA).[60] PFA and ionophores produce a more reliable 0 mV point than high K^+ treatments, but they interact with the plasma membrane itself, which can change the fluorescence properties of the voltage sensor.[64] Furthermore, there is no reliable way to access the sensitivity (slope) of the calibration from a single point determined by pharmacology. On the other hand, in samples with well-described intrinsic electrical responses, these electrical responses can provide an approximate calibration. Demonstrated reference voltage signals include sustained hyperpolarization in Purkinje cells,[65] depolarization resulting from glutamate uncaging,[66] and back-propagating action potentials in dendrites.[67] Such strategies are non-invasive but are limited to the small subset of samples where a useful and consistent V_{mem} signal can be identified.

In many cases, this limited set of calibration options is inadequate. Recently developed optical strategies for V_{mem} control may eventually provide an alternative to the above approaches, although they have yet to demonstrate V_{mem} tuning to defined voltages. Engineering efforts for optical V_{mem} actuators have focused on channelrhodopsins, proteins which pass current in response to light. For setting V_{mem} optically, step-function opsins may be particularly useful, as they continue to pass current for minutes after initial activation.[68,69] More recently, light sensitivity was engineered into mammalian ion channels via domain insertion, allowing diverse channels to serve

as optogenetic actuators.[70] These strategies could eventually allow precise setting of V_{mem} without an electrode, moving close to truly all-optical electrophysiology.

Single-Color, Fluorescence Intensity Recordings

We now turn to the optical platforms themselves. Single color fluorescence intensity is the simplest fluorescent V_{mem} sensor, wherein the fluorescence of a probe is modulated by the membrane potential. A variety of V_{mem} sensing triggers have been documented, [71–74] and many of these probes display sufficiently fast kinetics to follow millisecond-time action potentials. State-of-the-art systems can achieve cell-resolved recording of single action potentials in vivo from superficial brain regions, often with subcellular detail.[75–77] However, single color fluorescence intensity is best suited for V_{mem} event detection, or at most quantification of relative V_{mem} changes. Fluorescence intensity by itself cannot be stably calibrated as a proxy for absolute membrane potential, as it is subject to artifacts arising from variable loading/trafficking, morphology, photobleaching, quenching, and illumination intensity. As a result, single color fluorescence intensity measurements are ill equipped to describe voltage states that change on timescales longer than seconds.

Some attempts have been made to circumvent this issue by performing calibrations on every cell of interest, partially cancelling out the contribution of non-V_{mem} artifacts to the fluorescence signal. Electrophysiological calibration of each individual cell is impractical, so fluorescence intensity calibrations are generally performed with less-accurate pharmacological strategies. For example, gramicidin-based calibrations and the V_{mem} indicator Archaerhodopsin (Arch) revealed subcellular differences in the action potential waveform.[62] Such studies are broadly useful for understanding dendritic computation and are perhaps the only viable strategy for provide spatially resolved, simultaneous recording of V_{mem} across the neuronal arbor.

Nevertheless, while calibration of a single color V_{mem} sensor has seen some success, single color fluorescence intensity recordings generally display poor V_{mem} resolution and are prone to artifacts. When calibrating from a single pharmacological set point rather than a range of V_{mem} set by an electrode, the researcher must assume that the fractional change in fluorescence (%$\Delta F/F$) per mV of the indicator is the same for all samples. In reality, the $\Delta F/F$ response to a ΔV_{mem} will depend on the ratio of productively engaged sensor to background sensor, which may vary in space with trafficking or loading of the sensor. Furthermore, many voltage sensors display sensitivity to membrane composition,[78] which varies not only between cells but also within cells with intricate protrusions and processes.[79]

Ratio-based Fluorescent Sensors Improve Reproducibility

Ratio-based voltage sensors, based on comparison between the fluorescence intensity in two channels, provide more reproducible voltage measurements than single-color fluorescence intensity. If the stoichiometry between the two signals is known, the second channel can be used to correct for variability due to cell morphology, dye loading, and/or other confounding factors associated with intensity-based imaging. Ideally, the corrected signal would then be a stable proxy for absolute V_{mem} across many cells without recalibration. Three strategies for ratio-based fluorescent V_{mem} sensors have been investigated in the literature: molecular beacons, FRET, and electrochromism.

One architecture for ratio-based sensors uses a molecular beacon, where the sensor contains one fluorophore that is voltage-sensitive and a second fluorophore as a voltage-independent reference. To this end, Yamuna Krishnan and co-workers recently developed Voltair,[80] a membrane potential probe comprised of the VoltageFluor RVF5 [81] and the reference probe ATTO 647N. Using this strategy, combined with DNA-based delivery, they recorded resting membrane potentials of organelle membranes. This work demonstrates the superior spatial resolution and reach of optical tools versus electrophysiology, although they did dissolve the plasma membrane with digitonin for probe delivery. Because organelles are difficult to interrogate with electrodes, calibration of Voltair in organellar membranes only performed pharmacologically. As a result, it is difficult to estimate the V_{mem} resolution of Voltair or document any V_{mem}-independent artifacts. Improvements in calibration strategies will enable better benchmarking of organellar probes.

Another class of ratio-based voltage sensors employ Förster resonance energy transfer (FRET), wherein energy transfer from a donor to an acceptor fluorophore is V_{mem}-sensitive. Because the fluorescence intensities of the donor and acceptor are voltage sensitive in opposite directions, the ratio of the two can provide better fractional responses and higher signal to noise than a single color alone. Although a variety of FRET-based V_{mem} sensors exist,[82] we are not aware of their use to document absolute V_{mem}, largely due to variable stoichiometry between the donor and acceptor. For genetically encoded systems, different rates of photobleaching, folding, and productive trafficking to the plasma membrane lead to variability in FRET ratios between cells.[83] Screening more directly for correct localization, as recently shown with a single-color GEVI,[76] could produce improved FRET-based GEVIs in the future. With small molecule FRET-oxonol systems, differences in loading between the two lipophilic indicators leads to variability in the $\%\Delta F/F$.[84] As a result, FRET-based sensors do not produce ratio-based measurements that are stable between samples. In practice, these probes are primarily used to detect action potentials, with the second color existing to improve signal to noise or reduce motion artifacts.

Electrochromic dyes, such as the ANEPPS[85] and ANNINE[86] classes, show V_{mem}-dependent excitation and/or emission spectra. A ratio-based signal can be obtained by comparing the emission in a fixed band produced by excitation at two different wavelengths (or vice versa with a fixed excitation and two emission bands). Because electrochromic sensors are based on a charge shift mechanism, they have sub-millisecond temporal responses. ANEPPS fluorescence ratios can be calibrated with electrophysiology, revealing 5 mV resolution for quantifying V_{mem} *changes* on an individual cell.[87,88] To achieve this accuracy, ANEPPS fluorescence ratios must be calibrated with an electrode on each cell of interest, limiting throughput dramatically. The origin of the variability of the absolute ratio between cells is unclear; it likely depends on a complex combination of temperature, membrane composition, and probe loading. Nevertheless, normalized ANEPPS ratios are useful for mapping V_{mem} across cells. In combination with random access microscopy, di-8-ANEPPS ratios can report the action potential waveform in absolute V_{mem} optically with excellent spatiotemporal resolution (0.5 ms and 2 μm).[88]

Spectroscopic Approaches: Measurement of Intrinsic Properties

A more recent strategy for absolute voltage imaging is to record an intrinsic property of a probe instead of the extrinsic fluorescence intensity. Fluorescence lifetime (τ_{fl}), or the amount of time that probe molecules remain in the fluorescent excited state, has recently garnered attention as a relatively general way to access absolute optical readouts from a single fluorescence channel [89]. τ_{fl}

is independent of fluorophore concentration, cellular morphology, and (mostly) photobleaching, although it displays sensitivity to parameters such as temperature and viscosity. The primary downside to lifetime imaging is its poor temporal resolution, with most acquisition times on the order of seconds. If the lifetime of a V_{mem} sensor is V_{mem}-sensitive, it ideally will be a stable proxy for V_{mem}. We focus below on the most complete demonstrations of FLIM as a reporter for V_{mem}, namely those with genetically encoded voltage indicators (GEVIs) [83,90] and small molecule voltage sensors based on photoinduced electron transfer (this work).[33] V_{mem}-sensitive FLIM has been demonstrated for FRET-oxonol V_{mem} sensors[91] and for accumulation-based sensors of mitochondrial potential,[92] but no estimation of the absolute V_{mem} resolution was made in these systems.

Raman imaging has also been investigated as a strategy for absolute V_{mem} recordings. Recently, the Stimulated Raman Scattering (SRS) signal of near-infrared opsins was investigated in *E. coli* membranes. Some bulk depolarization following cell sonication was detectable, but absolute V_{mem} determinations were not made. In addition, SRS has been previously demonstrated to be a useful strategy for detection of neuronal action potentials[93] (i.e. not absolute V_{mem} determination). Although the voltage resolution of these approaches remains unknown, they are potentially interesting avenues for absolute V_{mem} sensing.

The excited state properties of certain single color GEVIs can report absolute V_{mem}, using the temporal dynamics of the indicator[83] and, in some cases, the fluorescence lifetime.[90] Use of a complex pump-probe system to probe temporal dynamics enables 10 mV absolute V_{mem} resolution between cells,[83] an unprecedented value. However, access to and interpretation of such data is challenging for most laboratories, limiting its utility as a general V_{mem} sensing platform. Using fluorescence lifetime alone, a much more accessible platform, reveals a 20 mV accuracy for quantifying voltage *changes* on a given cell in a one second bandwidth, but without the ability to quantify absolute V_{mem} between cells with biologically useful resolution. The source of variability in this lifetime-only measurement is likely the complex dynamics of rhodopsin fluorescence, as well as the presence of intracellular fluorescence signal from incorrectly trafficked protein.

Fluorescence lifetime-based absolute V_{mem} imaging was developed further in this dissertation, using small-molecule VoltageFluors (VFs) instead of GEVIs as the voltage indicator. VoltageFluors localize to the outer leaflet of the cell membrane, where they report V_{mem} through changes in the rate of photoinduced electron transfer (PeT) from a membrane-localized electron donor ("molecular wire") to a fluorophore.[94] PeT provides a nonradiative decay pathway for the fluorophore excited state; increases in PeT lead to decreases in fluorescence.[95] Because the PeT process is sensitive to the electric field created by V_{mem}, VFs exhibit rapid, linear fluorescence responses to V_{mem}. The PeT V_{mem} sensing trigger can be engineered via modifications to the molecular wire,[96,97] and it is generalizable to fluorophores across the electromagnetic spectrum.[98–100]

Because PeT offers an additional pathway for relaxation to the ground state from the fluorescent excited state, it leads to V_{mem}-dependent changes in both the fluorescence intensity and the fluorescence lifetime. In this dissertation, we show that the fluorescence lifetime of the fluorescein-based VoltageFluor VF2.1.Cl (VF-FLIM) can be calibrated to report absolute V_{mem}. These recordings exhibit a resolution of 5 mV for quantifying voltage changes on individual cells and a resolution of 20 mV for determining absolute V_{mem}. Because VF-FLIM calibrations are consistent

for a given cell line, we were able to obtain V_{mem} distributions across thousands of cells after an initial electrode-based calibration on only a few cells. We applied VF-FLIM to study a 15 mV hyperpolarizing response to growth factor stimulation in cancer cells, showcasing its potential for elucidating diverse signaling roles of V_{mem} (**Chapter 2**, **Chapter 3**).[33] We also explore the relationship between VF structure and lifetime response to V_{mem} (**Chapter 4**), as well as the use of VFs for absolute V_{mem} recording under two-photon illumination (**Chapter 6**).

A key limitation of VF-FLIM based on VF2.1.Cl is its temporal resolution, which is limited by the 15 to 30 second acquisition times. Using a red-shifted, carborhodamine-based VoltageFluor and a microscope with improved photon collection efficiency, we improved the temporal resolution 300-fold, recording spontaneous action potentials in cardiomyocytes in real time (20 Hz frame rates, **Chapter 5**). Improvements to photon counting FLIM hardware, as well as fast frequency-domain FLIM strategies,[101] may enable even faster VF-FLIM recordings. Overall, FLIM-based absolute V_{mem} imaging method extends the timescale over which V_{mem} can be recorded and displays some of the best V_{mem} resolution to date for optical systems.

Outlook

V_{mem} signals run the gamut from milliseconds to days and from subcellular to tissue-level (**Figure 1.3**). The existing V_{mem} toolkit can record most cellular V_{mem} signals and some subcellular ones, with time resolutions ranging from milliseconds to minutes. V_{mem} signals in tissues are still almost completely unexplored, especially those occurring over hours to days.

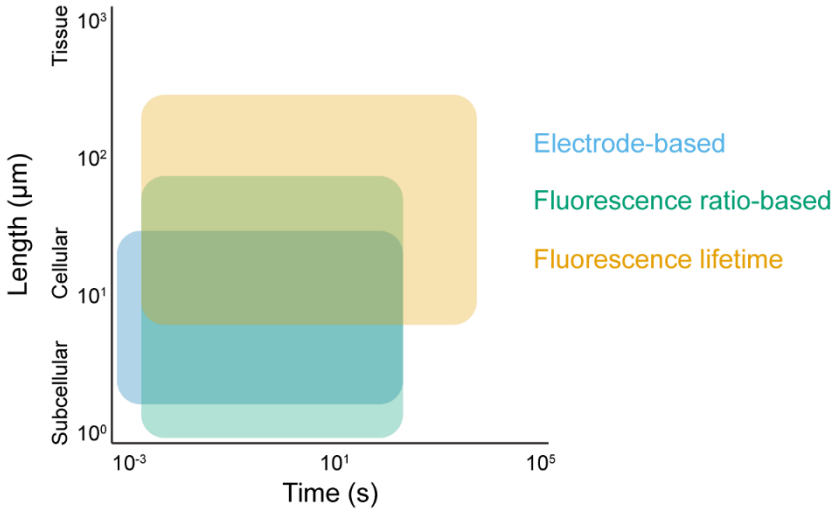

Figure 1.3. Biological scope of the absolute V_{mem} recording toolkit.
Absolute V_{mem} can be recorded with an electrode (blue), with fluorescence ratio-based measurements (green), or with fluorescence lifetime (yellow). Shaded area represents the space and time scales over which each technique has been demonstrated (including in this dissertation), not necessarily their full potential. Each strategy has its own V_{mem} resolution, as well as different spatial and temporal resolution. V_{mem} measurements over days or on the scale of tissues remain challenging for all strategies.

Electrode-based absolute V_{mem} recordings have defined the field for years and will remain essential, as engineering efforts continue to improve throughput and reduce invasiveness. On the other hand, progress in optical approaches for absolute membrane potential recording, especially the fluorescence-lifetime based strategies discussed herein, have already expanded the range of space and time over which V_{mem} can be recorded. We look forward to application of this absolute V_{mem} toolkit to some of the biological questions outlined above (**Figure 1.1**).

A key limitation of optical, absolute V_{mem} recording is the need for calibration in the cell or tissue of interest; we excitedly await improved optical actuators for V_{mem}. Further improvements in voltage-sensitive dyes and proteins stand to increase the absolute V_{mem} resolution of existing optical approaches, as well as enable additional spectroscopic strategies for V_{mem} quantification. The temporal resolution of optical V_{mem} recording in vivo can be further improved by combination with lattice light-sheet imaging[102] and other fast volumetric imaging strategies.[103]

With these technological improvements, we are beginning to construct a picture of V_{mem} across biological time and space scales. However, much remains to be done before we have a comprehensive catalog of V_{mem}. In particular, the functional link between V_{mem} "at rest" and ion channel activity remains unclear. In many systems, ion channel expression data hints at potential V_{mem} signaling, but no functional recordings of V_{mem} have been made. In other arenas, ion channel block causes dramatic cellular phenotypes, but no concrete tie to V_{mem} is established. These paradigms are common in the cancer literature, where ion channels are increasingly under investigation as targets for antiproliferative drugs.[4,104] Direct V_{mem} recordings in these arenas will illuminate whether these ion channels are transmitting information via V_{mem} or through some other pathway.

More fundamentally, the information carried by V_{mem} signals in diverse contexts is unknown, and the molecular mechanism of V_{mem} responses are obfuscated. As new V_{mem} signals are documented, they raise additional questions: How does the cell bring about these V_{mem} changes? Which cellular components respond to V_{mem}? How are these signals transduced to downstream cellular processes? A step toward addressing these questions was made with Patch-Seq, which combined electrophysiological recordings with single cell RNA sequencing.[105] Uncovering the signaling networks surrounding V_{mem} will require more V_{mem} sensing platforms that interface with other cell profiling and "omics" techniques. With such efforts, we move ever closer to a systems-level understanding of membrane potential in all its diverse glory.

References

(1) Rolfe, D. F. S.; Brown, G. C. Cellular Energy Utilization and Molecular Origin of Standard Metabolic Rate in Mammals. *Physiol. Rev.* **1997**, *77* (3), 731–758. https://doi.org/10.1152/physrev.1997.77.3.731.

(2) Abdul Kadir, L.; Stacey, M.; Barrett-Jolley, R. Emerging Roles of the Membrane Potential: Action beyond the Action Potential. *Front. Physiol.* **2018**, *9*, 1661. https://doi.org/10.3389/fphys.2018.01661.

(3) Cone, C. D.; Cone, C. M. Induction of Mitosis in Mature Neurons in Central Nervous System by Sustained Depolarization. *Science* **1976**, *192* (4235), 155–158. https://doi.org/10.1126/science.56781.

(4) Huang, X.; Jan, L. Y. Targeting Potassium Channels in Cancer. *J. Cell Biol.* **2014**, *206* (2), 151–162. https://doi.org/10.1083/jcb.201404136.

(5) Tsuchiya, W.; Okada, Y. Membrane Potential Changes Associated with Differentiation of Enterocytes in the Rat Intestinal Villi in Culture. *Dev. Biol.* **1982**, *94* (2), 284–290. https://doi.org/10.1016/0012-1606(82)90348-7.

(6) Chen, L.; Becker, T. M.; Koch, U.; Stauber, T. The LRRC8/VRAC Anion Channel Facilitates Myogenic Differentiation of Murine Myoblasts by Promoting Membrane Hyperpolarization. *J. Biol. Chem.* **2019**, No. 3, jbc.RA119.008840. https://doi.org/10.1074/jbc.ra119.008840.

(7) Levin, M. Molecular Bioelectricity: How Endogenous Voltage Potentials Control Cell Behavior and Instruct Pattern Regulation in Vivo. *Mol. Biol. Cell* **2014**, *25* (24), 3835–3850. https://doi.org/10.1091/mbc.E13-12-0708.

(8) Prindle, A.; Liu, J.; Asally, M.; Ly, S.; Garcia-Ojalvo, J.; Suel, G. M.; Süel, G. M. Ion Channels Enable Electrical Communication in Bacterial Communities. *Nature* **2015**, *527* (7576), 59–63. https://doi.org/10.1038/nature15709.

(9) Larkin, J.; Garcia-Ojalvo, J.; Prindle, A.; Liu, J.; Gabalda-Sagarra, M.; Süel, G. M.; Lee, D. D.; Martinez-Corral, R. Coupling between Distant Biofilms and Emergence of Nutrient Time-Sharing. *Science (80-.).* **2017**, *356* (6338), 638–642. https://doi.org/10.1126/science.aah4204.

(10) Lee, D. D.; Galera-Laporta, L.; Bialecka-Fornal, M.; Moon, E. C.; Shen, Z.; Briggs, S. P.; Garcia-Ojalvo, J.; Süel, G. M. Magnesium Flux Modulates Ribosomes to Increase Bacterial Survival. *Cell* **2019**, 352–360. https://doi.org/10.1016/j.cell.2019.01.042.

(11) Cang, C.; Bekele, B.; Ren, D. The Voltage-Gated Sodium Channel TPC1 Confers Endolysosomal Excitability. *Nat. Chem. Biol.* **2014**, *10* (6), 463–469. https://doi.org/10.1038/nchembio.1522.

(12) Zorova, L. D.; Popkov, V. A.; Plotnikov, E. Y.; Silachev, D. N.; Pevzner, I. B.; Jankauskas, S. S.; Babenko, V. A.; Zorov, S. D.; Balakireva, A. V.; Juhaszova, M.; et al. Mitochondrial Membrane Potential. *Anal. Biochem.* **2018**, *552*, 50–59. https://doi.org/10.1016/j.ab.2017.07.009.

(13) Zhang, J.; Chen, X.; Xue, Y.; Gamper, N.; Zhang, X. Beyond Voltage-Gated Ion Channels: Voltage-Operated Membrane Proteins and Cellular Processes. *J. Cell. Physiol.* **2018**, *233* (10), 6377–6385. https://doi.org/10.1002/jcp.26555.

(14) Murata, Y.; Iwasaki, H.; Sasaki, M.; Inaba, K.; Okamura, Y. Phosphoinositide Phosphatase Activity Coupled to an Intrinsic Voltage Sensor. *Nature* **2005**, *435* (7046), 1239–1243. https://doi.org/10.1038/nature03650.

(15) Rinne, A.; Birk, A.; Bünemann, M. Voltage Regulates Adrenergic Receptor Function. *Proc. Natl. Acad. Sci. U. S. A.* **2013**, *110* (4), 1536–1541. https://doi.org/10.1073/pnas.1212656110.

(16) Rinne, A.; Mobarec, J. C.; Mahaut-Smith, M.; Kolb, P.; Bünemann, M. The Mode of Agonist Binding to a G Protein-Coupled Receptor Switches the Effect That Voltage Changes Have on Signaling. *Sci. Signal.* **2015**, *8* (401), ra110. https://doi.org/10.1126/scisignal.aac7419.

(17) Zhou, Y.; Wong, C.; Cho, K.; van der Hoeven, D.; Liang, H.; Thakur, D. P.; Luo, J.; Babic, M.; Zinsmaier, K. E.; Zhu, M. X.; et al. Membrane Potential Modulates Plasma Membrane Phospholipid Dynamics and K-Ras Signaling. *Science (80-.).* **2015**, *349* (6250), 873–876. https://doi.org/10.1126/science.aaa5619.

(18) Yuste, R. Electrical Compartmentalization in Dendritic Spines. *Annu. Rev. Neurosci.* **2013**, *36* (1), 429–449. https://doi.org/10.1146/annurev-neuro-062111-150455.

(19) Loewenstein, W. R.; Kanno, Y. Studies on an Epithelial (Gland) Cell Junction I. Modifications of Surface Membrane Permeability. *J. Cell Biol.* **1964**, *22*, 565–586.

(20) Rohr, S. Role of Gap Junctions in the Propagation of the Cardiac Action Potential. *Cardiovasc. Res.* **2004**, *62* (2), 309–322. https://doi.org/10.1016/j.cardiores.2003.11.035.

(21) Ceriani, F.; Mammano, F. A Rapid and Sensitive Assay of Intercellular Coupling by Voltage Imaging of Gap Junction Networks. *Cell Commun. Signal.* **2013**, *11* (1), 78. https://doi.org/10.1186/1478-811X-11-78.

(22) Bean, B. P. The Action Potential in Mammalian Central Neurons. *Nat. Rev. Neurosci.* **2007**, *8* (6), 451–465. https://doi.org/10.1038/nrn2148.

(23) Sada, N.; Lee, S.; Katsu, T.; Otsuki, T.; Inoue, T. Targeting LDH Enzymes with a Stiripentol Analog to Treat Epilepsy. *Science (80-.).* **2015**, *347* (6228), 1362–1367. https://doi.org/10.1126/science.aaa1299.

(24) LeSauter, J.; Silver, R.; Cloues, R.; Witkovsky, P. Light Exposure Induces Short- and Long-Term Changes in the Excitability of Retinorecipient Neurons in Suprachiasmatic Nucleus. *J. Neurophysiol.* **2011**, *106* (2), 576–588. https://doi.org/10.1152/jn.00060.2011.

(25) Tyzio, R.; Ivanov, A.; Bernard, C.; Holmes, G. L.; Ben-Ari, Y.; Khazipov, R. Membrane Potential of CA3 Hippocampal Pyramidal Cells During Postnatal Development. *J. Neurophysiol.* **2003**, *90*, 2964–2972. https://doi.org/10.1152/jn.00172.2003.

(26) Kasper, E. M.; Larkman, A. U.; Lübke, J.; Blakemore, C. Pyramidal Neurons in Layer 5 of

the Rat Visual Cortex. II. Development of Electrophysiological Properties. *J. Comp. Neurol.* **1994**, *339* (4), 475–494. https://doi.org/10.1002/cne.903390403.

(27) McCormick, D. A.; Prince, D. A. Post-natal Development of Electrophysiological Properties of Rat Cerebral Cortical Pyramidal Neurones. *J. Physiol.* **1987**, *393* (1), 743–762. https://doi.org/10.1113/jphysiol.1987.sp016851.

(28) Wonderlin, W. F.; Woodfork, K. A.; Strobl, J. S. Changes in Membrane Potential during the Progression of MCF-7 Human Mammary Tumor Cells through the Cell Cycle. *J. Cell. Physiol.* **1995**, *165* (1), 177–185. https://doi.org/10.1002/jcp.1041650121.

(29) Wang, S. Y.; Melkoumian, Z.; Woodfork, K. A.; Cather, C.; Davidson, A. G.; Wonderlin, W. F.; Strobl, J. S. Evidence for an Early G1 Ionic Event Necessary for Cell Cycle Progression and Survival in the MCF-7 Human Breast Carcinoma Cell Line. *J. Cell. Physiol.* **1998**, *176* (3), 456–464. https://doi.org/10.1002/(sici)1097-4652(199809)176:3<456::aid-jcp2>3.0.co;2-n.

(30) Arcangeli, A.; Bianchi, L.; Becchetti, A.; Faravelli, L.; Coronnello, M.; Mini, E.; Olivotto, M.; Wanke, E. A Novel Inward-rectifying K+ Current with a Cell-cycle Dependence Governs the Resting Potential of Mammalian Neuroblastoma Cells. *J. Physiol.* **1995**, *489* (2), 455–471. https://doi.org/10.1113/jphysiol.1995.sp021065.

(31) Pandiella, A.; Magni, M.; Lovisolo, D.; Meldolesi, J. The Effects of Epidermal Growth Factor on Membrane Potential. *J. Biol. Chem.* **1989**, *264* (22), 12914–12921.

(32) Magni, M.; Meldolesi, J.; Pandiella, A. Ionic Events Induced by Epidermal Growth Factor: Evidence That Hyperpolarization and Stimulated Cation Influx Play a Role in the Stimulation of Cell Growth. *J. Biol. Chem.* **1991**, *266* (10), 6329–6335.

(33) Lazzari-Dean, J. R.; Gest, A. M. M.; Miller, E. W. Optical Estimation of Absolute Membrane Potential Using Fluorescence Lifetime Imaging. *Elife* **2019**, *8*, e44522. https://doi.org/10.7554/elife.44522.

(34) Stuart, G. J.; Spruston, N. Dendritic Integration: 60 Years of Progress. *Nat. Neurosci.* **2015**, *18* (12), 1713–1721. https://doi.org/10.1038/nn.4157.

(35) Kole, M. H. P.; Stuart, G. J. Signal Processing in the Axon Initial Segment. *Neuron* **2012**, *73* (2), 235–247. https://doi.org/10.1016/j.neuron.2012.01.007.

(36) Beaulieu-Laroche, L.; Toloza, E. H. S.; van der Goes, M. S.; Lafourcade, M.; Barnagian, D.; Williams, Z. M.; Eskandar, E. N.; Frosch, M. P.; Cash, S. S.; Harnett, M. T. Enhanced Dendritic Compartmentalization in Human Cortical Neurons. *Cell* **2018**, *175* (3), 643-651.e14. https://doi.org/10.1016/j.cell.2018.08.045.

(37) Sánchez, A.; Urrego, D.; Pardo, L. A. Cyclic Expression of the Voltage-gated Potassium Channel K V 10.1 Promotes Disassembly of the Primary Cilium. *EMBO Rep.* **2016**, *17* (5), 708–723. https://doi.org/10.15252/embr.201541082.

(38) Jacquemet, G.; Baghirov, H.; Georgiadou, M.; Sihto, H.; Peuhu, E.; Cettour-Janet, P.; He, T.; Perälä, M.; Kronqvist, P.; Joensuu, H.; et al. L-Type Calcium Channels Regulate Filopodia Stability and Cancer Cell Invasion Downstream of Integrin Signalling. *Nat.*

Commun. **2016**, *7*, 13297. https://doi.org/10.1038/ncomms13297.

(39) Rad, M. S.; Cohen, L. B.; Braubach, O.; Baker, B. J. Monitoring Voltage Fluctuations of Intracellular Membranes. *Sci. Rep.* **2018**, *8* (1), 1–9. https://doi.org/10.1038/s41598-018-25083-7.

(40) Xu, H.; Martinoia, E.; Szabo, I. Organellar Channels and Transporters. *Cell Calcium* **2015**, *58* (1), 1–10. https://doi.org/10.1016/j.ceca.2015.02.006.

(41) Cervera, J.; Alcaraz, A.; Mafe, S. Bioelectrical Signals and Ion Channels in the Modeling of Multicellular Patterns and Cancer Biophysics. *Sci. Rep.* **2016**, *6* (January), 1–14. https://doi.org/10.1038/srep20403.

(42) Cervera, J.; Meseguer, S.; Mafe, S. The Interplay between Genetic and Bioelectrical Signaling Permits a Spatial Regionalisation of Membrane Potentials in Model Multicellular Ensembles. *Sci. Rep.* **2016**, *6* (October), 35201. https://doi.org/10.1038/srep35201.

(43) Brette, R.; Destexhe, A. Intracellular Recording. In *Handbook of Neural Activity Measurement*; 2012; pp 44–91.

(44) Li, W.-C.; Soffe, S. R.; Roberts, A. A Direct Comparison of Whole Cell Patch and Sharp Electrodes by Simultaneous Recording From Single Spinal Neurons in Frog Tadpoles. *J. Neurophysiol.* **2004**, *92* (1), 380–386. https://doi.org/10.1152/jn.01238.2003.

(45) Sigworth, F. J.; Neher, E. Single Na+ Channel Currents Observed in Cultured Rat Muscle Cells. *Nature* **1980**, *287* (October), 447–449.

(46) Malinow, R.; Tsien, R. W. Presynaptic Enhancement Shown by Whole-Cell Recordings of Long-Term Potentiation in Hippocampal Slices. *Nature* **1990**, *346* (6280), 177–180. https://doi.org/10.1038/346177a0.

(47) Kodandaramaiah, S. B.; Franzesi, G. T.; Chow, B. Y.; Boyden, E. S.; Forest, C. R. Automated Whole-Cell Patch-Clamp Electrophysiology of Neurons in Vivo. *Nat. Methods* **2012**, *9* (6), 585–587. https://doi.org/10.1038/nmeth.1993.

(48) Delling, M.; Decaen, P. G.; Doerner, J. F.; Febvay, S.; Clapham, D. E. Primary Cilia Are Specialized Calcium Signalling Organelles. *Nature* **2013**, *504* (7479), 311–314. https://doi.org/10.1038/nature12833.

(49) Holcman, D.; Yuste, R. The New Nanophysiology: Regulation of Ionic Flow in Neuronal Subcompartments. *Nat. Rev. Neurosci.* **2015**. https://doi.org/10.1038/nrn4022.

(50) Perkins, K. L. Cell-Attached Voltage-Clamp and Current-Clamp Recording and Stimulation Techniques in Brain Slices. *J. Neurosci. Methods* **2006**, *154* (1–2), 1–18. https://doi.org/10.1016/j.jneumeth.2006.02.010.

(51) Verheugen, J. a; Fricker, D.; Miles, R. Noninvasive Measurements of the Membrane Potential and GABAergic Action in Hippocampal Interneurons. *J. Neurosci.* **1999**, *19* (7), 2546–2555.

(52) Horn, R.; Marty, A. Muscarinic Activation of Ionic Currents Measured by a New Whole-Cell Recording Method. *J. Gen. Physiol.* **1988**, *92* (2), 145–159.

https://doi.org/10.1085/jgp.92.2.145.

(53) Linley, J. E. Perforated Whole-Cell Patch-Clamp Recording. In *Ion Channels: Methods and Protocols, Methods in Molecular Biology*; 2013; Vol. 998, pp 149–157. https://doi.org/10.1007/978-1-62703-351-0.

(54) Korn, S. J.; Horn, R. Influence of Sodium-Calcium Exchange on Calcium Current Rundown and the Duration of Calcium-Dependent Chloride Currents in Pituitary Cells, Studied with Whole Cell and Perforated Patch Recording. *J. Gen. Physiol.* **1989**, *94* (5), 789–812. https://doi.org/10.1085/jgp.94.5.789.

(55) Spruston, N.; Johnston, D. Perforated Patch-Clamp Analysis of the Passive Membrane Properties of Three Classes of Hippocampal Neurons. *J. Neurophysiol.* **1992**, *67* (3), 508–529. https://doi.org/10.1152/jn.1992.67.3.508.

(56) Fertig, N.; Blick, R. H.; Behrends, J. C. Whole Cell Patch Clamp Recording Performed on a Planar Glass Chip. *Biophys. J.* **2002**, *82* (6), 3056–3062. https://doi.org/10.1016/S0006-3495(02)75646-4.

(57) Jayant, K.; Hirtz, J. J.; Plante, I. J.-L.; Tsai, D. M.; De Boer, W. D. A. M.; Semonche, A.; Peterka, D. S.; Owen, J. S.; Sahin, O.; Shepard, K. L.; et al. Targeted Intracellular Voltage Recordings from Dendritic Spines Using Quantum-Dot-Coated Nanopipettes. *Nat. Nanotechnol.* **2017**, *12* (4), 335–342. https://doi.org/10.1038/nnano.2016.268.

(58) Jayant, K.; Wenzel, M.; Bando, Y.; Hamm, J. P.; Mandriota, N.; Rabinowitz, J. H.; Plante, I. J. La; Owen, J. S.; Sahin, O.; Shepard, K. L.; et al. Flexible Nanopipettes for Minimally Invasive Intracellular Electrophysiology In Vivo. *Cell Rep.* **2019**, *26* (1), 266-278.e5. https://doi.org/10.1016/j.celrep.2018.12.019.

(59) Maric, D.; Maric, I.; Smith, S. V.; Serafini, R.; Hu, Q.; Barker, J. L. Potentiometric Study of Resting Potential, Contributing K+ Channels and the Onset of Na+ Channel Excitability in Embryonic Rat Cortical Cells. *Eur. J. Neurosci.* **1998**, *10* (8), 2532–2546. https://doi.org/10.1046/j.1460-9568.1998.00284.x.

(60) Klapperstück, T.; Glanz, D.; Klapperstück, M.; Wohlrab, J. Methodological Aspects of Measuring Absolute Values of Membrane Potential in Human Cells by Flow Cytometry. *Cytom. Part A* **2009**, *75* (7), 593–608. https://doi.org/10.1002/cyto.a.20735.

(61) Novo, D.; Perlmutter, N. G.; Hunt, R. H.; Shapiro, H. M. Accurate Flow Cytometric Membrane Potential Measurement in Bacteria Using Diethyloxacarbocyanine and a Ratiometric Technique. *Cytometry* **1999**, *35* (1), 55–63. https://doi.org/10.1002/(SICI)1097-0320(19990101)35:1<55::AID-CYTO8>3.0.CO;2-2.

(62) Hoppa, M. B.; Gouzer, G.; Armbruster, M.; Ryan, T. A. Control and Plasticity of the Presynaptic Action Potential Waveform at Small CNS Nerve Terminals. *Neuron* **2014**, *84* (4), 778–789. https://doi.org/10.1016/j.neuron.2014.09.038.

(63) Krasznai, Z.; Márián, T.; Balkay, L.; Emri, M.; Trón, L. Flow Cytometric Determination of Absolute Membrane Potential of Cells. *J. Photochem. Photobiol. B Biol.* **1995**, *28* (1), 93–99. https://doi.org/10.1016/1011-1344(94)07099-A.

(64) Montana, V.; Farkas, D. L.; Loew, L. M. Dual-Wavelength Ratiometric Fluorescence Measurements of Membrane Potential. *Biochemistry* **1989**, *28* (11), 4536–4539. https://doi.org/10.1021/bi00437a003.

(65) Canepari, M.; Vogt, K.; Zecevic, D. Combining Voltage and Calcium Imaging from Neuronal Dendrites. *Cell. Mol. Neurobiol.* **2008**, *28* (8), 1079–1093. https://doi.org/10.1007/s10571-008-9285-y.

(66) Vogt, K. E.; Gerharz, S.; Graham, J.; Canepari, M. Combining Membrane Potential Imaging with L-Glutamate or Gaba Photorelease. *PLoS One* **2011**, *6* (10). https://doi.org/10.1371/journal.pone.0024911.

(67) Palmer, L. M.; Stuart, G. J. Membrane Potential Changes in Dendritic Spines during Action Potentials and Synaptic Input. *J. Neurosci.* **2009**, *29* (21), 6897–6903. https://doi.org/10.1523/jneurosci.5847-08.2009.

(68) Berndt, A.; Yizhar, O.; Gunaydin, L. A.; Hegemann, P.; Deisseroth, K. Bi-Stable Neural State Switches. *Nat. Neurosci.* **2009**, *12* (2), 229–234. https://doi.org/10.1038/nn.2247.

(69) Yizhar, O.; Fenno, L. E.; Prigge, M.; Schneider, F.; Davidson, T. J.; Ogshea, D. J.; Sohal, V. S.; Goshen, I.; Finkelstein, J.; Paz, J. T.; et al. Neocortical Excitation/Inhibition Balance in Information Processing and Social Dysfunction. *Nature* **2011**, *477* (7363), 171–178. https://doi.org/10.1038/nature10360.

(70) Coyote-Maestas, W.; He, Y.; Myers, C. L.; Schmidt, D. Domain Insertion Permissibility-Guided Engineering of Allostery in Ion Channels. *Nat. Commun.* **2019**, *10* (1), 1–14. https://doi.org/10.1038/s41467-018-08171-0.

(71) Kulkarni, R. U.; Miller, E. W. Voltage Imaging: Pitfalls and Potential. *Biochemistry* **2017**, *56* (39), 5171–5177. https://doi.org/10.1021/acs.biochem.7b00490.

(72) Miller, E. W. Small Molecule Fluorescent Voltage Indicators for Studying Membrane Potential. *Curr. Opin. Chem. Biol.* **2016**, *33*, 74–80. https://doi.org/10.1016/j.cbpa.2016.06.003.

(73) Xu, Y.; Zou, P.; Cohen, A. E. Voltage Imaging with Genetically Encoded Indicators. *Curr. Opin. Chem. Biol.* **2017**, *39*, 1–10. https://doi.org/10.1016/j.cbpa.2017.04.005.

(74) Yang, H. H.; St-Pierre, F. Genetically Encoded Voltage Indicators: Opportunities and Challenges. *J. Neurosci.* **2016**, *36* (39), 9977–9989. https://doi.org/10.1523/jneurosci.1095-16.2016.

(75) Abdelfattah, A. S.; Kawashima, T.; Singh, A.; Novak, O.; Liu, H.; Shuai, Y.; Huang, Y.-C.; Campagnola, L.; Seeman, S. C.; Yu, J.; et al. Bright and Photostable Chemigenetic Indicators for Extended in Vivo Voltage Imaging. *Science (80-.).* **2019**, *6416* (August), eaav6416. https://doi.org/10.1126/science.aav6416.

(76) Piatkevich, K. D.; Jung, E. E.; Straub, C.; Linghu, C.; Park, D.; Suk, H. J.; Hochbaum, D. R.; Goodwin, D.; Pnevmatikakis, E.; Pak, N.; et al. A Robotic Multidimensional Directed Evolution Approach Applied to Fluorescent Voltage Reporters Article. *Nat. Chem. Biol.* **2018**, *14* (4), 352–360. https://doi.org/10.1038/s41589-018-0004-9.

(77) Adam, Y.; Kim, J. J.; Lou, S.; Zhao, Y.; Xie, M. E.; Brinks, D.; Wu, H.; Mostajo-radji, M. A.; Kheifets, S.; Parot, V.; et al. Voltage Imaging and Optogenetics Reveal Behaviour-Dependent Changes in Hippocampal Dynamics. *Nature* **2019**, *569*, 413–417. https://doi.org/10.1038/s41586-019-1166-7.

(78) Gross, E.; Bedlack, R. S.; Loew, L. M. Dual-Wavelength Ratiometric Fluorescence Measurement of the Membrane Dipole Potential. *Biophys. J.* **1994**, *67* (1), 208–216. https://doi.org/10.1016/S0006-3495(94)80471-0.

(79) Bedlack, R. S.; Wei, M. de; Fox, S. H.; Gross, E.; Loew, L. M. Distinct Electric Potentials in Soma and Neurite Membranes. *Neuron* **1994**, *13* (5), 1187–1193. https://doi.org/10.1016/0896-6273(94)90056-6.

(80) Saminathan, A.; Devany, J.; Pillai, K. S.; Veetil, A. T.; Schwake, M.; Krishnan, Y. A DNA-Based Voltmeter for Organelles. *bioRxiv* **2019**, 523019. https://doi.org/10.1101/523019.

(81) Kulkarni, R. U.; Kramer, D. J.; Pourmandi, N.; Karbasi, K.; Bateup, H. S.; Miller, E. W. Voltage-Sensitive Rhodol with Enhanced Two-Photon Brightness. *Proc. Natl. Acad. Sci.* **2017**, 201610791. https://doi.org/10.1073/pnas.1610791114.

(82) Mishina, Y.; Mutoh, H.; Song, C.; KnÃ¶pfel, T. Exploration of Genetically Encoded Voltage Indicators Based on a Chimeric Voltage Sensing Domain. *Front. Mol. Neurosci.* **2014**, *7* (September), 1–8. https://doi.org/10.3389/fnmol.2014.00078.

(83) Hou, J. H.; Venkatachalam, V.; Cohen, A. E. Temporal Dynamics of Microbial Rhodopsin Fluorescence Reports Absolute Membrane Voltage. *Biophys. J.* **2014**, *106* (3), 639–648. https://doi.org/10.1016/j.bpj.2013.11.4493.

(84) Maher, M. P.; Wu, N. T.; Ao, H. PH-Insensitive FRET Voltage Dyes. *J. Biomol. Screen.* **2007**, *12* (5), 656–667. https://doi.org/10.1177/1087057107302113.

(85) Loew, L. M.; Scully, S.; Simpson, L.; Waggoner, A. S. Evidence for a Charge-Shift Electrochromic Mechanism in a Probe of Membrane Potential [21]. *Nature* **1979**, *281* (5731), 497–499. https://doi.org/10.1038/281497a0.

(86) Fromherz, P.; Hübener, G.; Kuhn, B.; Hinner, M. J. ANNINE-6plus, a Voltage-Sensitive Dye with Good Solubility, Strong Membrane Binding and High Sensitivity. *Eur. Biophys. J.* **2008**, *37* (4), 509–514. https://doi.org/10.1007/s00249-007-0210-y.

(87) Zhang, J.; Davidson, R. M.; Wei, M. De; Loew, L. M. Membrane Electric Properties by Combined Patch Clamp and Fluorescence Ratio Imaging in Single Neurons. *Biophys. J.* **1998**, *74* (1), 48–53. https://doi.org/10.1016/S0006-3495(98)77765-3.

(88) Bullen, A.; Saggau, P. High-Speed, Random-Access Fluorescence Microscopy: II. Fast Quantitative Measurements with Voltage-Sensitive Dyes. *Biophys. J.* **1999**, *76* (4), 2272–2287. https://doi.org/10.1016/S0006-3495(99)77383-2.

(89) Yellen, G.; Mongeon, R. Quantitative Two-Photon Imaging of Fluorescent Biosensors. *Curr. Opin. Chem. Biol.* **2015**, *27*, 24–30. https://doi.org/10.1016/J.CBPA.2015.05.024.

(90) Brinks, D.; Klein, A. J.; Cohen, A. E. Two-Photon Lifetime Imaging of Voltage Indicating

Proteins as a Probe of Absolute Membrane Voltage. *Biophys. J.* **2015**, *109* (5), 914–921. https://doi.org/10.1016/j.bpj.2015.07.038.

(91) Dumas, D.; Stoltz, J. F. New Tool to Monitor Membrane Potential by FRET Voltage Sensitive Dye (FRET-VSD) Using Spectral and Fluorescence Lifetime Imaging Microscopy (FLIM). Interest in Cell Engineering. *Clin. Hemorheol. Microcirc.* **2005**, *33* (3), 293-302.

(92) Okkelman, I. A.; Papkovsky, D. B.; Dmitriev, R. I. Estimation of the Mitochondrial Membrane Potential Using Fluorescence Lifetime Imaging Microscopy. *Cytom. Part A* **2019**. https://doi.org/10.1002/cyto.a.23886.

(93) Lee, H. J.; Zhang, D.; Jiang, Y.; Wu, X.; Shih, P.-Y.; Liao, C.-S.; Bungart, B.; Xu, X.-M.; Drenan, R. M.; Bartlett, E.; et al. Label-Free Vibrational Spectroscopic Imaging of Neuronal Membrane Potential. *J. Phys. Chem. Lett.* **2017**, acs.jpclett.7b00575. https://doi.org/10.1021/acs.jpclett.7b00575.

(94) Miller, E. W.; Lin, J. Y.; Frady, E. P.; Steinbach, P. A.; Kristan, W. B.; Tsien, R. Y. Optically Monitoring Voltage in Neurons by Photo-Induced Electron Transfer through Molecular Wires. *Proc. Natl. Acad. Sci. U. S. A.* **2012**, *109* (6), 2114–2119. https://doi.org/10.1073/pnas.1120694109.

(95) Lakowicz, J. R. *Principles of Fluorescence Spectroscopy*, 3rd ed.; Springer, 2011. https://doi.org/10.1007/978-0-387-46312-4.

(96) Woodford, C. R.; Frady, E. P.; Smith, R. S.; Morey, B.; Canzi, G.; Palida, S. F.; Araneda, R. C.; Kristan, W. B.; Kubiak, C. P.; Miller, E. W.; et al. Improved PeT Molecules for Optically Sensing Voltage in Neurons. *J. Am. Chem. Soc.* **2015**, *137* (5), 1817–1824. https://doi.org/10.1021/ja510602z.

(97) Boggess, S. C.; Gandhi, S. S.; Siemons, B. A.; Huebsch, N.; Healy, K. E.; Miller, E. W. New Molecular Scaffolds for Fluorescent Voltage Indicators. *ACS Chem. Biol.* **2019**, *14* (3), 390–396. https://doi.org/10.1021/acschembio.8b00978.

(98) Liu, P.; Miller, E. W. Electrophysiology, Unplugged: Imaging Membrane Potential with Fluorescent Indicators. *Acc. Chem. Res.* **2019**, *ASAP*. https://doi.org/10.1021/acs.accounts.9b00514.

(99) Huang, Y. L.; Walker, A. S.; Miller, E. W. A Photostable Silicon Rhodamine Platform for Optical Voltage Sensing. *J. Am. Chem. Soc.* **2015**, *137* (33), 10767–10776. https://doi.org/10.1021/jacs.5b06644.

(100) Deal, P. E.; Kulkarni, R. U.; Al-Abdullatif, S. H.; Miller, E. W. Isomerically Pure Tetramethylrhodamine Voltage Reporters. *J. Am. Chem. Soc.* **2016**, *138* (29), 9085–9088. https://doi.org/10.1021/jacs.6b05672.

(101) Raspe, M.; Kedziora, K. M.; van den Broek, B.; Zhao, Q.; de Jong, S.; Herz, J.; Mastop, M.; Goedhart, J.; Gadella, T. W. J.; Young, I. T.; et al. SiFLIM: Single-Image Frequency-Domain FLIM Provides Fast and Photon-Efficient Lifetime Data. *Nat. Methods* **2016**, No. October 2015, 1–6. https://doi.org/10.1038/nmeth.3836.

(102) Chen, B. C.; Legant, W. R.; Wang, K.; Shao, L.; Milkie, D. E.; Davidson, M. W.; Janetopoulos, C.; Wu, X. S.; Hammer, J. A.; Liu, Z.; et al. Lattice Light-Sheet Microscopy: Imaging Molecules to Embryos at High Spatiotemporal Resolution. *Science (80-.).* **2014**, *346* (6208). https://doi.org/10.1126/science.1257998.

(103) Kazemipour, A.; Novak, O.; Flickinger, D.; Marvin, J. S.; Abdelfattah, A. S.; King, J.; Borden, P. M.; Kim, J. J.; Al-Abdullatif, S. H.; Deal, P. E.; et al. Kilohertz Frame-Rate Two-Photon Tomography. *Nat. Methods* **2019**, *16* (8), 778–786. https://doi.org/10.1038/s41592-019-0493-9.

(104) Pardo, L. A.; Stühmer, W. The Roles of K + Channels in Cancer. *Nat. Rev. Cancer* **2014**, *14* (1), 39–48. https://doi.org/10.1038/nrc3635.

(105) Cadwell, C. R.; Palasantza, A.; Jiang, X.; Berens, P.; Deng, Q.; Yilmaz, M.; Reimer, J.; Shen, S.; Bethge, M.; Tolias, K. F.; et al. Electrophysiological, Transcriptomic and Morphologic Profiling of Single Neurons Using Patch-Seq. *Nat. Biotechnol.* **2016**, *34* (2), 199–203. https://doi.org/10.1038/nbt.3445.

Chapter 2

Optical Estimation of Absolute Membrane Potential with Fluorescence Lifetime Imaging

Portions of this work were published in the following scientific journal:

Lazzari-Dean, J. R.; Gest, A. M. M.; Miller, E. W. Optical Estimation of Absolute Membrane Potential Using Fluorescence Lifetime Imaging. *Elife* **2019**, *8*, e44522. https://doi.org/10.7554/elife.44522.

Portions of this work were performed in collaboration with the following person:

Anneliese Gest assisted with collection and analysis of fluorescence lifetime imaging data.

Abstract

All cells maintain ionic gradients across their plasma membranes, producing transmembrane potentials (V_{mem}). Mounting evidence suggests a relationship between resting V_{mem} and the physiology of non-excitable cells with implications in diverse areas, including cancer, cellular differentiation, and body patterning. A lack of non-invasive methods to record absolute V_{mem} limits our understanding of this fundamental signal. To address this need, we developed a fluorescence lifetime-based approach (VF-FLIM) to visualize and optically quantify V_{mem} with single-cell resolution in mammalian cell culture. Using VF-FLIM, we report V_{mem} distributions over thousands of cells, a 100-fold improvement relative to electrophysiological approaches. In human carcinoma cells, we visualize the voltage response to growth factor stimulation, stably recording a 10-15 mV hyperpolarization over minutes. Using pharmacological inhibitors, we identify the source of the hyperpolarization as the Ca^{2+}-activated K^+ channel $K_{Ca}3.1$. The ability to optically quantify absolute V_{mem} with cellular resolution will allow a re-examination of its signaling roles.

Introduction

Membrane potential (V_{mem}) is an essential facet of cellular physiology. In electrically excitable cells, such as neurons and cardiomyocytes, voltage-gated ion channels enable rapid changes in membrane potential. These fast membrane potential changes, on the order of milliseconds to seconds, trigger release of neurotransmitters in neurons or contraction in myocytes. The resting membrane potentials of these cells, which change over longer timescales, affect their excitability. In non-electrically excitable cells, slower changes in V_{mem}—on the order of seconds to hours—are linked to a variety of fundamental cellular processes [1], including mitosis [2], cell cycle progression [3], and differentiation [4]. Mounting lines of evidence point to the importance of electrochemical gradients in development, body patterning, and regeneration [5].

Despite the importance of membrane potential to diverse processes over a range of time scales, the existing methods for recording V_{mem} are inadequate for characterizing distributions of V_{mem} states in a sample or studying gradual shifts in resting membrane potential (**Table 2.1**). Patch clamp electrophysiology remains the gold standard for recording cellular electrical parameters, but it is low throughput, highly invasive, and difficult to implement over extended time periods. Where reduced invasiveness or higher throughput analyses of V_{mem} are required, optical methods for detecting events involving V_{mem} changes (e.g. whether an action potential occurred) are often employed [6–8]. However, optical approaches generally use fluorescence intensity values as a readout, which cannot report either the value of V_{mem} in millivolts ("absolute V_{mem}") or the millivolt amount by which V_{mem} changed [9]. Variations in dye environment [10], dye loading, illumination intensity, fluorophore bleaching, and/or cellular morphology complicate fluorescence intensity measurements, making calibration and determination of absolute membrane potential difficult or impossible. This limitation restricts optical analysis to detection of acute V_{mem} changes, which can be analyzed without comparisons of V_{mem} between cells or over long timescales.

	Patch-clamp electro-physiology	Single color fluorescence intensity imaging	Two component ratiometric fluorescent sensors (FRET-oxonol)	Ratiometric, electrochromic fluorescent sensors (ANEPPS)	GEVI-based FLIM approaches	FLIM with VoltageFluors (VF-FLIM, ***this work***)
Absolute V_{mem} resolution (between cell comparisons)	excellent	none[a]	very poor[b]	poor[c]	very poor[d]	good
Quantification of V_{mem} changes on a given cell	excellent	none[a]	poor[b]	poor[c]	poor[d]	excellent
Compatibility with long time scales	poor[e]	poor[f]	good[g]	good[g]	good	good
Temporal resolution	sub-millisecond	~1 ms[h]	2-500 ms[i]	~1 ms[h]	seconds[j]	seconds[j]
Minimal invasiveness, damage	very poor[e]	good	poor[k]	good	good	good
Throughput (cells/day)	10s	1000s	1000s	1000s	1000s	1000s
Spatial resolution	Single value per electrode[l]	Subcellular	Subcellular	Subcellular	Single value per laser path[m]	Single cell[n]

Table 2.1. Comparison of available approaches for measuring membrane potential in cells

[a]Measurements vary too much to be converted to absolute voltage or interpreted across populations of cells. This variability is attributable to numerous confounding factors, including dye loading, photobleaching, and sample movement [9]. [b]While in principle less variable than a single-color fluorescence intensity measurement, in practice, the signal depends strongly on the loading of two independent lipophilic indicators [11,12], which can vary substantially. [c]ANEPPS excitation ratios depend on a variety of non-voltage factors, in particular the membrane composition, leading to substantial artifacts in optical V_{mem} determinations [13,14]. [d]With the GEVI CAESR in our hands, apparently poor protein trafficking produces large amounts of non-voltage-sensitive signal, which contaminates the FLIM recording and contributes to high cell to cell variability (**Fig. 2.5, Methods**). [e]Patch-clamp electrophysiology requires physical contact with the cell of interest, which causes damage to the cell and, in whole cell configurations, washout of intracellular factors. Slight movement of the cell or sample generally result in loss of the patch. [f]Movement of the cell and photobleaching of the dye both cause large changes to the signal over seconds to minutes. [g]Ratio-calibrated imaging approaches use a second signal (usually another color of fluorescence) to correct for differences in dye concentration or changes in the region of interest that contaminate single-color intensity signals. If the rate of photobleaching is the same for both components, photobleaching artifacts can also be avoided. [h]Limited by photon count rates. [i]Limited by probe movement in the membrane, which depends mostly on lipophilicity [15]. [j]Photon counting based lifetime imaging, like epifluorescence intensity imaging, is limited by photon count rates. Large numbers of photons per pixel must be collected to fit TCSPC FLIM data, often using a line scanning confocal approach, leading to slower acquisition speeds than epifluorescence-based intensity imaging. [k]Toxicity from capacitive load of the sensor [15]. [l]The spatial resolution of electrophysiology is compromised by space clamp error, preventing interpretation of V_{mem} in

regions far from the electrode (e.g. many neuronal processes) [16,17]. [m]As demonstrated by Cohen and co-workers [27]; in our hands with CAESR, we also experienced significant improvements in voltage resolution by fitting a single curve per FLIM image instead of processing the images pixel-wise. [n]In this work, we calibrated VF-FLIM for V_{mem} measurements with single cell resolution. In principle, subcellular spatial resolution could be achieved with the VF-FLIM technique.

One strategy to address these fluorescence intensity artifacts and quantify cellular parameters optically is ratio-based imaging. For V_{mem} specifically, ratio-based signals can be accessed either with a two-component system or with an electrochromic voltage sensitive dye, but neither strategy has enabled accurate absolute V_{mem} recordings. Two-component FRET-oxonol systems, with independent chromophores for ratio-based calibration, have seen limited success [18], and they confer significant capacitive load on the cell [15]. Further, their performance hinges on carefully tuned loading procedures of multiple lipophilic indicators [11], which can be challenging to reproduce across different samples and days. On the other hand, electrochromic probes report voltage as changes in excitation and emission wavelengths of a single chromophore [19]. While they benefit from simpler loading procedures, signals from electrochromic styryl dyes require normalization with an electrode on each cell of interest to determine absolute V_{mem} accurately [14,20,21]. As a result, ratiometric V_{mem} sensors cannot be used to optically quantify slow signals in the resting V_{mem}, which may be on the order of tens of millivolts. Indeed, ratiometric V_{mem} probes are most commonly applied to detect - rather than quantify - fast changes in V_{mem} [14], much like their single wavelength counterparts.

An alternative approach to improved quantification in optical measurements is fluorescence lifetime (τ_{fl}) imaging (FLIM), which measures the excited state lifetime of a population of fluorophores. Because fluorescence lifetime is an intrinsic property, FLIM can avoid many of the artifacts that confound extrinsic fluorescence intensity measurements, such as uneven dye loading, fluorophore bleaching, variations in illumination intensity, and detector sensitivity [22,23] If a fluorescent probe responds to the analyte of interest via changes in the lifetime of its excited state, there is the opportunity to use fluorescence lifetime to provide a more quantitative estimate of analyte parameters than can be achieved with fluorescence intensity alone. Although FLIM measurements can be affected by environmental factors such as temperature, ionic strength and local environment [22], FLIM has been widely employed to record a number of biochemical and biophysical parameters, including intracellular Ca^{2+} concentration [24], viscosity [25], GTPase activity [26], kinase activity [27], and redox state ($NADH/NAD^+$ ratio)[28], among others [23]. Attempts to record absolute voltage with FLIM, however, have been limited in success [29–31]. Previous work focused on genetically encoded voltage indicators (GEVIs), which either possess complex relationships between τ_{fl} and voltage [30] or show low sensitivity to voltage in lifetime [31] and require complex and technically challenging measurements of fast photochemical kinetic to estimate voltage [30]. Because of this poor voltage resolution, the fluorescence lifetimes of GEVIs cannot be used to detect most biologically relevant voltage changes, which are on the order of tens of millivolts.

Fluorescent voltage indicators that use photoinduced electron transfer (PeT) as a voltage-sensing mechanism are promising candidates for a FLIM-based approach to optical V_{mem} quantification. Because PeT affects the nonradiative decay rate of the fluorophore excited state, it has been successfully translated from intensity to τ_{fl} imaging with a number of small molecule probes for

Ca^{2+} [32]. We previously established that VoltageFluor (VF)-type dyes transduce changes in cellular membrane potential to changes in fluorescence intensity and that the voltage response of VF dyes is consistent with a photoinduced electron transfer (PeT)-based response mechanism [33,34]. Changes in the transmembrane potential alter the rate of PeT [35,36] from an electron-rich aniline donor to a fluorescent reporter, thereby modulating the fluorescence intensity of VF dyes [33] (**Fig. 2.1A,B**). VoltageFluors also display low toxicity and rapid, linear responses to voltage.

Here, we develop fluorescence lifetime imaging of VoltageFluor dyes (VF-FLIM) as a quantitative, all-optical approach for recording absolute membrane potential with single cell resolution. Using patch-clamp electrophysiology as a standard, we demonstrate that VF-FLIM reports absolute membrane potential in single trials with 10 to 23 mV accuracy (root mean square deviation, RMSD; 15 second acquisition), depending on the cell line. In all cases tested, VF-FLIM tracks membrane potential *changes* with better than 5 mV accuracy (RMSD). We benchmark VF-FLIM against previously reported optical absolute V_{mem} recording approaches and demonstrate resolution improvements of 8-fold over ratiometric strategies and 19-fold over other lifetime-based strategies. To highlight the increased throughput relative to manual patch-clamp electrophysiology, we document resting membrane potentials of thousands of cells. To our knowledge, this work represents the first broad view of the distribution of resting membrane potentials present *in situ*. VF-FLIM is limited to acquisition speeds on the order of seconds, but it is well-suited for studying gradual V_{mem} dynamics. Using VF-FLIM, we quantify and track the evolution of a 10-15 mV V_{mem} hyperpolarization over minutes following epidermal growth factor (EGF) stimulation of human carcinoma cells. Through pharmacological perturbations, we conclude that the voltage changes following EGF stimulation arise from activation of the calcium-activated potassium channel $K_{Ca}3.1$. Our results show that fluorescence lifetime of VF dyes is a generalizable and effective approach for studying resting membrane potential in a range of cell lines.

Results

VoltageFluor Fluorescence Lifetime Varies Linearly with Membrane Potential

To characterize how the photoinduced electron transfer process affects fluorescence lifetime, we compared the τ_{fl} of the voltage-sensitive dye VF2.1.Cl with its voltage-insensitive counterpart VF2.0.Cl (**Fig. 2.1B**). We recorded the τ_{fl} of bath-applied VF dyes in HEK293T cells using time-correlated single-photon counting (TCSPC) FLIM (**Fig. 2.1C-E**). VF2.1.Cl is localized to the plasma membrane and exhibits a biexponential τ_{fl} decay with decay constants of approximately 0.9 and 2.6 ns (**Fig. 2.2**). For all subsequent analysis of VF2.1.Cl lifetime, we refer to the weighted average τ_{fl}, which is approximately 1.6 ns in HEK293T cell membranes at rest. VF2.1.Cl fit model selection is discussed in detail below (**Chapters 4 and 7**). VF2.0.Cl (**Fig. 2.1B),** which lacks the aniline substitution and is therefore voltage-insensitive [34], shows a τ_{fl} of 3.5 ns in cell membranes, which is similar to the lifetime of an unsubstituted fluorescein [37] (**Table 2.2**) We also examined VoltageFluor lifetimes at a variety of dye loading concentrations to test for concentration-dependent changes in dye lifetime, which have been reported for fluorescein derivatives [38]. Shortened VF lifetimes were observed at high dye concentrations (**Fig. 2.3**). All subsequent VF-FLIM studies were conducted using at most 100 nM dye, which is well below this concentration-dependent change in lifetime.

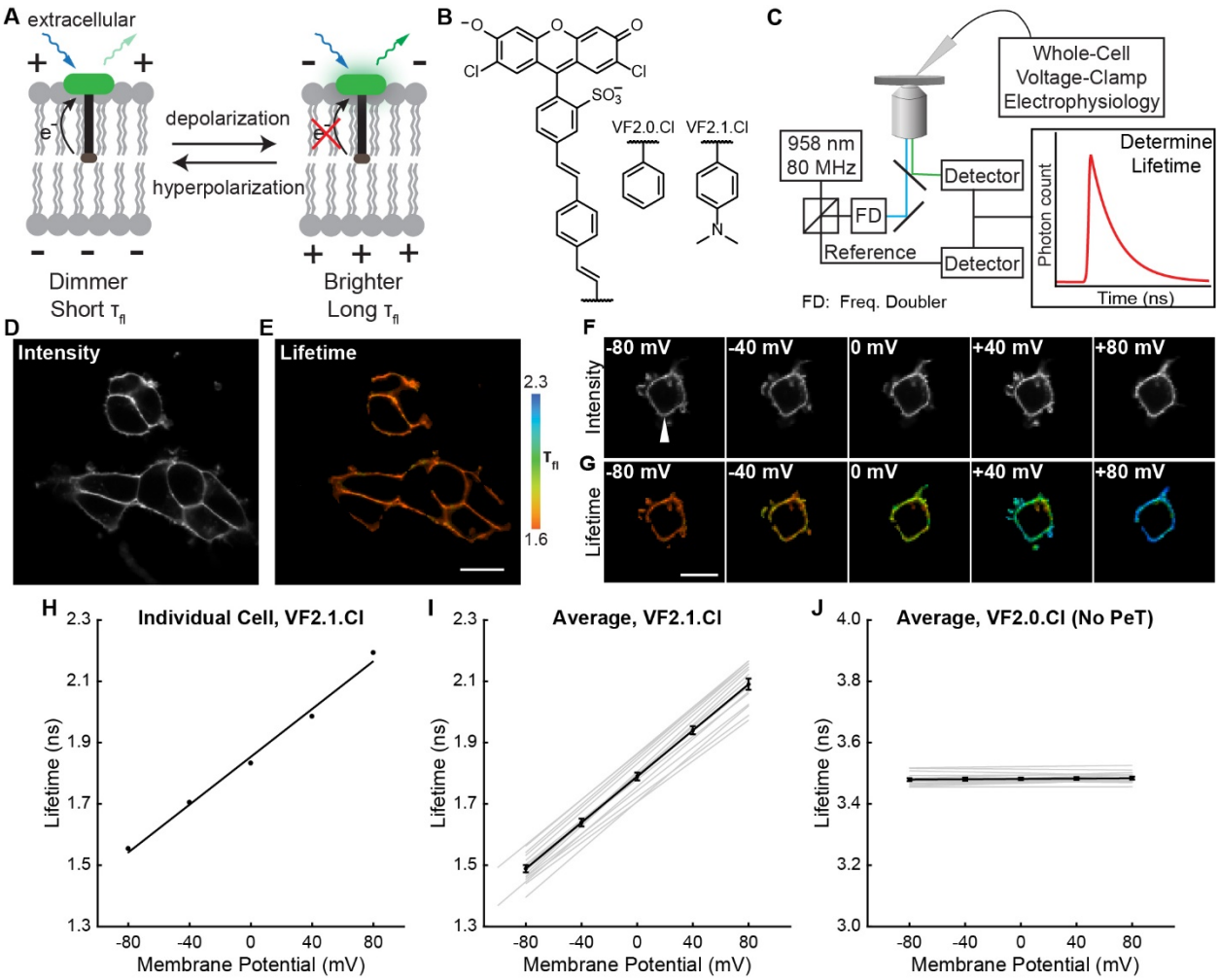

Figure 2.1. VoltageFluor FLIM linearly reports absolute membrane potential.
(A) Mechanism of VoltageFluor dyes, in which depolarization of the membrane potential attenuates the rate of photoinduced electron transfer. (B) Structures of the VF molecules used in this study. (C) Schematic of the TCSPC system used to measure fluorescence lifetime. Simultaneous electrophysiology was used to establish lifetime-voltage relationships. FD = Frequency doubler. (D) Fluorescence intensity and (E) lifetime of HEK293T cells loaded with 100 nM VF2.1.Cl. (F) Intensity and (G) lifetime images of HEK293T cells voltage clamped at the indicated membrane potential. (H) Quantification of the single trial shown in (G), with a linear fit to the data. (I) Evaluation of VF2.1.Cl lifetime-voltage relationships in many individual HEK293T cells. Gray lines represent linear fits on individual cells. Black line is the average lifetime-voltage relationship across all cells (n=17). (J) VF2.0.Cl lifetime does not exhibit voltage-dependent changes. Gray lines represent linear fits on individual cells, and the black line is the average lifetime-voltage relationship across all cells (n=17). Scale bars represent 20 μm. Error bars represent mean ± SEM.

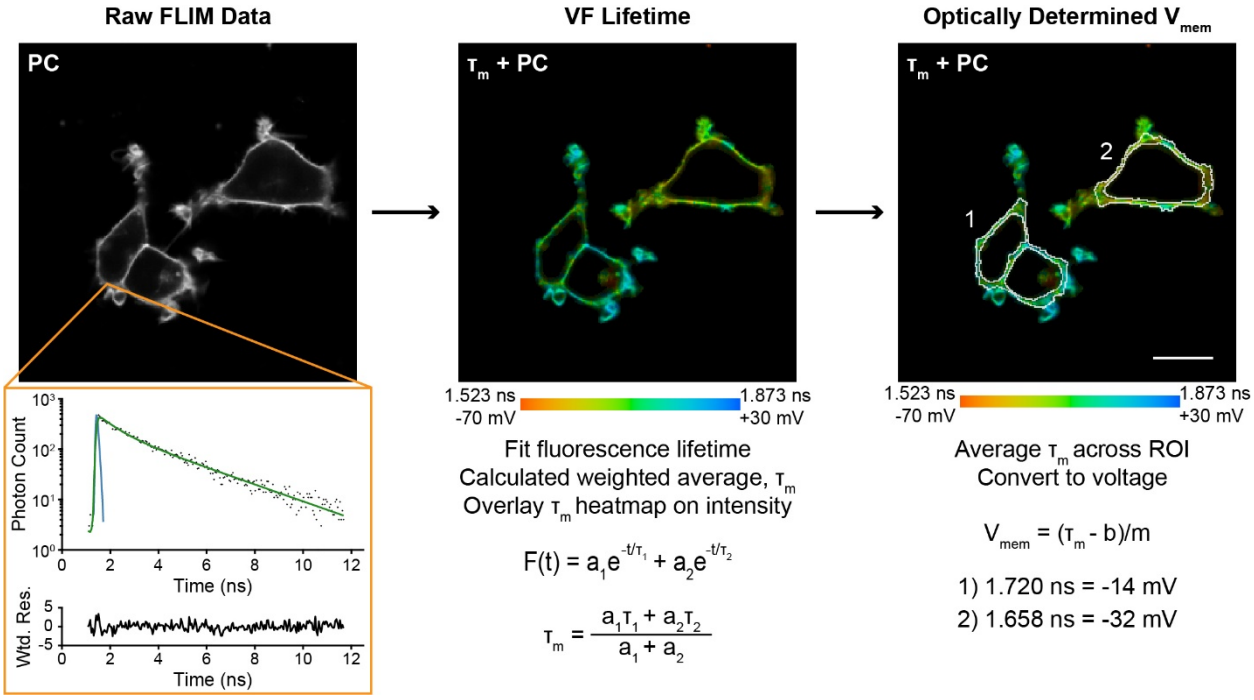

Figure 2.2. Overview of data processing to obtain membrane potential recordings from fluorescence lifetime.
Representative time-correlated photon counting data were obtained from HEK293T cells loaded with 100 nM VF2.1.Cl (black dots, first panel). Data collected at each pixel were fit to an exponential decay model (green) with iterative reconvolution of the instrument response function (IRF, blue). The two components of the fluorescence lifetimes were converted to a weighted average (middle panel). Cell membranes (white outlines) were identified, and τ_m was averaged within each of these regions of interest (ROIs, right panel). These lifetimes were then converted to voltage via a previously determined lifetime-V_{mem} standard curve with slope m and y-intercept b. Additional details of this process are provided in the **Methods**. Wtd. Res.: weighted residuals of the fit, τ_m: weighted average fluorescence lifetime, PC: photon count. τ_m + PC represents an overlay of the lifetime data (color heat map) onto the photon count image. Pixels that appear black in τ_m + PC images were below the required photon count threshold for fitting lifetime data; PC only images show photon counts without any such thresholds applied. Scale bar is 20 µm.

	%ΔF/F	%Δτ/τ	Lifetime (ns)
Fluorescein	N/A	N/A	4.008 ± 0.009
Erythrosin B	N/A	N/A	0.083 ± 0.001
VF2.1.Cl	27	22.4 ± 0.4%	1.77 ± 0.02
VF2.0.Cl	0	0.11 ± 0.05%	3.482 ± 0.004

Table 2.2. Properties of lifetime standards and VoltageFluor dyes.
Fluorescein and erythrosin B standards were measured in drops of solution placed on a coverslip. For VF dyes, voltage sensitivities from intensity-based fluorescence imaging in HEK293T cells (%ΔF/F, percent change in fluorescence intensity for a voltage step from -60 mV to +40 mV) are from previously published work [34]. Lifetime data were obtained from voltage-clamp

electrophysiology of HEK293T cells loaded with 100 nM VF. Lifetime listed here is the average 0 mV lifetime from the electrophysiology calibration. % $\Delta\tau/\tau$ is the percent change in lifetime corresponding to a 100 mV step from -60 mV to +40 mV. Lifetime sample sizes: fluorescein 25, erythrosin B 25, VF2.1.Cl 17, VF2.0.Cl 17. For lifetime standards, each measurement was taken on a separate day. VF2.1.Cl data in HEK293T is duplicated in **Table 2.4**. Values are tabulated as mean ± SEM.

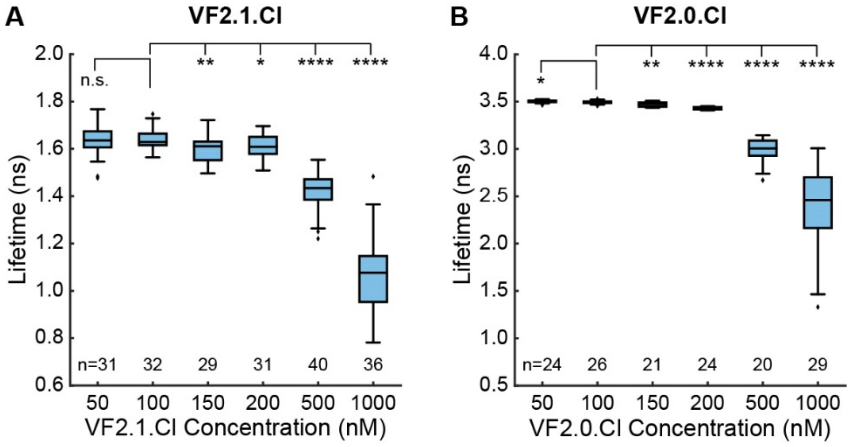

Figure 2.3. Concentration dependence of VoltageFluor lifetimes in HEK293T cells.
Changes in lifetime arising from addition of a range of concentrations of (A) VF2.1.Cl or (B) voltage-insensitive control VF2.0.Cl in HEK293T cells. Biexponential fit models were used for all VF2.1.Cl concentrations and 1 μM VF2.0.Cl; a monoexponential model was used for all other VF2.0.Cl concentrations. Box plots represent the interquartile range, with whiskers and outliers determined with the Tukey method. Sample sizes indicate number of cell groups. Data were obtained over 2 to 4 different days from a total of 3 or 4 coverslips at each concentration. Asterisks indicate significant differences between the indicated concentration and the VF concentration used for electrophysiology experiments (n.s. $p > 0.05$, * $p < 0.05$, ** $p < 0.01$, *** $p < 0.001$, **** $p < 0.0001$, two-sided, unpaired, unequal variances t-test).

To assess the voltage dependence of VoltageFluor τ_{fl}, we controlled the plasma membrane potential of HEK293T cells with whole-cell voltage-clamp electrophysiology while simultaneously measuring the τ_{fl} of VF2.1.Cl (**Fig. 2.1C**). Single-cell recordings show a linear τ_{fl} response to applied voltage steps, and individual measurements deviate minimally from the linear fit (**Fig. 2.1F-H**). VF2.1.Cl τ_{fl} is reproducible across different cells at the same resting membrane potential, allowing determination of V_{mem} from τ_{fl} images taken without concurrent electrophysiology (**Fig. 2.1I**). Voltage-insensitive VF2.0.Cl shows no τ_{fl} change in response to voltage (**Fig. 2.1J, Fig. 2.4**), consistent with a τ_{fl} change in VF2.1.Cl arising from a voltage-dependent PeT process. In HEK293T cells, VF2.1.Cl exhibits a sensitivity of 3.50 ± 0.08 ps/mV and a 0 mV lifetime of 1.77 ± 0.02 ns, corresponding to a fractional change in τ_{fl} ($\Delta\tau/\tau$) of 22.4 ± 0.4% per 100 mV. These values are in good agreement with the 27% $\Delta F/F$ intensity change per 100 mV originally observed for VF2.1.Cl [33,34]. Because $\%\Delta F/F$ is a fluorescence intensity-based

metric, it cannot be used to measure absolute V_{mem}; however, agreement between %ΔF/F and %Δτ/τ is consistent with a PeT-based V_{mem} sensing mechanism in VFs. To estimate the voltage resolution of VF-FLIM, we analyzed the variability in successive measurements on the same cell (intra-cell resolution) and on different cells (inter-cell resolution, see **Methods**). We estimate that the resolution for tracking and quantifying voltage changes in a single HEK293T cell is 3.5 ± 0.4 mV (intra-cell resolution, average RMSD from each electrophysiological calibration, **Scheme 2.2**), whereas the resolution for single-trial determination of a particular HEK293T cell's absolute V_{mem} is 19 mV (inter-cell resolution, RMSD of each calibration slope to the average calibration, **Scheme 2.2**) within a 15 second bandwidth.

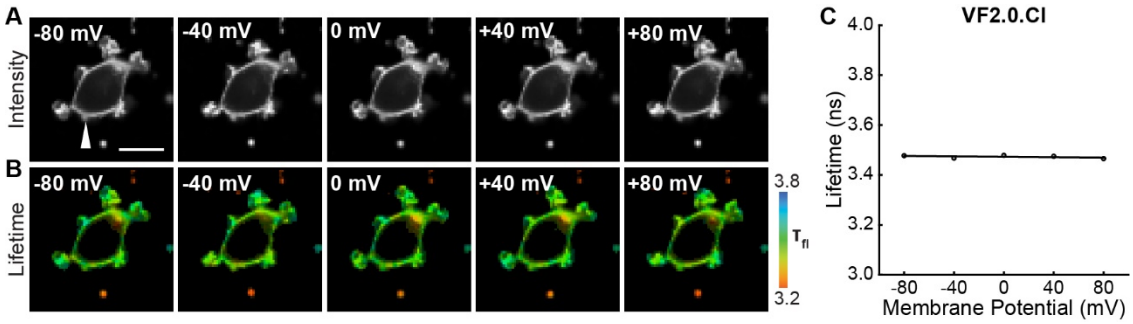

Figure 2.4. VF2.0.Cl lifetime does not depend on membrane potential.
(A) Photon count and (B) lifetime images of a single HEK293T cell loaded with 100 nM VF2.0.Cl, with the membrane potential held at the indicated value via whole-cell voltage clamp electrophysiology. White arrow indicates patch pipette. Scale bar is 20 μm. (C) Quantification of images shown in (B) for this individual cell. Black line is the line of best fit.

We compared the performance of VF-FLIM in HEK293T cells to that of two previously documented strategies for optical absolute V_{mem} determination. We first tested the voltage resolution of CAESR, the best previously reported GEVI for recording absolute V_{mem} with FLIM [31]. Using simultaneous FLIM and voltage-clamp electrophysiology, we determined the relationship between τ_{fl} and V_{mem} for CAESR under 1 photon excitation (**Figure 2.5**). We recorded a sensitivity of -1.2 ± 0.1 ps/mV and a 0 mV lifetime of 2.0 ± 0.2 ns, which corresponds to a -6.1 ± 0.8% Δτ/τ per 100 mV (mean ± SEM of 9 measurements), in agreement with the reported sensitivity of -0.9 ps/mV and 0 mV lifetime of 2.7 ns with 2 photon excitation [31]. Relative to VF2.1.Cl, CAESR displays 3-fold lower sensitivity (-1.2 ps/mV vs 3.5 ps/mV in HEK293T cells) and 7-fold higher voltage-independent variability in lifetime (0.46 ns vs 0.07 ns, standard deviation of the 0 mV lifetime measurement). For CAESR in HEK293T cells, we calculate a voltage resolution of 33 ± 7 mV for quantifying voltage changes on an individual cell (intra-cell RMSD, compared to 3.5 mV for VF2.1.Cl, see **Methods**) and resolution of 370 mV for determination of a particular cell's absolute V_{mem} (inter-cell RMSD, compared to 19 mV for VF2.1.Cl).

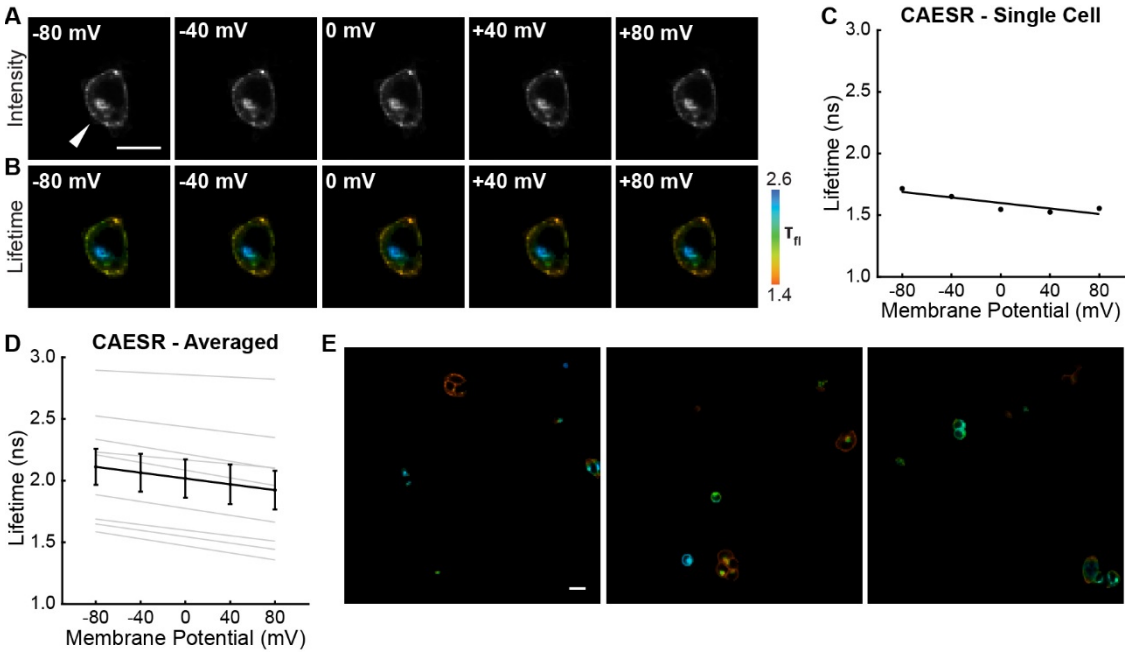

Figure 2.5. The GEVI CAESR shows variable lifetime-voltage relationships.
(A) Photon count and (B) lifetime images of a HEK293T cell expressing CAESR and held at the indicated V_{mem} with voltage-clamp electrophysiology. White arrow indicates voltage-clamped cell. (C) Lifetime-V_{mem} relationship from the cell in (B), based on a single fit from combined fluorescence decays of all pixels in the cell membrane at each potential (see **Methods**). Points indicate recordings at a given potential; solid line is line of best fit. (D) Evaluation of VF2.1.Cl lifetime-voltage relationships in many individual CAESR-expressing HEK293T cells. Gray lines represent linear fits on individual cells. Black line is the average fit across all cells (n=9). (E) Representative lifetime images of CAESR in HEK293T cells. Scale bars represent 20 μm.

We also measured the absolute voltage resolution of the ratio-based sensor di-8-ANEPPS, which reports membrane potential by the wavelength of its excitation and emission spectra [19]. Ratio-based imaging can be achieved by comparing the fluorescence emission at different excitation wavelengths [14]; here, we used the ratio, R, of the blue-excited emission to the green-excited emission (see **Methods**). Via simultaneous ratio imaging and whole cell voltage clamp electrophysiology, we record a sensitivity of 0.0039 ± 0.0004 R per mV, with a y-intercept (0 mV) R value of 1.8 ± 0.2 (**Figure 2.6**; mean ± SEM of n=16 HEK293T cells). R depends on the excitation and emission conditions used but should be relatively reproducible on a given microscope rig. To compare R from our system with previous work, we normalized all R values to the R value at 0 mV for each cell. Using the above data, we obtain a sensitivity of 0.0022 ± 0.0002 normalized R per mV, with a 0 mV normalized R of 1.02 ± 0.02, in good agreement with reported values (0.0015 normalized R per mV) [14]. For analysis of voltage resolution, we compare VF-FLIM to the non-normalized R, since normalization requires an electrode-based measurement for every recording and is thus not a truly optical strategy. From the non-normalized di-8-ANEPPS R, we obtain an intra-cell resolution (RMSD) of 18 ± 3 mV (5-fold less accurate than VF-FLIM) and an inter-cell resolution (RMSD) of 150 mV (8-fold less accurate than VF-FLIM). The

sensitivities and resolutions of VF-FLIM, CAESR, and di-8-ANEPPS in HEK293T are tabulated in **Table 2.3**. Because cellular resting membrane potentials and voltage changes (e.g. action potentials) are on the order of tens of millivolts, the resolution improvements achieved by VF-FLIM enable biologically relevant absolute V_{mem} recordings: impossible with previous approaches.

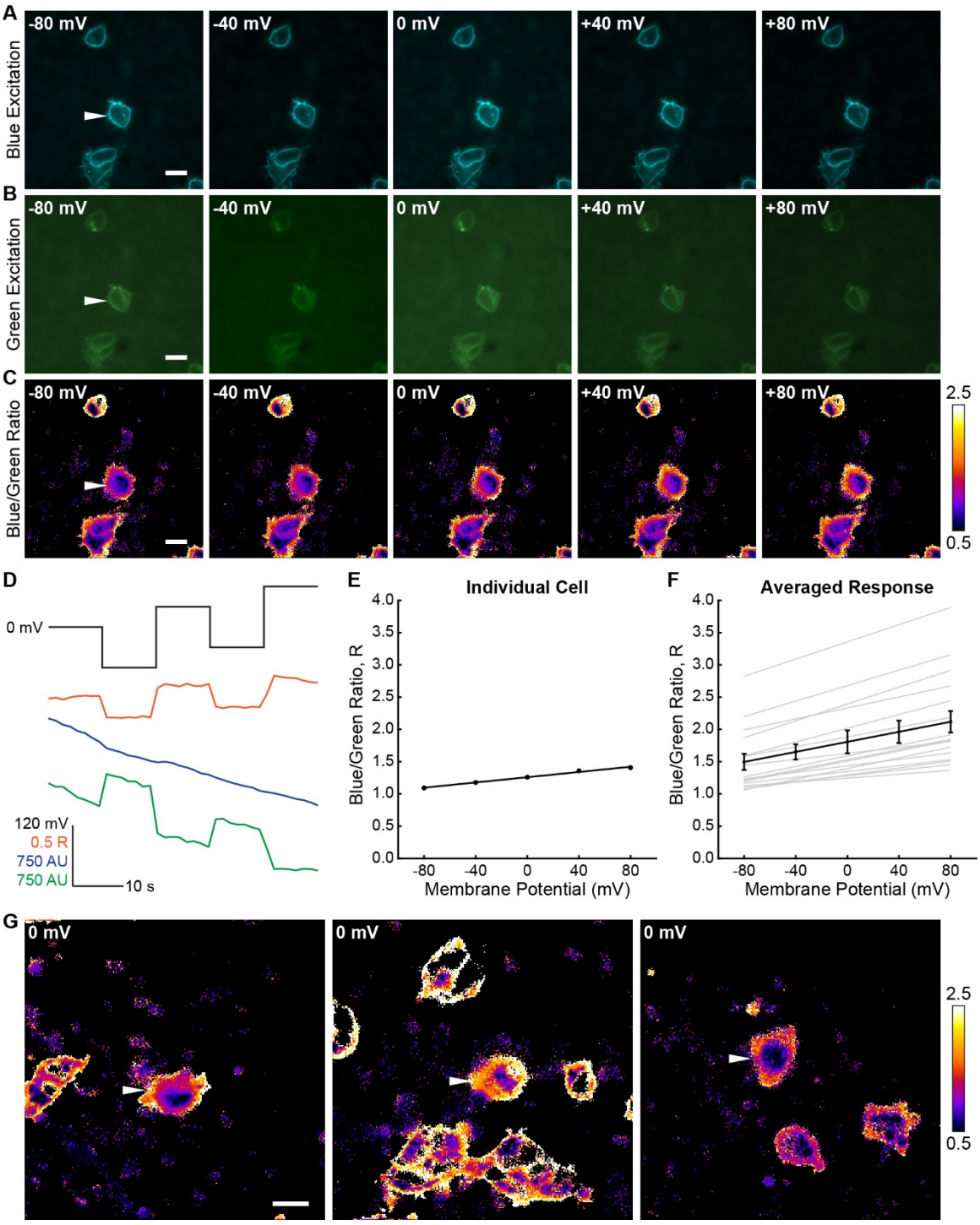

Figure 2.6. Ratiometric V_{mem} determinations with Di-8-ANEPPS in HEK293T cells.
Different fluorescence excitation wavelengths (blue and green) were used to generate ratiometric images; emission wavelengths were constant throughout the experiment. Details of epifluorescence ratiometric imaging and data processing are described in the **Methods**. Simultaneous ratiometric imaging and whole cell patch clamp electrophysiology were used to determine the ratio between the blue and green excitation channels (blue/green ratio, R). Representative images of (A) blue-excited signal (440 ± 10 nm), (B) green-excited signal (550 ± 7.5 nm) and (C) R of a HEK293T cell held at the indicated membrane potential with whole cell voltage clamp electrophysiology. White arrow indicates voltage clamped cell. Differences in background brightness between images are attributable to photobleaching of the probe; images were acquired in the order: 0, -80, +40, -40, +80 mV. (D) Time course of the voltage step protocol used for each cell (black line, top), along with a representative response in the fluorescence ratio (orange), blue excited fluorescence intensity (blue) and green excited fluorescence intensity (green). AU, arbitrary units. (E) R at various potentials for an individual HEK293T cell (black dots), along with an R-V_{mem} line of best fit (black line). Values shown are the average of all ratio images from a particular cell at a given potential, excluding the first and last ratio image taken for each V_{mem} value. Data shown in (D) and (E) are from the cell depicted in (A)-(C). (F) Aggregated lines of best fit (gray) for R-V_{mem} calibrations on multiple HEK293T cells. Average response is shown in black; ratios at each potential are depicted as mean ± SEM (n = 16 cells). (G) Additional representative R images of Di-8-ANEPPS in HEK293T cells. The cell indicated with the white arrow is held at 0 mV with electrophysiology; other cells are unperturbed. Images represent one frame at the given voltage and are not averaged. Regions of interest (ROIs) were drawn around the membrane only, avoiding both the internalized dye signal and the artificially high ratios just outside the cells (which appear as white edges) as much as possible. Scale bars represent 20 μm.

Strategy	Sensitivity	0 mV value	Intra-cell RMSD	Inter-cell RMSD
VF2.1.Cl fluorescence lifetime	3.50 ± 0.08 ps/mV	1.77 ± 0.02 ns	3.5 ± 0.4 mV	19 mV
CAESR fluorescence lifetime	-1.2 ± 0.1 ps/mV	2.0 ± 0.2 ns	33 ± 7 mV	370 mV
di-8-ANEPPS excitation ratio	0.0039 ± 0.0004 R/mV	1.8 ± 0.2	18 ± 3 mV	150 mV

Table 2.3. Comparison of optical approaches to absolute V_{mem} determination in HEK293T cells.
Data are compiled from **Fig. 2.1** (VF-FLIM, this work), **Fig. 2.5** (CAESR [31]), and **Fig. 2.6** (Di-8-ANEPPS [14]). All data were obtained by simultaneous whole cell voltage clamp electrophysiology and optical recording in HEK293T (VF-FLIM n=17 cells, CAESR n=9, di-8-ANEPPS n=16). Calculation of intra and inter cell accuracies are performed via root-mean-square deviation (RMSD) and discussed in detail in the Methods. Regions of interest were chosen at the plasma membrane in all cases. Di-8-ANEPPS data are presented as the ratio of signal obtained with blue

excitation to signal obtained with green excitation (R, see **Methods**) and are not normalized to the 0 mV R.

Evaluation of VF-FLIM across Cell Lines and Culture Conditions

To test the generalizability of VF-FLIM, we determined τ_{fl}-V_{mem} calibrations in four additional commonly used cell lines: A431, CHO, MDA-MB-231, and MCF-7 (**Fig. 2.7, Fig. 2.8, Fig. 2.9**). We observe a linear τ_{fl} response in all cell lines tested. The slope (voltage sensitivity) and y-intercept (0 mV lifetime) of the τ_{fl}-V_{mem} response varied slightly across cell lines, with average sensitivities of 3.1 to 3.7 ps/mV and average 0 mV lifetimes ranging from 1.74 to 1.87 ns. In all cell lines, we observed better voltage resolution for quantification of V_{mem} changes on a given cell versus comparisons of absolute V_{mem} between cells. Changes in voltage for a given cell could be quantified with resolutions at or better than 5 mV (intra-cell resolution, **Methods**). For absolute V_{mem} determination of a single cell, we observed voltage resolutions ranging from 10 to 23 mV (inter-cell resolution, 15 second acquisition time, **Table 2.4**). Statistically significant differences among the cell lines tested were observed for cellular τ_{fl}-V_{mem} calibrations in both the slope (One-way ANOVA with Welch's correction: $F(4, 23.07) = 18.12$, $p < 0.0001$) and average 0 mV lifetime (One-way ANOVA: $F(4, 67) = 14.43$, $p < 0.0001$). There were no statistically significant differences between A431, CHO, and HEK293T cells ($p > 0.05$, Games-Howell and Tukey-Kramer post hoc tests for the slope and 0 mV lifetime respectively). MDA-MB-231 and MCF-7 cells showed statistically significant variability from other cell lines in slope and/or 0 mV lifetime.

To verify that VF-FLIM was robust in groups of cells in addition to the isolated, single cells generally used for patch clamp electrophysiology, we determined lifetime-voltage relationships for small groups of A431 cells (**Fig. 2.10A-E**). We found that calibrations made in small groups of cells are nearly identical to those obtained on individual cells, indicating that VF-FLIM only needs to be calibrated once for a given type of cell. For pairs or groups of three cells we recorded a sensitivity of 3.3 ± 0.2 ps/mV and a 0 mV lifetime of 1.78 ± 0.02 ns (mean ± SEM of 7 cells (5 pairs and 2 groups of 3); values are for the entire group, not just the cell in contact with the electrode), which is similar to the sensitivity of 3.55 ± 0.08 ps/mV and 0 mV lifetime of 1.74 ± 0.02 ns we observe in single A431 cells. The slight reduction in sensitivity seen in cell groups is likely attributable to space clamp error, which prevents complete voltage clamp of the cell group [16,17]. Indeed, when we analyzed only the most responsive cell in the group (in contact with the electrode), we obtained a slope of 3.7 ± 0.1 ps/mV and 0 mV lifetime of 1.79 ± 0.02 ns, in good agreement with the single cell data. The space clamp error can be clearly visualized in **Fig. 2.10E**, where one cell in the group of 3 responded much less to the voltage command.

To test whether VF-FLIM is also extensible to cells maintained with different culture conditions, we recorded lifetime-V_{mem} relationship in serum-starved A431 cells (**Fig. 2.10F-K**), obtaining an average sensitivity of 3.6 ± 0.1 ps/mV and a 0 mV lifetime of 1.76 ± 0.01 ns (n=7; 2 single cells, 2 pairs, 3 groups of 3 cells; values are average lifetime across the whole cell group), in excellent agreement with the values obtained for non-serum starved cells. We also tested for concentration-dependent changes in VF lifetime in all five cell lines and in serum starvation conditions. Similar to VF2.1.Cl lifetime in HEK293T cells (**Fig. 2.3**), we observed shortening of VF2.1.Cl lifetimes beginning between 200 and 500 nM dye in all cases (**Fig. 2.11**). All subsequent experiments were carried out with VF2.1.Cl concentrations of ≤100 nM, well below the regime where VF concentration-dependent lifetime changes were observed.

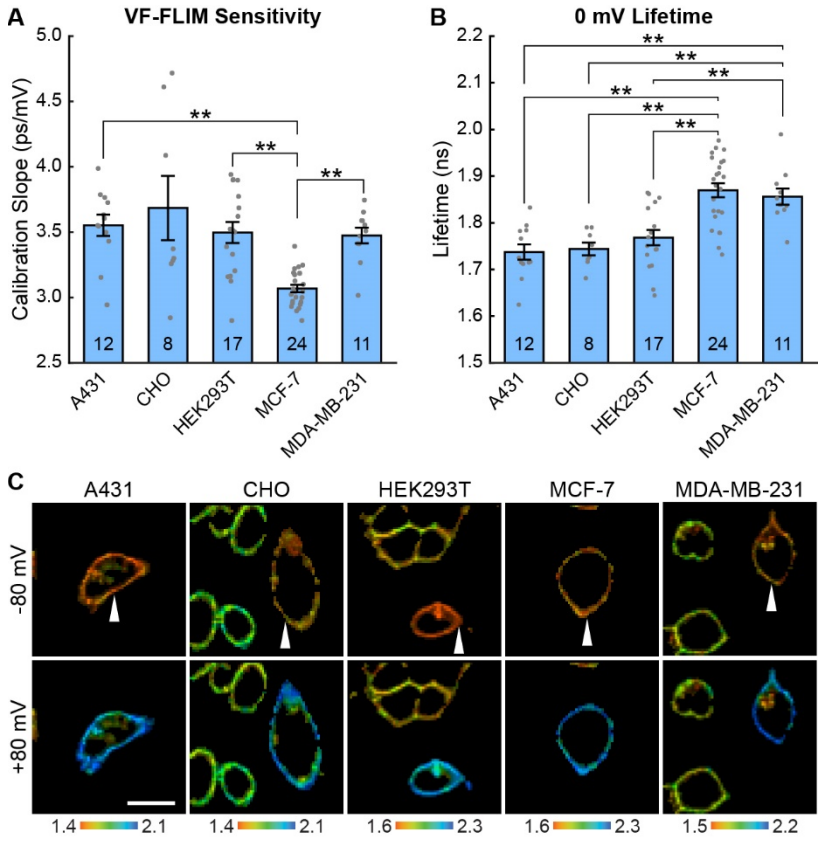

Figure 2.7. VF-FLIM is a general and portable method for optically determining membrane potential.

VF2.1.Cl lifetime-voltage relationships were determined with whole cell voltage clamp electrophysiology in five cell lines. (A) Slopes of the linear fits for single cell lifetime-voltage relationships, shown as mean ± S.E.M. Gray dots indicate results from individual cells. Statistically significant differences exist between groups (One-way ANOVA with Welch's correction: $F(4, 23.07) = 18.12$, $p < 0.0001$). Data were tested for normality (Shapiro-Wilk test, $p > 0.05$ for all cell lines) and homoscedasticity (Levene's test on the median, $F(4,67) = 5.07$, $p = 0.0013$). ** indicates $p < 0.01$; if significance is not indicated, $p > 0.05$ (Games-Howell post hoc test). (B) 0 mV reference point of linear fits for the lifetime-voltage relationship, shown as mean ± S.E.M. Gray dots indicate results from individual cells. Significant differences exist between groups (One-way ANOVA: $F(4, 67) = 14.43$, $p < 0.0001$). Data were tested for normality (Shapiro-Wilk test, $p > 0.05$ for all cell lines) and homoscedasticity (Levene's test on the median, $F(4,67) = 1.29$, $p = 0.28$). ** indicates $p < 0.01$; if significance is not indicated, $p > 0.05$ (Tukey-Kramer post hoc test). (C) Representative lifetime-intensity overlay images for each cell line with the indicated cells (white arrow) held at -80 mV (top) or +80 mV (bottom). Lifetime scales are in ns. Scale bar is 20 µm.

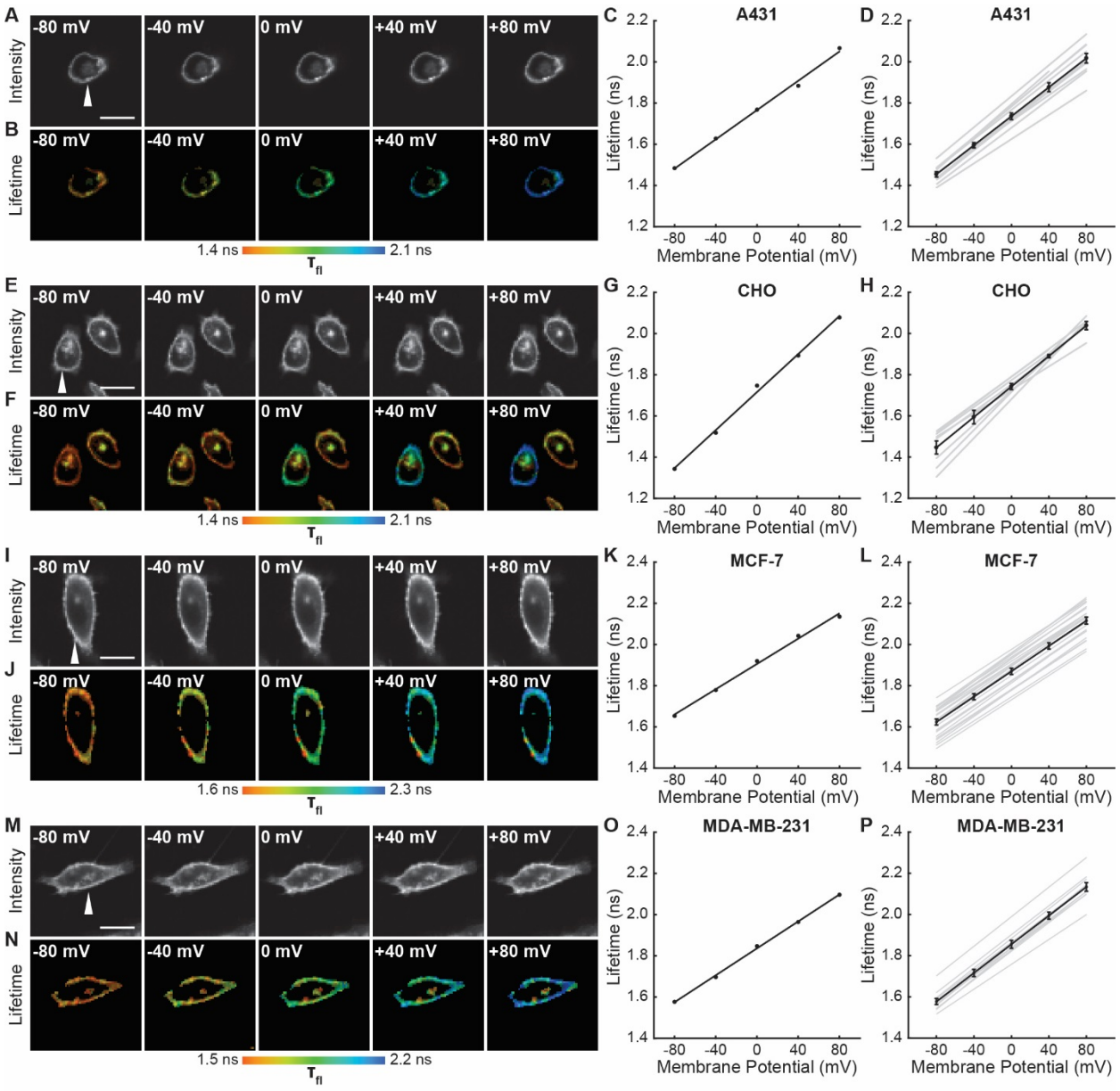

Figure 2.8. VoltageFluor lifetime reports voltage in diverse cell lines.
(A) Representative photon count and (B) lifetime images of a VF2.1.Cl in A431 cells with V_{mem} held at the indicated value with voltage-clamp electrophysiology. A431 cells were not serum starved for these experiments. (C) Quantification of the images in (B), with the line of best fit for this single trial. (D) Lines of best fit for the lifetime-V_{mem} relationships of 12 A431 cells (gray lines). Average lifetime at each potential is shown as mean ± SEM, with the average line of best fit in black. (E)-(H) Lifetime-V_{mem} standard curve determination in CHO cells (n=8). (I)-(L) Lifetime-V_{mem} standard curve determination in MCF-7 cells (n=24). (M)-(P) Lifetime-V_{mem} standard curve determination in MDA-MB-231 cells (n=11). VF2.1.Cl concentration was 100 nM in all cases. White arrows indicate the voltage-clamped cell. Scale bars are 20 μm.

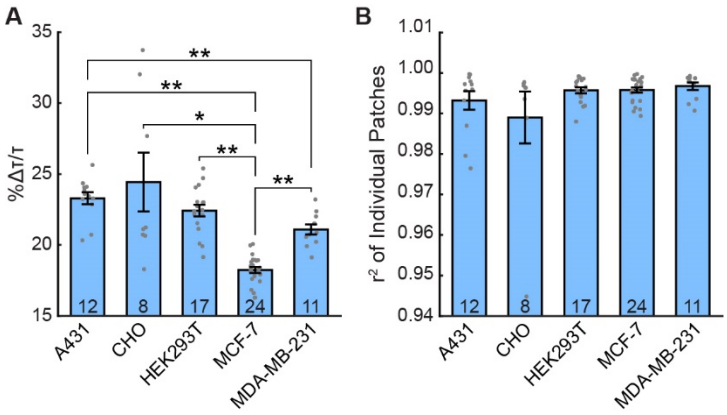

Figure 2.9. Additional parameters of linear lifetime-voltage standard curves.
(A) Percent change in VF2.1.Cl lifetime per 100 mV change in voltage, relative to the lifetime at -60 mV. Significant differences exist between cell lines (one-way ANOVA with Welch's correction, $F(4,24.08) = 41.75$, $p < 0.0001$). Data were tested for normality (Shapiro-Wilk test, $p > 0.05$ for all cell lines) and homoscedasticity (Levene's test on the median, $F(4,67) = 5.74$, $p = 0.00049$). Asterisks indicate statistically significant differences (* $p < 0.05$, ** $p < 0.01$, Games-Howell post hoc test). (B) Correlation coefficients (r^2) for the lines of best fit of VF2.1.Cl lifetime versus membrane potential. No significant differences exist in r^2 values between cell lines (Kruskal-Wallis test, $H = 3.20$, 4 degrees of freedom, $p = 0.53$). Data were tested for normality (Shapiro-Wilk test, $p < 0.05$ for 4 of 5 cell lines) and homoscedasticity (Levene's test on the median, $F(4,67) = 1.55$, $p = 0.20$). In both (A) and (B), data are shown as mean ± S.E.M., with gray dots indicating values from individual patches.

Cell Line	Slope (ps/mV)	0 mV lifetime (ns)	%Δτ/τ	RMSD, intra-cell (mV)	RMSD, inter-cell (mV)
A431	3.55 ± 0.08	1.74 ± 0.02	23.3 ± 0.4%	3.8 ± 0.7	15
CHO	3.68 ± 0.25	1.74 ± 0.01	24 ± 2%	5 ± 1	10
HEK293T	3.50 ± 0.08	1.77 ± 0.02	22.4 ± 0.4%	3.5 ± 0.4	19
MCF-7	3.07 ± 0.03	1.87 ± 0.01	18.2 ± 0.2%	3.4 ± 0.3	23
MDA-MB-231	3.47 ± 0.06	1.86 ± 0.02	21.1 ± 0.4%	3.0 ± 0.4	16

Table 2.4. Lifetime-V_{mem} standard curves for VF2.1.Cl lifetime in various cell lines.
Whole-cell voltage-clamp electrophysiology was used to determine the relationship between VF2.1.Cl lifetime and membrane potential in five different cell lines. Parameters of this linear model are listed above. The %Δτ/τ is the percent change in the lifetime observed for a voltage step from -60 mV to +40 mV. The intra-cell RMSD represents the accuracy for quantifying voltage changes in a particular cell (see **Methods**). The inter-cell RMSD represents the expected variability in single-trial absolute V_{mem} determinations. Sample sizes: A431 12, CHO 8, HEK293T 17, MCF-7 24, MDA-MB-231 11. All values are tabulated as mean ± SEM.

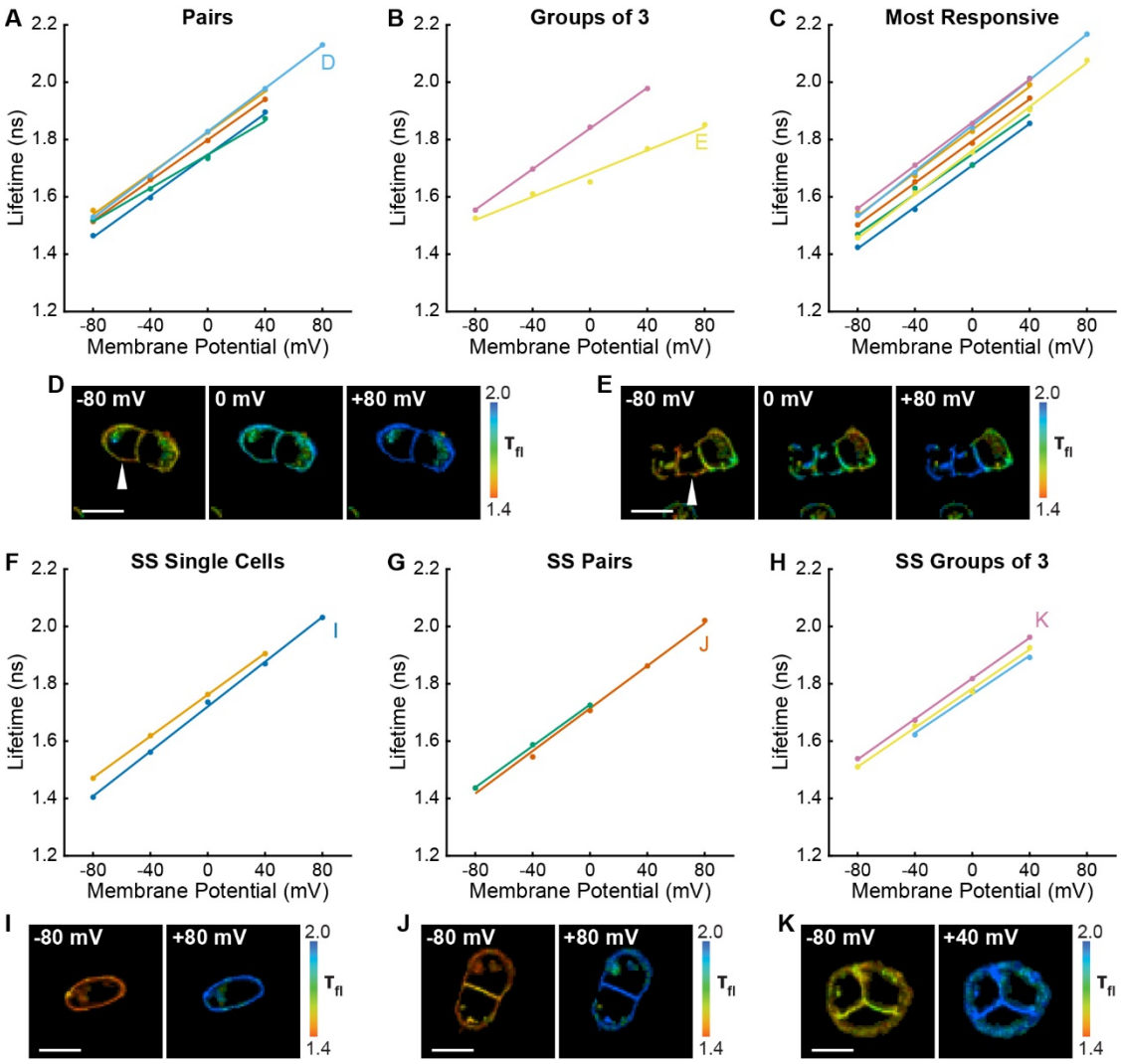

Figure 2.10. Relationship between lifetime and membrane potential extends to groups of cells and across culture conditions.

Electrophysiological calibration of lifetime was performed on small groups of A431 cells and on serum starved (SS) A431 cells to verify that the V_{mem}-lifetime standard curves for a given cell line are generalizable across many cellular growth conditions. For all graphs, each line represents a group of cells. Letters on the graphs indicate the subfigure where images from that recording are shown. (A) Lifetime-voltage relationships in cell pairs, in which only one cell was directly controlled with voltage-clamp electrophysiology. (B) Lifetime-voltage relationships in groups of three cells, in which only one cell was directly controlled with voltage-clamp electrophysiology. (C) Lifetime for the most responsive cell from pairs and groups of three in (A) and (B). Line color codes are maintained from (A) and (B). (D, E) Representative lifetime images from (A) and (B) respectively. White arrow indicates cell directly controlled with electrophysiology. (F) Lifetime-voltage relationship in SS single cells, (G) pairs, and (H) groups of three cells. (I)-(K) Representative images from (F)-(H). Scale bars are 20 μm.

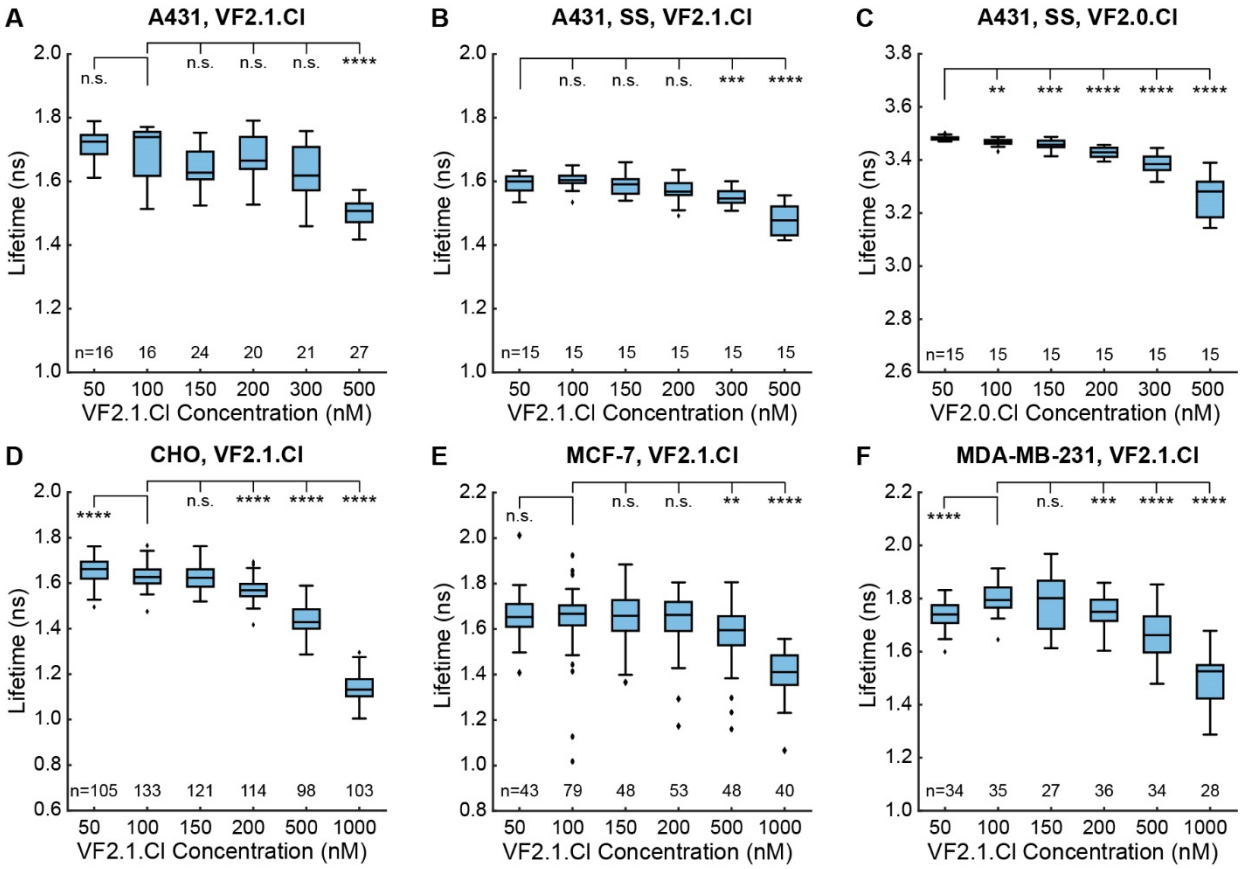

Figure 2.11. Concentration dependence of VoltageFluor lifetime in four cell lines.
A431 cells were analyzed with VF2.1.Cl both in (A) full serum and (B) serum-starved conditions. (C) VF2.0.Cl in serum-starved A431 cells. (D) VF2.1.Cl in CHO cells. (E) VF2.1.Cl in MCF-7 cells. (F) VF2.1.Cl in MDA-MB-231 cells. All VF2.1.Cl data were fit with a biexponential model, and all VF2.0.Cl data were fit with a monoexponential model. Box plots represent the interquartile range, with whiskers and outliers determined with the Tukey method. Sample sizes indicate number of cell groups. Data were acquired over 2 to 4 different days from a total of 3 or 4 coverslips at each concentration. Asterisks indicate significant differences between the indicated concentration and the VF concentration selected for additional experiments (n.s. $p > 0.05$, * $p < 0.05$, ** $p < 0.01$, *** $p < 0.001$, **** $p < 0.0001$, two-sided, unpaired, unequal variances t-test).

Optical Determination of Resting Membrane Potential Distributions

The throughput of VF-FLIM enables cataloging of resting membrane potentials of thousands of cells in only a few hours of the experimenter's time. We optically recorded resting membrane potential distributions for A431, CHO, HEK293T, MCF-7, and MDA-MB-231 cells using VF-FLIM (**Fig. 2.12**, **Fig. 2.13**, **Fig. 2.14**). We report resting membrane potentials by cell group (**Methods, Fig. 2.2**) because adjacent cells in these cultures are electrically coupled to some degree via gap junctions [39]. Each group of cells represents an independent sample for V_{mem}. In addition, the fluorescent signal originating from membranes of adjacent cells cannot be separated with a conventional optical microscope, so assignment of a region of membrane connecting multiple cells would be arbitrary. VF-FLIM images (**Fig. 2.12**, **Fig. 2.13**, **Fig. 2.14**).) contain spatially resolved voltage information, but caution should be employed in interpreting pixel to pixel differences in lifetime. Because VF-FLIM was calibrated here using the average plasma membrane τ_{fl} for each cell, optical V_{mem} should be interpreted per cell or cell group.

Mean resting membrane potentials recorded by VF-FLIM range from -53 to -29 mV, depending on the cell line. These average V_{mem} values fall within the range reported in the literature for all of the cell lines we measured (**Table 2.5**). We also recorded resting membrane potentials in a high K^+ buffer (120 mM K^+, "high K^+ HBSS"), where we observed a depolarization of 15 to 41 mV, bringing the mean V_{mem} up to -26 mV to +4 mV, again depending on the cell line. Although 120 mM extracellular K^+ should be strongly depolarizing, it will not necessarily produce a membrane potential of 0 mV. Because few literature reports of electrophysiological measurements in 120 mM K^+ exist as a point of comparison, we obtained a rough estimate of V_{mem} in 6 mM extracellular K^+ and 120 mM extracellular K^+ using the Goldman-Hodgkin-Katz (GHK) equation [40]. Under our imaging conditions and with a broad range of possible ion permeabilities and intracellular ion concentrations, the GHK equation allows V_{mem} ranging from -91 to -27 mV in 6 mM extracellular K^+ and -25 to +2 mV in 120 mM extracellular K^+ (see **Methods**). Recorded VF-FLIM values fall well within this allowed range. Notably, although the GHK equation can determine ranges of reasonable V_{mem} values, GHK-based V_{mem} results are approximate at best because of the difficulty in obtaining accurate values of permeabilities and intracellular ion concentrations for specific cell lines. Direct measurement of V_{mem}, rather than theoretical calculation, is required to obtain accurate values.

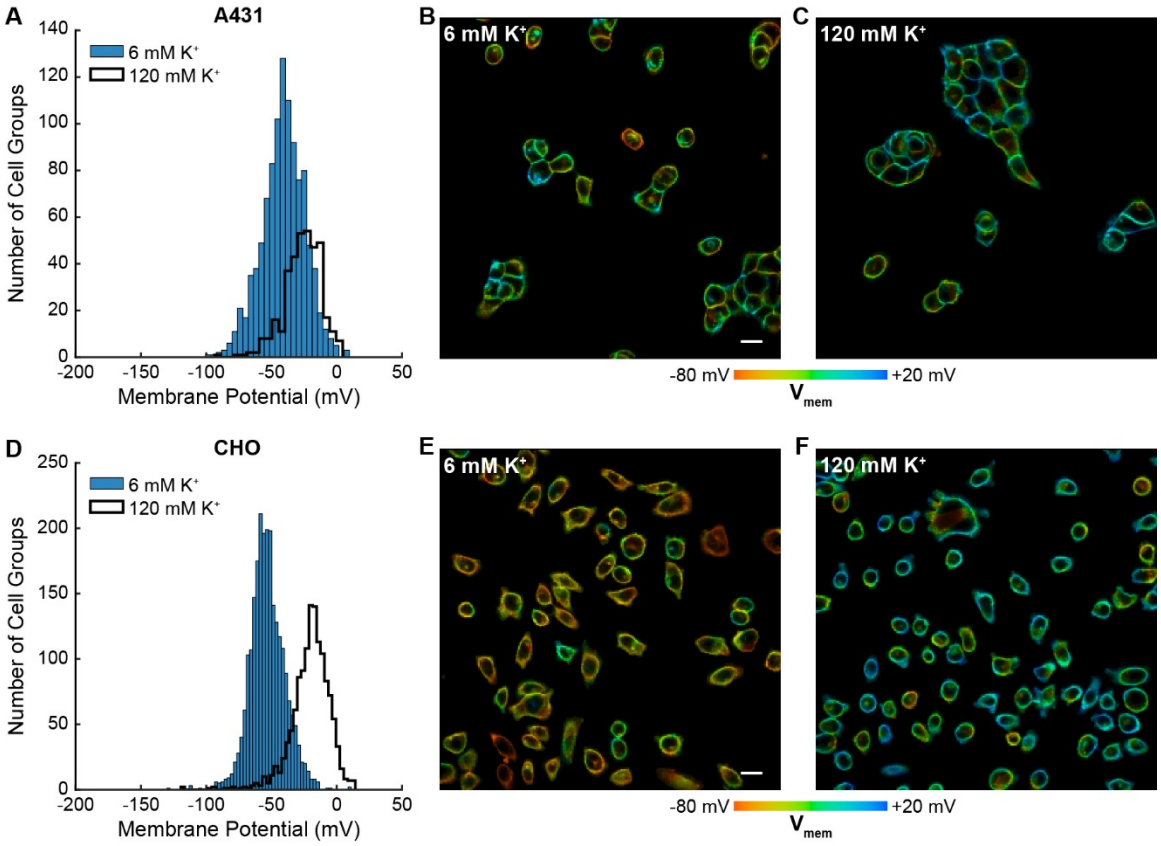

Figure 2.12. Rapid optical profiling of V_{mem} at rest and in high extracellular K^+.
Fluorescence lifetime images of cells incubated with 100 nM VF2.1.Cl were used to determine V_{mem} from previously performed electrophysiological calibration (**Fig. 2.7**). (A) Histograms of V_{mem} values recorded in A431 cells incubated with 6 mM extracellular K^+ (commercial HBSS, n=1056) or 120 mM K^+ (high K^+ HBSS, n=368). (B) Representative lifetime image of A431 cells in 6 mM extracellular K^+. (C) Representative lifetime image of A431 cells in 120 mM extracellular K^+. (D) Histograms of V_{mem} values observed in CHO cells under normal (n=2410) and high K^+ (n=1310) conditions. Representative lifetime image of CHO cells in (E) 6 mM and (F) 120 mM extracellular K^+. Histogram bin sizes were determined by the Freedman-Diaconis rule. Intensities in the lifetime-intensity overlay images are not scaled to each other. Scale bars, 20 μm.

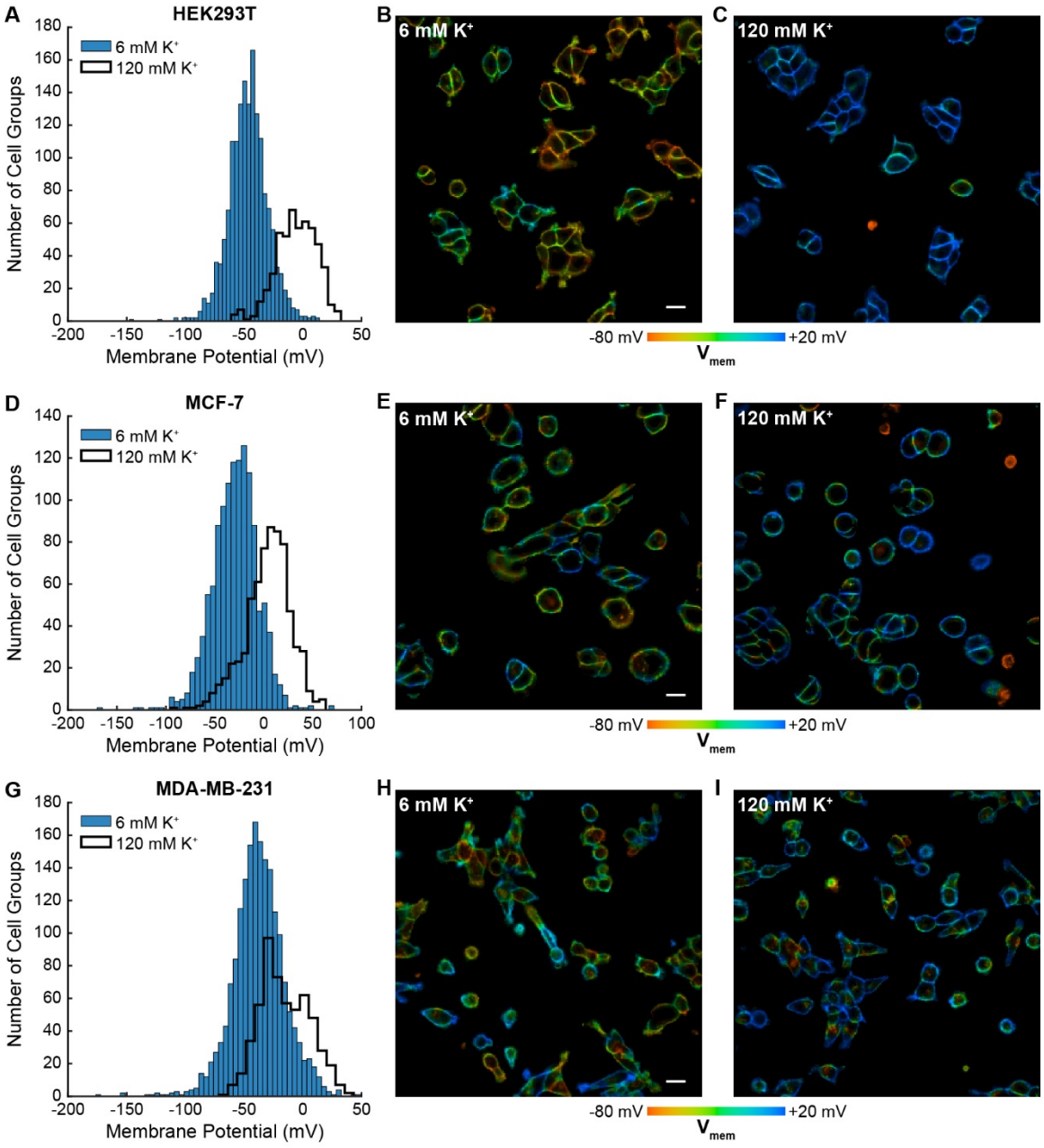

Figure 2.13. Optically recorded V_{mem} distributions in HEK293T, MCF-7 and MDA-MB-231 cells.

Fluorescence lifetime images of cells incubated with 100 nM VF2.1.Cl were used to determine V_{mem} from previously performed electrophysiological calibration (**Fig. 2.7**). (A) Histograms of V_{mem} values recorded in HEK293T cells incubated with 6 mM extracellular K^+ (commercial HBSS, n=1613) or 120 mM K^+ (high K^+ HBSS, n=520). (B) Representative lifetime image of HEK293T cells with 6 mM extracellular K^+. (C) Representative lifetime image of HEK293T cells in 120 mM extracellular K^+. (D) Histograms of V_{mem} values observed in MCF-7 cells under normal (n=1259) and high K^+ (n=681) conditions. Representative lifetime images of MCF-7 cells in (E) 6 mM and (F) 120 mM extracellular K^+. (G) Histograms of V_{mem} values observed in MDA-MB-231 cells under normal (n=1840) and high K^+ (n=558) conditions. Representative lifetime images of

MDA-MB-231 cells in (H) 6 mM and (I) 120 mM extracellular K^+. Histogram bin sizes were determined by the Freedman-Diaconis rule. Intensities in the lifetime-intensity overlay images are not scaled to each other. Scale bars, 20 μm.

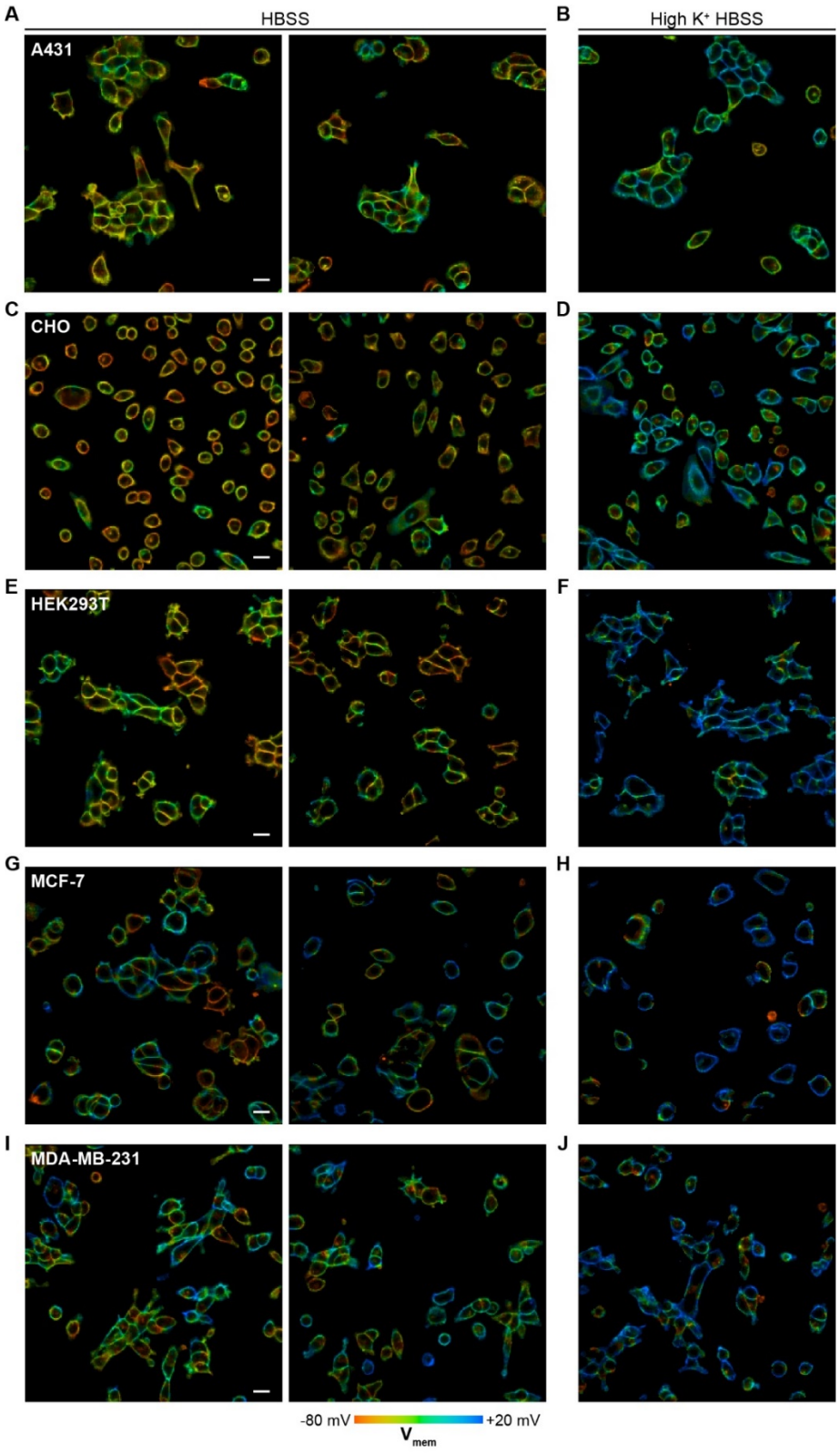

Figure 2.14. Representative images of cultured cell resting membrane potential.

Representative VF-FLIM images of cells in standard imaging buffer (HBSS, 6 mM extracellular K^+) and high K^+ imaging buffer (high K^+ HBSS, 120 mM extracellular K^+). Membrane potential was calculated per cell group; analyses of pixel by pixel differences in lifetime fall beyond the resolution limit of the VF-FLIM calibrations in this work. Images depict A431 cells in (A) HBSS and (B) high K^+ HBSS; CHO cells in (C) HBSS and (D) high K^+ HBSS; HEK293T cells in (E) HBSS and (F) high K^+ HBSS; MCF-7 cells in (G) HBSS and (H) high K^+ HBSS, and MDA-MB-231 cells in (I) HBSS and (J) high K^+ HBSS.

	VF-FLIM		Patch-clamp electrophysiology	
Cell Line	Resting V_{mem} (mean ± SEM)	High K^+ V_{mem} (mean ± SEM)	Compiled reported average or median V_{mem} in cells at rest	Mean of ephys. values
A431	-41 ± 5	-26 ± 5	-64 ± 1 (mean ± SEM)[41]	-64
CHO	-53 ± 4	-20 ± 4	-21 ± 2 (mean ± SEM, 4 cells)[42] -31 ± 2.6 (mean ± SEM)[43] -35 (ranging -10 to -65 mV)[44]	-30
HEK293T	-47 ± 5	-6 ± 5	-45 (ranging -40 to -50 mV)[45] -52 ± 1 (mean ± SEM)[46] -35 ± 2 (mean ± SEM)[47]	-44
MCF-7	-29 ± 5	4 ± 5	-23 ± 1 (median ± SE of median)[48] -36 ± 5 (mean ± SEM)[49] -41 ± 20 (mean ± SD)[50] -42 (no error given)[51] -42 ± 5 (mean ± SEM)[52]	-36
MDA-MB-231	-38 ± 5	-15 ± 5	-19 ± 3 (mean ± SEM)[53] -26 ± 8 (mean ± SEM)[54] -39 ± 5 (mean ± SEM)[49]	-28

Table 2.5. V_{mem} measurements made with VF-FLIM agree with previously reported values. Comparison of optically-determined resting membrane potential values (in millivolts) and previously reported values. This table summarizes data presented in **Fig. 2.12** and **Fig. 2.13**. Optically determined membrane potentials were calculated from lifetime-V_{mem} standard curves (**Table 2.4**). For tabulated literature values, measures of error and central tendency were used from the original publication. In some cases, none were given or only ranges were discussed. The mean of the reported ephys values is the mean of the values listed here. Sample sizes for resting and elevated K^+, respectively: A431 1056, 368; CHO 2410, 1310; HEK293T 1613, 520; MCF-7 1259, 681; MDA-MB-231 1840, 558.

Membrane Potential Dynamics in Epidermal Growth Factor Signaling

We thought VF-FLIM was a promising method for elucidating the roles of membrane potential in non-excitable cell signaling. Specifically, we wondered whether VF-FLIM might be well-suited to dissect conflicting reports surrounding changes in membrane potential during EGF/EGF receptor (EGFR)-mediated signaling. Receptor tyrosine kinase (RTK)-mediated signaling is a canonical signaling paradigm for eukaryotic cells, transducing extracellular signals into changes in cellular state. Although the involvement of second messengers like Ca^{2+}, cyclic nucleotides, and lipids are well characterized, membrane potential dynamics and their associated roles in non-excitable cell signaling remain less well-defined. In particular, the activation of EGFR via EGF has variously been reported to be depolarizing [55], hyperpolarizing [56], or electrically silent [41,57].

We find that treatment of A431 cells with EGF results in a 15 mV hyperpolarization within 60-90 seconds in approximately 80% of cells (**Fig. 2.15A-C, Fig. 2.16, Fig. 2.17**), followed by a slow return to baseline within 15 minutes (**Fig. 2.15D-F, Fig. 2.18, 30 second acquisitions**). The voltage response to EGF is dose-dependent, with an EC_{50} of 90 ng/mL (14 nM) (**Fig. 2.19**). Vehicle-treated cells show very little τ_{fl} change (**Fig. 2.15A-F**). Identical experiments with voltage-insensitive VF2.0.Cl (**Fig. 2.15G-H, Fig. 2.16**, **Fig. 2.18**, **Fig. 2.20**) reveal little change in τ_{fl} upon EGF treatment, indicating the drop in τ_{fl} arises from membrane hyperpolarization. We observe the greatest hyperpolarization 1 to 3 minutes after treatment with EGF, which is abolished by inhibition of EGFR and ErbB2 tyrosine kinase activity with the covalent inhibitor canertinib (**Fig. 2.15I-J, Fig. 2.21**). Blockade of the EGFR kinase domain with gefitinib, a non-covalent inhibitor of EGFR, also results in a substantial decrease in the EGF-evoked hyperpolarization (**Fig. 2.15I-J, Fig. 2.21**). Together, these results indicate that A431 cells exhibit an EGF-induced hyperpolarization, which depends on the kinase activity of EGFR and persists on the timescale of minutes.

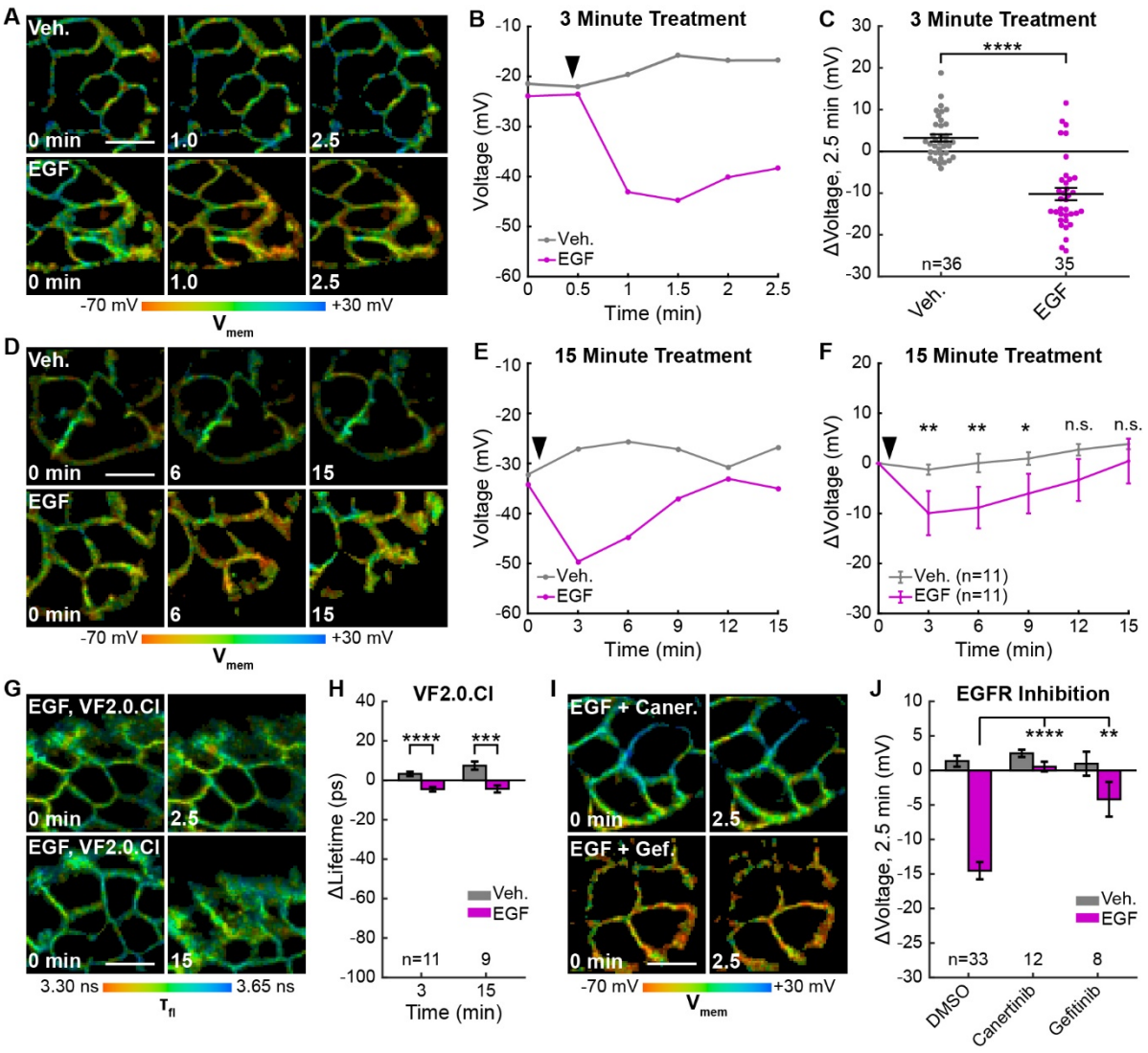

Figure 2.15. EGFR-mediated receptor tyrosine kinase activity produces a transient hyperpolarization in A431 cells.

(A) Representative VF-FLIM time series of A431 cells treated with imaging buffer vehicle (top) or 500 ng/mL EGF (80 nM, bottom). (B) Quantification of images in (A), with Vehicle (Veh.)/EGF added at black arrow. (C) Aggregated responses for various trials of cells treated with vehicle or EGF. (D) Lifetime images of longer-term effects of vehicle (top) or EGF (bottom) treatment. (E) Quantification of images in (D). (F) Average response of cells over the longer time course. (G) Images of VF2.0.Cl (voltage insensitive) lifetime before and after EGF treatment. No τ_{fl} change is observed 2.5 (top) or 15 minutes (bottom) following EGF treatment. (H) Average VF2.0.Cl lifetime changes following EGF treatment. VF2.0.Cl graphs and images are scaled across the same lifetime range (350 ps) as VF2.1.Cl plots and images. The small drift observed would correspond to 2-4 mV of voltage change in VF2.1.Cl lifetime. (I) Lifetime images of A431 cells before and after EGF addition, with 500 nM canertinib (top) or 10 µM gefitinib (bottom). (J) Voltage changes 2.5 minutes after EGF addition in cells treated with DMSO (vehicle control) or an EGFR inhibitor. Scale bars are 20 µm. (C,F,H): Asterisks indicate significant differences between vehicle and EGF

at that time point. (J): Asterisks reflect significant differences between EGF-induced voltage responses with DMSO vehicle or an EGFR inhibitor (n.s. $p>0.05$, * $p<0.05$, ** $p<0.01$, *** $p<0.001$, **** $p<0.0001$, two-tailed, unpaired, unequal variances t-test).

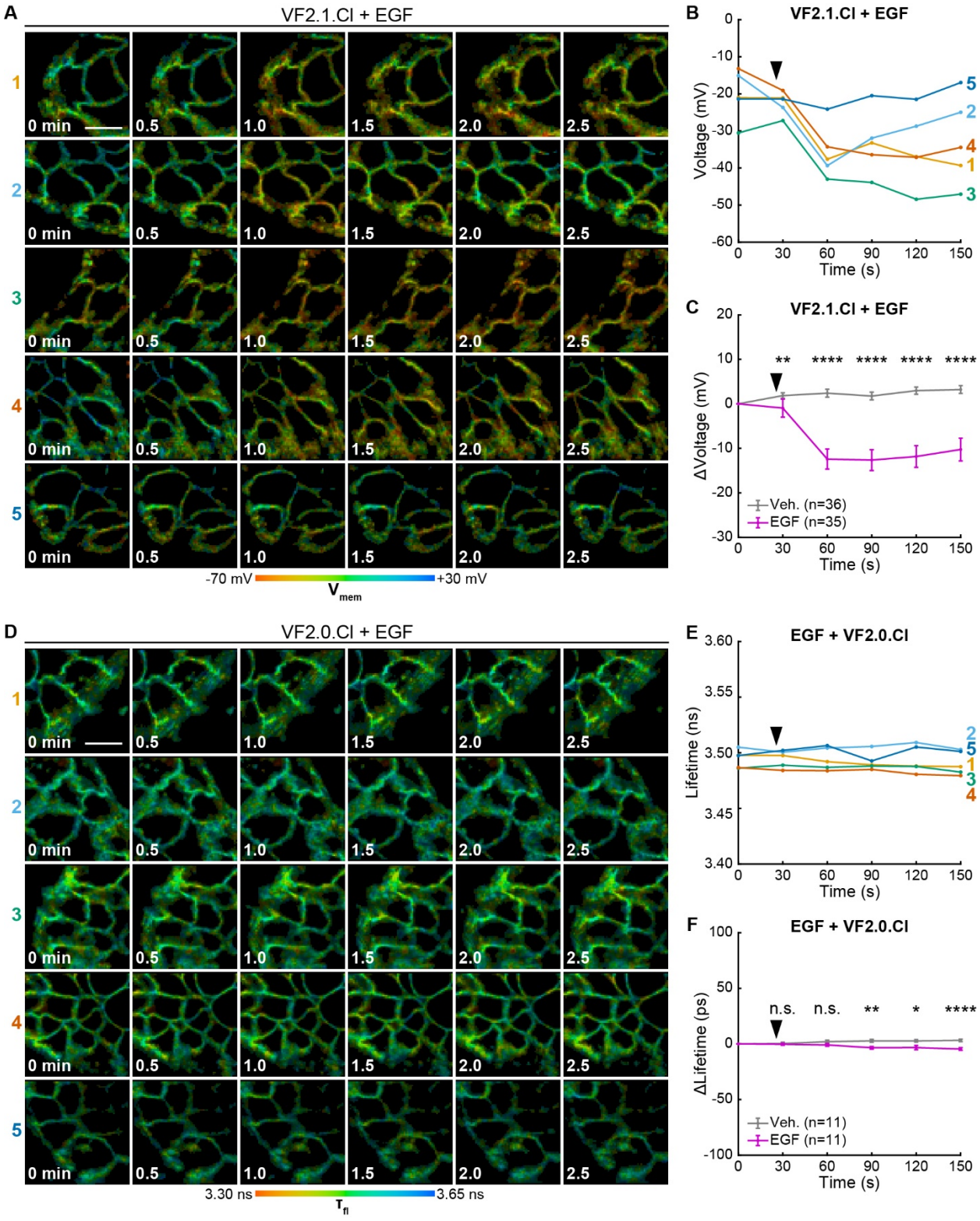
A
VF2.1.Cl + EGF
1
2
3
4
5
0 min
0.5
1.0
1.5
2.0
2.5
-70 mV
+30 mV
V_mem
B
VF2.1.Cl + EGF
Voltage (mV)
Time (s)
C
VF2.1.Cl + EGF
ΔVoltage (mV)
** **** **** **** ****
Veh. (n=36)
EGF (n=35)
Time (s)
D
VF2.0.Cl + EGF
3.30 ns
3.65 ns
T_fl
E
EGF + VF2.0.Cl
Lifetime (ns)
Time (s)
F
EGF + VF2.0.Cl
ΔLifetime (ps)
n.s. n.s. ** * ****
Veh. (n=11)
EGF (n=11)
Time (s)

Figure 2.16. Individual VF-FLIM recordings of A431 EGF response.
(A) Representative 3 minute VF-FLIM recordings of A431 cells loaded with 50 nM VF2.1.Cl. 500 ng/mL EGF was added 30 seconds into the time series (black arrow). (B) Quantification of the images in (A), with a single trace per image series shown. (C) Average voltage change in A431 cells following the addition of imaging buffer vehicle (gray) or EGF (purple). (D) Control VF2.0.Cl (not voltage sensitive, 50 nM) images of A431 cells treated as in (A). Images are scaled across the same amount of lifetime space (350 ps) as the VF2.1.Cl images. (E) Quantification of the images in (D). (F) Average VF2.0.Cl lifetime change seen in A431 cells following the addition of imaging buffer vehicle (gray) or EGF (purple) in A431 cells. Graph is scaled across the same amount of lifetime space as the VF2.1.Cl data in (C). Asterisks indicate significant differences between vehicle and EGF treated cells at a given time point (n.s. $p > 0.05$, * $p < 0.05$, ** $p < 0.01$, *** $p < 0.001$, **** $p < 0.0001$, two-sided, unpaired, unequal variances t-test). Scale bars are 20 μm.

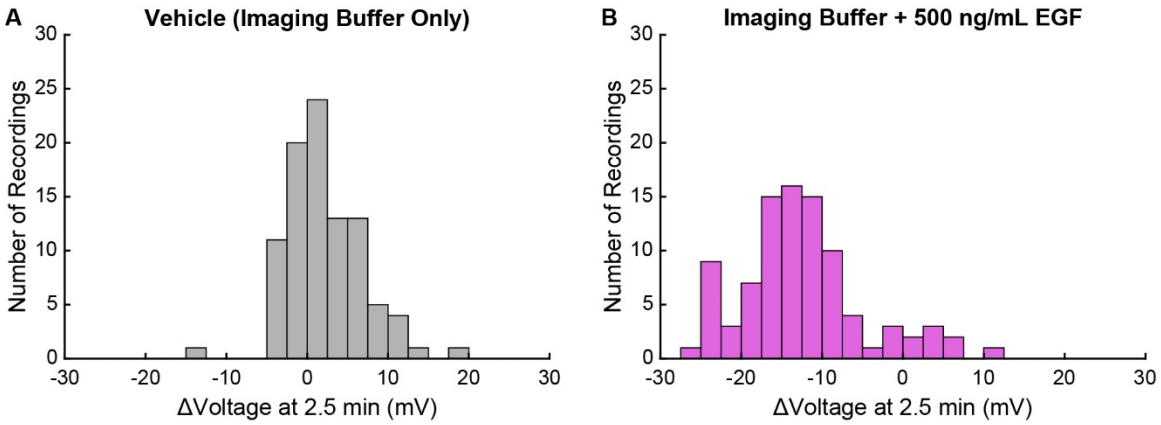

Figure 2.17. Membrane potential changes in A431 cells 2.5 minutes after EGF treatment.
Comparison of V_{mem} changes observed in A431 cells 2.5 minutes after treatment with (A) imaging buffer vehicle or (B) 500 ng/mL EGF. Data shown here are compiled from **Fig. 2.15C** and **Fig. 2.22A** to provide a sense of overall distribution of the responses. Each recording contained a single group of approximately 5 to 10 cells. Sample sizes (number of recordings): Vehicle 93, EGF 92.

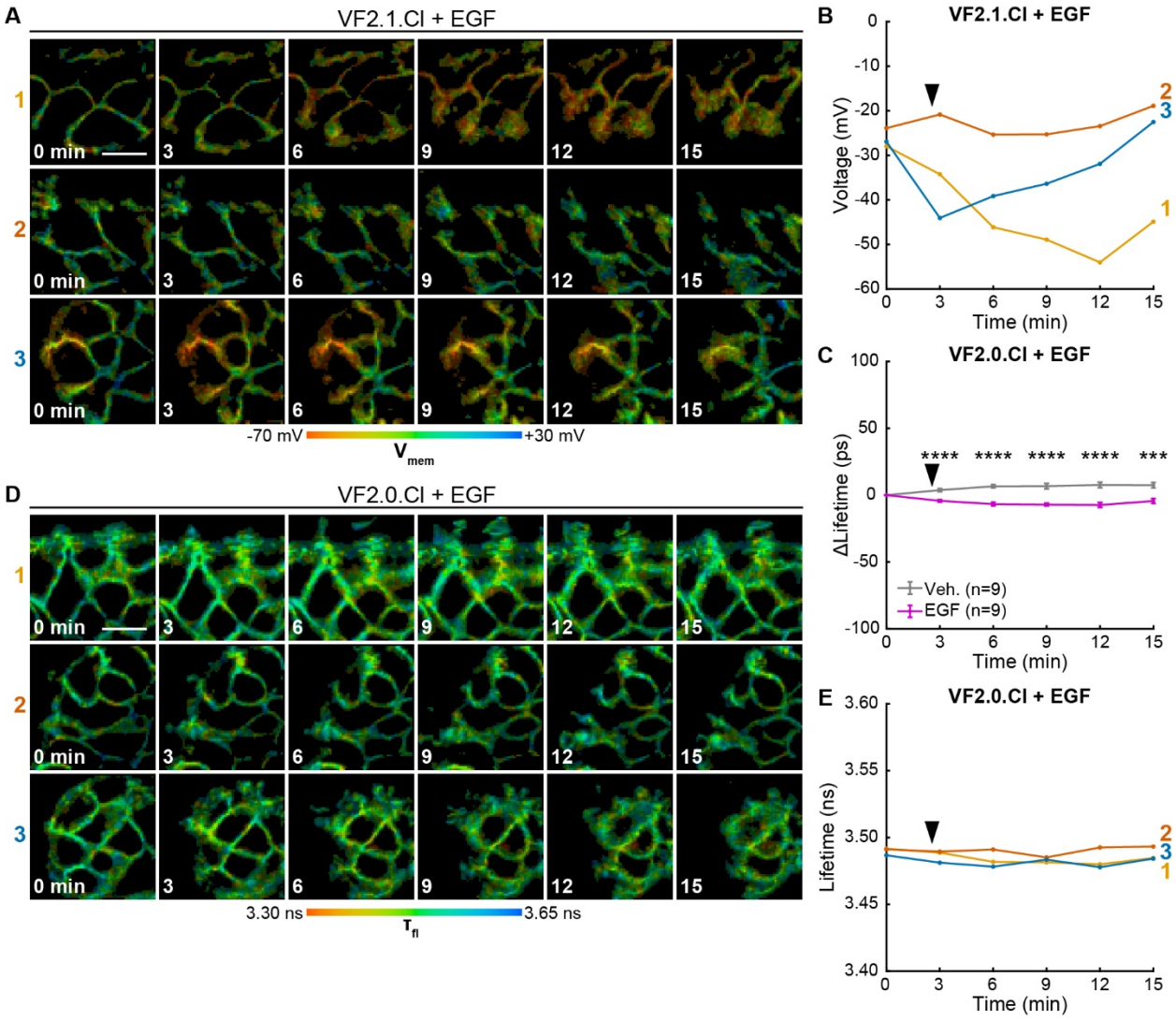

Figure 2.18. VF-FLIM reports A431 V_{mem} changes over 15 minutes.
(A) Representative longer term VF-FLIM recordings of A431 cells loaded with 50 nM VF2.1.Cl. 500 ng/mL EGF was added 30 seconds into the time series. (B) Quantification of the images in (A), with a single trace per image series shown. (C) Control VF2.0.Cl (not voltage sensitive, 50 nM) images of A431 cells treated as in (A). Images are scaled across the same total lifetime range (350 ps) as the VF2.1.Cl images. (D) Quantification of the recordings in (C). (E) Average VF2.0.Cl lifetime change seen in A431 cells following the addition of imaging buffer vehicle (gray) or EGF (purple). Asterisks indicate significant differences between vehicle and EGF treated cells at a given time point (*** $p < 0.001$, **** $p < 0.0001$, two-sided, unpaired, unequal variances t-test). Scale bars are 20 μm.

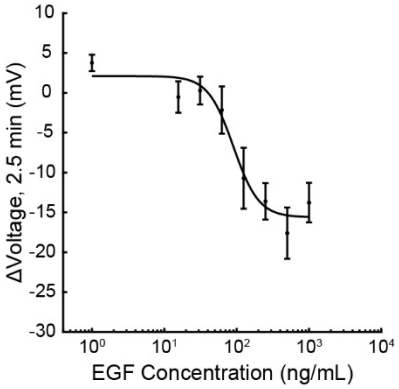

Figure 2.19. Dose-response relationship of A431 voltage response to EGF.
Data were fit to a four-parameter logistic function to obtain an EC_{50} of 90 ng/mL (95% CI: 47-130 ng/mL). Response to each EGF concentration is shown as mean ± SEM of 6 or 7 recordings (one group of 5-10 cells per recording).

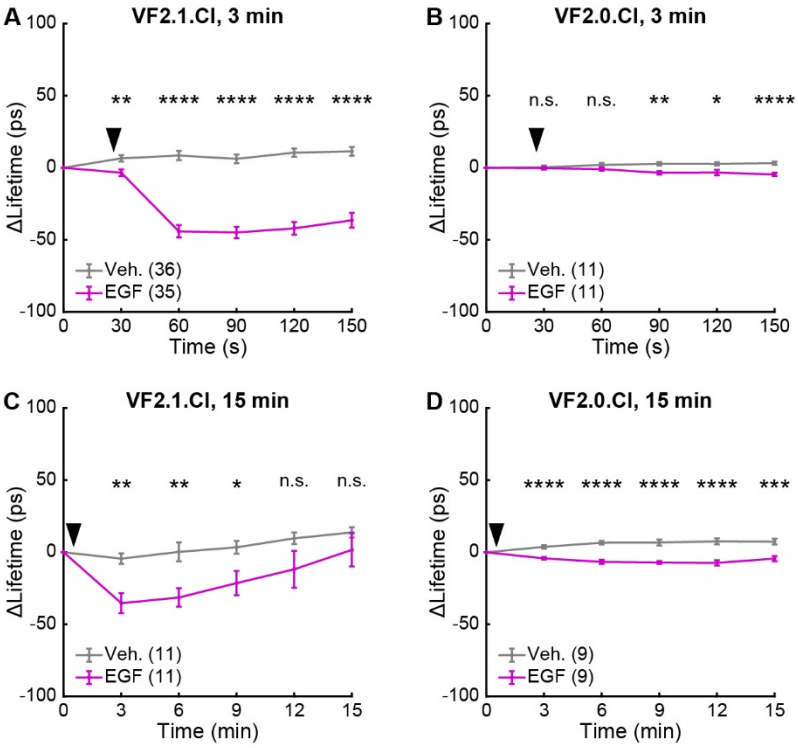

Figure 2.20. Effect sizes of VF2.1.Cl and VF2.0.Cl response to EGF treatment.
Average lifetime changes observed in A431 cells following the addition (black arrow) of imaging buffer vehicle (gray) or 500 ng/mL EGF (purple). (**A**) Cells incubated with 50 nM VF2.1.Cl and imaged for 3 minutes. (**B**) Cells incubated with 50 nM VF2.0.Cl (not voltage sensitive) and imaged for 3 minutes. (**C**) Cells incubated with 50 nM VF2.1.Cl and imaged intermittently for 15 minutes. (**D**) Cells incubated with 50 nM VF2.0.Cl (not voltage sensitive) and imaged intermittently for 15

minutes. Data are reproduced from **Fig. 2.15**, **Fig. 2.16**, and **Fig. 2.18**, but here data are scaled in units of lifetime rather than voltage for facile comparison. Data are shown as mean ± SEM for the indicated number of recordings (one group of 5-10 cells per recording). Asterisks indicate significant differences between vehicle and EGF treated cells at a given time point (n.s. $p > 0.05$, * $p < 0.05$, ** $p < 0.01$, *** $p < 0.001$, **** $p < 0.0001$, two-sided, unpaired, unequal variances t-test).

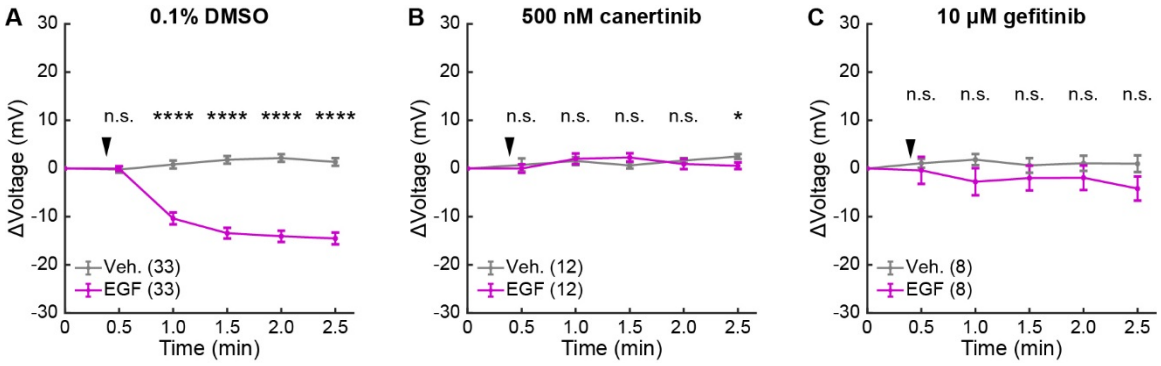

Figure 2.21. EGFR inhibitors abolish voltage response to EGF in A431 cells.
Average V_{mem} changes following the addition (black arrow) of imaging buffer vehicle (gray) or 500 ng/mL EGF (purple) to A431 cells pre-treated with the indicated drug or DMSO vehicle. 2.5 minute time points from this data are shown elsewhere (**Fig. 2.15J**); entire time series are shown here. Data are presented as mean ± SEM for the indicated number of recordings (one group of 5-10 cells per recording). Asterisks indicate significant differences between vehicle and EGF treated cells at a given time point (n.s. $p > 0.05$, * $p < 0.05$, ** $p < 0.01$, *** $p < 0.001$, **** $p < 0.0001$, two-sided, unpaired, unequal variances t-test).

Outward K^+ currents could mediate EGF-induced hyperpolarization. Consistent with this hypothesis, dissipation of the K^+ driving force by raising extracellular [K^+] completely abolishes the typical hyperpolarizing response to EGF and instead results in a small depolarizing potential of approximately 3 mV (**Fig. 2.22A, Fig. 2.23B**). Blockade of voltage-gated K^+ channels (K_v) with 4-aminopyridine (4-AP) prior to EGF treatment enhances the hyperpolarizing response to EGF (**Fig. 2.22A-B, Fig. 2.23C**). In contrast, blockade of Ca^{2+}-activated K^+ channels (K_{Ca}) with charybdotoxin (CTX) results in a depolarizing potential of approximately 4 mV after exposure to EGF, similar to that observed with high extracellular [K^+] (**Fig. 2.22A-B**, **Fig. 2.23D**). TRAM-34, a specific inhibitor of the intermediate-conductance Ca^{2+} activated potassium channel $K_{Ca}3.1$ [58], also abolishes EGF-induced hyperpolarization (**Fig. 2.22A, Fig. 2.23E**). CTX treatment has little effect on the resting membrane potential, while TRAM-34 or 4-AP depolarizes cells by approximately 5-10 mV (**Fig. 2.24**).

To explore the effects of other components of the EGFR pathway on EGF-induced hyperpolarization, we perturbed intra- and extracellular Ca^{2+} concentrations during EGF stimulation. Reduction of extracellular Ca^{2+} concentration did not substantially alter the EGF response (**Fig. 2.22A, Fig. 2.23F**). However, sequestration of intracellular Ca^{2+} with BAPTA-AM disrupts the hyperpolarization response. BAPTA-AM treated cells show a small, 4 mV

depolarization in response to EGF treatment, similar to CTX-treated cells (**Fig. 2.22A, Fig. 2.23G**). Perturbation of Ca^{2+} levels had little effect on the resting membrane potential (**Fig. 2.24**). Introduction of wortmannin (1 μM) to block downstream kinase activity has no effect on the membrane potential response to EGF, while orthovanadate addition (Na_3VO_4, 100 μM) to block phosphatase activity results in a small increase in the hyperpolarizing response (**Fig. 2.22A, Fig. 2.23H-I**). These results support a model for EGF-EGFR mediated hyperpolarization in which RTK activity of EGFR causes release of internal Ca^{2+} stores to in turn open K_{Ca} channels and hyperpolarize the cell (**Fig. 2.22C**).

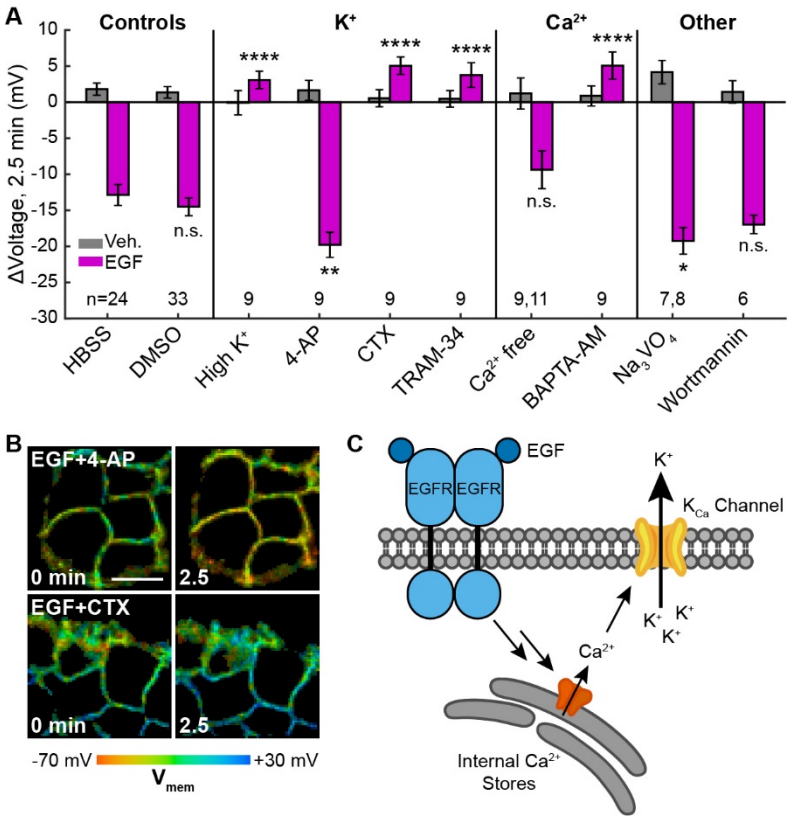

Figure 2.22. EGF-induced hyperpolarization is mediated by a Ca^{2+} activated K^+ channel. (A) Comparison of the V_{mem} change 2.5 minutes after EGF addition in cells incubated in unmodified imaging buffer (HBSS) or in modified solutions. (B) Lifetime images of A431 cells treated with 4-AP or CTX. (C) Model for membrane hyperpolarization following EGFR activation. Scale bar is 20 μm. Bars are mean ± SEM. Sample sizes listed are (Veh, EGF); where only one number is given, sample size was the same for both. Asterisks reflect significant differences in EGF-stimulated V_{mem} change between the unmodified control (HBSS or DMSO) and modified solutions (n.s. $p>0.05$, * $p<0.05$, ** $p<0.01$, *** $p<0.001$, **** $p<0.0001$, two-tailed, unpaired, unequal variances t-test). DMSO: 0.1% DMSO, high K^+: 120 mM K^+, 4-AP: 5 mM 4-aminopyridine, CTX: 100 nM charybdotoxin, TRAM-34: 200 nM TRAM-34, Ca^{2+} free: 0 mM Ca^{2+} and Mg^{2+}, BAPTA-AM: 10 μM bisaminophenoxyethanetetraacetic acid acetoxymethyl ester, Na_3VO_4: 100 μM sodium orthovanadate, wortmannin: 1 μM wortmannin.

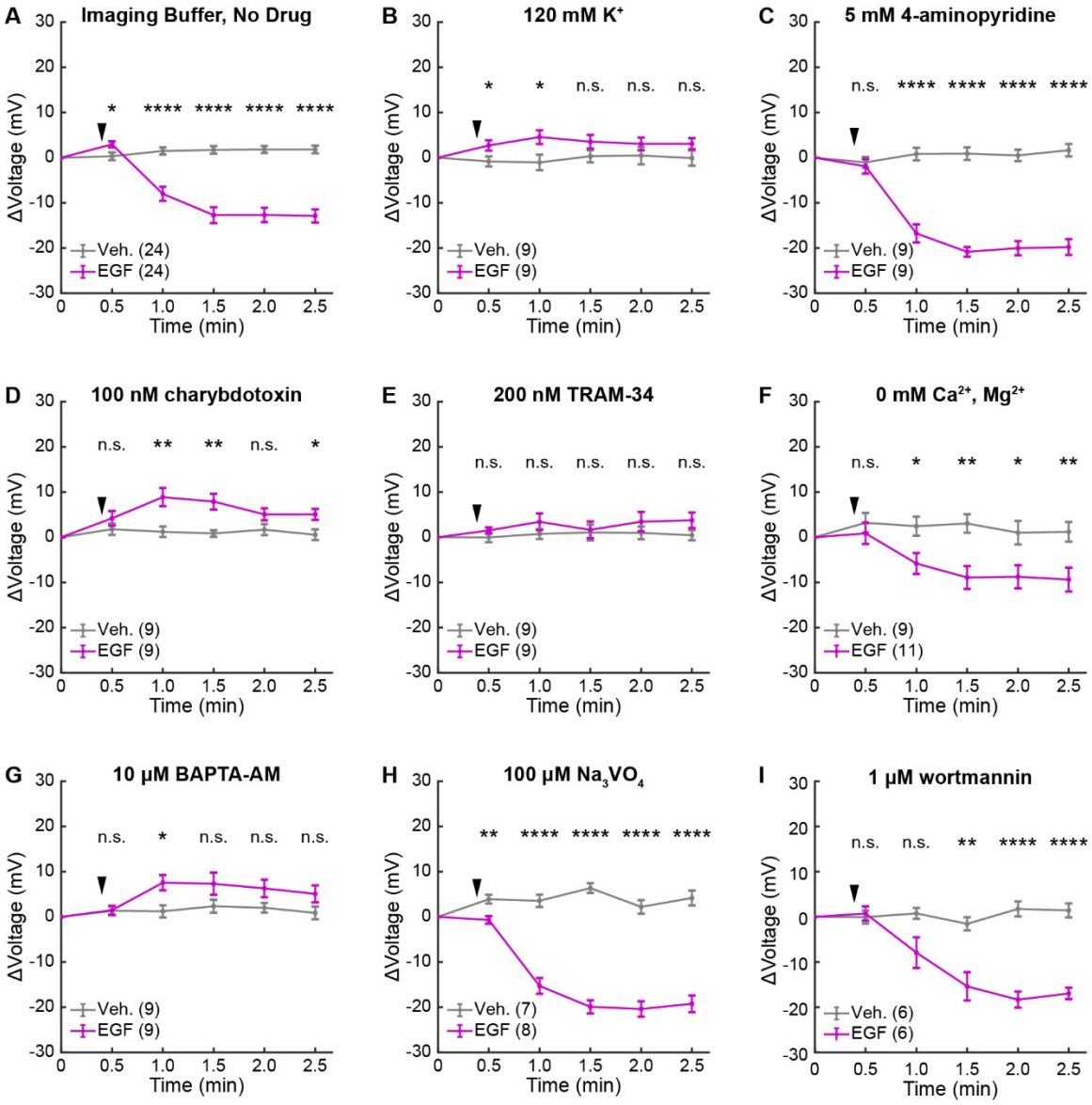

Figure 2.23. A431 voltage response to EGF with pharmacological intervention.
Average V_{mem} changes following the addition (black arrow) of imaging buffer vehicle (gray) or 500 ng/mL EGF (purple) to A431 cells pre-treated with the indicated drug or ionic composition change. 2.5 minute time points from this data are shown elsewhere (**Fig. 2.22**); entire time series are shown here to illustrate the time courses of the large hyperpolarizing current and small depolarizing current. Data are shown as mean ± SEM for the indicated number of recordings (one group of 5-10 cells per recording). Asterisks indicate significant differences between vehicle and EGF treated cells at a given time point (n.s. $p > 0.05$, * $p < 0.05$, ** $p < 0.01$, *** $p < 0.001$, **** $p < 0.0001$, two-sided, unpaired, unequal variances t-test).

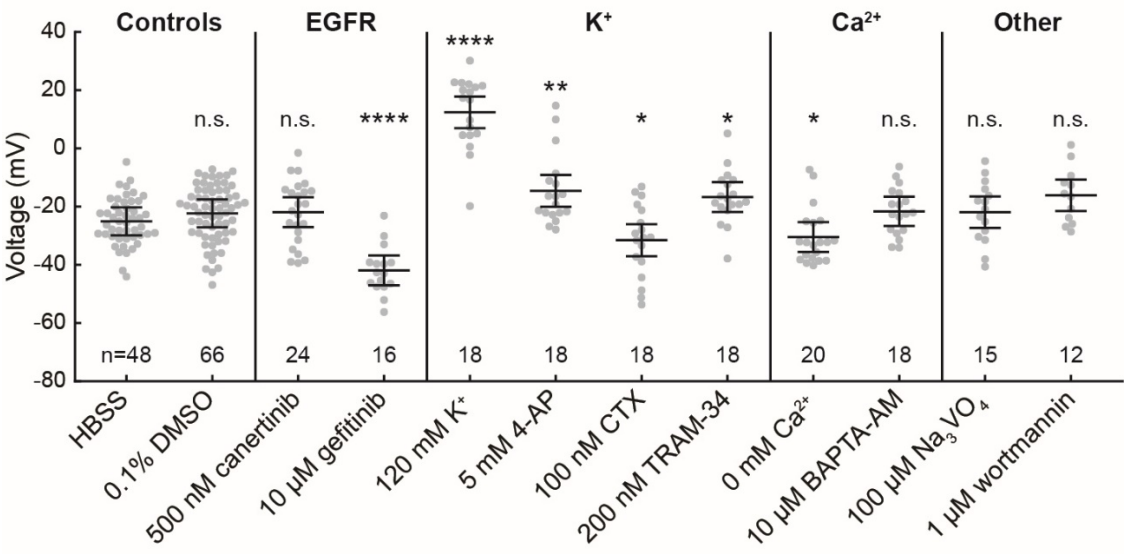

Figure 2.24. Effects of pharmacological and ionic perturbations on A431 resting membrane potential.
Data are the initial V_{mem} reference images for recordings used in EGF addition time series. Data are shown as mean ± SEM for the indicated number of images (one group of 5-10 cells per image), and gray dots represent individual images. Asterisks indicate significant differences between the appropriate vehicle (HBSS or 0.1% DMSO) and pharmacology treated cells (n.s. $p > 0.05$, * $p < 0.05$, ** $p < 0.01$, *** $p < 0.001$, **** $p < 0.0001$, two-sided, unpaired, unequal variances t-test). CTX = charybdotoxin, 4-AP = 4-aminopyridine, BAPTA-AM = bisaminophenoxyethanetetraacetic acid acetoxymethyl ester.

Discussion

We report the design and implementation of a new method for optically quantifying absolute membrane potential in living cells. VF-FLIM enjoys 100-fold improved throughput over patch clamp electrophysiology, as well as improved spatial resolution. The performance of VF-FLIM hinges on a balance between resolution in three dimensions: membrane potential, space, and time. We discuss the advantages and disadvantages of VF-FLIM in this light, as well as the new application space that is made accessible by VF-FLIM.

Resolution of VF-FLIM: Voltage, Space, and Time

The key advantage of VF-FLIM over previously reported optical approaches is its superior V_{mem} resolution. Resolution can be interpreted as stability of the τ_{fl}-V_{mem} calibration over time and between cells. Any factors other than V_{mem} that change τ_{fl} decrease resolution. VF-FLIM exhibits a 19-fold improvement in inter-cell V_{mem} resolution over FLIM with the GEVI CAESR [31] and a 8-fold improvement over di-8-ANEPPS excitation ratios [14]. Although all optical strategies, including VF-FLIM, have worse V_{mem} resolution than modern electrophysiology, the greater throughput, improved spatial resolution, and reduced invasiveness of optical strategies make them a powerful complement to electrode-based recordings.

The sources of variability that reduce resolution of optical V_{mem} measurements are manifold, but two major contributors are membrane specificity of the stain and the complexity of the lipid environment. Nonspecific staining is fluorescence signal from anywhere other than the plasma membrane, such as contaminating intracellular staining from poorly trafficked (CAESR) or internalized (ANEPPS) sensor. In contrast, exogenously loaded VF2.1.Cl exhibits little fluorescence contribution from regions other than the plasma membrane. Secondly, membrane composition and dipole potential can vary between cells and cell lines, changing the local environment of the fluorescent indicator [59,60]. Styryl dyes like di-8-ANEPPS can respond to changes in dipole potential[13,14], and VF dyes may be similarly sensitive to dipole potential. Additionally, fluorescence lifetime depends on certain environmental factors (e.g. temperature, viscosity, ionic strength) [22], which may introduce variability. These parameters are usually determined by the biological system under study, and re-calibration is important if they change dramatically in an experiment.

VF-FLIM, like all optical approaches, improves upon the spatial resolution of patch clamp electrophysiology. While VF-FLIM records the V_{mem} of an optically defined region of interest (in this study a cell or cell group), electrophysiology records V_{mem} at an individual cell or part of a cell where the electrode makes contact, which may or may not reflect the V_{mem} of the entire cell or group. In this study, we interpret VF-FLIM at the whole cell level only, since that is the smallest unit in which the V_{mem} can be reliably calibrated by whole cell patch clamp electrophysiology. Intriguingly, there are differences in lifetime within some cells in VF-FLIM images at the pixel to pixel level. In small, mostly spherical cells under voltage clamp, one would expect uniform membrane potential [17], so these subcellular differences are most likely noise in the measurement. We speculate that most of this pixel-to-pixel noise comes from variability in fitting the biexponential lifetime model. Lifetime estimates at each pixel are calculated from 20 to 100-fold fewer photons than the lifetime value for the entire ROI. These lower photon counts at the single pixel level produce V_{mem} estimates that are less precise than the V_{mem} estimate for the entire ROI. Collection of more photons at each pixel could likely reduce this noise but would require longer acquisition times. We also cannot fully rule out an alternative explanation that the observed subcellular variability is the result of local differences in membrane composition [13].

V_{mem} recordings in systems too large or too small for electrophysiological study could be an important application of VF-FLIM. Despite the improbability of V_{mem} compartmentalization in individual HEK293T cells, other cells with complex morphology and processes may display real, subcellular V_{mem} differences. In addition, delocalized V_{mem} patterns across tissues could in theory be stable [61] and have been proposed to contribute to tissue development [5]. One remaining challenge in expanding VF-FLIM to these areas is the requirement for an initial calibration with voltage clamp electrophysiology. Alternative ways to control V_{mem}, such as ionophores or optogenetic actuators [62], may prove useful in these systems. When applying VF-FLIM to tissues, the cellular specificity of the VF stain becomes a consideration, as the VF2.1.Cl indicator used in this study labels all cell membranes efficiently. Looking ahead, recordings in tissue are an exciting area for future development of VF-FLIM, particularly in conjunction with cellular and sub-cellular strategies for targeting VF dyes [63,64].

To obtain absolute V_{mem} measurements with fluorescence lifetime, VF-FLIM sacrifices some of the temporal resolution of electrophysiology or intensity-based voltage imaging. VF-FLIM acquisition times are limited by the large numbers of photons needed per pixel in time-correlated

single photon counting (see **Methods**). As a result, VF-FLIM in its current implementation can track V_{mem} events lasting longer than a few seconds. For "resting" membrane potential or V_{mem} dynamics associated with cell growth or differentiation, this temporal resolution is likely sufficient. Nevertheless, in the future, we envision allying VF-FLIM with recently developed, faster lifetime imaging technology to enable optical quantification of more rapid V_{mem} responses [65,66].

Resting Membrane Potential Distributions in Cultured Cells

Using the improved V_{mem} resolution and throughput of VF-FLIM, we optically documented resting membrane potential distributions in cultured cells to characterize the membrane potential state(s) present. The presence and significance of distinct V_{mem} states in cell populations is mostly uncharacterized due to the throughput limitations of patch-clamp electrophysiology, but some reports suggest that distinct V_{mem} states arise during the various phases of the cell cycle [48,50]. V_{mem} histograms presented in this work appear more or less unimodal, showing no clear sign of cell cycle-related V_{mem} states (**Fig. 2.12**, **Fig. 2.13**). We considered the possibility that VF-FLIM does not detect cell-cycle-related V_{mem} states because we report average V_{mem} across cell groups in cases where cells are in contact (**Fig. 2.2**). This explanation is unlikely for two reasons. First, V_{mem} distributions for CHO cells appear unimodal, even though CHO cultures were mostly comprised of isolated cells under the conditions tested (**Fig. 2.12D-F**). Second, theoretical work suggests that dramatically different V_{mem} states in adjacent cells are unlikely, as electrical coupling often leads to equilibration of V_{mem} across the cell group [61,67]. Although we cannot rule out the possibility of poorly separated V_{mem} populations (i.e. with a mean difference in voltage below our resolution limit), VF-FLIM both prompts and enables a re-examination of the notion that bi- or multimodal V_{mem} distributions exist in cultured cells. Furthermore, VF-FLIM represents an exciting opportunity to experimentally visualize theorized V_{mem} patterns in culture and in more complex tissues. Studies towards this end are ongoing in our laboratory.

Epidermal Growth Factor Induces V_{mem} Signaling in A431 Cells

In the present study, we use VF-FLIM to provide the first cell-resolved, direct visualization of voltage changes induced by growth factor signaling. For long term V_{mem} recordings during growth-related processes, an optical approach is more attractive than an electrode-based one. Electrophysiology becomes increasingly challenging as time scale lengthens, especially if cells migrate, and washout of the cytosol with pipette solution can change the very signals under study [68,69]. Previous attempts to electrophysiologically record V_{mem} in EGF-stimulated A431 cells were unsuccessful due to these technical challenges [56]. Because whole cell voltage-clamp electrophysiology was intractable, the V_{mem} response in EGF-stimulated A431 cells was addressed indirectly through model cell lines expressing EGFR exogenously [56], bulk measurements on trypsinized cells in suspension [70], or cell-attached single channel recordings [71–73]. By stably recording V_{mem} during EGF stimulation, VF-FLIM enables direct study of V_{mem} signaling in otherwise inaccessible pathways.

In conjunction with physiological manipulations and pharmacological perturbations, we explore the molecular mechanisms underlying EGF-induced hyperpolarization. We find that signaling along the EGF-EGFR axis results in a robust hyperpolarizing current carried by K^+ ions, passed

by the Ca^{2+}-activated K^+ channel $K_{Ca}3.1$, and mediated by intracellular Ca^{2+} (**Fig. 2.22C**). We achieve a complete loss of the hyperpolarizing response to EGF by altering the K^+ driving force ("High K^+" **Fig. 2.22A**, **Fig. 2.23B**), blocking calcium-activated K^+ currents directly ("CTX" and "TRAM-34", **Fig. 2.22A**, **Fig. 2.23D,E**), or intercepting cytosolic Ca^{2+} ("BAPTA-AM", **Fig. 2.22A**, **Fig. 2.23G**). These results, combined with transcriptomic evidence that $K_{Ca}3.1$ is the major K_{Ca} channel in A431 cells [74], indicate that $K_{Ca}3.1$ mediates the observed hyperpolarization. Interestingly, under some conditions where K^+-mediated hyperpolarization is blocked ("CTX," "high K^+", "BAPTA-AM"), VF-FLIM reveals a small, secondary depolarizing current not visible during normal EGF stimulation. This current likely arises from initial Ca^{2+} entry into the cell, as previously observed during EGF signaling [75,76]. Although we have obtained direct and conclusive evidence of EGF-induced hyperpolarization in A431 cells, the interactions between this voltage change and downstream targets of EGFR remain incompletely characterized. Enhancing EGF signaling by blockade of cellular tyrosine phosphatases with orthovanadate [77] correspondingly increases EGF-mediated hyperpolarization ("Na_3VO_4" **Fig. 2.22A**, **Fig. 2.23H**), but inhibition of downstream kinase activity appears to have little effect on hyperpolarization ("wortmannin" **Fig. 2.22A**, **Fig. 2.23I**).

In the context of RTK signaling, V_{mem} may serve to modulate the driving force for external Ca^{2+} entry [3,78] and thereby act as a regulator of this canonical signaling ion. Alternatively, V_{mem} may play a more subtle biophysical role, such as potentiating lipid reorganization in the plasma membrane [79]. Small changes in V_{mem} likely affect signaling pathways in ways that are currently completely unknown, but high throughput discovery of V_{mem} targets remains challenging. Combination of electrophysiology with single cell transcriptomics has begun to uncover relationships between V_{mem} and other cellular pathways in excitable cells [80]; such approaches could be coupled to higher throughput VF-FLIM methods to explore pathways that interact with V_{mem} in non-excitable contexts.

VF-FLIM represents a novel and general approach for interrogating the roles of membrane potential in fundamental cellular physiology. Future improvements to the voltage resolution could be made by use of more sensitive indicators, which may exhibit larger changes in fluorescence lifetime [34]. VF-FLIM can be further expanded to include the entire color palette of PeT-based voltage indicators [81,82], allied with targeting methods to probe absolute membrane potential in heterogeneous cellular populations [63,64], and coupled to high-speed imaging techniques for optical quantification of fast voltage events [65,66].

Materials

VoltageFluor (VF) dyes VF2.1.Cl and VF2.0.Cl were synthesized in house according to previously described syntheses [34]. VFs were stored either as solids at room temperature or as 1000x DMSO stocks at -20°C. VF stock concentrations were normalized to the absorption of the dichlorofluorescein dye head via UV-Vis spectroscopy in Dulbecco's phosphate buffered saline (dPBS, Thermo Fisher Scientific, Waltham, MA) pH 9 with 0.1% sodium dodecyl sulfate (w/v, SDS). Di-8-ANEPPS was purchased from Thermo Fisher Scientific. Di-8-ANEPPS was prepared as a 2 mM (2000x) stock solution in DMSO and stored at -20°C. Di-8-ANEPPS concentrations were determined via UV-Vis spectroscopy in methanol (ε at 498 nm: 41,000 cm^{-1} M^{-1} according to the manufacturer's certificate of analysis).

All salts and buffers were purchased from either Sigma-Aldrich (St. Louis, MO) or Fisher Scientific. TRAM-34, 4-aminopyridine, and charybdotoxin were purchased from Sigma-Aldrich. Gefitinib, wortmannin, sodium orthovanadate, and BAPTA-AM were purchased from Fisher Scientific. Canertinib was a gift from the Kuriyan laboratory at UC Berkeley. Gefitinib, wortmannin, canertinib, and TRAM-34 were made up as 1000x-10000x stock solutions in DMSO and stored at -20°C. Charybdotoxin was made up as a 1000x solution in water and stored at -80°C. 4-aminopyridine was made up as a 20x stock in imaging buffer (HBSS) and stored at 4°C. Recombinantly expressed epidermal growth factor was purchased from PeproTech (Rocky Hill, NJ) and aliquoted as a 1 mg/mL solution in water at -80°C.

Solid sodium orthovanadate was dissolved in water and activated before use [83]. Briefly, orthovanadate solutions were repeatedly boiled and adjusted to pH 10 until the solution was clear and colorless. 200 mM activated orthovanadate stocks were aliquoted and stored at -20°C.

Unless otherwise noted, all imaging experiments were performed in Hank's Balanced Salt Solution (HBSS; Gibco/Thermo Fisher Scientific). HBSS composition in mM: 137.9 NaCl, 5.3 KCl, 5.6 D-glucose, 4.2 $NaHCO_3$, 1.3 $CaCl_2$, 0.49 $MgCl_2$, 0.44 KH_2PO_4, 0.41 $MgSO_4$, 0.34 Na_2HPO_4. High K^+ HBSS was made in-house to 285 mOsmol and pH 7.3, containing (in mM): 120 KCl, 23.3 NaCl, 5.6 D-glucose, 4.2 $NaHCO_3$, 1.3 $CaCl_2$, 0.49 $MgCl_2$, 0.44 KH_2PO_4, 0.41 $MgSO_4$, 0.34 Na_2HPO_4. Nominally Ca^{2+}/Mg^{2+} free HBSS (Gibco) contained, in mM: 137.9 NaCl, 5.3 KCl, 5.6 D-glucose, 4.2 $NaHCO_3$, 0.44 KH_2PO_4, 0.34 Na_2HPO_4.

Methods

Cell Culture

All cell lines were obtained from the UC Berkeley Cell Culture Facility and discarded after twenty-five passages. A431, HEK293T, MCF-7, and MDA-MB-231 cells were authenticated by short tandem repeat (STR) profiling. All cells were routinely tested for mycoplasma contamination. Cells were maintained in Dulbecco's Modified Eagle Medium (DMEM) with 4.5 g/L D-glucose supplemented with 10% FBS (Seradigm (VWR); Radnor, PA) and 2 mM GlutaMAX (Gibco) in a 5% CO_2 incubator at 37°C. Media for MCF-7 cells was supplemented with 1 mM sodium pyruvate (Life Technologies/Thermo Fisher Scientific) and 1x non-essential amino acids (Thermo Fisher Scientific). Media for CHO.K1 (referred to as CHO throughout the text) cells was supplemented with 1x non-essential amino acids. HEK293T and MDA-MB-231 were dissociated with 0.05%

Trypsin-EDTA with phenol red (Thermo Fisher Scientific) at 37°C, whereas A431, CHO, and MCF-7 cells were dissociated with 0.25% Trypsin-EDTA with phenol red at 37°C. To avoid potential toxicity of residual trypsin, all cells except for HEK293T were spun down at 250xg or 500xg for 5 minutes and re-suspended in fresh complete media during passaging.

For use in imaging experiments, cells were plated onto 25 mm diameter poly-D-lysine coated #1.5 glass coverslips (Electron Microscopy Sciences) in 6 well tissue culture plates (Corning; Corning, NY). To maximize cell attachment, coverslips were treated before use with 1-2 M HCl for 2-5 hours and washed overnight three times with 100% ethanol and three times with deionized water. Coverslips were sterilized by heating to 150°C for 2-3 hours. Before use, coverslips were incubated with poly-D-lysine (Sigma-Aldrich, made as a 0.1 mg/mL solution in phosphate-buffered saline with 10 mM Na_3BO_4) for 1-10 hours at 37°C and then washed twice with water and twice with Dulbecco's phosphate buffered saline (dPBS, Gibco).

A431, CHO, HEK293T, and MCF-7 were seeded onto glass coverslips 16-24 hours before microscopy experiments. MDA-MB-231 cells were seeded 48 hours before use because it facilitated formation of gigaseals during whole-cell voltage clamp electrophysiology. Cell densities used for optical resting membrane potential recordings (in 10^3 cells per cm^2) were: A431 42; CHO 42; HEK293T 42; MCF-7 63; MDA-MB-231 42. To ensure the presence of single cells for whole-cell voltage clamp electrophysiology, fast-growing cells were plated more sparsely (approximately 20% confluence) for electrophysiology experiments. Cell densities used for electrophysiology (in 10^3 cells per cm^2) were: A431 36-52; CHO 21; HEK293T 21; MCF-7 63; MDA-MB-231 42. To reduce their rapid growth rate, HEK293T cells were seeded onto glass coverslips in reduced glucose (1 g/L) DMEM with 10% FBS, 2 mM GlutaMAX, and 1 mM sodium pyruvate for electrophysiology experiments.

Cellular Loading of VoltageFluor Dyes

Cells were loaded with 1x VoltageFluor in HBSS for 20 minutes in a 37°C incubator with 5% CO_2. For most experiments, 100 nM VoltageFluor was used. Serum-starved A431 cells were loaded with 50 nM VoltageFluor. After VF loading, cells were washed once with HBSS and then placed in fresh HBSS for imaging. All imaging experiments were conducted at room temperature under ambient atmosphere. Cells were used immediately after loading the VF dye, and no cells were kept for longer than an hour at room temperature.

Whole Cell Patch-Clamp Electrophysiology

Pipettes were pulled from borosilicate glass with filament (Sutter Instruments, Novato, CA) with resistances ranging from 4 to 7 MΩ with a P97 pipette puller (Sutter Instruments). Internal solution composition, in mM (pH 7.25, 285 mOsmol/L): 125 potassium gluconate, 10 KCl, 5 NaCl, 1 EGTA, 10 HEPES, 2 ATP sodium salt, 0.3 GTP sodium salt. EGTA (tetraacid form) was prepared as a stock solution in either 1 M KOH or 10 M NaOH before addition to the internal solution. Pipettes were positioned with an MP-225 micromanipulator (Sutter Instruments). A liquid junction potential of -14 mV was determined by the Liquid Junction Potential Calculator in the pClamp software package [84] (Molecular Devices, San Jose, CA), and all voltage step protocols were corrected for this offset.

For VF-FLIM and CAESR, electrophysiology recordings for VF-FLIM and CAESR were made with an Axopatch 200B amplifier and digitized with a Digidata 1440A (Molecular Devices). The

software package used was pClamp 10.3. Signals were filtered with a 5 kHz low-pass Bessel filter. Correction for pipette capacitance was performed in the cell attached configuration. Voltage-lifetime calibrations were performed in V-clamp mode, with the cell held at the potential of interest for 15 or 30 seconds while lifetime was recorded. Potentials were applied in random order, and membrane test was conducted between each step to verify the quality of the patch. For single cell patching, recordings were only included if they maintained a 30:1 ratio of membrane resistance (R_m) to access resistance (R_a) and an R_a value below 30 MΩ throughout the recording. Due to the reduced health of HEK293T cells transfected with CAESR, recordings were used as long as they maintained a 10:1 R_m:R_a ratio, although most recordings were better than 30:1 R_m:R_a. Only recordings stable for at least 4 voltage steps (roughly 2 minutes) were included in the dataset.

For di-8-ANEPPS, electrophysiology recordings were made in the same manner as the above, with the following minor differences. Signals were digitized with a Digidata 1550B; the pClamp 10.6 software package was used (Molecular Devices). Potentials were applied in the order 0 mV, -80 mV, +40 mV, -40 mV, +80 mV for ten seconds at each step. Patch parameters were tested at the beginning and end of the patch program, rather than between each step. Only patches that retained a 30:1 ratio of Rm to Ra and access resistance below 30 MΩ throughout the recording were included in the dataset.

For electrophysiology involving small groups of cells (**Fig. 2.10**), complete voltage clamp across the entire cell group was not possible. Recordings were used as long as R_a remained below 30 MΩ for at least three voltage steps. Most recordings also retained R_m:R_a ratios greater than 20:1.

Epidermal Growth Factor Treatment

A431 cells were serum starved prior to epidermal growth factor studies. Two days before the experiment, cells were trypsizined and suspended in complete media with 10% FBS. Cells were then spun down for 5 minutes at 500xg and re-suspended in reduced serum DMEM (2% FBS, 2 mM GlutaMAX, 4.5 g/L glucose). Cells were seeded onto 25 mm coverslips in 6 well plates at a density of 84 x 10^3 cells per cm^2. 4-5.5 hours before the experiment, the media was exchanged for serum-free DMEM (0% FBS, 2 mM GlutaMAX, 4.5 g/L glucose).

After 4-5.5 hours in serum-free media, cells were loaded with 50 nM VF dye as described above. In pharmacology experiments, the drug or vehicle was also added to the VF dye loading solution. All subsequent wash and imaging solutions also contained the drug or vehicle. For changes to buffer ionic composition, VoltageFluor dyes were loaded in unmodified HBSS to avoid toxicity from prolonged incubation with high K^+ or without Ca^{2+}. Immediately prior to use, cells were washed in the modified HBSS (120 mM K^+ or 0 mM Ca^{2+}) and recordings were made in the modified HBSS.

For analysis of short-term responses to EGF (3 minute time series), VF lifetime was recorded in 6 sequential 30 second exposures. Immediately after the conclusion of the first frame (30-35 seconds into the recording), EGF or vehicle (imaging buffer only) was added to the indicated final concentration from a 2x solution in HBSS imaging buffer. For analysis of long-term responses to EGF (15 minute time series), EGF addition occurred in the same way, but a gap of 150 seconds (without laser illumination) was allotted between each 30 second lifetime recording. Times given throughout the text correspond to the start of an exposure. Voltage changes at 2.5 minutes were

calculated from the difference between an initial image (taken before imaging buffer vehicle or EGF addition) and a final image (a 30 second exposure starting 2.5 minutes into the time series).

Transfection and Imaging of CAESR in HEK293T

The CAESR plasmid was obtained as an agar stab (FCK-Quasar2-Citrine, Addgene #59172), cultured overnight in LB with 100 μg/mL ampicillin, and isolated via a spin miniprep kit (Qiagen). HEK293T cells were plated at a density of 42,000 cells per cm^2 directly onto a 6 well tissue culture plate and incubated at 37°C in a humidified incubator for 24 hours prior to transfection. Transfections were performed with Lipofectamine 3000 according to the manufacturer's protocol (Thermo Fisher Scientific). Cells were allowed to grow an additional 24 hours after transfection before they were plated onto glass coverslips for microscopy experiments (as described above for electrophysiology of untransfected HEK293T cells).

Determination of EC_{50} for EGF in A431 Cells

Average voltage changes 2.5 minutes after addition of EGF to serum deprived A431 cells were determined at different EGF concentrations, and these means were fit to a four parameter logistic function in MATLAB (MathWorks, Natick, MA).

Goldman-Hodgkin-Katz Estimation of V_{mem} Ranges in Different Imaging Buffers

If intracellular and extracellular concentrations, as well as relative permeabilities, of all ionic species are known, the Goldman-Hodgkin-Katz (GHK) equation (eqn. 1) can be used to calculate the resting membrane potential of a cell [40]. In practice, the intracellular ion concentrations $[X]_{in}$ and relative permeabilities P_x are difficult to determine, so the GHK equation is not a substitute for direct measurement of V_{mem}. To obtain a range of reasonable V_{mem} values in systems where these concentrations and relative permeabilities are not known, we calculated possible V_{mem} using the "standard" parameters derived from the work of Hodgkin and Katz [40], as well as a value above and a value below each "standard" point. The values evaluated were the following: P_K 1; P_{Na} 0.01, 0.05, 0.2; P_{Cl} 0.2, 0.45, 0.9; $[K^+]_{in}$ 90, 150, 200 mM; $[Na^+]_{in}$ 5, 15, 50 mM; $[Cl^-]_{in}$ 2, 10, 35 mM. Extracellular ion concentrations $[X]_{out}$ were known (see **Materials**). In eqn. 2-1, R is the universal gas constant, T is the temperature (293 K for this experiment), and F is Faraday's constant.

$$V_{mem} = \frac{RT}{F} ln \frac{P_K[K^+]_{out} + P_{Na}[Na^+]_{out} + P_{Cl}[Cl^-]_{in}}{P_K[K^+]_{in} + P_{Na}[Na^+]_{in} + P_{Cl}[Cl^-]_{out}} \quad [2\text{-}1]$$

Fluorescence Lifetime Data Acquisition

Fluorescence lifetime imaging was conducted on a LSM 510 inverted scanning confocal microscope (Carl Zeiss AG, Oberkochen, Germany) equipped with an SPC-150 or SPC-150N single photon counting card (Becker & Hickl GmbH, Berlin, Germany) (**Scheme 2.1**). 80 MHz pulsed excitation was supplied by a Ti:Sapphire laser (MaiTai HP; SpectraPhysics, Santa Clara, CA) tuned to 958 nm and frequency-doubled to 479 nm. The laser was cooled by a recirculating water chiller (Neslab KMC100). Excitation light was directed into the microscope with a series of silver mirrors (Thorlabs, Newton, NJ or Newport Corporation, Irvine, CA).

Excitation light power at the sample was controlled with a neutral density (ND) wheel and a polarizer (P) followed by a polarizing beamsplitter (BS). Light was titrated such that VoltageFluor lifetime did not drift during the experiment, no phototoxicity was visible, and photon pile-up was not visible on the detector. For recordings at high VoltageFluor concentrations (**Fig. 2.3, Fig. 2.11**), reduced power was used to keep count rates below the pile-up limit. For optical voltage determinations using 50 or 100 nM VoltageFluor, typical average power at the sample was 5 μW.

Fluorescence emission was collected through a 40x oil immersion objective (Zeiss) coated with immersion oil (Immersol 518F, Zeiss). Emitted photons were detected with a hybrid detector, HPM-100-40 (Becker & Hickl), based on a Hamamatsu R10467 GaAsP hybrid photomultiplier tube. Detector dark counts were kept below 1000 per second during acquisition. Emission light was collected through a 550/49 bandpass filter (Semrock, Rochester, NY) after passing through a 488 LP dichroic mirror (Zeiss). The reference photons for determination of photon arrival times were detected with a PHD-400-N high speed photodiode (Becker & Hickl). Data were acquired with 256 time bins in the analog-to-digital-converter and either 64x64 or 256x256 pixels of spatial resolution (see discussion of pixel size below).

Routine evaluation of the proper functioning of the lifetime recording setup was performed by measurement of three standards (**Table 2.2**): 2 μM fluorescein in 0.1 N NaOH, 1 mg/mL erythrosin B in water (pH 7), and the instrument response function (IRF). The IRF was determined from a solution of 500 μM fluorescein and 12.2 M sodium iodide in 0.1 N NaOH. Because of the high concentration of iodide quencher, the IRF solution has a lifetime shorter than the detector response time, allowing approximation of the instrument response function under identical excitation and emission conditions as data acquisition [85].

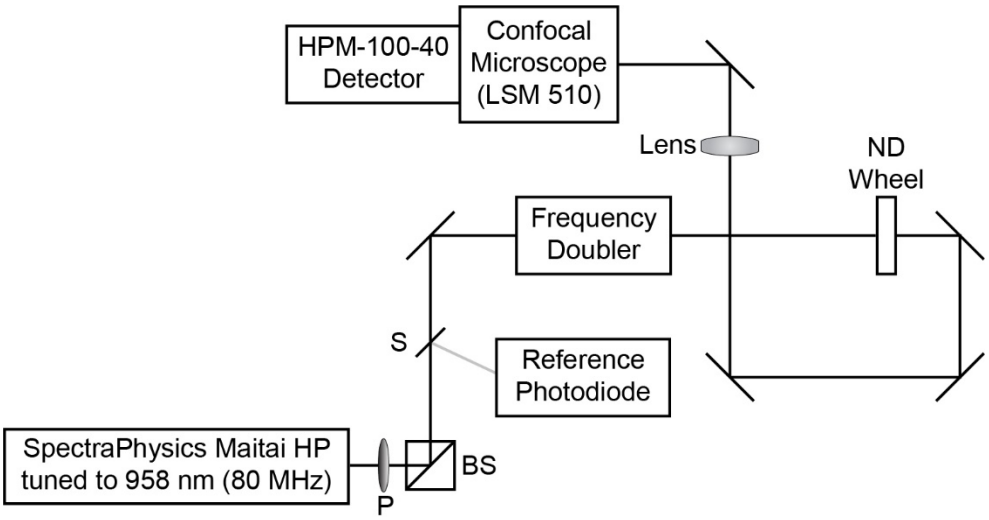

Scheme 2.1. Optical diagram for time correlated single photon counting microscope.
Excitation light was supplied by a Ti:Sapphire laser tuned to 958 nm. A small amount of light was redirected by a beam sampler (S) to a reference photodiode. The remaining light was passed through a frequency doubler to obtain 479 nm excitation light, which entered the LSM510 confocal microscope. A polarizer (P) followed by a polarizing beamsplitter (BS), as well as a neutral density (ND) wheel, allowed control of the amount of light passed to the sample.

IRF Deconvolution

Signal from photons detected in a TCSPC apparatus are convolved with the instrument response (IRF). IRFs can be approximated by the SPCImage fitting software, but consistency of lifetime fits on VF-FLIM datasets was improved by using a measured IRF. Measured IRFs were incorporated by the iterative reconvolution method using SPCImage analysis software [86].

VoltageFluor Lifetime Fitting Model

All VoltageFluor lifetime data were fit using SPCImage (Becker & Hickl), which solves the nonlinear least squares problem using the Levenberg-Marquadt algorithm. VF2.1.Cl lifetime data were fit to a sum of two exponential decay components (eqn. 2-2). Attempts to fit the VF2.1.Cl data with a single exponential decay (eqn. 2-3) were unsatisfactory.

$$F(t) = a_1 e^{-t/\tau_1} + a_2 e^{-t/\tau_2} \quad [2\text{-}2]$$

The fluorescence lifetime of VF2.0.Cl was adequately described by a single exponential decay for almost all data (eqn. 2-3). A second exponential component was necessary to fit data at VF2.0.Cl concentrations above 500 nM, likely attributable to the concentration-dependent decrease in lifetime that was observed high VF concentrations.

$$F(t) = a e^{-t/\tau} \quad [2\text{-}3]$$

For all data fit with the two component model, the weighted average of the two lifetimes, τ_m (eqn. 2-4), was used in subsequent analysis.

$$\tau_m = \frac{a_1\tau_1 + a_2\tau_2}{a_1 + a_2} \quad [2\text{-}4]$$

All lifetime images are represented as an overlay of photon count (pixel intensity) and weighted average lifetime (pixel color) throughout the text (τ_m + PC, **Figure 2.2**). Pixels with insufficient signal to fit a fluorescence decay are shown in black. The photon counts, as well as the lifetimes, in image sequences on the same set of cells are scaled across the same range.

Additional Fit Parameters for VoltageFluor Lifetimes

Pixels with photon counts below 300 (VF2.1.Cl) or 150 (VF2.0.Cl) photons at the peak of the decay (time bin with the most signal) were omitted from analysis to ensure reproducible fits. Because the lifetime of VFs does not fully decay to baseline in a single 12.5 ns laser cycle, the incomplete multiexponentials fitting option was used, allowing the model to attribute some signal early in the decay to the previous laser cycle. Out of 256 time bins from the analog-to-digital

converter (ADC), only data from time bins 23 to 240 were used in the final fit. The offset parameter (detector dark counts per ADC time bin per pixel) was set to zero. The number of iterations for the fit in SPCImage was increased to 20 to obtain converged fits. Shift between the IRF and the decay trace was fixed to 0.5 (in units of ADC time bins), which consistently gave lifetimes of standards erythrosin B (1 mg/mL in H_2O) [87] and fluorescein (2 μM in 0.1 N NaOH, H_2O) [37] closest to reported values (**Table 2.2**).

Acquisition Time and Effective Pixel Size in Lifetime Data

To obtain sufficient photons but keep excitation light power minimal, binning between neighboring pixels was employed during fitting. This procedure effectively takes the lifetime as a spatial moving average across the image by including adjacent pixels in the decay for a given pixel. To obtain larger photon counts, the confocal pinhole was set between 2.5 and 3.5 airy units, which corresponds to optical section thickness of approximately 2.5 μm.

Data Type	Acquired Pixel Width (μm)	Binned Pixel Width (μm)	Acquisition Time (s)	Img Size (pixels)
Concentration Curve (**Fig. 2.3**, **Fig. 2.11**)	0.44	3.08	75-90	256 x 256
V_{mem} Distributions (**Fig. 2.12**)	1.24	8.68	90-120	256 x 256
Electrophysiology Recording	1.00	3.01	15-30	64 x 64
EGF Time Series	0.88	2.64	30	64 x 64

Table 2.6. Acquisition Times and Effective Pixel Sizes.
All tabulated values are for an individual frame, although multiple sequential frames were recorded in both the electrophysiology and EGF experiments. For each recording type, the width of each pixel at acquisition is reported, as well as the width of the area included in the binned lifetime signal during fitting. All pixels are square. The acquisition time reflects the total time to collect the image, not the total time exposing each pixel. All FLIM images have 256 time bins in the ns regime, so a 256x256 spatial image size represents a 256x256x256 total dataset. Img = image.

Determination of Regions of Interest

Images were divided into cell groups, with each cell group as a single region of interest (ROI). ROIs were determined from photon count images, either manually from the cell morphology in FIJI [88] or automatically by sharpening and then thresholding the signal intensity with custom MATLAB code. Regions of images that were partially out of the optical section or contained punctate debris were omitted. Sample ROIs are shown in **Fig. 2.2**.

For cells that adjoin other cells, attribution of a membrane region to one cell versus the other is not possible. As such, we chose to interpret each cell group as an independent sample ('n') instead of extracting V_{mem} values for individual cells. Adjacent cells in a group are electrically coupled to varying degrees, and their resting membrane potentials are therefore not independent [39]. While this approach did not fully utilize the spatial resolution of VF-FLIM, it prevented overestimation of biological sample size for the effect in question.

Conversion of Lifetime to Transmembrane Potential

The mean τ_m across all pixels in an ROI was used as the lifetime for that ROI. Lifetime values were mapped to transmembrane potential via the lifetime-V_{mem} standard curves determined with

whole-cell voltage-clamp electrophysiology. For electrophysiology measurements, the relationship between the weighted average lifetime (eqn. 4) and membrane potential for each patched cell was determined by linear regression, yielding a sensitivity (*m,* ps/mV) and a 0 mV lifetime (*b*, ps) for each cell (eqn. 2-5). The average sensitivity and 0 mV point across all cells of a given type were used to convert subsequent lifetime measurements (τ) to V_{mem} (**Table 2.4**, eqn. 2-6). For quantifying changes in voltage (ΔV_{mem}) from changes in lifetime ($\Delta\tau$), only the average sensitivity is necessary (eqn. 2-7).

$$\tau = m * V_{mem} + b \quad [2\text{-}5]$$

$$V_{mem} = \frac{(\tau - b)}{m} \quad [2\text{-}6]$$

$$\Delta V_{mem} = \frac{(\Delta\tau)}{m} \quad [2\text{-}7]$$

Where standard error of the mean of a voltage determination (δV_{mem}) is given, error was propagated to include the standard errors of the slope (δm) and y-intercept (δb) of the voltage calibration, as well as the standard error of the lifetime measurements ($\delta\tau$) in the condition of interest (eqn. 2-8). For error in a voltage change ($\delta\Delta V_{mem}$), only error in the calibration slope was included in the propagated error (eqn. 2-9). Where standard deviation of VF-FLIM derived V_{mem} values is shown, a similar error propagation procedure was applied, using the standard deviation of the average sensitivity and 0 mV lifetime for that cell line.

$$\delta V_{mem} = |V_{mem}| \sqrt{\left(\frac{\sqrt{\delta\tau^2 + \delta b^2}}{\tau - b}\right)^2 + \left(\frac{\delta m}{m}\right)^2} \quad [2\text{-}8]$$

$$\delta\Delta V_{mem} = |\Delta V_{mem}| \sqrt{\left(\frac{\delta\Delta\tau}{\Delta\tau}\right)^2 + \left(\frac{\delta m}{m}\right)^2} \quad [2\text{-}9]$$

Resolution of VF-FLIM Voltage Determination

The intrinsic nature of fluorescence lifetime introduces a point of reference into the voltage measurement, from which a single lifetime image can be interpreted as resting membrane potential. Differences in this reference point (reported here as the 0 mV lifetime) over time and across cells provides an estimate of the voltage-independent noise in VF-FLIM. We report resolution as the root-mean-square deviation (RMSD) between the optically calculated voltage (V_{FLIM}) and the voltage set by whole-cell voltage clamp (V_{ephys}), which is analogous to the resolution calculations described previously by Cohen and co-workers [30]. The RMSD of n measurements (eqn. 2-10) can

be determined from the variance σ^2 (eqn. 2-11) and the bias (eqn. 2-12) of the estimator (in this case, VF-FLIM) relative to the "true" value (in this case, electrophysiology). These calculations are described graphically in **Scheme 2.2** below.

$$RMSD = \sqrt{\sigma^2 + Bias^2} \quad [2\text{-}10]$$

$$\sigma^2 = \frac{1}{n}\sum_{i=1}^{n}(V_{FLIM,i} - V_{ephys,i})^2 \quad [2\text{-}11]$$

$$Bias = \frac{1}{n}\sum_{i=1}^{n} V_{FLIM,i} - \frac{1}{n}\sum_{i=1}^{n} V_{ephys,i} \quad [2\text{-}12]$$

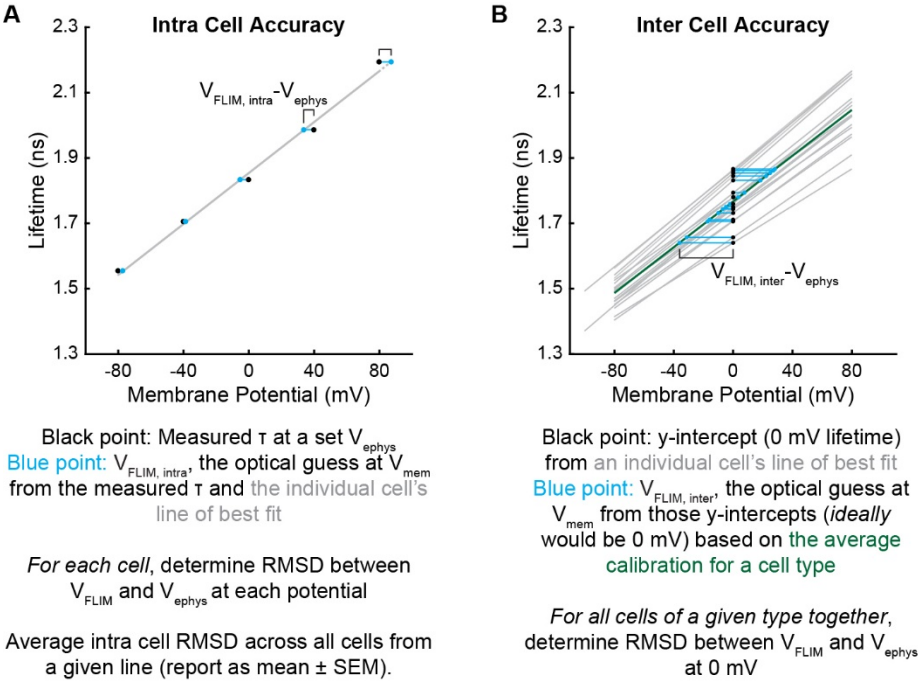

Black point: Measured τ at a set V_{ephys}
Blue point: $V_{FLIM, intra}$, the optical guess at V_{mem} from the measured τ and the individual cell's line of best fit

For each cell, determine RMSD between V_{FLIM} and V_{ephys} at each potential

Average intra cell RMSD across all cells from a given line (report as mean ± SEM).

Black point: y-intercept (0 mV lifetime) from an individual cell's line of best fit
Blue point: $V_{FLIM, inter}$, the optical guess at V_{mem} from those y-intercepts (*ideally* would be 0 mV) based on the average calibration for a cell type

For all cells of a given type together, determine RMSD between V_{FLIM} and V_{ephys} at 0 mV

Scheme 2.2. Intra and inter-cell V_{mem} resolution calculations.
Data are taken directly from **Figure 2.1H,I** as an example. (A) Intra cell values are the RMSD between the voltage equivalent of the measured lifetime (V_{FLIM}) and voltage set by electrophysiology (V_{ephys}). V_{FLIM} values are calculated using that particular cell's line of best fit, so one value is obtained per cell. Here, we present intra cell error as the mean ± SEM of all cells from a given cell line. (B) Inter cell errors are the RMSD between the voltage-equivalent of the 0 mV lifetime for all cells tested from a cell line (V_{FLIM}, determined with the average slope and y-intercept for that cell line) and the ground truth value of 0 mV. Inter-cell accuracy is calculated from all of the calibration data for a cell line, so there is one value per cell line. Black points are experimental y-intercepts and blue points are the V_{FLIM} optical voltage determinations from those lifetimes. Gray lines are lines of best fit for individual cells. Green line in (B) represents the average τ_{fl}-V_{mem} relationship for a cell line.

The voltage-independent variations in lifetime are much larger between cells than within a cell. Therefore, the error in measuring absolute voltage *changes* on a given cell ("intra-cell" comparisons) is lower than the error in determining the absolute V_{mem} of that cell ("inter-cell" comparisons, since the calibration used is from another cell). We can therefore determine an "intra-cell" RMSD and an "inter-cell" RMSD to reflect the voltage resolution of these two types of measurements. To calculate "intra-cell" error, we look at the RMSD between V_{ephys} and V_{FLIM} using the τ_{fl}-V_{mem} relationship *for that specific cell*. Phrased another way, we are looking at the amount of error that would be expected in estimating V_{mem} of a cell if its exact τ_{fl}-V_{mem} relationship were known. This "intra cell" RMSD estimates the error expected in quantifying changes in V_{mem} on a given cell. We calculate an intra cell error for each cellular recording, so intra cell errors are reported throughout the text as a mean ± SEM of the intra cell errors for all individual cells of a given type. The average intra cell error was at or below 5 mV for all cell lines tested (**Table 2.4**).

The error in the absolute membrane potential determination ("inter-cell") is calculated here as the RMSD between the y-intercept (0 mV lifetime) of all of the individual cells' lifetime-voltage relationships and the 0 mV value for the averaged calibration *for all cells of a given type*. This metric quantifies how well the lifetime-V_{mem} relationship for a given cell line is likely to represent an individual cell's lifetime-V_{mem} relationship. This "inter cell" RMSD ranged from 10 to 23 mV for the tested cell lines (**Table 2.4**). Much smaller errors for a population value of V_{mem} can be obtained by averaging V_{mem} recordings from multiple cells.

This method of calculating error assumes that the electrophysiology measurement is perfectly accurate and precise. Realistically, it is likely that some of the variation seen is due to the quality of the voltage clamp. As a result, these RMSD values provide a conservative upper bound for the voltage errors in VF-FLIM.

Analysis of CAESR Lifetimes

For sample images of CAESR in HEK293T (**Fig. 2.5**), fluorescence decays were fit using SPCImage to a biexponential decay model as described for VF2.1.Cl above, using a peak photon threshold of 150 and a bin of 2 (binned pixel width of 5 μm). To better match the studies by Cohen and co-workers [31], which isolated the membrane fluorescence from cytosolic fluorescence by directing the laser path, the lifetime-voltage relationships were not determined with these square-binned images. Instead, membranes were manually identified, and the fluorescence decays from all membrane pixels were summed together before fitting once per cell. (This is in contrast to the processing of VoltageFluor data, where the superior signal to noise and localization enables fitting and analysis of the lifetime on a pixel by pixel basis). This "one fit per membrane" analysis of CAESR was performed in custom MATLAB code implementing a Nelder-Mead algorithm (adapted from Enderlein and Erdmann [89]). CAESR data were fit to a biexponential model with the offset fixed to 0 and the color shift as a free parameter.

Di-8-ANEPPS Ratio-based Imaging

In preparation for imaging, HEK293T cells were plated as described above for electrophysiology. 1 μM di-8-ANEPPS was loaded for ten minutes in HBSS at room temperature and atmospheric CO_2. Coverslips were washed twice in HBSS and transferred to fresh HBSS for imaging. No surfactants were used in the loading (e.g. Pluronic F-127) because their presence worsened cell robustness for whole-cell patch-clamp electrophysiology. All recordings were made with HBSS

as an extracellular solution; no cells were kept for more than 30 minutes after dye loading due to the increasing presence of internalized dye.

Epifluorescence imaging was performed with an inverted Observer.Z1 (Carl Zeiss Microscopy) controlled with μManager 1.4 (Open Imaging) [90]. Images were acquired with an Orca Flash 4 Digital CMOS camera (Hamamatsu Corporation; San Jose, CA). Excitation light was provided with a Spectra X light engine (Lumencor, Inc.; Beaverton, OR). Excitation wavelengths were selected with built-in filters in the Spectra X (440/20 bandpass filter for blue and 550/15 bandpass filter for green). Blue-excited images were obtained with an excitation power of 71 mW/mm^2 and an exposure time of 50 ms. Green-excited images were obtained with an excitation power of 136 mW/mm^2 and an exposure time of 500 ms. Emission light was collected with a 40x magnification oil immersion objective lens using Immersol 518F immersion oil (Zeiss). Fluorescence emission was selected with a 562 nm long pass dichroic mirror and further filtered by a 593/40 bandpass filter (Semrock). Excitation and emission wavelengths were selected to match previous work with this probe as closely as possible [14] (current excitation[blue]: 440 ± 10 nm; reported excitation[blue]: 440 ± 15 nm; current excitation [green]: 550 ± 7.5 nm; reported excitation: 530 ± 15 nm; current dichroic: 562 nm long-pass; reported dichroic: 565 nm; current emission: 593 ± 20 nm; reported emission: 570 nm long pass)

Di-8-ANEPPS Data Analysis

Single color (e.g. blue excited or green excited) fluorescence images were background subtracted at each pixel before ratios were calculated. The background value was determined from a region of interest near the center of the image that contained no cells and minimal fluorescent debris. Excitation ratios ("R", blue signal divided by green signal, B/G) were then calculated pixelwise from the background subtracted fluorescence images. Pixels with less than 100 arbitrary units of signal in either the blue or the green channel were excluded from analysis and are depicted in black. Regions of interest (ROIs) were manually selected in ImageJ to include only area corresponding to the cell membrane. The ratio was averaged across all pixels in a given ROI (similar to the treatment for VF-FLIM, as described in **Figure 2.2**). The ratio values per value of V_{mem} (set by whole cell patch clamp electrophysiology) in **Fig. 2.6** are the average of these cell-averaged ratios obtained in 6 or 7 sequential images acquired while the V_{mem} was held at the indicated value.

Where normalized R values are discussed, these values were calculated by dividing the ratio at a given potential (averaged for an ROI as discussed above) by the ratio at 0 mV, as reported previously [14]. This normalization procedure requires electrode-based calibration for every individual recording and cannot be stably extended to all cells from a particular cell line. Therefore, it is not analogous to VF-FLIM and is not the point of comparison for voltage resolution.

Statistical Analysis

Mean ± standard error of the mean (S.E.M.) of data is reported throughout the text. Hypothesis testing was performed as indicated with either analysis of variance (ANOVA) followed by appropriate post hoc tests or two-sided, unpaired, unequal variances t-tests. Statistical tests were performed in Python 2 or 3 with the SciPy, pandas and Pingouin [91] packages. Unless otherwise noted, all data shown reflect at least three biological replicates (independent cultures measured on different days). Each of these biological replicates contained between 1 and 5 technical replicates

(different samples of cells that were measured on the same day and had been prepared from the same cell stock). For tandem electrophysiology-FLIM measurements, each τ_{fl}-V_{mem} calibration includes three biological replicates to capture the variability expected during applications of VF-FLIM. No power analyses were performed before data were collected. Sample sizes throughout the text refer to the total number of cells or cell groups of a given type analyzed across all biological and technical replicates. Cell group identification is discussed in **Methods**. For experiments where resting membrane potential or resting membrane potential changes are compared to a baseline, both control measurements and their physiologically or pharmacologically altered counterparts were recorded on each experimental day. Masking was not used during data collection or analysis.

References

(1) Abdul Kadir, L.; Stacey, M.; Barrett-Jolley, R. Emerging Roles of the Membrane Potential: Action beyond the Action Potential. *Front. Physiol.* **2018**, *9*, 1661. https://doi.org/10.3389/fphys.2018.01661.

(2) Cone, C. D.; Cone, C. M. Induction of Mitosis in Mature Neurons in Central Nervous System by Sustained Depolarization. *Science* **1976**, *192* (4235), 155–158. https://doi.org/10.1126/science.56781.

(3) Huang, X.; Jan, L. Y. Targeting Potassium Channels in Cancer. *J. Cell Biol.* **2014**, *206* (2), 151–162. https://doi.org/10.1083/jcb.201404136.

(4) Tsuchiya, W.; Okada, Y. Membrane Potential Changes Associated with Differentiation of Enterocytes in the Rat Intestinal Villi in Culture. *Dev. Biol.* **1982**, *94* (2), 284–290. https://doi.org/10.1016/0012-1606(82)90348-7.

(5) Levin, M. Molecular Bioelectricity: How Endogenous Voltage Potentials Control Cell Behavior and Instruct Pattern Regulation in Vivo. *Mol. Biol. Cell* **2014**, *25* (24), 3835–3850. https://doi.org/10.1091/mbc.E13-12-0708.

(6) Huang, C. J.; Harootunian, A.; Maher, M. P.; Quan, C.; Raj, C. D.; McCormack, K.; Numann, R.; Negulescu, P. A.; González, J. E. Characterization of Voltage-Gated Sodium-Channel Blockers by Electrical Stimulation and Fluorescence Detection of Membrane Potential. *Nat. Biotechnol.* **2006**, *24* (4), 439–446. https://doi.org/10.1038/nbt1194.

(7) McKeithan, W. L.; Savchenko, A.; Yu, M. S.; Cerignoli, F.; Bruyneel, A. A. N.; Price, J. H.; Colas, A. R.; Miller, E. W.; Cashman, J. R.; Mercola, M. An Automated Platform for Assessment of Congenital and Drug-Induced Arrhythmia with HiPSC-Derived Cardiomyocytes. *Front. Physiol.* **2017**, *8*, 766. https://doi.org/10.3389/fphys.2017.00766.

(8) Zhang, H.; Reichert, E.; Cohen, A. E. Optical Electrophysiology for Probing Function and Pharmacology of Voltage-Gated Ion Channels. *Elife* **2016**, *5*. https://doi.org/10.7554/eLife.15202.

(9) Peterka, D. S.; Takahashi, H.; Yuste, R. Imaging Voltage in Neurons. *Neuron* **2011**, *69* (1), 9–21. https://doi.org/10.1016/j.neuron.2010.12.010.

(10) Ross, W. N.; Reichardt, L. F. Species-Specific Effects on the Optical Signals of Voltage-Sensitive Dyes. *J. Membr. Biol.* **1979**, *48* (4), 343–356. https://doi.org/10.1007/BF01869445.

(11) Adams, D. S.; Levin, M. General Principles for Measuring Resting Membrane Potential and Ion Concentration Using Fluorescent Bioelectricity Reporters. *Cold Spring Harb. Protoc.* **2012**, *7* (4), 385–397. https://doi.org/10.1101/pdb.top067710.

(12) Maher, M. P.; Wu, N. T.; Ao, H. PH-Insensitive FRET Voltage Dyes. *J. Biomol. Screen.* **2007**, *12* (5), 656–667. https://doi.org/10.1177/1087057107302113.

(13) Gross, E.; Bedlack, R. S.; Loew, L. M. Dual-Wavelength Ratiometric Fluorescence Measurement of the Membrane Dipole Potential. *Biophys. J.* **1994**, *67* (1), 208–216.

https://doi.org/10.1016/S0006-3495(94)80471-0.

(14) Zhang, J.; Davidson, R. M.; Wei, M. De; Loew, L. M. Membrane Electric Properties by Combined Patch Clamp and Fluorescence Ratio Imaging in Single Neurons. *Biophys. J.* **1998**, *74* (1), 48–53. https://doi.org/10.1016/S0006-3495(98)77765-3.

(15) Briggman, K. L.; Kristan, W. B.; González, J. E.; Kleinfeld, D.; Tsien, R. Y. Monitoring Integrated Activity of Individual Neurons Using FRET-Based Voltage-Sensitive Dyes. In *Membrane Potential Imaging in the Nervous System: Methods and Applications*; 2010; pp 61–70. https://doi.org/10.1007/978-1-4419-6558-5_6.

(16) Williams, S. R.; Mitchell, S. J. Direct Measurement of Somatic Voltage Clamp Errors in Central Neurons. *Nat. Neurosci.* **2008**, *11* (7), 790–798. https://doi.org/10.1038/nn.2137.

(17) Armstrong, C. M.; Gilly, W. F. Access Resistance and Space Clamp Problems Associated with Whole-Cell Patch Clamping. *Methods Enzymol.* **1992**, *207*, 100–122. https://doi.org/10.1016/0076-6879(92)07007-B.

(18) Gonzalez, J. E.; Tsien, R. Y. Improved Indicators of Cell Membrane Potential That Use Fluorescence Resonance Energy Transfer. *Chem. Biol.* **1997**, *4* (4), 269-77. https://doi.org/10.1002/1097-0320(20010801)44:4<361::AID-CYTO1128>3.0.CO;2-3.

(19) Loew, L. M.; Scully, S.; Simpson, L.; Waggoner, A. S. Evidence for a Charge-Shift Electrochromic Mechanism in a Probe of Membrane Potential [21]. *Nature* **1979**, *281* (5731), 497–499. https://doi.org/10.1038/281497a0.

(20) Montana, V.; Farkas, D. L.; Loew, L. M. Dual-Wavelength Ratiometric Fluorescence Measurements of Membrane Potential. *Biochemistry* **1989**, *28* (11), 4536–4539. https://doi.org/10.1021/bi00437a003.

(21) Bullen, A.; Saggau, P. High-Speed, Random-Access Fluorescence Microscopy: II. Fast Quantitative Measurements with Voltage-Sensitive Dyes. *Biophys. J.* **1999**, *76* (4), 2272–2287. https://doi.org/10.1016/S0006-3495(99)77383-2.

(22) Berezin, M. Y.; Achilefu, S. Fluorescence Lifetime Measurements and Biological Imaging. *Chem. Rev.* **2010**, *110* (5), 2641–2684. https://doi.org/10.1021/cr900343z.

(23) Yellen, G.; Mongeon, R. Quantitative Two-Photon Imaging of Fluorescent Biosensors. *Curr. Opin. Chem. Biol.* **2015**, *27*, 24–30. https://doi.org/10.1016/J.CBPA.2015.05.024.

(24) Zheng, K.; Bard, L.; Reynolds, J. P.; King, C.; Jensen, T. P.; Gourine, A. V; Rusakov, D. A. Time-Resolved Imaging Reveals Heterogeneous Landscapes of Nanomolar Ca2+ in Neurons and Astroglia. *Neuron* **2015**, *88* (2), 277–288. https://doi.org/10.1016/j.neuron.2015.09.043.

(25) Levitt, J. A.; Kuimova, M. K.; Yahioglu, G.; Chung, P.; Suhling, K.; Phillips, D. Membrane-Bound Molecular Rotors Measure Viscosity in Live Cells via Fluorescence Lifetime Imaging. *J. Phys. Chem. C* **2009**, *113*, 11634–11642. https://doi.org/10.1021/jp9013493.

(26) Harvey, C. D.; Yasuda, R.; Zhong, H.; Svoboda, K. The Spread of Ras Activity Triggered by Activation of a Single Dendritic Spine. *Science (80-.).* **2008**, *321* (5885), 136–140.

https://doi.org/10.1126/science.1159675.

(27) Lee, S. J. R.; Escobedo-Lozoya, Y.; Szatmari, E. M.; Yasuda, R. Activation of CaMKII in Single Dendritic Spines during Long-Term Potentiation. *Nature* **2009**, *458* (7236), 299–304. https://doi.org/10.1038/nature07842.

(28) Blacker, T. S.; Duchen, M. R. Investigating Mitochondrial Redox State Using NADH and NADPH Autofluorescence. *Free Radic. Biol. Med.* **2016**, *100*, 53–65. https://doi.org/10.1016/j.freeradbiomed.2016.08.010.

(29) Dumas, D.; Stoltz, J. F. New Tool to Monitor Membrane Potential by FRET Voltage Sensitive Dye (FRET-VSD) Using Spectral and Fluorescence Lifetime Imaging Microscopy (FLIM). Interest in Cell Engineering. *Clin. Hemorheol. Microcirc.* **2005**, *33* (3), 293-302.

(30) Hou, J. H.; Venkatachalam, V.; Cohen, A. E. Temporal Dynamics of Microbial Rhodopsin Fluorescence Reports Absolute Membrane Voltage. *Biophys. J.* **2014**, *106* (3), 639–648. https://doi.org/10.1016/j.bpj.2013.11.4493.

(31) Brinks, D.; Klein, A. J.; Cohen, A. E. Two-Photon Lifetime Imaging of Voltage Indicating Proteins as a Probe of Absolute Membrane Voltage. *Biophys. J.* **2015**, *109* (5), 914–921. https://doi.org/10.1016/j.bpj.2015.07.038.

(32) Lakowicz, J. R.; Szmacinski, H.; Johnson, M. L. Calcium Imaging Using Fluorescence Lifetimes and Long-Wavelength Probes. *J. Fluoresc.* **1992**, *2* (1), 47–62. https://doi.org/10.1007/BF00866388.

(33) Miller, E. W.; Lin, J. Y.; Frady, E. P.; Steinbach, P. A.; Kristan, W. B.; Tsien, R. Y. Optically Monitoring Voltage in Neurons by Photo-Induced Electron Transfer through Molecular Wires. *Proc. Natl. Acad. Sci. U. S. A.* **2012**, *109* (6), 2114–2119. https://doi.org/10.1073/pnas.1120694109.

(34) Woodford, C. R.; Frady, E. P.; Smith, R. S.; Morey, B.; Canzi, G.; Palida, S. F.; Araneda, R. C.; Kristan, W. B.; Kubiak, C. P.; Miller, E. W.; et al. Improved PeT Molecules for Optically Sensing Voltage in Neurons. *J. Am. Chem. Soc.* **2015**, *137* (5), 1817–1824. https://doi.org/10.1021/ja510602z.

(35) Li, L. S. Fluorescence Probes for Membrane Potentials Based on Mesoscopic Electron Transfer. *Nano Lett.* **2007**, *7* (10), 2981–2986. https://doi.org/10.1021/nl071163p.

(36) de Silva, A. P.; Gunaratne, H. Q. N.; Habib-Jiwan, J.-L.; McCoy, C. P.; Rice, T. E.; Soumillion, J.-P. New Fluorescent Model Compounds for the Study of Photoinduced Electron Transfer: The Influence of a Molecular Electric Field in the Excited State. *Angew. Chem. Int. Ed. Engl.* **1995**, *34* (16), 1728–1731. https://doi.org/10.1002/anie.199517281.

(37) Magde, D.; Rojas, G. E.; Seybold, P. G. Solvent Dependence of the Fluorescence Lifetimes of Xanthene Dyes. *Photochem. Photobiol.* **1999**, *70* (5), 737–744. https://doi.org/10.1111/j.1751-1097.1999.tb08277.x.

(38) Chen, R. F.; Knutson, J. R. Mechanism of Fluorescence Concentration Quenching of Carboxyfluorescein in Liposomes: Energy Transfer to Nonfluorescent Dimers. *Anal.*

Biochem. **1988**, *172* (1), 61–77. https://doi.org/10.1016/0003-2697(88)90412-5.

(39) Meşe, G.; Richard, G.; White, T. W. Gap Junctions: Basic Structure and Function. *J. Invest. Dermatol.* **2007**, *127* (11), 2516–2524. https://doi.org/10.1038/sj.jid.5700770.

(40) Hodgkin, A. L.; Katz, B. The Effect of Sodium Ions on the Electrical Activity of the Giant Axon of the Squid. *J. Physiol.* **1949**, *108*, 37–77.

(41) Moolenaar, W. H.; Aerts, R. J.; Tertoolen, L. G. J.; De Laat, S. W. The Epidermal Growth Factor-Induced Calcium Signal in A431 Cells. *J. Biol. Chem.* **1986**, *261* (1), 279–284.

(42) Defarias, F. P.; Stevens, S. P.; Leonard, R. J. Stable Expression of Human Kv1.3 Potassium Channels Resets the Resting Membrane Potential of Cultured Mammalian Cells. *Receptors Channels* **1995**, *3* (4), 273–281.

(43) Walker, B. D.; Valenzuela, S. M.; Singleton, C. B.; Tie, H.; Bursill, J. A.; Wyse, K. R.; Qiu, M. R.; Breit, S. N.; Campbell, T. J. Inhibition of HERG Channels Stably Expressed in a Mammalian Cell Line by the Antianginal Agent Perhexiline Maleate. *Br. J. Pharmacol.* **1999**, *127* (1), 243–251. https://doi.org/10.1038/sj.bjp.0702502.

(44) Cone, C. D.; Tongier, M. Contact Inhibition of Division: Involvement of the Electrical Transmembrane Potential. *J. Cell. Physiol.* **1973**, *82* (3), 373.

(45) Fliegert, R.; Glassmeier, G.; Schmid, F.; Cornils, K.; Genisyuerek, S.; Harneit, A.; Schwarz, J. R.; Guse, A. H. Modulation of Ca2+ Entry and Plasma Membrane Potential by Human TRPM4b. *FEBS J.* **2007**, *274* (3), 704–713. https://doi.org/10.1111/j.1742-4658.2006.05614.x.

(46) Babai, N.; Kanevsky, N.; Dascal, N.; Rozanski, G. J.; Singh, D. P.; Fatma, N.; Thoreson, W. B. Anion-Sensitive Regions of L-Type CaV1.2 Calcium Channels Expressed in HEK293 Cells. *PLoS One* **2010**, *5* (1). https://doi.org/10.1371/journal.pone.0008602.

(47) Hsu, K.; Han, J.; Shinlapawittayatorn, K.; Deschenes, I.; Marbán, E. Membrane Potential Depolarization as a Triggering Mechanism for Vpu-Mediated HIV-1 Release. *Biophys. J.* **2010**, *99* (6), 1718–1725. https://doi.org/10.1016/j.bpj.2010.07.027.

(48) Wonderlin, W. F.; Woodfork, K. A.; Strobl, J. S. Changes in Membrane Potential during the Progression of MCF-7 Human Mammary Tumor Cells through the Cell Cycle. *J. Cell. Physiol.* **1995**, *165* (1), 177–185. https://doi.org/10.1002/jcp.1041650121.

(49) Berzingi, S.; Newman, M.; Yu, H.-G. Altering Bioelectricity on Inhibition of Human Breast Cancer Cells. *Cancer Cell Int.* **2016**, *16*, 72. https://doi.org/10.1186/s12935-016-0348-8.

(50) Ouadid-Ahidouch, H.; Le Bourhis, X.; Roudbaraki, M.; Toillon, R. A.; Delcourt, P.; Prevarskaya, N. Changes in the K+ Current-Density of MCF-7 Cells during Progression through the Cell Cycle: Possible Involvement of a h-Ether.a-Gogo K+ Channel. *Receptors Channels* **2001**, *7* (5), 345–356. https://doi.org/10.1111/j.1464-410X.2009.08500.x.

(51) Wang, S. Y.; Melkoumian, Z.; Woodfork, K. A.; Cather, C.; Davidson, A. G.; Wonderlin, W. F.; Strobl, J. S. Evidence for an Early G1 Ionic Event Necessary for Cell Cycle Progression and Survival in the MCF-7 Human Breast Carcinoma Cell Line. *J. Cell.*

Physiol. **1998**, *176* (3), 456–464. https://doi.org/10.1002/(sici)1097-4652(199809)176:3<456::aid-jcp2>3.0.co;2-n.

(52) Marino, A. A.; Iliev, I. G.; Schwalke, M. A.; Gonzalez, E.; Marler, K. C.; Flanagan, C. A. Association between Cell Membrane Potential and Breast Cancer. *Tumor Biol.* **1994**, *15* (2), 82–89. https://doi.org/10.1159/000217878.

(53) Hammadi, M.; Chopin, V.; Matifat, F.; Dhennin-Duthille, I.; Chasseraud, M.; Sevestre, H.; Ouadid-Ahidouch, H. Human Ether À-Gogo K+ Channel 1 (HEag1) Regulates MDA-MB-231 Breast Cancer Cell Migration through Orai1-Dependent Calcium Entry. *J. Cell. Physiol.* **2012**, *227* (12), 3837–3846. https://doi.org/10.1002/jcp.24095.

(54) Thurber, A. E.; Nelson, M.; Frost, C. L.; Levin, M.; Brackenbury, W. J.; Kaplan, D. L. IK Channel Activation Increases Tumor Growth and Induces Differential Behavioral Responses in Two Breast Epithelial Cell Lines. *Oncotarget* **2017**, *8* (26), 42382–42397. https://doi.org/10.18632/oncotarget.16389.

(55) Rothenberg, P.; Reuss, L.; Glaser, L. Serum and Epidermal Growth Factor Transiently Depolarize Quiescent BSC-1 Epithelial Cells. *Proc. Natl. Acad. Sci. U. S. A.* **1982**, *79* (24), 7783–7787. https://doi.org/10.1073/pnas.79.24.7783.

(56) Pandiella, A.; Magni, M.; Lovisolo, D.; Meldolesi, J. The Effects of Epidermal Growth Factor on Membrane Potential. *J. Biol. Chem.* **1989**, *264* (22), 12914–12921.

(57) Moolenaar, W. H.; Yarden, Y.; de Laat, S. W.; Schlessinger, J. Epidermal Growth Factor Induces Electrically Silent Na+ Influx in Human Fibroblasts. *J. Biol. Chem.* **1982**, *257* (14), 8502–8506. https://doi.org/10.1117/12.771968.

(58) Wulff, H.; Miller, M. J.; Hänsel, W.; Grissmer, S.; Cahalan, M. D.; Chandy, K. G. Design of a Potent and Selective Inhibitor of the Intermediate-Conductance Ca2+-Activated K+ Channel, IKCa1: A Potential Immunosuppressant. *Proc. Natl. Acad. Sci.* **2000**, *97* (14), 8151–8156. https://doi.org/10.1073/PNAS.97.14.8151.

(59) Wang, L. Measurements and Implications of the Membrane Dipole Potential. *Annu. Rev. Biochem.* **2012**, *81*, 615–635. https://doi.org/10.1146/annurev-biochem-070110-123033.

(60) Brügger, B. Lipidomics: Analysis of the Lipid Composition of Cells and Subcellular Organelles by Electrospray Ionization Mass Spectrometry. *Annu. Rev. Biochem.* **2014**, *83* (1), 79–98. https://doi.org/10.1146/annurev-biochem-060713-035324.

(61) Cervera, J.; Alcaraz, A.; Mafe, S. Bioelectrical Signals and Ion Channels in the Modeling of Multicellular Patterns and Cancer Biophysics. *Sci. Rep.* **2016**, *6* (January), 1–14. https://doi.org/10.1038/srep20403.

(62) Berndt, A.; Yizhar, O.; Gunaydin, L. A.; Hegemann, P.; Deisseroth, K. Bi-Stable Neural State Switches. *Nat. Neurosci.* **2009**, *12* (2), 229–234. https://doi.org/10.1038/nn.2247.

(63) Liu, P.; Grenier, V.; Hong, W.; Muller, V. R.; Miller, E. W. Fluorogenic Targeting of Voltage-Sensitive Dyes to Neurons. *J. Am. Chem. Soc.* **2017**, *139* (48), 17334–17340. https://doi.org/10.1021/jacs.7b07047.

(64) Grenier, V.; Daws, B. R.; Liu, P.; Miller, E. W. Spying on Neuronal Membrane Potential with Genetically Targetable Voltage Indicators. *J. Am. Chem. Soc.* **2019**, *141*, 1349–1358. https://doi.org/10.1021/jacs.8b11997.

(65) Raspe, M.; Kedziora, K. M.; van den Broek, B.; Zhao, Q.; de Jong, S.; Herz, J.; Mastop, M.; Goedhart, J.; Gadella, T. W. J.; Young, I. T.; et al. SiFLIM: Single-Image Frequency-Domain FLIM Provides Fast and Photon-Efficient Lifetime Data. *Nat. Methods* **2016**, No. October 2015, 1–6. https://doi.org/10.1038/nmeth.3836.

(66) Gao, L.; Liang, J.; Li, C.; Wang, L. V. Single-Shot Compressed Ultrafast Photography at One Hundred Billion Frames per Second. *Nature* **2014**, *516* (729), 74–77. https://doi.org/10.1038/nature14005.

(67) Cervera, J.; Meseguer, S.; Mafe, S. The Interplay between Genetic and Bioelectrical Signaling Permits a Spatial Regionalisation of Membrane Potentials in Model Multicellular Ensembles. *Sci. Rep.* **2016**, *6* (October), 35201. https://doi.org/10.1038/srep35201.

(68) Horn, R.; Korn, S. J. Prevention of Rundown in Electrophysiological Recording. *Methods Enzymol.* **1992**, *207*, 149–155. https://doi.org/10.1016/0076-6879(92)07010-L.

(69) Malinow, R.; Tsien, R. W. Presynaptic Enhancement Shown by Whole-Cell Recordings of Long-Term Potentiation in Hippocampal Slices. *Nature* **1990**, *346* (6280), 177–180. https://doi.org/10.1038/346177a0.

(70) Magni, M.; Meldolesi, J.; Pandiella, A. Ionic Events Induced by Epidermal Growth Factor: Evidence That Hyperpolarization and Stimulated Cation Influx Play a Role in the Stimulation of Cell Growth. *J. Biol. Chem.* **1991**, *266* (10), 6329–6335.

(71) Peppelenbosch, M. P.; Tertoolen, L. G. J.; De Laat, S. W. Epidermal Growth Factor-Activated Calcium and Potassium Channels. *J. Biol. Chem.* **1991**, *266* (30), 19938–19944.

(72) Lückhoff, A.; Clapham, D. E. Calcium Channels Activated by Depletion of Internal Calcium Stores in A431 Cells. *Biophys. J.* **1994**, *67* (1), 177–182. https://doi.org/10.1016/S0006-3495(94)80467-9.

(73) Mozhayeva, G. N.; Naumov, A. P.; Kuryshev, Y. A. Epidermal Growth Factor Activates Calcium-Permeable Channels in A 431 Cells. *Biochim. Biophys. Acta - Mol. Cell Res.* **1989**, *1011* (2–3), 171–175. https://doi.org/10.1016/0167-4889(89)90206-1.

(74) Thul, P. J.; Åkesson, L.; Wiking, M.; Mahdessian, D.; Geladaki, A.; Ait Blal, H.; Alm, T.; Asplund, A.; Björk, L.; Breckels, L. M.; et al. A Subcellular Map of the Human Proteome. *Science (80-.).* **2017**, *356* (6340), eaal3321. https://doi.org/10.1126/science.aal3321.

(75) Pandiella, A.; Malgaroli, A.; Meldolesi, J.; Vicentini, L. M. EGF Raises Cytosolic Ca2+ in A431 and Swiss 3T3 Cells by a Dual Mechanism: Redistribution from Intracellular Stores and Stimulated Influx. *Exp. Cell Res.* **1987**, *170* (1), 175–185. https://doi.org/10.1016/0014-4827(87)90127-3.

(76) Marquèze-Pouey, B.; Mailfert, S.; Rouger, V.; Goaillard, J. M.; Marguet, D. Physiological Epidermal Growth Factor Concentrations Activate High Affinity Receptors to Elicit Calcium Oscillations. *PLoS One* **2014**, *9* (9), e106803.

https://doi.org/10.1371/journal.pone.0106803.

(77) Reddy, R. J.; Gajadhar, A. S.; Swenson, E. J.; Rothenberg, D. A.; Curran, T. G.; White, F. M. Early Signaling Dynamics of the Epidermal Growth Factor Receptor. *Proc. Natl. Acad. Sci. U. S. A.* **2016**, *113* (11), 3114–3119. https://doi.org/10.1073/pnas.1521288113.

(78) Yang, M.; Brackenbury, W. J. Membrane Potential and Cancer Progression. *Front. Physiol.* **2013**, *4* (July), 1–10. https://doi.org/10.3389/fphys.2013.00185.

(79) Zhou, Y.; Wong, C.; Cho, K.; van der Hoeven, D.; Liang, H.; Thakur, D. P.; Luo, J.; Babic, M.; Zinsmaier, K. E.; Zhu, M. X.; et al. Membrane Potential Modulates Plasma Membrane Phospholipid Dynamics and K-Ras Signaling. *Science (80-.).* **2015**, *349* (6250), 873–876. https://doi.org/10.1126/science.aaa5619.

(80) Cadwell, C. R.; Palasantza, A.; Jiang, X.; Berens, P.; Deng, Q.; Yilmaz, M.; Reimer, J.; Shen, S.; Bethge, M.; Tolias, K. F.; et al. Electrophysiological, Transcriptomic and Morphologic Profiling of Single Neurons Using Patch-Seq. *Nat. Biotechnol.* **2016**, *34* (2), 199–203. https://doi.org/10.1038/nbt.3445.

(81) Huang, Y. L.; Walker, A. S.; Miller, E. W. A Photostable Silicon Rhodamine Platform for Optical Voltage Sensing. *J. Am. Chem. Soc.* **2015**, *137* (33), 10767–10776. https://doi.org/10.1021/jacs.5b06644.

(82) Deal, P. E.; Kulkarni, R. U.; Al-Abdullatif, S. H.; Miller, E. W. Isomerically Pure Tetramethylrhodamine Voltage Reporters. *J. Am. Chem. Soc.* **2016**, *138* (29), 9085–9088. https://doi.org/10.1021/jacs.6b05672.

(83) Gordon, J. A. Use of Vanadate as Protein-Phosphotyrosine Phosphatase Inhibitor. *Methods Enzymol.* **1991**, *201*, 477–482.

(84) Barry, P. H. JPCalc, a Software Package for Calculating Liquid Junction Potential Corrections in Patch-Clamp, Intracellular, Epithelial and Bilayer Measurements and for Correcting Junction Potential Measurements. *J. Neurosci. Methods* **1994**, *51* (1), 107–116. https://doi.org/10.1016/0165-0270(94)90031-0.

(85) Liu, M.; Jia, M.; Pan, H.; Li, L.; Chang, M.; Ren, H.; Argoul, F.; Zhang, S.; Xu, J. Instrument Response Standard in Time-Resolved Fluorescence Spectroscopy at Visible Wavelength: Quenched Fluorescein Sodium. *Appl. Spectrosc.* **2014**, *68* (5), 577–583. https://doi.org/10.1366/13-07236.

(86) Becker, W. *The Bh TCSPC Handbook*, 5th edn.; Becker & Hickl, 2012.

(87) Boens, N.; Qin, W.; Basaric, N.; Hofkens, J.; Ameloot, M.; Pouget, J.; Lefevre, J.-P.; Valeur, B.; Gratton, E.; VandeVen, M.; et al. Fluorescence Lifetime Standards for Time and Frequency Domain Fluorescence Spectroscopy. *Anal. Chem.* **2007**, *79* (5), 2137–2149. https://doi.org/10.1021/ac062160k.

(88) Schindelin, J.; Arganda-Carreras, I.; Frise, E.; Kaynig, V.; Longair, M.; Pietzsch, T.; Preibisch, S.; Rueden, C.; Saalfeld, S.; Schmid, B.; et al. Fiji: An Open-Source Platform for Biological-Image Analysis. *Nat. Methods* **2012**, *9* (7), 676–682. https://doi.org/10.1038/nmeth.2019.

(89) Enderlein, J.; Erdmann, R. Fast Fitting of Multi-Exponential Decay Curves. *Opt. Commun.* **1997**, *134*, 371–378.

(90) Edelstein, A. D.; Tsuchida, M. A.; Amodaj, N.; Pinkard, H.; Vale, R. D.; Stuurman, N. Advanced Methods of Microscope Control Using MManager Software. *J. Biol. Methods* **2014**, *1* (2), 10. https://doi.org/10.14440/jbm.2014.36.

(91) Vallat, R. Pingouin: Statistics in Python. *J. Open Source Softw.* **2018**, *3* (31), 1026. https://doi.org/10.21105/joss.01026.

Chapter 3

Generality and Possible Biological Effects of EGF-Induced Hyperpolarization

Abstract

Transmembrane potential, V_{mem}, has been discussed as possible regulator of cellular growth and division. In particular, we observed that activation of epidermal growth factor receptor (EGFR) by its ligand epidermal growth factor (EGF) produced a transient hyperpolarization in the human carcinoma cell line A431. We followed up on this key observation by investigating two additional dimensions: [1] the generality of EGF-induced V_{mem} signals and [2] the biological effects of EGF-induced hyperpolarization. To establish whether the V_{mem} response seen in A431 cells was generalizable to other systems, we investigated the V_{mem} effects of EGF stimulation in a heterologous expression system (HEK293T cells). Results of these studies were largely inconclusive. We observed different V_{mem} dynamics in HEK293T cells expressing EGFR than we did in A431 cells, and we did not observe dramatic changes in either Ca^{2+} handling or tyrosine phosphorylation following EGF stimulation in A431. Overall, these data suggest that, if they have a physiological effect, V_{mem} changes associated with the A431 response to EGF act through a pathway other than those investigated here, perhaps involving an additional factor that was not present in the heterologous expression system.

Introduction

Epidermal growth factor receptor is implicated in a variety of cellular processes, and its regulation is complex. A variety of positive and negative feedback loops from other cellular signaling motifs and second messengers can amplify or reduce the strength of a particular ligand's signal.[1] The existence of a hyperpolarizing V_{mem} signal following EGF stimulation of A431 carcinoma cells is intriguing, and it prompts further questions as to how that V_{mem} signal interacts with the broader picture of EGFR signaling.

One possible area of interaction between V_{mem} and more canonical EGFR signaling pathways is the EGF-induced Ca^{2+} signal. Two main types of EGF-induced Ca^{2+} signals exist. Most directly, EGFR induces large, often oscillatory Ca^{2+} signals via activation of phospholipase C, generation of IP_3, and release of Ca^{2+} from internal stores.[1] Subsequently, the depletion of Ca^{2+} in internal stores triggers store-operated calcium entry (SOCE).[2,3] In this context, V_{mem} could modulate the driving force for SOCE, as well as regulate the resting Ca^{2+} level in the cytosol. Similar V_{mem}-Ca^{2+} interactions have been hypothesized in migration and cell cycle progression.[4]

An alternative hypothesis is that V_{mem} affects membrane organization or protein conformation direction. Such V_{mem}-dependent effects on the plasma membrane have been previously reported in the context of K-Ras, where V_{mem} potentiated reorganization of certain anionic phospholipids.[5] , This membrane reorganization changed MAPK phosphorylation in both cultured cell lines and the *Drosophila* embryo. In the context of EGFR, many of the signaling factors, including EGFR itself, are localized to the plasma membrane and therefore could perhaps respond to V_{mem} directly or to membrane organization.

The EGFR signaling network has been extensively studied, and many of the downstream interaction partners are known. In particular, a series of cytosolic tyrosine residues on the C-terminal tail of EGFR interfaces with downstream binding partners. Autophosphorylation at these sites can occur when EGFR is activated by a ligand, recruiting the downstream interaction partner. Of particular interest for potential interaction with V_{mem} is Tyr 992, which is necessary and

sufficient to trigger downstream Ca^{2+} activation through phospholipase C binding.[6] In addition, Tyr 1068 forms part of the binding site for Grb2,[7] and Tyr 1173 forms part of the binding site for Shc.[8] Both of these components cause, among other things, downstream activation of mitogen activated protein kinase (MAPK). Another interesting site on the receptor is Tyr 845, which is not on the C terminal tail but is partially responsible for stabilizing the active form of EGFR.[9]

To understand the cell biology of the V_{mem} signal described in Chapter 2 more completely, we further investigated EGF-induced V_{mem} signals in three ways. First, we sought to reconstruct the EGFR signaling pathway through heterologous expression in HEK293T. In this system, we did not observe the same hyperpolarization as in A431 cells; instead, we observed a weak depolarization. Second, we monitored the effect of blocking the V_{mem} signal on EGF-induced Ca^{2+} dynamics. Third, we monitor changes in tyrosine phosphorylation when the V_{mem} signal is blocked, both at specific phosphorylation sites and globally within the cell. Taken together, these results do not connect EGF-induced V_{mem} to either Ca^{2+} dynamics or to tyrosine phosphorylation, but they also do not rule out a connection. Overall, these data indicate that the mechanism may be complex or involve heretofore uncharacterized signaling partners for V_{mem}.

Results and Discussion

HEK293T-EGFR show a slight, transient depolarization in response to EGF stimulation

We performed VF-FLIM in HEK293T cells transiently transfected with a plasmid containing EGFR fused to the fluorescent protein mCherry. We observed plasma membrane localized mCherry fluorescence, with some punctate internal signal (**Figure 3.1A**). As expected with transient transfection, the strength of the mCherry signal varied widely between cells; we selected cells with intermediate mCherry fluorescence for VF-FLIM imaging.

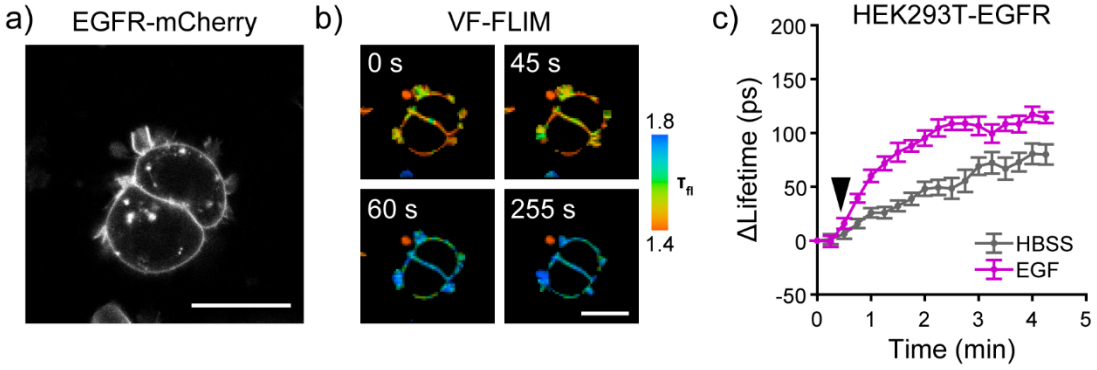

Figure 3.1. Slight depolarization follows EGF treatment in EGFR-mCherry HEK293T cells. HEK293T expressing EGFR fused to mCherry were treated with EGF and V_{mem} was recorded with VF-FLIM. a) Confocal image of mCherry signal in an EGFR expressing cell pair. b) VF-FLIM images from the same cell pair, which was treated with EGF (added 30 s into recording). c) Change in lifetime in cells treated with imaging buffer vehicle (HBSS, n=10) or HBSS containing 500 ng/mL EGF (EGF, n=8). Drug or vehicle was added at the black arrow. Data are shown as mean ± SEM. Scale bars represent 20 μm.

In cells expressing mCherry-EGFR, we observed an upward drift in the fluorescence lifetime during a 5 minute time series with vehicle only (HBSS, **Figure 3.1C**). This drift is likely the result of either phototoxicity of the dye (causing an increase in V_{mem}) or photodamage to the molecular wire (reducing the amount of photoinduced electron transfer in the molecule). When mCherry-EGFR cells were treated with EGF, the increase in lifetime was greater and faster, suggesting that there may be a depolarizing response to EGF. However, interpretation of this depolarization is hampered by the instabilities in the vehicle response.

No hyperpolarization was observed following EGF stimulation in HEK293T-mCherry, whereas robust hyperpolarization was observed in A431 cells. One possible explanation for difference is that the heterologous expression system in HEK293T did not have all necessary factors to activate the hyperpolarizing current. Although HEK293T transfected with EGFR have been used as a model system to study other aspects of the EGFR signaling cascade (e.g. multimerization[10]), they may lack sufficient expression of $K_{Ca}3.1$ to change the V_{mem}. Alternatively, there may be an uncharacterized additional level of regulation required for hyperpolarization in A431. We observed either depolarization or electrical silence in A431 without prior serum starvation (data not shown), suggesting that the factors necessary for hyperpolarization may only be expressed under certain conditions. Preliminary studies of the V_{mem} response of HeLa and A549 cells also showed either depolarization or electrical silence (data not shown), although serum starvation conditions were not optimized for these cell lines. Although HeLa and A549 are reported to transcribe both $K_{Ca}3.1$ and EGFR mRNA,[11] the protein expression profiles under our culture conditions could vary from the published values. Comparison of the transcriptomic or proteomic profiles across these systems and culture conditions could shed light on possible sources of the differences in V_{mem} signal.

EGF-Induced Ca^{2+} Dynamics in the Presence of $K_{Ca}3.1$ Blockers

To understand the relationship between EGF-induced hyperpolarization and Ca^{2+} signaling, we performed Ca^{2+} imaging experiments in A431 cells. Using the Ca^{2+} indicator Oregon Green BAPTA (OGB), we compared the Ca^{2+} signal in the presence and absence of the $K_{Ca}3.1$ blocker charybdotoxin (CTX). We previously showed that CTX suppresses hyperpolarization in EGF-treated A431 cells;[12] for spectral overlap reasons, we were unable to do simultaneous VF-FLIM and Ca^{2+} imaging with OGB.

We observed cytosolic staining with OGB in large groups of serum starved A431 cells (**Figure 3.2A**). Individual cells showed heterogeneous Ca^{2+} responses (**Figure 3.2B**). Regular oscillation, a transient spike, and a sustained elevation in the Ca^{2+} levels were all commonly observed. The average of these single cell responses peaked at 40% $\Delta F/F$ around 30 seconds after EGF addition. The Ca^{2+} signal decayed substantially but did not fully return to baseline within five minutes (total period of observation). The presence of charybdotoxin did not change the observed dynamics substantially (**Figure 3.2C**).

If V_{mem} hyperpolarization modulates the Ca^{2+} response, we would expect to see a change in the magnitude of the Ca^{2+} signal when hyperpolarization was blocked with CTX. The similarity between the control and CTX treated Ca^{2+} response suggests that V_{mem} is likely not playing a major role in the acute Ca^{2+} response to EGF. Indeed, it stands to reason that the large release of Ca^{2+}

from internal stores would dominate the short-term Ca^{2+} signal; this release of Ca^{2+} from internal stores is not known to be V_{mem} sensitive. This work does not fully rule out a role for V_{mem} in regulating SOCE or Ca^{2+} at "rest" following EGF stimulation. In future work, it may be informative to investigate the slower Ca^{2+} dynamics more directly by imaging at longer time points following EGF stimulation.

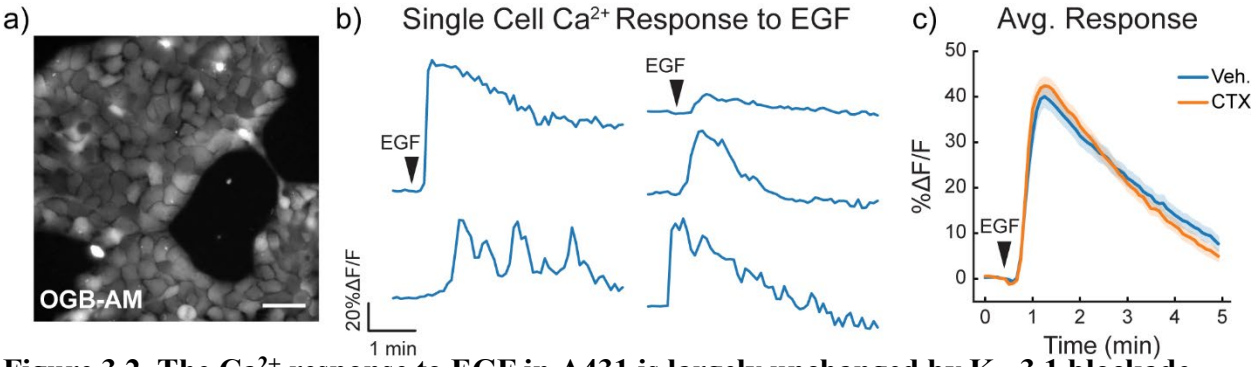

Figure 3.2. The Ca^{2+} response to EGF in A431 is largely unchanged by $K_{Ca}3.1$ blockade.
a) Epifluorescence image of serum starved A431 cells stained with the Ca^{2+} sensor OGB-AM. Scale bar is 50 µm. b) Five representative Ca^{2+} responses of A431 cells following EGF stimulation. Cells were isolated by morphology (hand-traced ROIs). c) Mean Ca^{2+} response of A431 cells treated with EGF and vehicle (blue) or 100 nM charybdotoxin (CTX, orange). Shading represents the 95% confidence interval. Number of cells (from 6 recordings per condition): vehicle 687, CTX 682.

Instead of looking only at the average Ca^{2+} response, we sought to directly relate V_{mem} changes with the Ca^{2+} signal on a single cell level. To this end, we turned to the red-shifted Ca^{2+} indicator Cal-590 (**Figure 3.3**). We were unable to image cells with VF-FLIM and Cal-590 simultaneously and continuously, so we took an initial and final VF-FLIM image and imaged Cal-590 continuously in the interim. We observed very weak staining with Cal-590; long loading times and the efflux pump inhibitor probenecid were required to obtain adequate signal. Even so, the signal from Cal-590 at 543 nm excitation was dimmer than cross excitation from VF2.1.Cl, so spectral bleedthrough is visible in the Cal-590 channel. We were able to spatially segregate the two signals, but a further red-shifted Ca^{2+} indicator may be advantageous in future studies.

We correlated the Ca^{2+} and V_{mem} signals from each cell to better understand any relationship between these two signaling elements. As with OGB, we observe large, heterogenous Ca^{2+} responses to EGF with Cal-590 (**Figure 3.3C**). Because plasma membranes from adjacent cells are indistinguishable under standard confocal microscopy, we were unable to separate V_{mem} signals completely. For this 'single cell' V_{mem} analysis, we selected all membrane signal around a cytosolic Ca^{2+} region of interest (**Figure 3.3D**). We observed no correlation between the peak height of the Ca^{2+} response (or the area under the curve, not shown) and the V_{mem} response as recorded with VF-FLIM. These data, along with the single color OGB data in **Figure 3.2**, suggest that V_{mem} does not strongly modulate the acute Ca^{2+} response to EGF in A431 cells.

Furthermore, the differences in spatial patterning between the V_{mem} and Ca^{2+} signals suggest that they may not be closely related in this system. The acute Ca^{2+} signal is highly heterogeneous between cells, but little difference in the V_{mem} signal was observed across groups of A431 (**Figure 3.2, 3.3**). Although they are sometimes used as a model system with low gap junction expression,[13] A431 cells exhibit at least some degree of V_{mem} delocalization between cells, as seen previously with simultaneous VF-FLIM and electrophysiology.[12] A driving force that is shared between adjacent cells would probably serve to homogenize cellular responses, rather than generate the stark differences seen in the Ca^{2+} signal.

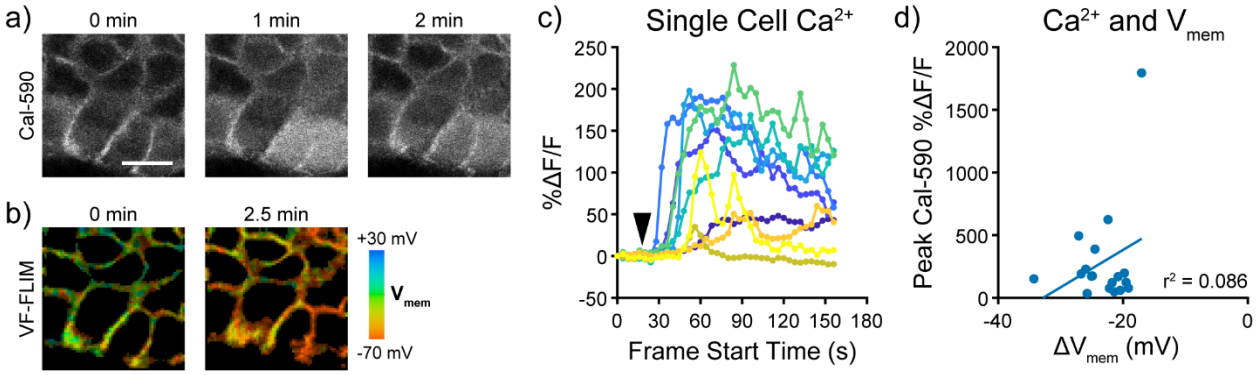

Figure 3.3. Simultaneous V_{mem} and Ca^{2+} Imaging of the A431 response to EGF.
A431 cells were treated with 500 ng/mL EGF and monitored with simultaneous VF-FLIM and intensity-based Ca^{2+} imaging with Cal-590. a) Cal-590 staining in A431. Cross-talk from the VF2.1.Cl channel is visible at the cell membranes; regions of interest were selected to only include cytosolic Ca^{2+} signal. b) VF-FLIM image of the same field of view as in (a). c) Quantification of the fractional change in the Ca^{2+} signal following EGF addition (black arrow). Each trace represents an individual cell from the images in (a) and (b). d) Correlation between the peak %ΔF/F of the Ca^{2+} signal and the change in V_{mem} seen for individual cells (see Methods regarding separation of V_{mem} signal from adjacent cells). Each point represents an individual cell from a total of two fields of view. The line of best fit is overlaid ($r^2 = 0.086$).

Depolarization Effects on the EGF-Induced Phospho-tyrosine Signal

To evaluate whether V_{mem} hyperpolarization modulates the signal in other components of the EGFR pathway, we exposed A431 cells to depolarizing conditions during EGF treatment. This perturbation has two effects: [1] It abolishes the expected hyperpolarization mediated by $K_{Ca}3.1$ and [2] it increases the resting membrane potential of A431 cells to near 0 mV. We then compared the phosphorylation pattern via Western Blot in normally responding (i.e. hyperpolarizing) and artificially depolarized A431 cells. We chose to monitor tyrosine phosphorylation because it is a critical form of EGFR-related signal transduction; these selected targets are by no means exhaustive.

Using a pan-specific antibody for phosphorylated tyrosine, we observed significant increase in the tyrosine phosphorylation (pY) in EGF treated cells versus their EGF untreated counterparts

(**Figure 3.4**). Within EGF treated cells, we looked for differences in the pY signature between vehicle treated and depolarized samples. A slight increase in the pY signal at certain bands was visible in cells treated with gramicidin for 30 minutes or with 120 mM K^+ for 10 minutes. However, the effects were weak and inconsistent across biological replicates, even those acquired on the same day.

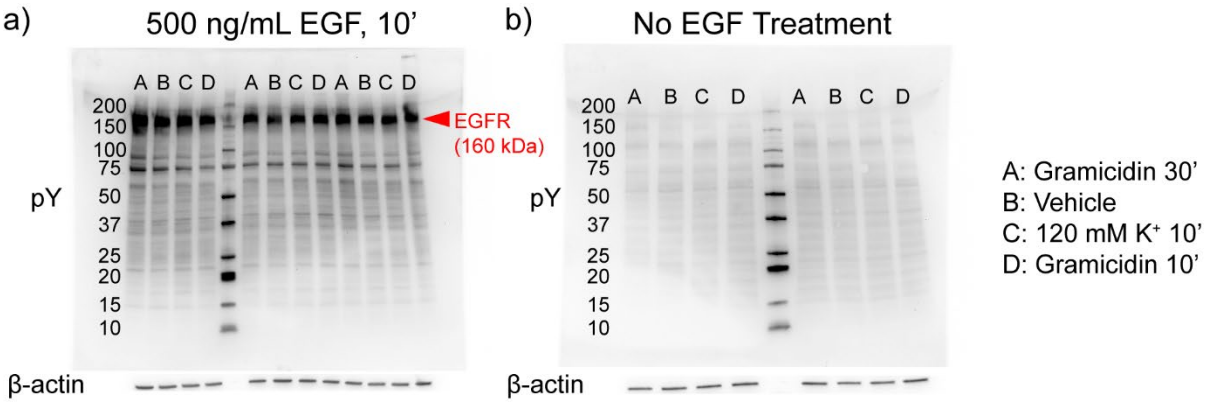

Figure 3.4. Changes to pY resulting from EGF stimulation under perturbed V_{mem} conditions. Western blots visualizing phospho-tyrosine (pY) in A431 cells after stimulation with 500 ng/mL EGF (a) or without EGF treatment (b). Each lane with the same letter corresponds to a different sample of cells lysed on the same day. Actin signal was obtained by stripping and re-probing of the membranes. Blots are representative of at least 2 independent experiments. Numbers indicate molecular weight based on a ladder (lane 5).

In the pan-pY experiment, there are many phosphorylated targets, and attribution of bands to specific protein targets is challenging. We reasoned that, even if there were changes in moderately phosphorylated targets, they would likely be invisible amid the large amounts of pY signal. To mitigate this, we chose a few specific phosphorylation patterns based on literature evidence (see above) and monitored changes at these sites as it related to V_{mem}. We selected the following targets: EGFR pY845 (activation loop, phosphorylated by c-Src),[9] EGFR pY992 (autophosphorylation site responsible for activating Ca^{2+} release),[6] EGFR pY1068 (autophosphorylation site partially responsible for Grb2 binding),[8] EGFR pY1173 (autophosphorylation site partially responsible for Sh2 binding),[8] and MAPK phosphorylation. Furthermore, we were concerned that bulk depolarization could have unwanted side effects, so we used charybdotoxin (CTX) to block $K_{Ca}3.1$ activation instead of bulk depolarization of the samples. In each case, we compared the EGF induced phosphorylation level with $K_{Ca}3.1$ activated (control) or blocked (CTX) (**Figure 3.5**).

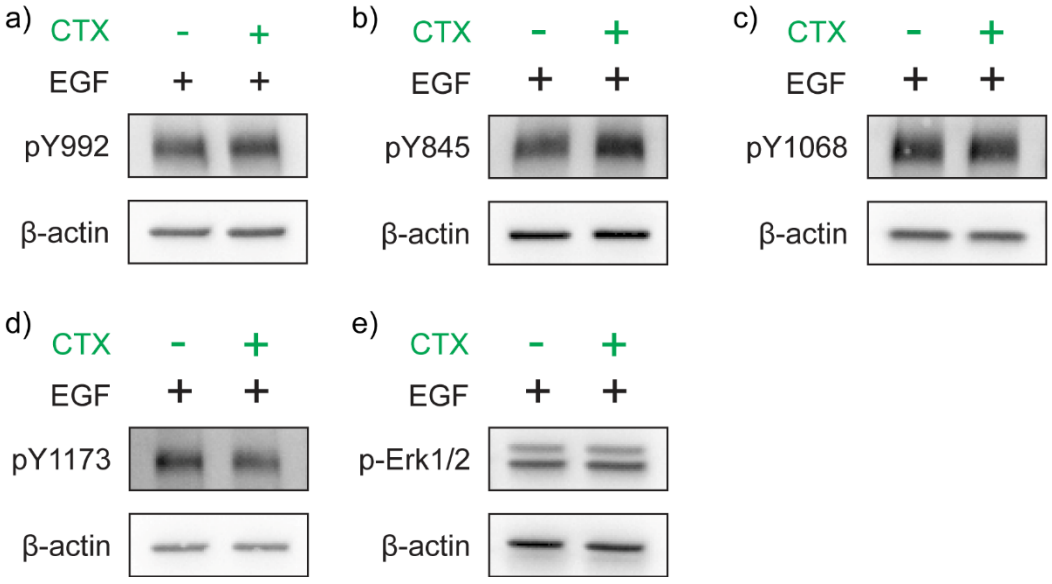

Figure 3.5. Effect of $K_{Ca}3.1$ blockade on EGF-induced protein phosphorylation in A431 cells. The phosphorylation response to EGF stimulation in A431 cells with normal V_{mem} signaling (CTX -) and $K_{Ca}3.1$ blockade (CTX +) was monitored via Western blotting. Antibodies against five particular targets were used: a) EGFR pY992, b) EGFR pY845, c) EGFR pY1067, d) EGFR pY1173, e) phospho-Erk1/2 (p44/42). Actin signal was obtained from stripping and re-probing the blots after probing for the phosphorylation signal.

Using these more specific antibodies, we observed distinct bands at the expected molecular weight for all phosphorylated targets **(Figure 3.5**). Consistent with the unchanged Ca^{2+} signal (**Figure 3.2, 3.3**), we did not see differences in the EGFR pY992 signal in normal and depolarized A431 cells (**Figure 3.5**). Despite evidence that, in the context of K-Ras signaling, V_{mem} can modulate MAPK phosphorylation levels,[5] we did not see differences in phosphorylation at EGFR pY1068, EGFR pY1173, or on MAPK directly. We observed a slight increase in pY signal at EGFR Y845 when the V_{mem} hyperpolarization was blocked, but the response was small relative to the limit of detection in Western blotting.

Taken together, these results are inconclusive regarding the physiological effect(s) of EGF-induced V_{mem} hyperpolarization. Given the lack of correlation between Ca^{2+} peak height and V_{mem} change, as well as the largely unchanged Ca^{2+} response with $K_{Ca}3.1$ blockade, it seems unlikely that V_{mem} affects the acute Ca^{2+} response to EGF. We cannot rule out regulation of resting Ca^{2+} or Ca^{2+} concentrations at later time points by the V_{mem} signal. The effect on phosphorylation is much less clear, as we only directly analyzed a small subset of potential targets. Furthermore, effects were generally at or near the limit of detection for Western blotting; analysis of phosphorylation levels by flow cytometry would likely yield clearer results. A top-down search for potential targets using an approach such as phosphoproteomics may also shed light on this pathway.

Materials and Methods

Materials

EGF was purchased from PeproTech and was stored as a 2000x (1 mg/mL) stock in deionized water at -80°C. The EGFR-mCherry plasmid (prepared by a Qiagen maxiprep kit) was a gift from the Kuriyan lab; it has been previously described.[10] All salts were purchased from either Sigma-Aldrich or Thermo Fisher Scientific. Media and supplements were purchased from Gibco (Life Technologies/Thermo Fisher Scientific). Osmolarity of all homemade solutions was checked with an osmometer (μOsmette, Precision Systems).

VF2.1.Cl was made in-house according to the published synthesis.[14] Oregon Green 488 BAPTA-AM 1 (OGB) was purchased from Molecular Probes/Life Technologies (#O-6807). Cal-590 was purchased from AAT Bioquest. Probes were stored as 1000-2000x DMSO stocks at -20°C. Pluronic F-127 was purchased from Life Technologies and stored as a 20% stock in DMSO at room temperature.

Cell Culture and Transfection

HEK293T cells were obtained from the UC Berkeley Cell Culture Facility and were maintained as described in **Chapter 2**. On day 0, HEK293T were plated at a density of 78,000-104,000 cells/cm^2 directly onto tissue culture treated 6 well plates (Corning). Cells were allowed to recover for 16-24 hours before transient transfection with Lipofectamine 3000. On day 1, transfection was performed according to the manufacturer's protocol with the following modifications to the reagent concentrations (per well): 0.5-1 μg of plasmid DNA in total were used, along with 1 μL of P3000 reagent and 3 uL lipofectamine in 200 uL Opti-MEM (Gibco). Cells were media changed into fresh complete DMEM 2-3 hours after transfection. On day 2, cells were seeded at a density of 21,000 cells/cm^2 in complete DMEM onto PDL-treated 25 mm glass coverslips in preparation for imaging. 5 hours after seeding, media was exchanged for DMEM without FBS (beginning of "serum starvation;" DMEM was supplemented with 4.5 g/L glucose and 2 mM GlutaMAX). Data shown here were from cells were incubated in DMEM without FBS for 16 hours; the V_{mem} response was similar at both shorter (2 hr) and longer (24 hr) serum starvation times.

A431 Cell Culture

A431 cells were obtained from the UC Berkeley Cell Culture facility. Cells were verified by STR profiling and were routinely tested for mycoplasma contamination. A431 cells were maintained at 37°C and 5% CO_2 in a humidified incubator in DMEM supplemented with 4.5 g/L glucose, 10% FBS, and 2 mM GlutaMAX. Cells were passaged every 2-5 days via dissociation with 0.25% Trypsin-EDTA (Life Technologies). Residual trypsin was removed by centrifugation at 300xg for five minutes followed by re-suspension in fresh complete media. Cells were discarded after twenty-five passages.

For serum starvation experiments, A431 cells were seeded at 83,000 cells/cm^2 onto a 6 well plate (tissue culture treated, Corning) in serum-deprivation DMEM (4.5 g/L glucose, 2% FBS, 2 mM GlutaMAX). For Western blotting, cells were seeded directly onto plastic; for imaging experiments, cells were seeded onto PDL-treated 25 mm #1.5 glass coverslips (see above). Two days after seeding, media was exchanged for serum-free DMEM (4.5 g/L glucose, 2 mM GlutaMAX); cells were serum starved for 4-6 hours prior to the start of EGF treatment.

Loading of Small Molecule Fluorescent Dyes

For OGB and VF2.1.Cl, cells were incubated for 20-25 minutes at 37°C and 5% CO_2 in Hank's Balanced Salt Solution (HBSS, Life Technologies #14025-134) containing 1x probe. Samples were washed once in HBSS without dye and transferred to fresh HBSS for imaging. 0.01% Pluronic F-127 was added to facilitate the loading of OGB. Cal-590 was loaded in HBSS for 80 minutes with 0.02% Pluronic F-127 and 1 mM probenecid to reduce probe efflux and obtain adequate signal. Working concentrations for probes were the following: 100 nM VF2.1.Cl, 1 μM OGB, 4 μM Cal-590.

EGF Stimulation (All Imaging Experiments)

Cells plated on 25 mm coverglass were placed into an Attofluor cell imaging chamber (Thermo Fisher Scientific) in 0.5 mL of HBSS. For HBSS control trials, 0.5 mL of HBSS was gently added approximately 30 seconds into the recording. For EGF stimulation, 0.5 mL of HBSS containing 1 μg/mL EGF (2x) was added instead. In general, two recordings were taken per sample – an initial recording of the HBSS (vehicle) response and a subsequent recording of the EGF response. In this case, 0.5 mL of solution was removed from the chamber in between the two recordings to retain the correct volume.

VF-FLIM Monitoring of V_{mem} During EGF Signaling

VF-FLIM images were acquired and fit to exponential decay models as described above **(Chapter 2**), with the following differences. A 540/50 nm bandpass emission filter (Semrock) was used to avoid bleedthrough of the mCherry signal into the fluorescence lifetime signal. Lifetime data were fit with 5 iterations in SPCImage software.

mCherry and Cal-590 were imaged with a 543 nm HeNe laser (Zeiss), using a 543 nm long pass dichroic, a 565 nm long pass secondary dichroic, and a 560 nm long pass emission filter (Zeiss). For HEK293T-mCherry recordings, data were acquired continuously and formed into FLIM images at 15 second intervals. For Cal-590 and VF-FLIM experiments on the same cells, an initial VF-FLIM image was taken, followed by 2.5 minutes of Ca^{2+} imaging , during which HBSS or EGF was added. A final VF-FLIM image was taken 3 minutes into the time series (2.5 minutes after HBSS/EGF addition).

Fluorescence Intensity Imaging of Ca^{2+} Response to EGF Stimulation with OGB

Serum-starved A431 cells were loaded with OGB as described above; where charybdotoxin (CTX) was used, it was included in both the dye loading solution and imaging solution at 100 nM. Coverslips were transferred to an Attofluor (Thermo Fisher Scientific) imaging chamber and visualized on an inverted epifluorescence microscope (Zeiss AxioObserver Z-1) controlled with μManager 1.4.[15] Excitation light was supplied from an LED source at 1 mW/cm^2 (2% intensity, Lumencor SpectraX Light Engine). Fluorescence emission was collected with a 40x oil/1.3 NA EC Plan Neofluar immersion objective (Zeiss) and passed through a 510 nm long pass dichroic and a 540/50 nm bandpass emission filter (Semrock). Images were formed onto a Hamamatsu Orca Flash4.0 sCMOS camera with an exposure of 400 ms and an interval of 5 seconds between the start of successive exposures. Time series were recorded for a total of 5 minutes. Images were binned 4x4 upon acquisition (total image size 133 x 133 μm^2).

Fluorescence Intensity Data Analysis

Regions of interest (ROIs) corresponding to individual cells were identified by hand from the cytosolic OGB or Cal-590 signal in FIJI.[16] The mean fluorescence intensity of a background region near the ROI was subtracted from the mean fluorescence in the ROI to give the fluorescence (F). To generate the percent change in fluorescence (%ΔF/F), the fluorescence values were normalized to the first frame (Cal-590) or to the average of the seventh and eighth frames (OGB) in the time series, which corresponds to the baseline immediately before EGF was added.

Preparation of Cell Lysates for Western Blotting

A431 cells were serum starved as indicated above for 4-6 hours. Following serum starvation, cells were incubated at room temperature and ambient atmosphere for 30 minutes in HBSS and various drugs to change V_{mem} or alter $K_{Ca}3.1$ currents (charybdotoxin, CTX) (**Table 3.1**). EGF concentration was 500 ng/mL in all cases; gramicidin was used at 400 ng/mL. The composition of high K^+ HBSS was as follows (in mM): 120 KCl, 23 NaCl, 5.6 D-glucose, 4.2 $NaHCO_3$, 1.26 $CaCl_2$, 0.49 $MgCl_2$, 0.44 KH_2PO_4, 0.41 $MgSO_4$, 0.34 NaH_2PO_4 (pH 7.25, 285 mOsm/L).

Figure, Condition	**Initial 20'**	**Final 10'**
Fig. 3.4, Gramicidin 30'	HBSS + 400 ng/mL gramicidin (HBSS/gram)	HBSS/gram or HBSS/gram + EGF
Fig. 3.4, HBSS only	HBSS	HBSS or HBSS + EGF
Fig. 3.4, 120 mM K^+ 10'	HBSS	High K^+ HBSS or High K^+ HBSS with EGF
Fig. 3.4, Gramicidin 10'	HBSS	HBSS/gram or HBSS/gram + EGF
Fig. 3.5, CTX -	HBSS	HBSS + EGF
Fig. 3.5, CTX +	HBSS + 100 nM CTX	HBSS + 100 nM CTX + EGF

Table 3.1. Treatment protocol for A431 cells prior to lysis and analysis by Western blot.

Following treatment, cells were placed on ice and washed once with ice cold dPBS without Ca^{2+} or Mg^{2+} (Gibco). Samples were incubated for 30 minutes on ice in lysis buffer (100 uL per sample). Lysis buffer was made fresh immediately before use from stocks of each component (stored at 4°C, -20°C, or -80°C, as indicated by the manufacturer) and contained 100 mM NaCl, 50 mM Tris-HCl, 0.5% Na deoxycholate, 1% Triton X-100, 0.1% SDS, 2 mM sodium orthovanadate, 10 mM NaF, 1 mM β-glycerophosphate disodium salt, 2.5 mM sodium pyrophosphate, 1x Roche cOmplete mini protease inhibitor. Tris-HCl stock solutions were set to pH 7.5 before storage. Sodium orthovanadate solutions were activated before storage at -20°C as described previously.[17]

Following lysis, samples were manually scraped from the plastic surface and centrifuged for 25 minutes at 4°C and 13,000xg with a benchtop centrifuge (Centrifuge 5424 R, Eppendorf). The lysate supernatant was isolated and used for all further experiments; insoluble pellets were discarded. Lysates were used immediately or were frozen at -20°C overnight for use the following day. Rapid degradation of the signal following days of storage at -20°C.

Total protein content of the lysate was estimated with a BCA assay according to the manufacturer's instructions (Pierce BCA Protein Assay Kit, Thermo Fisher Scientific). Bovine serum albumin

(BSA) standards were made in the lysis buffer described above. Following 30 minutes of incubation at 37°C, sample absorption was read at 562 nm with a Shimadzu 2501 Spectrophotometer in 1 cm path length plastic cuvettes (Brand-Tech BRAND, Fisher Scientific 13-878-123). Each sample was zeroed at 825 nm. Sample concentration was estimated based on a linear fit to the standard curve in the range 0-1 mg/mL. Lysates were diluted before BCA measurement to keep samples within this concentration range.

SDS-PAGE and Western Blotting

In preparation for analysis by SDS-PAGE, 5-20 ug of total protein from A431 lysates was mixed with MilliQ water and 4x Laemmli sample buffer (BioRad). β-mercaptoethanol was added to the Laemmli sample buffer immediately before use. Sham samples were prepared to fill any empty lanes. All samples were incubated at 95°C for 5 minutes and cooled on ice.

Samples were loaded into 4-20% Tris-glycine Mini-PROTEAN TGX or Mini-PROTEAN stain free precast gels (BioRad). BioRad Precision Plus Western C Standards were used to determine molecular weight. Gel electrophoresis was performed in a BioRad Tetra System attached to a PowerPac Basic power supply (BioRad). Gels were run at 200 V for 40 min or until loading dye front reached the bottom of the gel. Running buffer consisted of 25 mM Tris, 192 mM glycine, and 0.1% SDS in MilliQ water. Transfer stacks were set up with the TransBlot Turbo RTA Transfer Kit (PVDF membranes, BioRad) according to manufacturer's instructions. Protein transfer was performed with a BioRad TransBlot Turbo Transfer System using the manufacturer's Mixed MW or High MW protocol.

After transfer, membranes were placed in TBST wash buffer (20 mM Tris, 137 mM NaCl, 0.1% w/v Tween-20, pH 7.6). Membranes were blocked for 1 hour at room temperature in 5% BSA in TBST, pH 7. Membranes were incubated overnight at 4°C with gentle shaking in primary antibody at the dilution indicated below in 5% BSA in TBST. Membranes were washed five times for at least five minutes each at room temperature in TBST and then incubated for one hour at room temperature in secondary antibody at the concentration indicated below (in 5% BSA in TBST). Membranes were washed for five times for at least five minutes each at room temperature in TBST and then stored in fresh TBST before visualization.

Chemiluminescence was visualized with Perkin Elmer Western Lighting Plus reagent according to the manufacturer's protocol. Blots were imaged in a BioRad ChemiDoc Gel Imaging System after 3-8 minutes of treatment with the visualization reagent (exposures of 3-120 seconds, depending on the signal level).

The primary antibodies used were the following: mouse anti-phosphotyrosine (1:2000, CST #9411), rabbit anti-β-actin 13E5 (1:2000, CST #4970), rabbit anti-phosphoEGFR Y845 (1:1000 CST #2231), rabbit anti-phosphoEGFR Y992 (1:1000, Thermo Fisher Scientific #44-786G), rabbit anti-phosphoEGFR Y1068 (1:1000, CST #2234), mouse anti-phosphoEGFR Y1173 (1:500, SCBT #57545), rabbit anti-p44/42 Erk1/2 (1:1000, CST #4370). Secondary antibodies used were either anti-rabbit IgG HRP-linked antibody (1:2000, CST #7074) or anti-mouse IgG HRP-linked antibody (1:2000, CST #7076). Ladder was visualized with 1:10,000 streptactin HRP conjugate (BioRad) added during the primary antibody incubation step. CST = Cell Signaling Technologies. SCBT = Santa Cruz Biotechnology.

For stripping and re-probing of membranes to visualize β-actin for normalization, blots were incubated in stripping buffer (50 mM Tris-HCl, 2% SDS, 100 mM β-mercaptoethanol) at 55°C for 15-35 minutes. All blots were tested for residual signal after stripping; different stripping times were used based on what resulted in a completely blank blot for that particular antibody. After stripping, blots were washed five times for five minutes each in TBST at room temperature. The protocol was then resumed from the blocking step as above. 5% dry milk was used instead of 5% BSA for blocking and making up β-actin antibody solutions because it better suppressed nonspecific bands.

References

(1) Oda, K.; Matsuoka, Y.; Funahashi, A.; Kitano, H. A Comprehensive Pathway Map of Epidermal Growth Factor Receptor Signaling. *Mol. Syst. Biol.* **2005**, *1* (1). https://doi.org/10.1038/msb4100014.

(2) Emeriau, N.; de Clippele, M.; Gailly, P.; Tajeddine, N. Store Operated Calcium Entry Is Altered by the Inhibition of Receptors Tyrosine Kinase. *Oncotarget* **2018**, *9* (22), 16059–16073. https://doi.org/10.18632/oncotarget.24685.

(3) Crottès, D.; Lin, Y. H. T.; Peters, C. J.; Gilchrist, J. M.; Wiita, A. P.; Jan, Y. N.; Jan, L. Y. TMEM16A Controls EGF-Induced Calcium Signaling Implicated in Pancreatic Cancer Prognosis. *Proc. Natl. Acad. Sci. U. S. A.* **2019**, *116* (26), 13026–13035. https://doi.org/10.1073/pnas.1900703116.

(4) Yang, M.; Brackenbury, W. J. Membrane Potential and Cancer Progression. *Front. Physiol.* **2013**, *4* (July), 1–10. https://doi.org/10.3389/fphys.2013.00185.

(5) Zhou, Y.; Wong, C.; Cho, K.; van der Hoeven, D.; Liang, H.; Thakur, D. P.; Luo, J.; Babic, M.; Zinsmaier, K. E.; Zhu, M. X.; et al. Membrane Potential Modulates Plasma Membrane Phospholipid Dynamics and K-Ras Signaling. *Science (80-.).* **2015**, *349* (6250), 873–876. https://doi.org/10.1126/science.aaa5619.

(6) Gill, K.; Macdonald-Obermann, J. L.; Pike, L. J. Epidermal Growth Factor Receptors Containing a Single Tyrosine in Their C-Terminal Tail Bind Different Effector Molecules and Are Signaling-Competent. *J. Biol. Chem.* **2017**, *292* (50), 20744–20755. https://doi.org/10.1074/jbc.M117.802553.

(7) Rojas, M.; Yao, S.; Lint, Y. Z. Controlling Epidermal Growth Factor (EGF)-Stimulated Ras Activation in Intact Cells by a Cell-Permeable Peptide Mimicking Phosphorylated EGF Receptor. *J. Biol. Chem.* **1996**, *271* (44), 27456–27461. https://doi.org/10.1074/jbc.271.44.27456.

(8) Batzer, A. G.; Rotin, D.; Ureña, J. M.; Skolnik, E. Y.; Schlessinger, J. Hierarchy of Binding Sites for Grb2 and Shc on the Epidermal Growth Factor Receptor. *Mol. Cell. Biol.* **1994**, *14* (8), 5192–5201. https://doi.org/10.1128/mcb.14.8.5192.

(9) Sato, K. ichi. Cellular Functions Regulated by Phosphorylation of EGFR on TYR845. *Int. J. Mol. Sci.* **2013**, *14* (6), 10761–10790. https://doi.org/10.3390/ijms140610761.

(10) Huang, Y.; Bharill, S.; Karandur, D.; Peterson, S. M.; Marita, M.; Shi, X.; Kaliszewski, M. J.; Smith, A. W.; Isacoff, E. Y.; Kuriyan, J. Molecular Basis for Multimerization in the Activation of the Epidermal Growth Factor Receptor. *Elife* **2016**, *5* (MARCH2016), 1–27. https://doi.org/10.7554/eLife.14107.

(11) Thul, P. J.; Åkesson, L.; Wiking, M.; Mahdessian, D.; Geladaki, A.; Ait Blal, H.; Alm, T.; Asplund, A.; Björk, L.; Breckels, L. M.; et al. A Subcellular Map of the Human Proteome. *Science (80-.).* **2017**, *356* (6340), eaal3321. https://doi.org/10.1126/science.aal3321.

(12) Lazzari-Dean, J. R.; Gest, A. M. M.; Miller, E. W. Optical Estimation of Absolute Membrane Potential Using Fluorescence Lifetime Imaging. *Elife* **2019**, *8*, e44522. https://doi.org/10.7554/elife.44522.

(13) Giepmans, B. N. G.; Hengeveld, T.; Postma, F. R.; Moolenaar, W. H. Interaction of C-Src with Gap Junction Protein Connexin-43. **2001**, *276* (11), 8544–8549. https://doi.org/10.1074/jbc.M005847200.

(14) Miller, E. W.; Lin, J. Y.; Frady, E. P.; Steinbach, P. A.; Kristan, W. B.; Tsien, R. Y. Optically Monitoring Voltage in Neurons by Photo-Induced Electron Transfer through Molecular Wires. *Proc. Natl. Acad. Sci. U. S. A.* **2012**, *109* (6), 2114–2119. https://doi.org/10.1073/pnas.1120694109.

(15) Edelstein, A. D.; Tsuchida, M. A.; Amodaj, N.; Pinkard, H.; Vale, R. D.; Stuurman, N. Advanced Methods of Microscope Control Using MManager Software. *J. Biol. Methods* **2014**, *1* (2), 10. https://doi.org/10.14440/jbm.2014.36.

(16) Schindelin, J.; Arganda-Carreras, I.; Frise, E.; Kaynig, V.; Longair, M.; Pietzsch, T.; Preibisch, S.; Rueden, C.; Saalfeld, S.; Schmid, B.; et al. Fiji: An Open-Source Platform for Biological-Image Analysis. *Nat. Methods* **2012**, *9* (7), 676–682. https://doi.org/10.1038/nmeth.2019.

(17) Gordon, J. A. Use of Vanadate as Protein-Phosphotyrosine Phosphatase Inhibitor. *Methods Enzymol.* **1991**, *201*, 477–482.

Chapter 4

Tuning VoltageFluor Sensitivity and Brightness with Conformationally Restricted Anilines

This work was conducted in collaboration with the following individuals:

Steven Boggess synthesized VFs, characterized VFs in HEK293T and cardiomyocytes, and co-wrote the manuscript.

Benjamin Raliski synthesized VFs, performed UV-Vis spectroscopy, characterized VFs in neurons, co-wrote the manuscript.

Samuel Mun and Amy Li assisted with the synthesis of VFs

Abstract

Effective reporting of fast biological changes in transmembrane potential (V_{mem}) demands measurement with high temporal resolution and signal-to-noise. To meet these demands, V_{mem} sensitivity and cell brightness must be optimized. To this end, we report the design and synthesis of four PeT-based voltage sensitive dyes with conformationally modified anilines as electron donors. With these indicators, as well as existing PeT-based voltage indicators, we construct a library of sensors with a range of conformations in the electron donating moiety. We find that measurements of fluorescence sensitivity and lifetime across this library span an order of magnitude and seek to understand how aniline conformation modulates PeT. By comparing in-depth photophysical characterization with performance at action potential detection, we establish a detailed link between the probe conformation and ability to report V_{mem} events with high fidelity.

Introduction

Cell membrane potential (V_{mem}) arises from an unequal distribution of ions across a semi-permeable lipid bilayer. In excitable cells such as neurons and cardiomyocytes, V_{mem} changes on the order of milliseconds create action potentials (APs). These APs facilitate electrochemical communication across synapses and coordinate the contraction of millions of cells across the chambers of the heart. Measuring this electrical activity is critical to understanding cell physiology in health and disease.

To study these rapid changes in V_{mem}, a technique must have exquisite temporal resolution and signal-to-noise. The gold standard for measuring V_{mem} is patch-clamp electrophysiology, a series of techniques that use an electrode in direct contact with the cell of interest, allowing very precise measurement of V_{mem}. However, the low-throughput, high invasiveness, and low spatial resolution[1,2] of patch-clamp electrophysiology render it an incomplete V_{mem} measurement technique.

To record electrical activity in a less invasive and more highly multiplexed manner, our lab and others have undertaken the development of fluorescent voltage indicators, either as genetically encoded voltage indicators (GEVIs) or small molecule voltage sensitive dyes. Development of voltage sensors with sufficiently fast kinetics, bright signal, and high sensitivity poses a significant challenge in sensor engineering. State-of-the-art V_{mem} sensors are capable of recording electrophysiological signatures from individual cells with high fidelity.[3,4] Additional optimization of sensor limit-of-detection could improve the reporting of subthreshold V_{mem} events, as well as enable simultaneous recording across larger neuronal ensembles.

To meet the precise needs of V_{mem} imaging, the rational tunability of small molecules versus fluorescent proteins is a major advantage. Rational tuning of small molecules has produced major advances in biological sensing: chemical probes for Ca^{2+} have been rationally tuned across a range of dissociation constants,[5,6] small molecule fluorophores can be tuned to precise wavelengths via fluorination,[7] and reversible, intramolecular spirocyclization produces fluorophore blinking for super-resolution imaging.[8] Optimization of the brightness, sensitivity, color, and localization of small molecule voltage dyes has been fruitful,[4,9–11] but further investigation is required to obtain probes with sufficient signal-to-noise ratios for single-cell recordings in thick tissue.

Our lab has developed a class of small molecule voltage sensitive dyes (VoltageFluors, VFs) based on a photoinduced electron transfer (PeT)-based V_{mem} sensing trigger. Because PeT occurs from a membrane-localized electron donor, it is sensitive to the transmembrane electric field. We have previously demonstrated that the absorption and emission wavelength of VFs can be tuned through the incorporation of different chromophores,[9,12–14] and the sensitivity can be modulated via the electron density and attenuation of the molecular wire.[10,15]

To better understand the relationship between sensitivity and brightness, we investigated the coupling between the aniline donor and the molecular wire as a strategy for tuning VFs. Using VF2.1.Cl[16]. and VF2.0.Cl[10] as reference structures, we designed and synthesized four indicators with a range of dihedral angles between the aniline donor and the molecular wire. With this library of six aniline-tuned VFs, we investigated the response of fluorescence intensity and fluorescence lifetime (τ_{fl}) to V_{mem}. We find that modifying the aniline conformation can generate VFs that are both more and less PeT quenched than VF2.1.Cl, tuning both sensitivity and τ_{fl} across an order of magnitude. We identify a tradeoff between sensitivity and τ_{fl}, in which dyes with intermediate sensitivity and τ_{fl} have superior performance as voltage indicators. We compared the performance of the three best V_{mem} sensors in the series in the detection of both cardiac and neuronal action potentials. In doing so, we find that all three report APs with good signal to noise, and τ_{fl} is the best predictor of probe performance in detection of physiologically relevant V_{mem} signals.

Results and Discussion

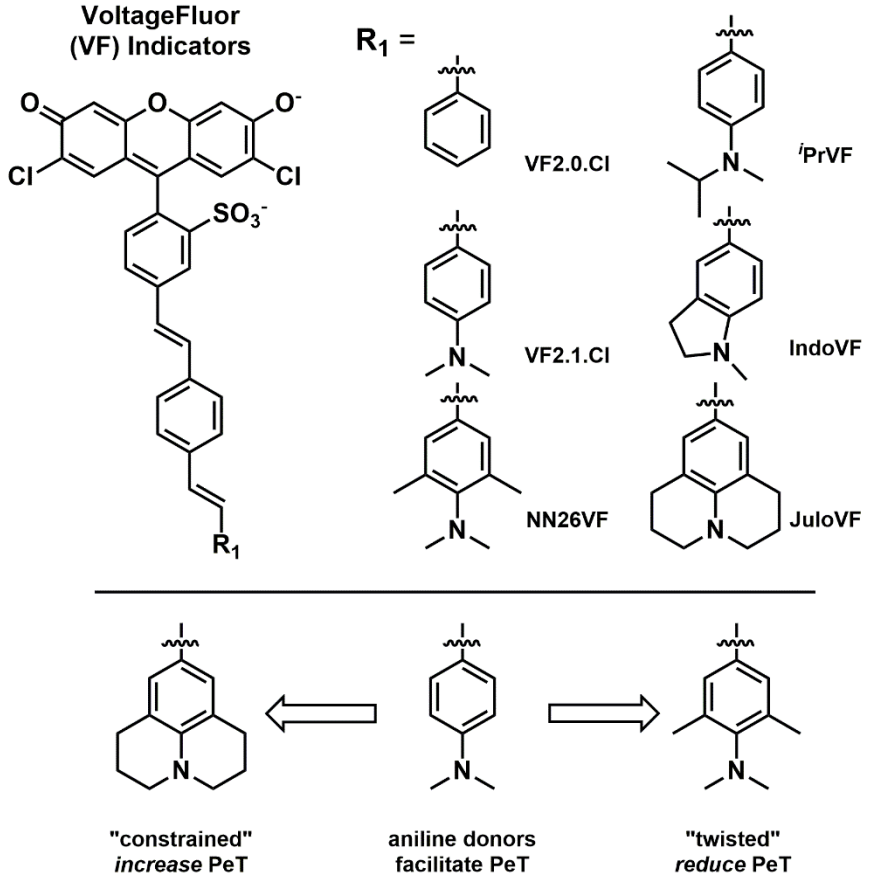

Scheme 4.1 Structures of VoltageFluors investigated in this study.

In Vitro Characterization Reveals Changes in Molecular Wire Moeity

We synthesized four voltage dyes with conformationally restricted anilines (**Scheme 4.1**). Further synthetic details are available in Steven Boggess's Ph.D. dissertation. Together with VF2.1.Cl and VF2.0.Cl as reference structures, we investigated this library of 6 VF derivatives.

We first evaluated this VF library with UV-Vis spectroscopy in ethanol with 0.1 M KOH (ethanol-KOH). Modification of aniline conformation altered the absorbance of the molecular wire region of these indicators, but not the absorbance of the xanthene chromophore region (**Figure 4.1a**, **Figure 4.2**). The wire region of JuloVF displayed an absorbance maximum at 406 nm, a red-shift of 17 nm relative to the wire region of VF2.1.Cl (**Table 4.1**). In contrast, the wire region of NN26VF displayed an absorbance maximum at 368 nm, a blue-shift of 21 nm relative to the wire region of VF2.1.Cl (**Table 4.1**). For comparison, the wire region of VF2.0.Cl, which completely lacks an aniline, displayed an absorbance maximum at 360 nm (**Table 4.1**). The wire regions of IndoVF and ^{i}PrVF displayed absorbance maxima very close to VF2.1.Cl (**Table 4.1**). Taken together, these data suggest that JuloVF contains an aniline with more sp^2 character than VF2.1.Cl, NN26VF contains an aniline with less sp^2 character than VF2.1.Cl, and IndoVF and ^{i}PrVF contain anilines with very similar sp^2 character to VF2.1.Cl. Furthermore, protonation of the aniline results

in a hypsochromatic shift in the wire absorbance maxima all to 360-365 nm (**Figure 4.3**). We reason that these shifts in the wire absorbance maxima result from differences in the electronic coupling of the aniline with the rest of the molecular wire.

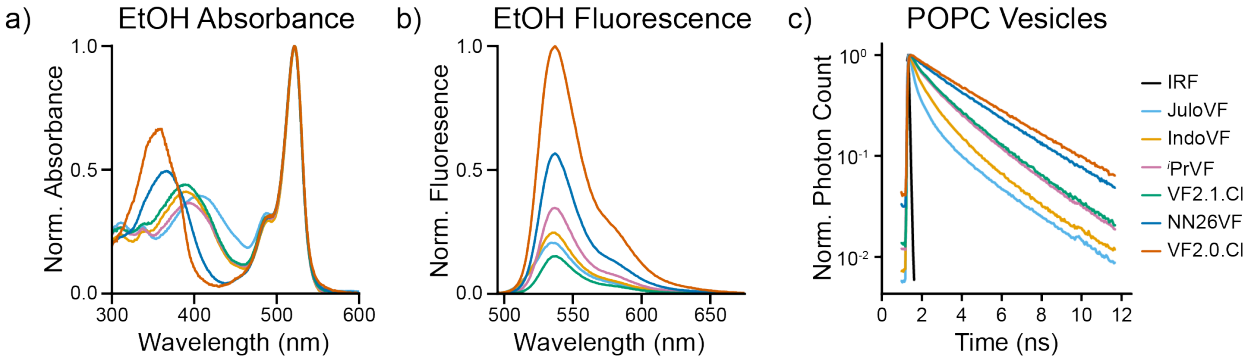

Figure 4.1. UV-VIS and fluorescence spectroscopy suggests conformational restriction in aniline modified VoltageFluors.
a) Absorbance spectra of VoltageFluors at 500 nM in Ethanol with 0.1 M KOH (Ethanol-KOH) normalized to their absorbance maxima. b) Emission spectra of VoltageFluors at 500 nM in Ethanol-KOH adjusted to their respective absorbance values at 485 nm and normalized to the VF2.0.Cl trace. c) Time-resolved fluorescence decays of VFs at 500 nM in POPC vesicles. Decays were normalized to the time channel with maximum photon counts. Black line indicates the instrument response function (IRF).

VF	Wire λ_{abs} (nm)	Φ_F[a]	τ_{fl}[a]	τ_{fl}[b]	Rel. brightness (HEK293T)	%ΔF/F, 100 mV	$\Delta\tau_{fl}$ per mV (ps)	τ_{fl} at 0 mV (ns)
JuloVF	406	0.10	0.63 ± 0.08	0.81 ± 0.05	0.021 ± 0.003[c] 0.037 ± 0.004[d]	34 ± 6[d]	0.73 ± 0.03[d]	0.31 ± 0.01[d]
IndoVF	390	0.14	0.52 ± 0.03	0.98 ± 0.02	0.28 ± 0.02	37 ± 2.4	1.49 ± 0.04	0.48 ± 0.02
iPrVF	392	0.28	1.04 ± 0.04	1.67 ± 0.03	0.29 ± 0.03	34 ± 1.6	2.97 ± 0.04	1.28 ± 0.01
VF2.1.Cl	389	0.12	0.53 ± 0.02	1.58 ± 0.05	0.361 ± 0.01[e] 1.0 ± 0.1[c]	23 ± 3[e] 26 ± 3[c]	3.11 ± 0.04[e] 3.05 ± 0.08[c]	1.68 ± 0.04[e] 1.57 ± 0.03[c]
NN26VF	368	0.44	1.66 ± 0.03	2.55 ± 0.06	0.44 ± 0.05	2.2 ± 0.05	0.50 ± 0.02	3.32 ± 0.01
VF2.0.Cl	360	0.83	3.18 ± 0.02	3.13 ± 0.10	0.62 ± 0.06[e] 1.8 ± 0.2[c]	-0.3 ± 0.002[e] -0.2 ± 0.001[c]	0.02 ± 0.03[e] 0.00 ± 0.03[c]	3.44 ± 0.01[e] 3.36 ± 0.03[c]

Table 4.1. Summarized properties of conformationally restricted VFs.
Solution phase τ_{fl} measurements were taken at 500 nM dye. Cellular measurements were conducted at 300 nM dye loading unless otherwise noted. [a]In ethanol-KOH. [b]In POPC. [c]Acquired at 300 nM dye concentration. [d]Acquired at 500 nM dye concentration. [e]Acquired at 100 nM dye concentration.

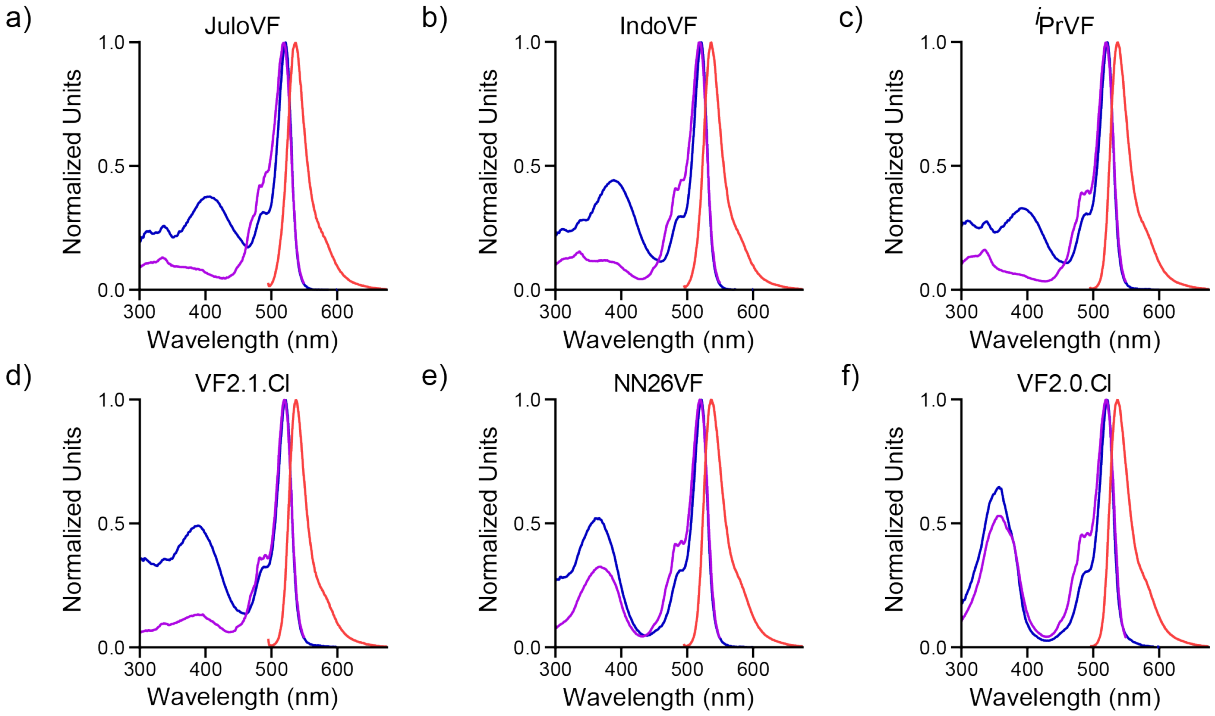

Figure 4.2. Absorbance, Emission, and Excitation Spectra of Aniline VFs.
Absorbance spectra (blue), emission spectra (red), and excitation spectra (purple) for JuloVF (a), IndoVF (b),.^{i}PrVF (c), VF2.1.Cl (d), NN26VF(e), and VF2.0.Cl (f) in ethanol with 0.1 M KOH. The VoltageFluors were diluted from DMSO stocks (500 µM-1 mM) to either 1 µM (JuloVF, IndoVF, ^{i}PrVF, VF2.1.Cl, NN26VF) or 500 nM (VF2.0.Cl) in ethanol with 0.1 M KOH. VF2.0.Cl was measured at 500 nM as the emission of 1 mM VF2.0.Cl was higher than the range of the detector for wavelengths near the emission maximum. Spectra were taken using the equipment described above in section **2**. Absorbance measurements were recorded at 1 nm intervals from 300 nm to 600 nm. Emission measurements were recorded at 1 nm intervals from 495 nm to 675 nm while exciting the VoltageFluors with 485 nm light. Excitation measurements were recorded by measuring the emission of each VoltageFluor at 570 nm while the excitation light was varied from 300 nm to 550 nm. 2 nm slit widths were used for each measurement. Each absorbance, emission, and excitation trace was normalized to the maximum value of absorbance, emission, or excitation respectively.

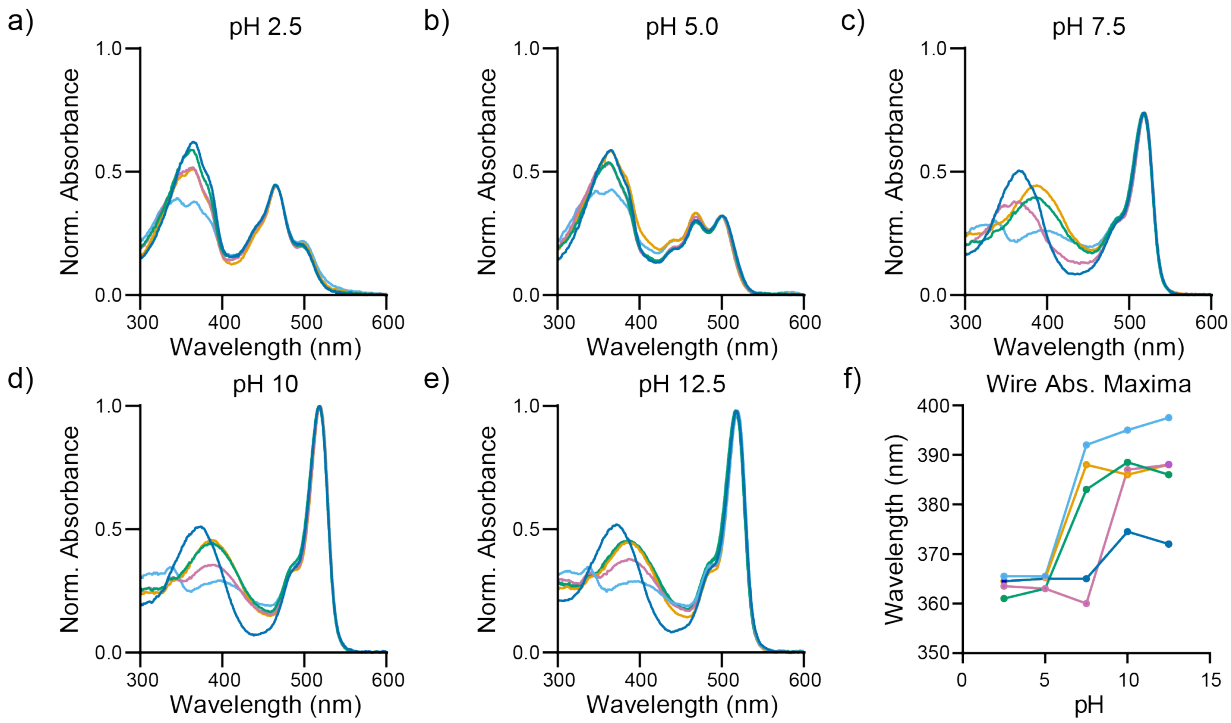

Figure 4.3. Full spectra for pH titrations.
Absorbance spectra for JuloVF (light blue), IndoVF (orange), ^{i}PrVF (pink), VF2.1.Cl (green), and NN26VF (dark blue) in buffered solutions with defined pH. All buffer solutions contain 0.1% w/v SDS to help solubilize the VoltageFluors. The VoltageFluors were diluted from DMSO stocks (500 µM-1 mM) to 500 nM in the following solutions. a) Absorbance spectra in 10 mM phosphate buffer which was adjusted to pH 2.5 with HCl/NaOH and adjusted to 56 mOsm with NaCl. b) Absorbance spectra in 10 mM acetate buffer which was adjusted to pH 5.0 with HCl/NaOH and adjusted to 56 mOsm with NaCl. c) Absorbance spectra in 10 mM phosphate buffer which was adjusted to pH 7.5 with HCl/NaOH and adjusted to 56 mOsm with NaCl. d) Absorbance spectra in 10 mM carbonate buffer which was adjusted to pH 10.0 with HCl/NaOH and adjusted to 56 mOsm with NaCl. e) Absorbance spectra in 10 mM KCl/NaOH buffer which was adjusted to pH 12.5 with HCl/NaOH and adjusted to 56 mOsm with NaCl. f) Plot of the wavelength of maximum absorbance for the wire peak of each VoltageFluor versus the pH of the solution. Absorbance measurements were recorded at 0.5 nm intervals from 300 nm to 600 nm. 2 nm slit widths were used for each measurement. The absorbance traces were first normalized to their respective absorbance values at 519 nm (pH 7.5, 10.0, and 12.5), 500 nm (pH 5.0), or 470 nm (pH 2.5). The absorbance of chloro-fluorescein varies as a function of pH and these wavelengths are the absorbance maxima for the chloro-fluorescein peaks at the respective pH values. Finally, the absorbance traces were multiplied by the ratio of the average raw absorbance values at the chloro-fluorescein peak for a given pH to the average raw absorbance values at 519 nm for the pH 10 traces. The pH 10 traces had the highest raw absorbance values at 519 nm.

Next, we measured the emission, quantum yield (Φ_{fl}), and fluorescence lifetime (τ_{fl}) of our VoltageFluor series. We hypothesized that VoltageFluors containing aniline groups with more sp^2 character would experience more PeT and display reduced Φ_{fl} and τ_{fl}, whereas VoltageFluors containing aniline groups with less sp^2 character would experience less PeT and display higher Φ_{fl} and τ_{fl}. We observed consistent shapes of the emission spectra from the shared dichlorofluorescein chromophore, but there were clear differences in the Φ_{fl} and τ_{fl} (**Figure 4.1b, Figure 4.4**). VF2.0.Cl had the highest measured quantum yield in Ethanol-KOH, followed by NN26VF, ^{i}PrVF, IndoVF, JuloVF, and VF2.1.Cl respectively (**Table 4.1**). With the exception of VF2.1.Cl, this decreasing trend in quantum yield matched our hypothesis regarding the sp^2 character of the aniline group.

We speculated that some of the differences between observed and hypothesized VF properties may be the result of solvent effects. To better mimic the lipid environment of the plasma membrane, we investigated τ_{fl} in vesicles of 1-palmitoyl-2-oleoyl-glycero-3-phosphocholine 16:0-18:1 PC (POPC) (**Table 4.1**, **Figure 4.1c**). The τ_{fl} trend in POPC matched more closely with our expectations, with VF2.1.Cl displaying an intermediate τ_{fl} similar to that of ^{i}PrVF. The lifetime of all aniline-containing VFs was longer in POPC, likely attributable to the effects of solvent dielectric constant on electron transfer rate.[17] Curiously, only VF2.1.Cl deviated from the τ_{fl} trend observed in Ethanol-KOH, suggesting that the dimethyl aniline has some additional mode of solvent dependence that is inaccessible to the other molecules. Minimal, if any, concentration dependence was seen for τ_{fl} in both Ethanol-KOH and POPC, suggesting that concentration quenching is not responsible for these trends (**Figure 4.4**).

Changes to the degree of electronic coupling between the wire and the aniline lone pair should be visible via ^{13}C NMR, with more electron dense molecular wires appearing upfield. Previous work found that the carbon *para* to the nitrogen displayed the strongest and clearest trends.[18] We analyzed the ^{13}C NMR chemical shifts of the benzaldehyde precursors to simplify identification of individual carbons in the spectrum (**Figure 4.5**). We observed a trend generally consistent with the expected aniline conformation; some deviations may be the result of inductive effects of methyl substitution on the benzene ring.

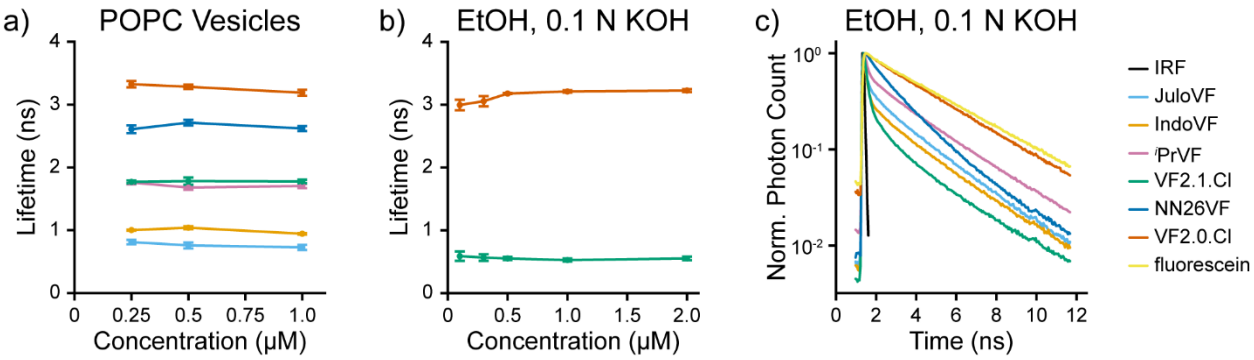

Figure 4.4. Concentration dependence of VoltageFluor fluorescence lifetimes in vesicles and in basic ethanol.
Fluorescence lifetime data for VoltageFluors in POPC vesicles and in ethanol with 0.1 N KOH (EtOH-KOH). In all cases, 500 nM was selected as the optimal working concentration. The fluorescence lifetime of VF2.0.Cl was modeled as a sum of two exponential components; all other probes were modeled with three exponential components. a) Concentration dependence of VF

fluorescence lifetime in POPC vesicles. Data were tested for homoscedasticity (Levene's test on the median, $p>0.05$ for 5/6 probes, $p>0.01$ for ^{i}PrVF). Differences between concentrations for each probe were evaluated with Fisher's one-way ANOVA. No significant differences were found between groups for 5 of the 6 probes ($p>0.05$). For IndoVF, significant differences were observed between groups ($F(2,24)=9.00$, $p<0.01$). Tukey-Kramer post hoc tests revealed significant differences between 500 nM IndoVF and 1µM IndoVF ($p<0.05$), as well as between 250 nM IndoVF and 1 µM IndoVF ($p<0.001$). b) Concentration dependence of the fluorescence lifetime of VF2.0.Cl and VF2.1.Cl in EtOH-KOH. The data for each probe were tested for homoscedasticity (Levene's test on the median, $p>0.05$ in both cases). Differences between concentrations were assessed via Fisher's one-way ANOVA. No significant differences were observed between VF2.1.Cl concentrations ($F(4,32)=0.254$, $p=0.91$). Significant differences were observed between VF2.0.Cl concentrations ($F(4,20)=3.61$, $p=0.023$). Tukey-Kramer post hoc tests revealed significant differences between 100 nM and 1 µM VF2.0.Cl and between 100 nM and 2 µM VF2.0.Cl ($p<0.05$); all other comparisons did not yield significant differences ($p>0.05$). c) Representative time-resolved fluorescence intensity of the library of VFs at 500 nM VF in EtOH-KOH. Color coding for VF identity is consistent throughout all plots. IRF= instrument response function. Data in (a) and (b) represent are displayed as the mean ± SEM of data taken on 3 or 4 independent samples, each with 1-3 technical replicates.

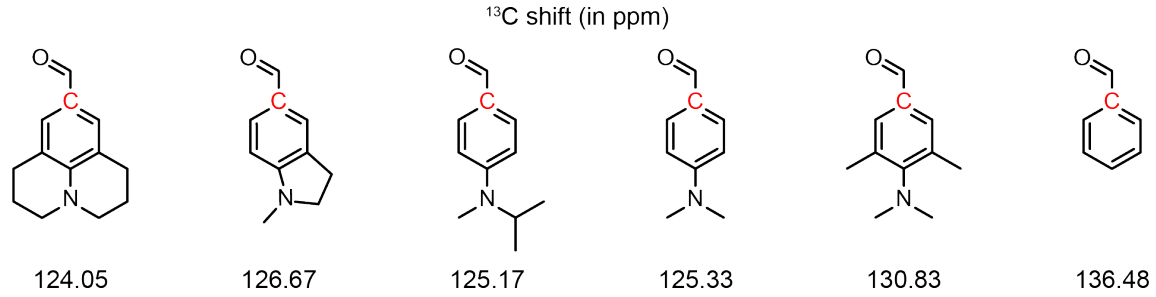

Figure 4.5. ^{13}C NMR shifts of the para-carbon in aniline series precursors.
^{13}C NMR shifts (in ppm) for the carbons labeled above in red. All spectra were taken in $CDCl_3$ (chloroform peak referenced to 77.16 ppm). Full spectra for each compound are located in **13. NMR Spectra**. In order from left to right: Compound **1**, 1-methylindoline-5-carbaldehyde, Compound **7**, 4-(dimethylamino)benzaldehyde, Compound **13**, and benzaldehyde.

Aniline Effects on Sensitivity in HEK293T

Having performed initial characterization of the VoltageFluor series of aniline donors *in vitro*, we next examined performance as a voltage sensor in cells (**Figure 4.6**). To measure voltage sensitivity of these indicators, we turned to whole-cell voltage clamp in HEK293T cells incubated in dye solution. By recording the changes in fluorescence intensity with epifluorescence microscopy when voltage steps from 100 to -100 mV are applied (in 20 mV increments), we observed a dramatic difference in voltage sensitivity based on the identity of the aniline donor. As previously reported, VF2.1.Cl has modest sensitivity to V_{mem} changes (23-26% per 100 mV, **Figure 4.6p, Table 4.1**) and VF2.0.Cl, lacking an aniline donor, possesses little to no sensitivity (-0.2% per 100 mV, **Figure 4.6r, Table 4.1**).

When methyl groups are added *ortho* to the aniline nitrogen (NN26VF, **20**), voltage sensitivity drops to 2.2% per 100 mV (**Figure 4.6q, Table 4.1)**, an order of magnitude lower than VF2.1.Cl. This is likely attributable to steric inhibition of resonance, which decreases PeT by uncoupling the aniline lone pair and the molecular wire. Interestingly, ^{i}PrVF had a larger response to V_{mem} changes (34% per 100 mV, **Figure 4.6o, Table 4.1**) than VF2.1.Cl. This suggests that the added bulk of the isopropyl group had not decreased coupling between the aniline lone pair and the molecular wire. It is possible that a steric effect between the aromatic ring and isopropyl substituent inhibits rotation of the Ar-N bond, maintaining planarity between then aniline and molecular wire.

The indicators with ring-fused anilines also had larger fluorescence responses to voltage changes as expected; IndoVF was the most sensitive at 37% per 100 mV change and JuloVF averaged 34% (**Figure 4.6m-n, Table 4.1)**. We observed a high degree of variability in the sensitivity of JuloVF (**Table 4.1**), which might be attributed to its overall dim signal in cells. For both indicators, the aniline lone pair is "locked" in a conformation that is in plane with the molecular wire, which would account for an increase in PeT and greater sensitivity to V_{mem}.

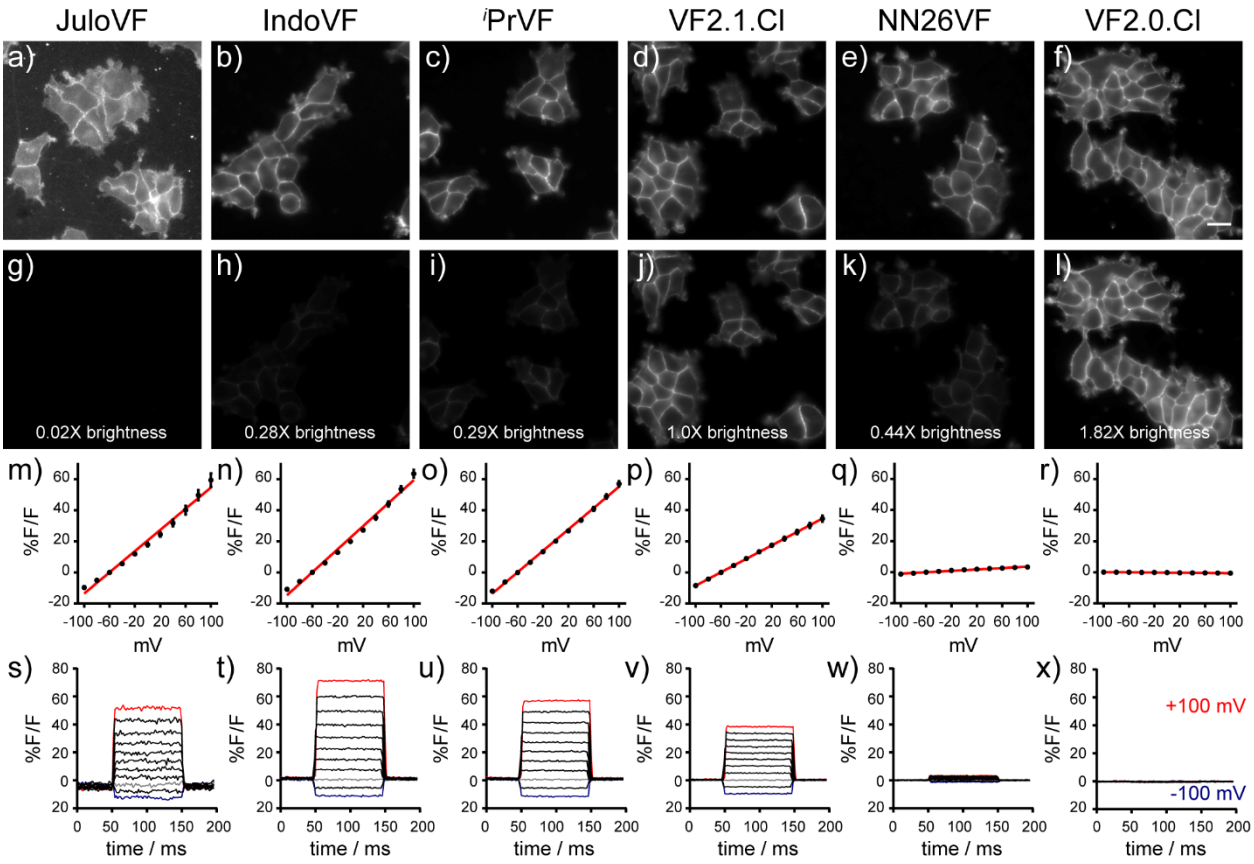

Figure 4.6. HEK293T intensity patching and relative brightness.
Voltage sensitivity and relative brightness comparison of VoltageFluor indicators in HEK293T cells with intensity-based imaging. Relative brightness was compared at a working concentration of 300 nM for all dyes. All brightness values are relative to VF2.1.Cl (d,j, 1.0X brightness), and were calculated as the difference between cell signal and the surrounding background (signal-background). Scale bar represents 20 µm. Top row (a-f) images are the same as Figure 2a-f, and display membrane localization for each indicator. The second row (g-l) features the same images, but with consistent pixel histograms across each image to illustrate the relative brightness of membrane staining. Linear plots (m-r) of the percent change in fluorescence versus V_{mem} from whole-cell voltage clamp (m, n=8 cells; n, n=4 cells; o, n=4 cells; p, n=8 cells; q, n=3 cells; r, n=5 cells). For whole-cell voltage clamp experiments, cells were loaded at optimized concentration for each indicator (JuloVF, 500 nM; IndoVF, 300 nM; ^{i}PrVF, 300 nM; VF2.1.Cl, 100 nM; NN26VF, 300 nM; VF2.0.Cl, 100 nM). Representative concatenated traces from a single patched cell (s-x) show the percent change in fluorescence over time as the holding potential is changed from +100 mV (red) to -100 mV (blue) in 20 mV increments.

Fluorescence Lifetime Reports Absolute Brightness and Sensitivity

We used fluorescence lifetime to investigate how these relative sensitivities (%ΔF/F) translated into absolute sensitivity of τ_{fl} to V_{mem}. %ΔF/F depends on both the starting fluorescence intensity of the probe and the change in fluorescence with a 100 mV V_{mem} change. Therefore, very dim probes with small V_{mem}-dependent fluorescence changes can appear highly sensitive in %ΔF/F. Fluorescence lifetime, on the other hand, allows for a more direct measure of the change in fluorescence with V_{mem}, as in does not depend on the initial fluorescence intensity of the sensor. By measuring the baseline τ_{fl}, as well as the V_{mem} dependent τ_{fl} change, we can determine differences in PeT in cells without confounding effects from probe brightness or loading.

We initially assessed the dependence of τ_{fl} on loading of each VF in HEK293T cells, testing probe concentrations ranging from 100 nM to 1 μM (**Figure 4.7**). As seen previously with VF2.1.Cl and VF2.0.Cl,[19] we observed concentration quenching[20] at high dye loading for all VFs, with concentration-independent τ_{fl} at lower dye loading. For IndoVF, ^{i}PrVF, and NN26VF, we were able to select working concentrations that avoided concentration quenching but retained sufficient signal for fluorescence lifetime imaging (300 nM). Interestingly, with these three dyes, we were able to load more probe before we observed concentration quenching than we were with either VF2.0.Cl or VF2.1.Cl.[19] One explanation for this difference is that, at the same nominal concentration of these new VFs, loading into the membrane is less efficient. Therefore, 300 nM of iPrVF may actually reflect a similar number of VF molecules in the membrane as 100 nM VF2.1.Cl. Nevertheless, concentration of VF molecules in a cell membrane is challenging to measure directly, so we cannot rule out the possibility that the propensity for concentration quenching differs across our library of VFs. Because JuloVF is rather dim in cells, we were not able to decrease loading below 500 nM. As a result, fluorescence lifetime data for JuloVF may contain contributions from autofluorescence and concentration quenching.

Using these optimized loading concentrations, we measured the dependence of fluorescence lifetime on V_{mem} in HEK293T cells with simultaneous fluorescence lifetime imaging and whole cell patch clamp electrophysiology (**Figure 4.8-4.14**). Our lifetime-V_{mem} calibrations for VF2.1.Cl and VF2.0.Cl are in good agreement with previous work (**Table 41**).[19] For processing of these τ_{fl}-V_{mem} calibrations, we selected exponential models for new VFs based on minimization of reduced chi squared without overfitting (**Methods, Figures 4.15-4.17**). For VF2.1.Cl, we explore the effects of using 1, 2, or 3 exponential components in detail (**Figures 4.15, 4.16**). Linear τ_{fl}-V_{mem} relationships with similar slopes were observed regardless of the fit model selected, although the 0 mV lifetimes differed considerably. Systematic errors in describing the time-resolved fluorescence decay in time were observed for a monoexponential model for VF2.1.Cl (**Figure 4.16**). These systematic errors were removed upon progression to a biexponential model; three exponential models resulted in increased variance between pixels (**Figure 4.15d-f**) without notable improvements in the residuals or reduced chi squared. A similar analysis was performed for all six VFs. Shorter lifetime VFs (e.g. JuloVF, IndoVF), could not be well described with fewer than 3 exponential decay components, but use of a 3 component decay model for the other probes resulted in overfitting.

All of the new aniline modified VFs show V_{mem} sensitive fluorescence lifetimes, with sensitivities (slope of lifetime-V_{mem} line of best fit) ranging from 0.50 to 2.97 ps/mV and 0 mV lifetimes ranging from 0.31 to 3.32 ns (**Table 4.1**). Good agreement was observed between the %ΔF/F and

%$\Delta\tau/\tau$ per 100 mV (**Figure 4.18**), which is consistent with a PeT-based V_{mem} sensing trigger and suggests that our selected fit models described the underlying data adequately. The 0 mV lifetimes (y-intercepts, in ns) observed were generally consistent with the expected degree of electronic coupling between the aniline lone pair and the molecular wire. JuloVF displayed the shortest fluorescence lifetime at 0 mV (0.31 ± 0.01 ns). NN26VF displayed the longest fluorescence lifetime (3.32 ± 0.01 ns), as expected with the steric inhibition of resonance between the aniline lone pair and the wire. IndoVF was most similar to JuloVF, with its slightly longer lifetime perhaps attributable to its increased flexibility. ^{i}PrVF exhibited a slightly shorter τ_{fl} than VF2.1.Cl, suggesting that it experiences increased PeT, either via increased substitution at the aniline or increasing planarity of the aniline resulting from steric inhibition of rotation.

Curiously, JuloVF, IndoVF, and ^{i}PrVF all displayed shorter τ_{fl} than VF2.1.Cl, implying that these molecular wires produce faster rates of PeT than the dimethyl aniline containing wire in VF2.1.Cl. JuloVF, IndoVF, and ^{i}PrVF are all more substituted at the aniline and bottom ring of the molecular wire than VF2.1.Cl. This methyl substitution could slightly increase electron density on the wire, but the magnitude of the lifetime change seems hard to attribute to an inductive effect. Another possible explanation is that the dimethyl aniline in VF2.1.Cl is rotated partially out of the plane of the wire in the membrane, but the fused rings or steric bulk of JuloVF, IndoVF, and ^{i}PrVF prevents them from accessing this conformation. The difference in VF2.1.Cl τ_{fl} in POPC vesicles and Ethanol-KOH adds further support to the idea of a solvent-dependent conformational change in the C-C-N-C dihedral angle, although additional studies are required to validate this.

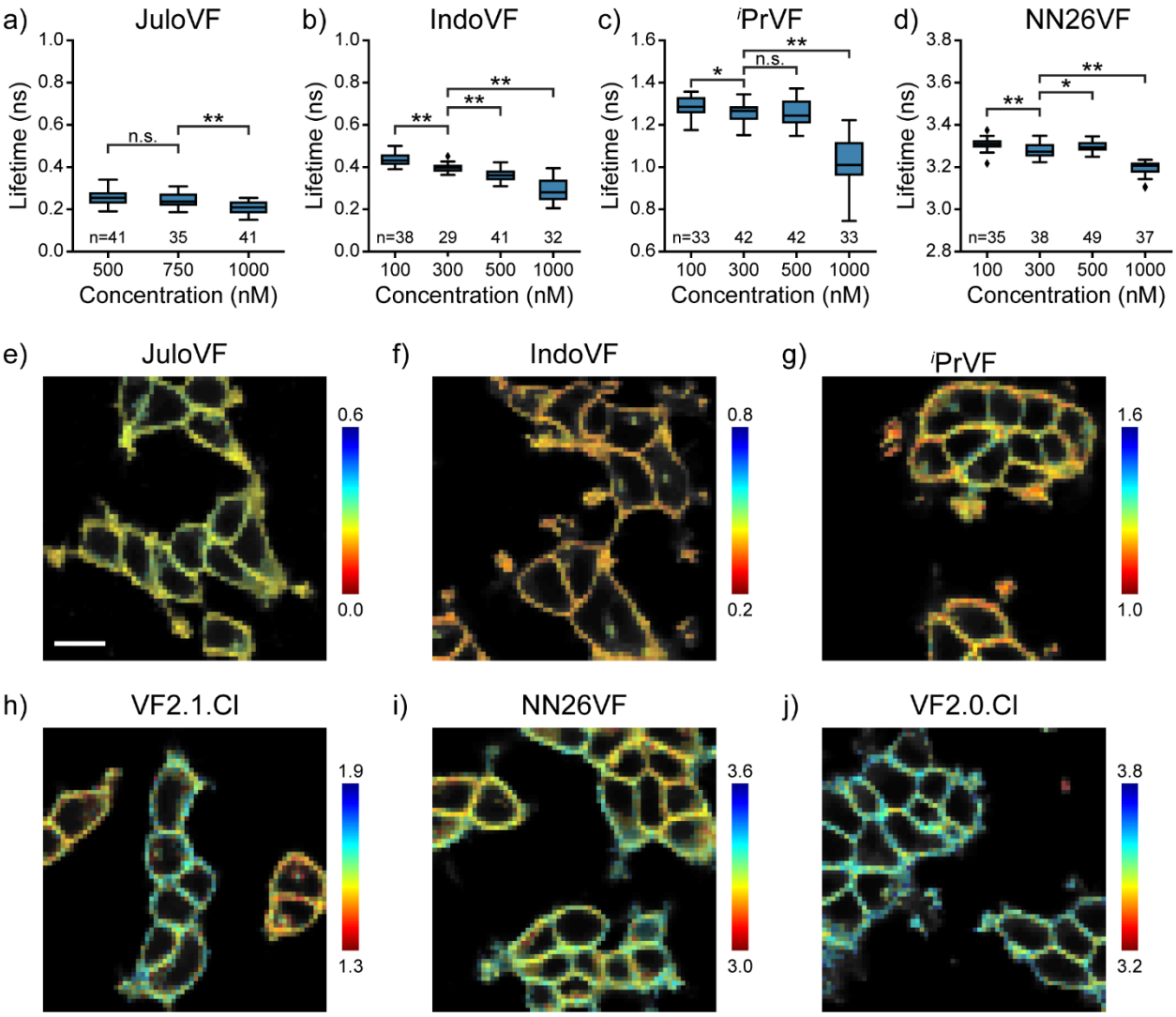

Figure 4.7. Concentration dependence of τ_n for four new VFs in HEK293T cells.
a-d) Box plots showing the effect of JuloVF, IndoVF, ^{i}PrVF, or NN26VF concentration on fluorescence lifetime in HEK293T cells at rest in imaging buffer. Diamonds represent datapoints more than 1.5 times the interquartile range past an edge of the box. Data were tested for homoscedasticity (Levene's test on the median, many with $p<0.05$). The statistical significance of differences between concentrations were evaluated with Welch's ANOVA; in all cases resulting in $p<0.05$. Asterisks indicate the significance level of Games-Howell post hoc tests (n.s. $p>0.05$, * $p<0.05$, ** $p<0.01$, *** $p<0.001$). For clarity, only the significance level of post hoc comparisons involving the concentration used in this study is shown (300 nM for all probes except JuloVF, where 500 nM was used). e-j) Representative fluorescence lifetime images overlaid on the fluorescence intensity for all six VFs used in this study. Lifetimes are scaled across the same range for electrophysiological studies (**Fig. 4.8-4.14**). Scale bar represents 20 µm.

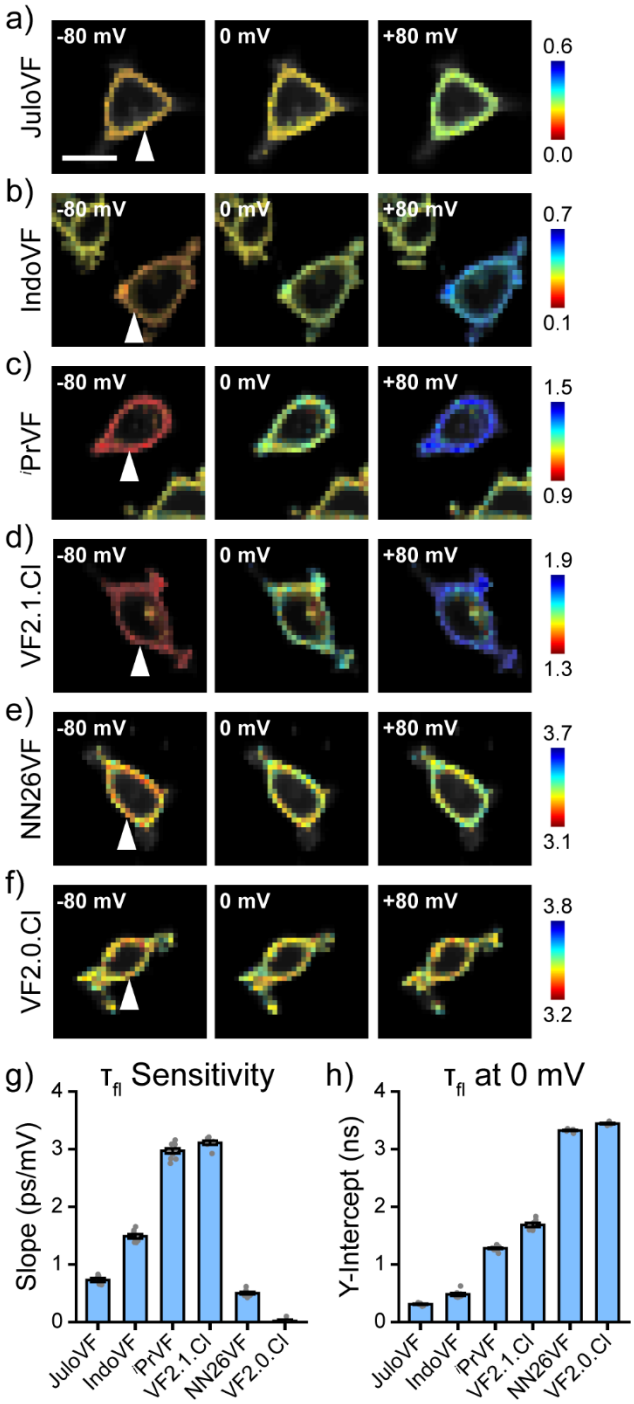

Figure 4.8. Fluorescence lifetime captures absolute sensitivity of VFs.
a-f) Lifetime intensity overlay images for HEK293T cells at different V_{mem} stained with JuloVF, IndoVF, ^{i}PrVF, VF2.1.Cl, NN26VF, and VF2.0.Cl, respectively. V_{mem} was held at the indicated value with whole cell voltage clamp electrophysiology. Lifetimes are scaled across the same lifetime range (0.6 ns) with different start and ending values. White arrow indicates voltage-clamped cell. Scale bar represents 20 μm. g) Slope of the line of best fit for the lifetime-V_{mem} calibration for the aniline modified VF library. Gray points represent measurements from

individual cells. h) Y-intercept (0 mV lifetime) from the same lines of best fit as in g. Data are shown as mean ± SEM for the following number of patched cells: JuloVF 6, IndoVF 8, ^{i}PrVF 10, VF2.1.Cl 7, NN26VF 8, VF2.0.Cl 5.

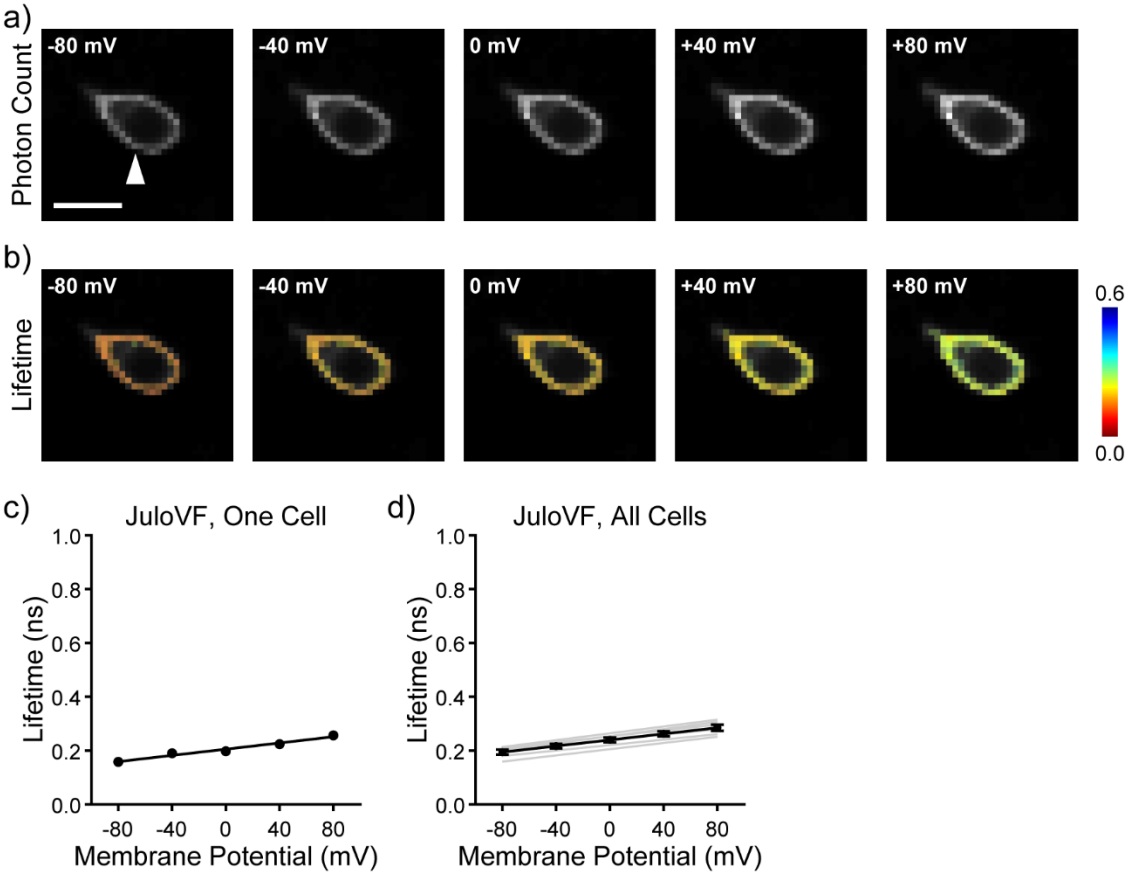

Figure 4.9. V_{mem} sensitivity of the fluorescence lifetime of JuloVF.
This is a more detailed view of data contained within **Figure 4.8**. a) Photon count images of JuloVF in a HEK293T cell held at the indicated V_{mem} by whole cell patch clamp electrophysiology. The white arrow indicates the patch pipette; scale bar represents 20 µm. b) Lifetime-intensity overlay images of JuloVF as in (a). The time-resolved fluorescence decay for JuloVF was modeled as a sum of three exponential terms; the weighted average is shown here. Lifetime scale is in ns. c) Quantification of average lifetime at the plasma membrane for the individual cell shown in (a-b). The line of best fit for τ_{fl} vs. V_{mem} is shown in black. d) The average τ_{fl}-V_{mem} relationship for JuloVF (black line), as well as lines of best fit for each individual patched cell (gray, n=6 cells).

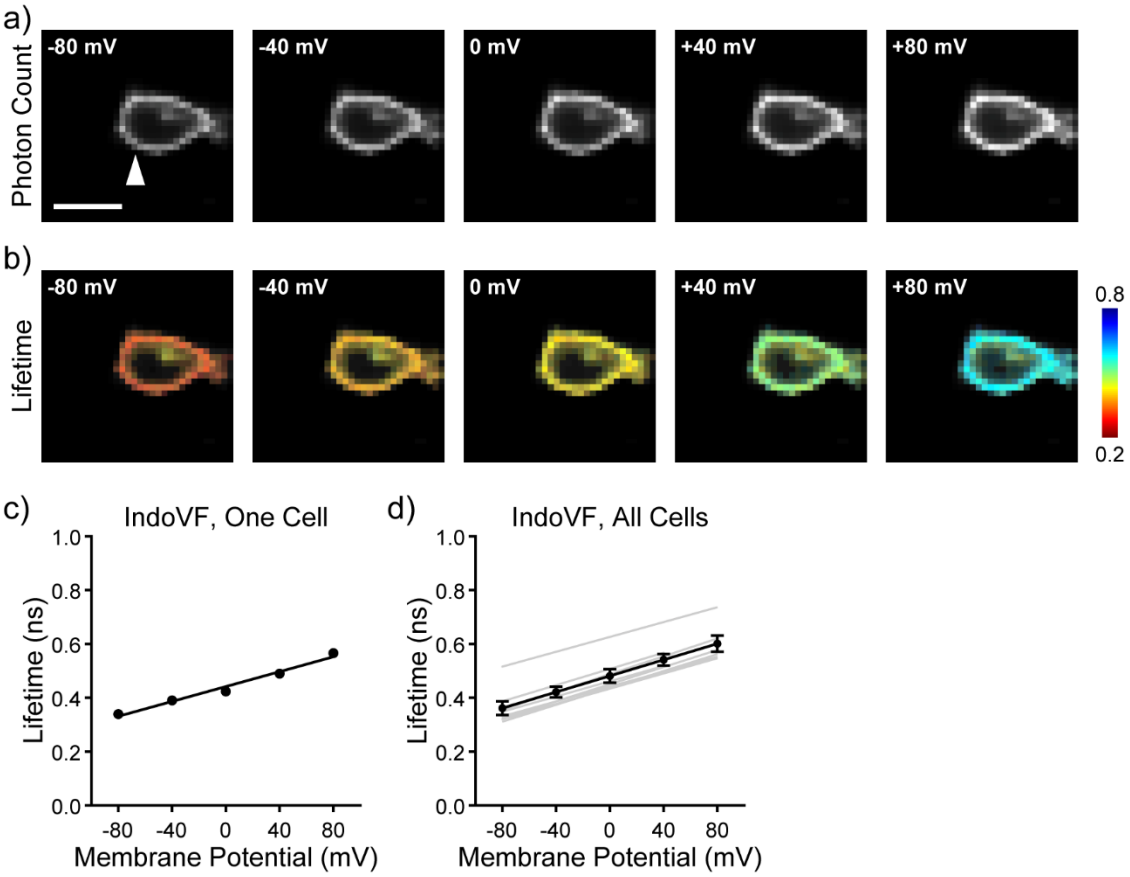

Figure 4.10. V_{mem} sensitivity of the fluorescence lifetime of IndoVF.
This is a more detailed view of data contained within **Figure 4.8**. a) Photon count images of IndoVF in a HEK293T cell held at the indicated V_{mem} by whole cell patch clamp electrophysiology. The white arrow indicates the patch pipette; scale bar represents 20 µm. b) Lifetime-intensity overlay images of IndoVF as in (a). The time-resolved fluorescence decay for IndoVF was modeled as a sum of three exponential terms; the weighted average is shown here. Lifetime scale is in ns. c) Quantification of average lifetime at the plasma membrane for the individual cell shown in (a-b). The line of best fit for τ_{fl} vs. V_{mem} is shown in black. d) The average τ_{fl}-V_{mem} relationship for IndoVF (black line), as well as lines of best fit for each individual patched cell (gray, n=8 cells).

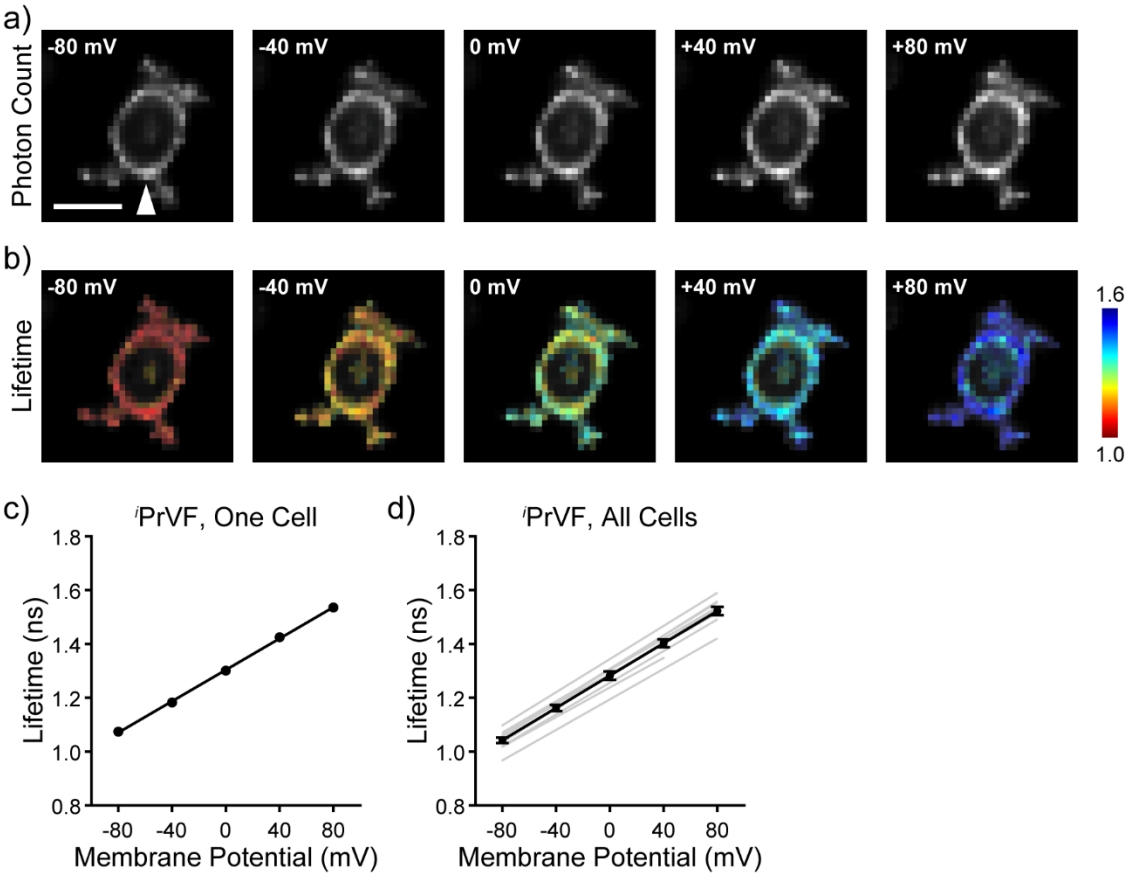

Figure 4.11. V_{mem} sensitivity of the fluorescence lifetime of ^{i}PrVF.
This is a more detailed view of data contained within **Figure 4.8**. a) Photon count images of ^{i}PrVF in a HEK293T cell held at the indicated V_{mem} by whole cell patch clamp electrophysiology. The white arrow indicates the patch pipette; scale bar represents 20 µm. b) Lifetime-intensity overlay images of ^{i}PrVF as in (a). The time-resolved fluorescence decay for ^{i}PrVF was modeled as a sum of two exponential terms; the weighted average is shown here. Lifetime scale is in ns. c) Quantification of average lifetime at the plasma membrane for the individual cell shown in (a-b). The line of best fit for τ_{fl} vs. V_{mem} is shown in black. d) The average τ_{fl}-V_{mem} relationship for ^{i}PrVF (black line), as well as lines of best fit for each individual patched cell (gray, n=10 cells).

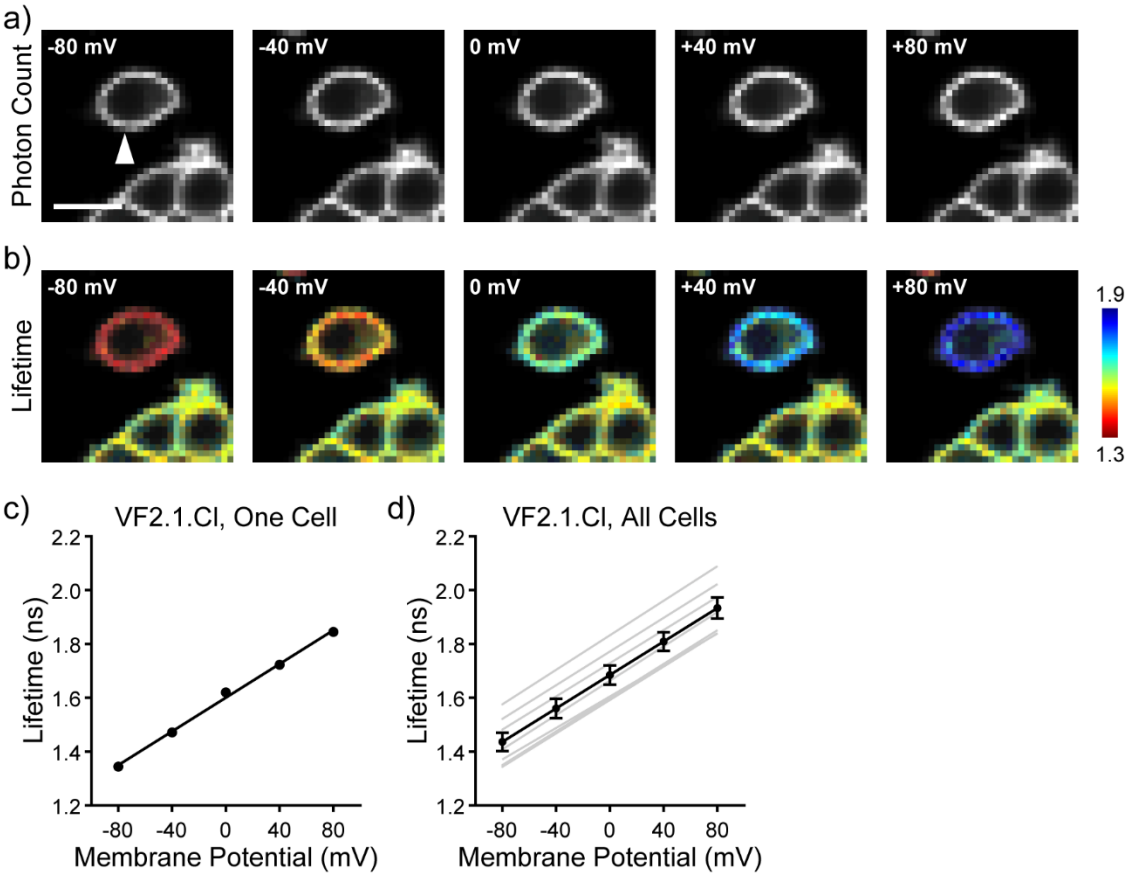

Figure 4.12. V_{mem} sensitivity of the fluorescence lifetime of VF2.1.Cl.
This is a more detailed view of data contained within **Figure 4.8**. The relationship between fluorescence lifetime and V_{mem} for VF2.1.Cl was previously reported by our lab (**Chapter 2**);[19] we repeated the experiment independently here for maximum comparability with the rest of the VF series presented here. These results are in good agreement with our previous work. a) Photon count images of VF2.1.Cl in a HEK293T cell held at the indicated V_{mem} by whole cell patch clamp electrophysiology. The white arrow indicates the patch pipette; scale bar represents 20 µm. b) Lifetime-intensity overlay images of VF2.1.Cl as in (a). The time-resolved fluorescence decay for ^{i}PrVF was modeled as a sum of two exponential terms; the weighted average is shown here. Lifetime scale is in ns. c) Quantification of average lifetime at the plasma membrane for the individual cell shown in (a-b). The line of best fit for τ_{fl} vs. V_{mem} is shown in black. d) The average τ_{fl}-V_{mem} relationship for VF2.1.Cl (black line), as well as lines of best fit for each individual patched cell (gray, n=7 cells).

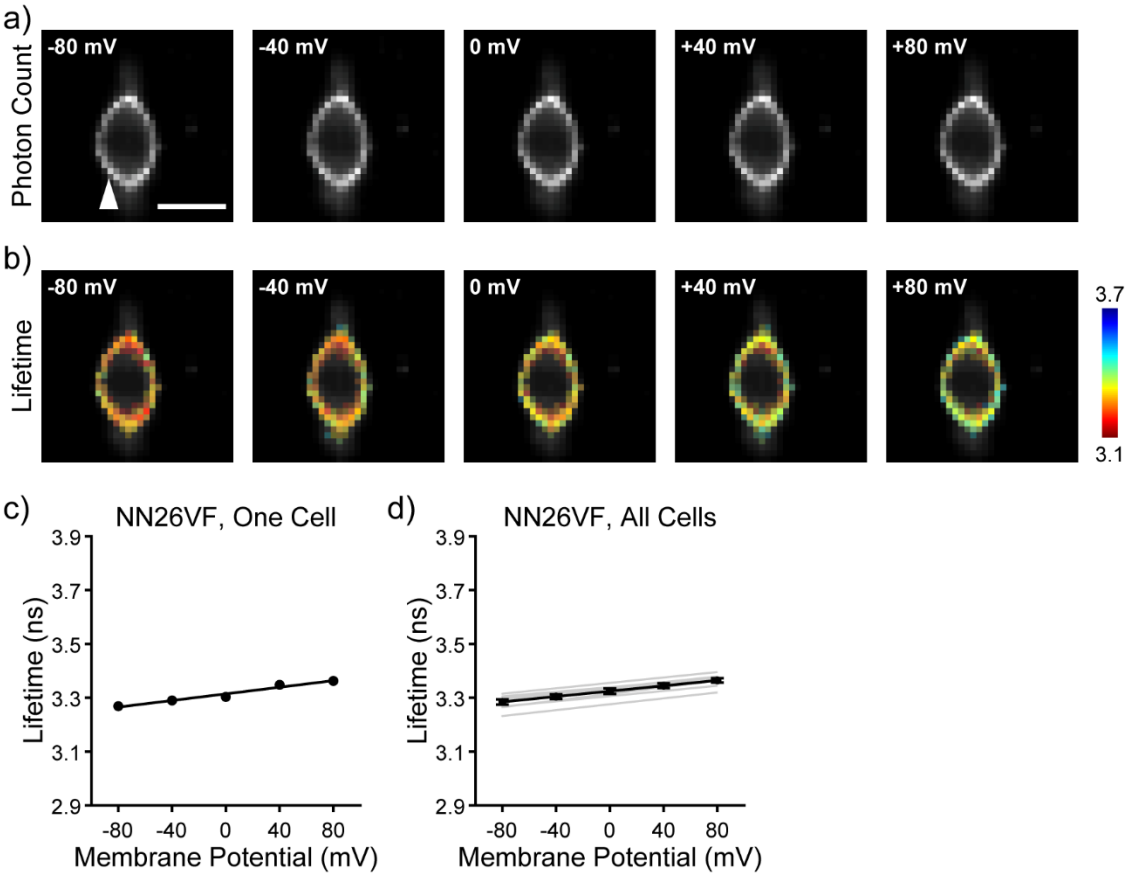

Figure 4.13. V_{mem} sensitivity of the fluorescence lifetime of NN26VF.
This is a more detailed view of data contained within **Figure 4.8**. a) Photon count images of NN26VF in a HEK293T cell held at the indicated V_{mem} by whole cell patch clamp electrophysiology. The white arrow indicates the patch pipette; scale bar represents 20 µm. b) Lifetime-intensity overlay images of NN26VF as in (a). The time-resolved fluorescence decay for NN26VF was described by a single exponential decay term. Lifetime scale is in ns. c) Quantification of the NN26VF fluorescence lifetime at the plasma membrane for the individual cell shown in (a-b). The line of best fit for τ_{fl} vs. V_{mem} is shown in black. d) The average τ_{fl}-V_{mem} relationship for NN26VF (black line), as well as lines of best fit for each individual patched cell (gray, n=8 cells).

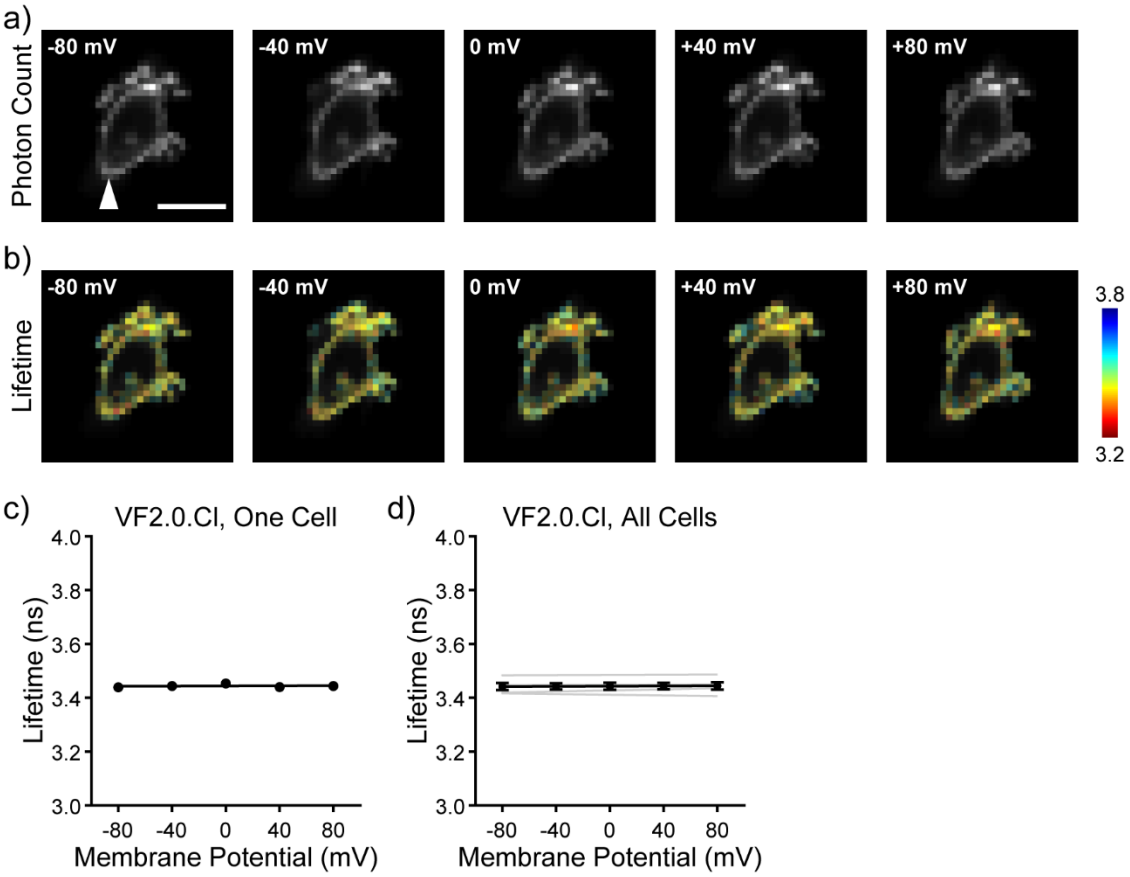

Figure 4.14. The fluorescence lifetime of VF2.0.Cl is not sensitive to V_{mem}.
This is a more detailed view of data contained within **Figure 4.8**. The voltage-insensitivity of the fluorescence lifetime of VF2.0.Cl was previously reported by our lab (**Chapter 2**);[19] we repeated the experiment independently here for maximum comparability with the rest of the VF series presented here. These results are in good agreement with our previous work. a) Photon count images of VF2.0.Cl in HEK293T cells held at the indicated V_{mem} by whole cell patch clamp electrophysiology. The white arrow indicates the patch pipette; scale bar represents 20 µm. b) Lifetime-intensity overlay images of VF2.1.Cl as in (a). The time-resolved fluorescence decay for VF2.0.Cl was modeled with a single exponential term. Lifetime scale is in ns. c) Quantification of average lifetime at the plasma membrane for the individual cell shown in (a-b). The line of best fit for τ_{fl} vs. V_{mem} is shown in black. d) The average τ_{fl}-V_{mem} relationship for VF2.0.Cl (black line), as well as lines of best fit for each individual patched cell (gray, n=7 cells).

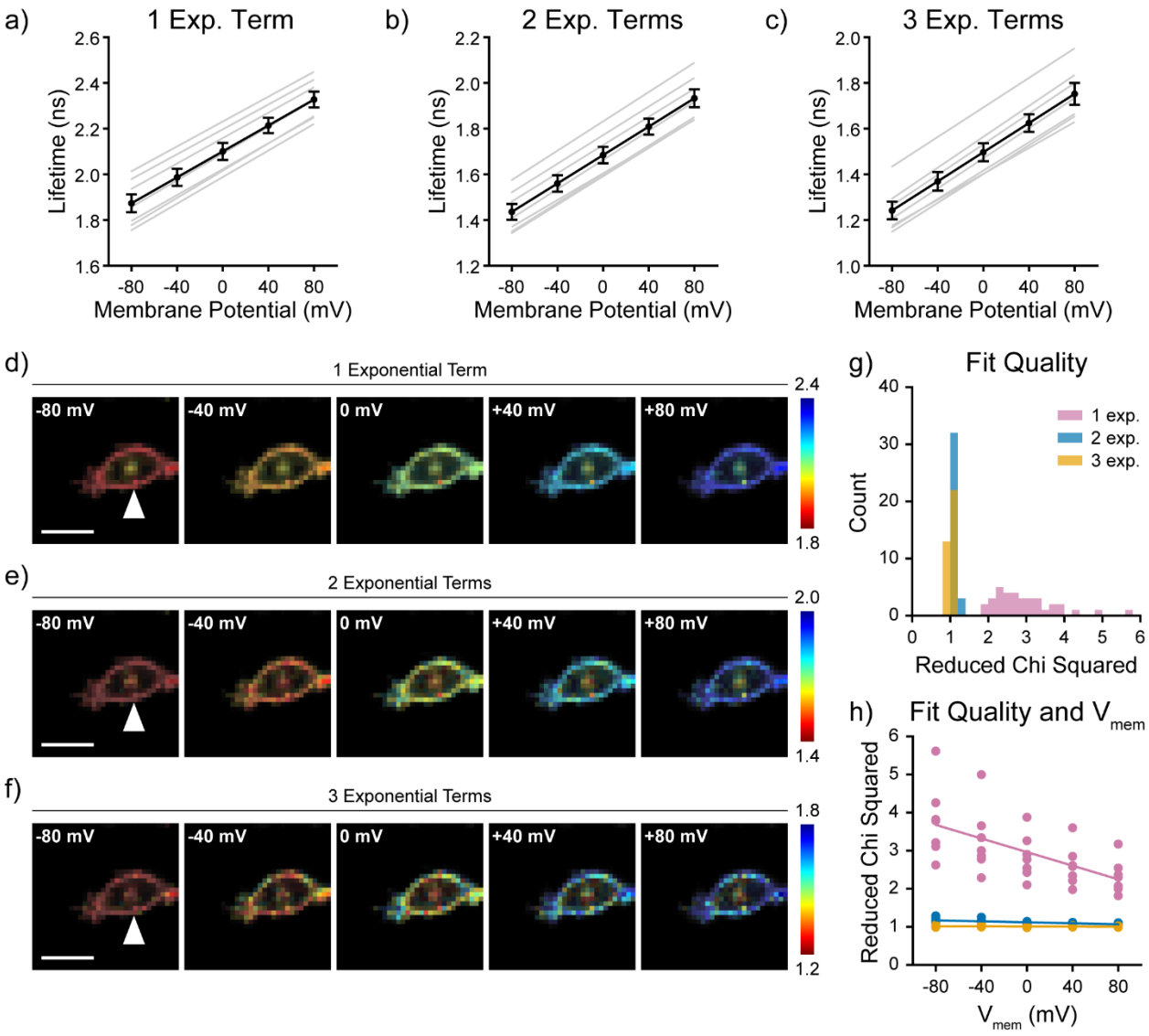

Figure 4.15. Effect of fit model on the value and the V_{mem} sensitivity of VF2.1.Cl fluorescence lifetime.

The relationship between V_{mem} and τ_{fl} of VF2.1.Cl in HEK293T was confirmed by whole cell patch clamp electrophysiology in HEK293T cells. V_{mem} was set with whole cell voltage clamp electrophysiology; the patch electrode is indicated by the white arrow. Previously reported τ_{fl} data for VF2.1.Cl was modeled with two exponential components;[19] here we show in details the process of selecting a satisfactory number of terms in a fluorescence lifetime decay model. a-c) The relationship between τ_{fl} and V_{mem} for VF2.1.Cl in HEK293T when VF2.1Cl τ_{fl} is described by a sum of one, two, or three exponential components (n=7 cells). The overall relationship is preserved, although the 0 mV lifetime shifts considerably across the three models. d-f) Representative images of the fluorescence lifetime of VF2.1.Cl fit pixel-by-pixel in a HEK293T cell. Increased variability between nearby pixels is observed when a third exponential component is added. Scale bar represents 20 µm. g) The quality of the exponential fit, as described by the reduced chi squared. Each value in the histogram is an individual measurement at a particular

V_{mem}; therefore, each patch is represented by 4 or 5 values in the histogram). h) V_{mem} dependence of the fit quality of the exponential fit. Each point represents an individual measurement as in (g); each line represents the line of best fit for χ^2 vs V_{mem}. If a fit model adequately describes the V_{mem} sensitivity of a VoltageFluor, there should be no V_{mem} dependence in χ^2.

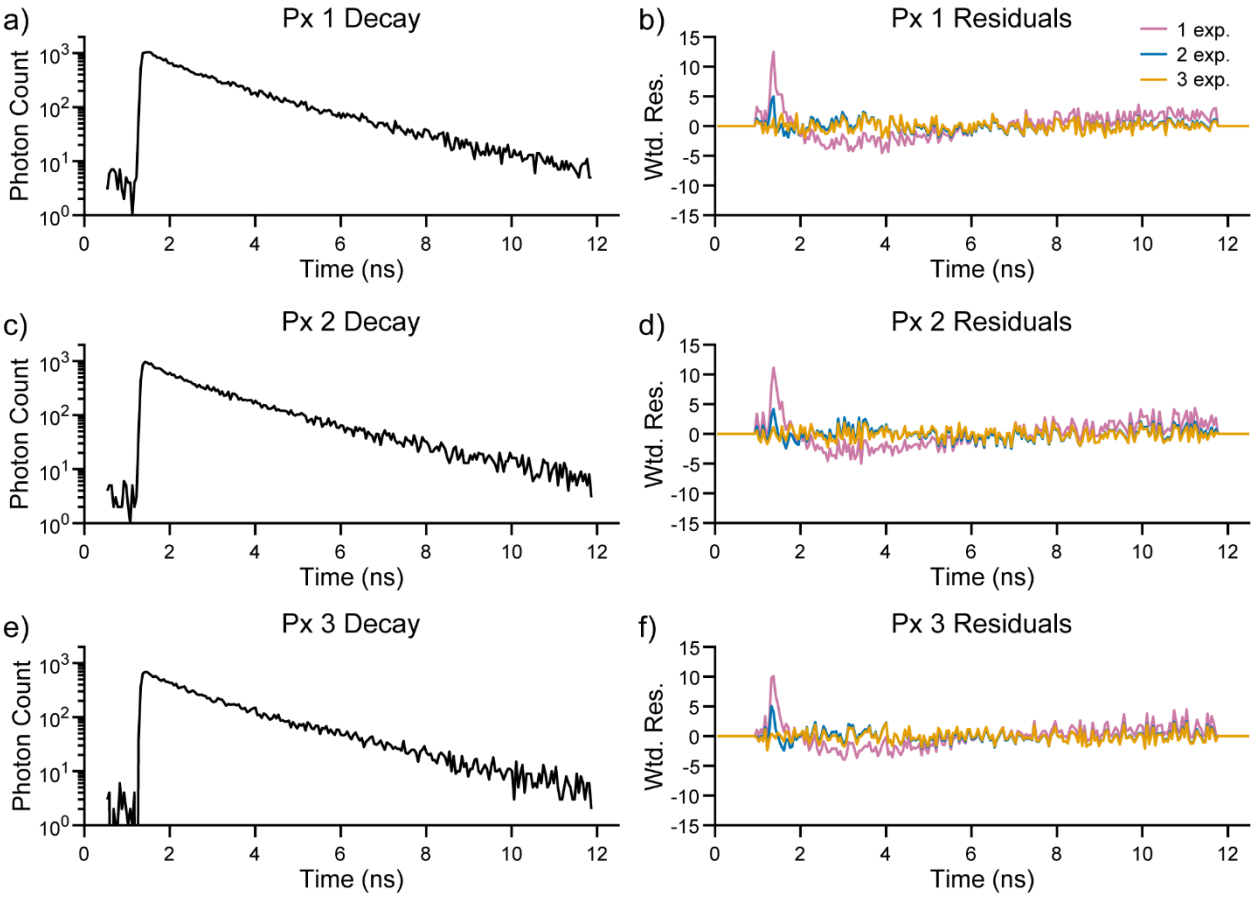

Figure 4.16. Pixel-level fit quality for VF2.1.Cl with 1, 2, or 3 exponential component models. a) Sample time correlated single photon counting decay for a representative single pixel (px) in a FLIM image of 100 nM VF2.1.Cl in HEK293T. b) Weighted residuals when the decay in (a) is modeled with 1, 2, or 3 exponential decay components. c,e) Additional representative decays individual pixels. d,f) Weighted residuals from the decays shown in (c) and (e). All pixels shown were selected from within the membrane region of interest in the -80 mV image from the data in **Figure 4.15d-f** (leftmost image).

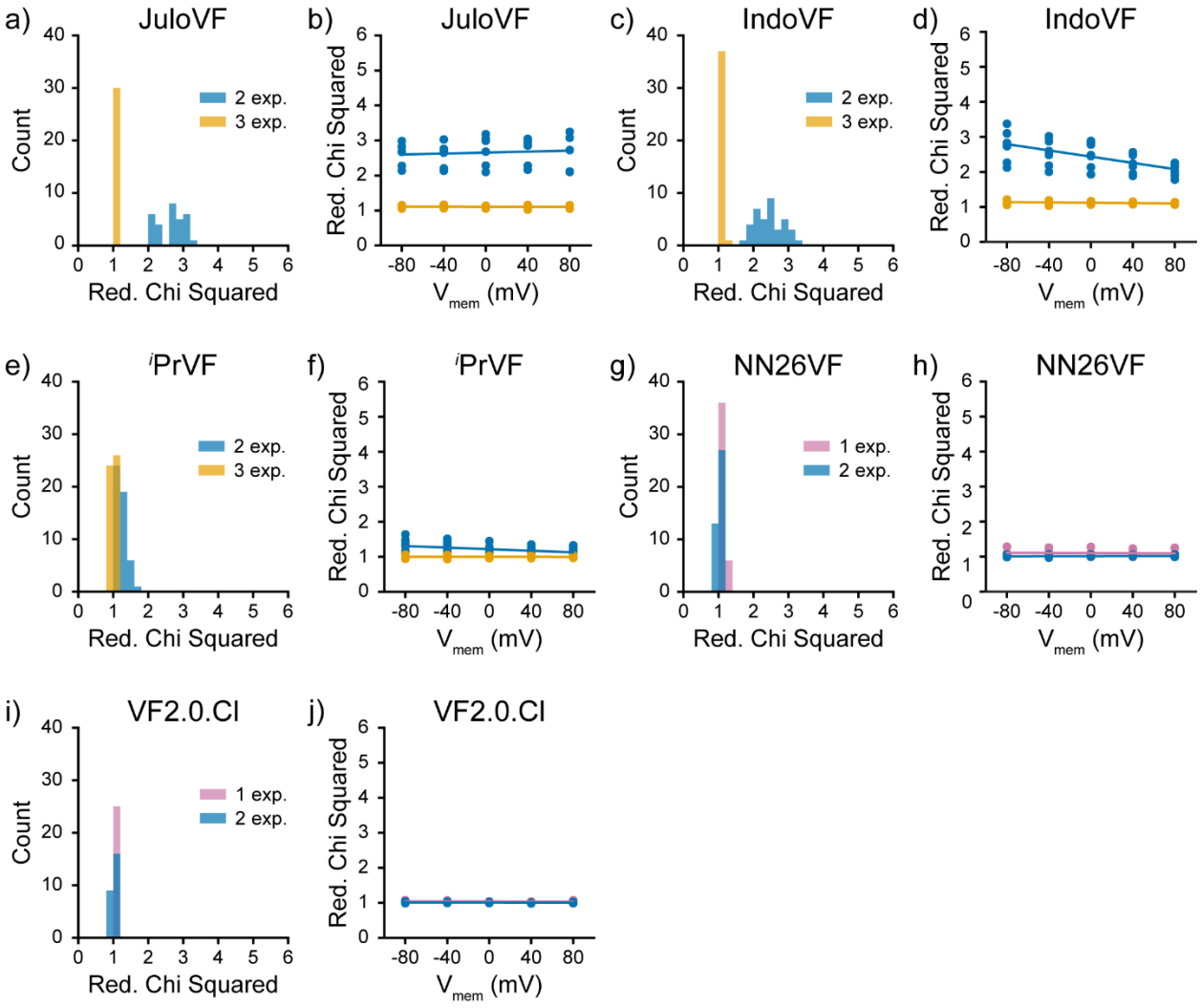

Figure 4.17. Fluorescence lifetime fit model selection for all VF derivatives.
Selection of the appropriate number of exponential terms in the fluorescence lifetime decay model was based on minimization of reduced chi squared χ^2 and avoidance of V_{mem} dependence in χ^2. These data are reproduced in **Fig. 4.8-4.14**. a) Comparison of χ^2 when the time resolved fluorescence decay of JuloVF is modeled as a sum of two or three exponential components b) Relationship between V_{mem} χ^2 for JuloVF. Measurements from individual cells are shown as markers; for closely spaced results, markers may overlap. The line of best fit for χ^2 vs. V_{mem} for each fit model is shown. c-d) Evaluation of χ^2 overall and as it relates to V_{mem} for IndoVF when its fluorescence lifetime is modeled as a sum of two or three exponential terms. e-f) Evaluation of χ^2 overall and as it relates to V_{mem} for ^{i}PrVF when modeled as a sum of two or three exponential terms. g-h) Evaluation of χ^2 overall and as it relates to V_{mem} for NN26VF when modeled as a single exponential decay or as a sum of two exponential terms. i-j) Evaluation of χ^2 overall and as it relates to V_{mem} for VF2.0.Cl when the fluorescence lifetime of VF2.0.Cl is modeled as a single exponential decay or as a sum of two exponential terms. Each measurement on each cell at a given potential is represented individually (i.e. each patch has 4 or 5 values in the histogram, one for each recorded V_{mem}). Sample sizes (number of HEK293T cells patched): JuloVF 6, IndoVF 8, ^{i}PrVF 10, NN26VF 8, VF2.0.Cl 5.

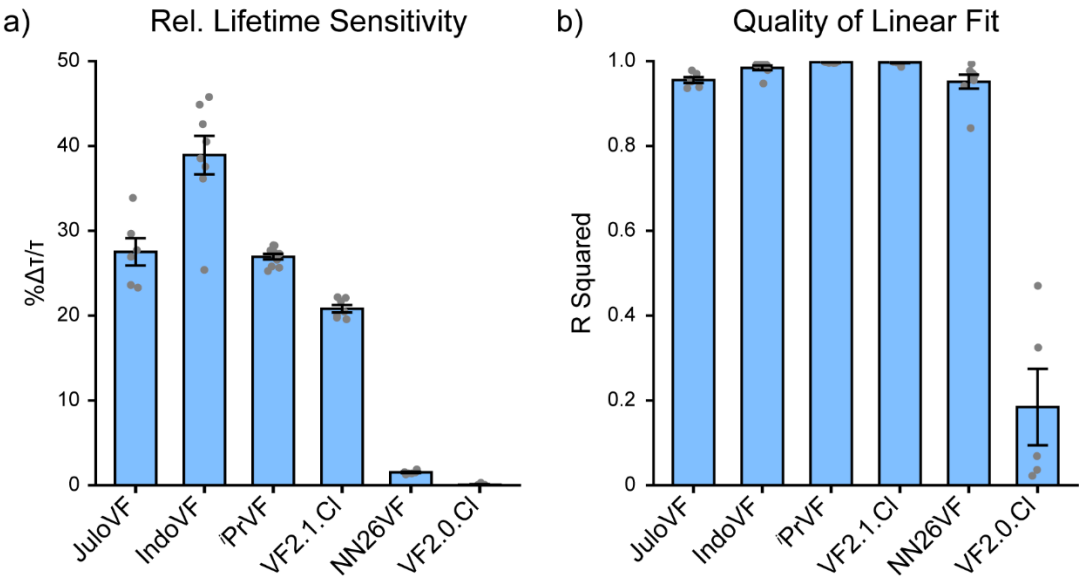

Figure 4.18. Percent change in τ_{fl} and goodness of linear fit for V_{mem}-τ_{fl} calibrations. These data accompany **Figure 4.8**. a) Percent change in τ_{fl} per 100 mV change, relative to the lifetime at -60 mV. b) Quality of the linear fit (as evaluated by the squared correlation coefficient, r^2) for the V_{mem}-τ_{fl} relationship of each VF. Each gray dot represents an individual patched HEK293T cell; bars represent mean ± SEM. Sample sizes (number of individual HEK293T cells): JuloVF 6, IndoVF 8, ^{i}PrVF 10, VF2.1.Cl 7, NN26VF 8, VF2.0.Cl 5.

Performance at Detection of Spontaneous Electrical Activity

We evaluated our three best aniline modified VFs for their ability to monitor spontaneous electrical activity in human induced pluripotent stem cell derived cardiomyocytes (hiPSC-CMs) and dissociated rat hippocampal neurons. We selected VF2.1.Cl, iPrVF, and IndoVF for these studies, as they displayed the best combination of sensitivity and brightness in HEK293T. All three indicators faithfully recorded action potential waveforms in spontaneously contracting monolayers of cardiomyocytes (**Figure 4.19**). The average signal-to-noise ratio (SNR) of these activity recordings was high in all cases, with ^{i}PrVF and VF2.1.Cl having the highest SNR values in excess of 400:1 when loaded at a concentration of 300 nM (**Figure 4.19g, Table 4.2**). IndoVF exhibited an average SNR that was similar to VF2.1.Cl loaded at lower concentrations, but is still capable of reporting cardiac action potential kinetics (**Figure 4.20**).

We also investigated the phototoxicity and photostability of these three derivatives, as we have previously observed difference in the phototoxicity of PeT-based voltage indicators with different wire structures.[15] We compared the phototoxicity of ^{i}PrVF and IndoVF to VF2.1.Cl during prolonged measurements of activity in iPSC-CM monolayers. With all three sensors, we were able to record action potentials (APs) without alterations to the AP waveform for up to 4 minutes (**Figure 4.21**). IndoVF appeared slightly less phototoxic than ^{i}PrVF or VF2.1.Cl, as AP kinetics remain unchanged for approximately 6 minutes of illumination in tissue. The initial photobleaching rates for all three indicators are similar in both HEK293T cells and iPSC-CMs (**Figure 4.22**). Taken together, these data suggest that modifying the aniline conformation has minimal effect on probe photobleaching and phototoxicity, and IndoVF, iPrVF, and VF2.1.Cl are all capable of reporting on cardiac electrophysiology with high SNR.

In dissociated rat hippocampal culture, IndoVF, ^{i}PrVF, and VF2.1.Cl all displayed good SNR in the detection of evoked action potentials (**Figure 4.19**, **4.23, Table 4.2**). 300 nM VF2.1.Cl showed the highest SNR, although action potentials were also clearly visible with 300 nM ^{i}PrVF and 300 nM IndoVF.

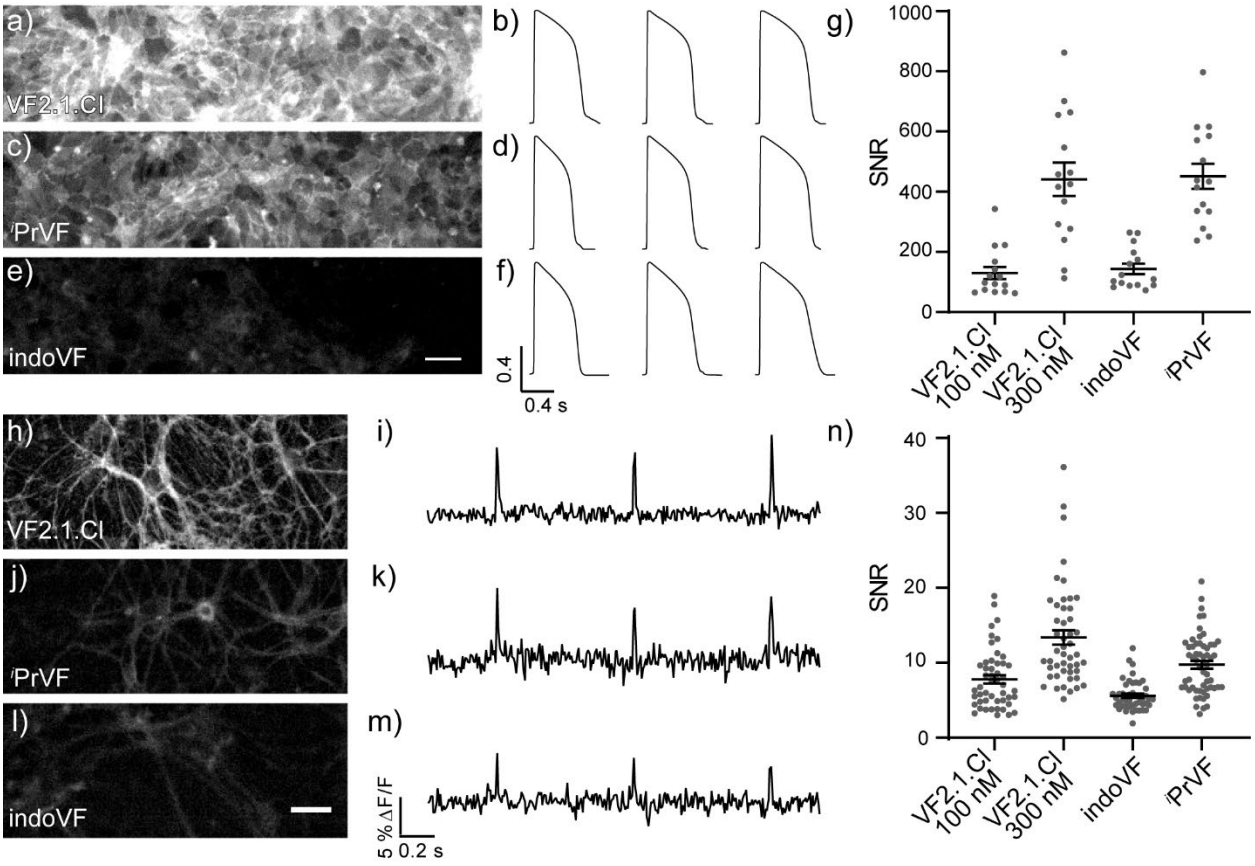

Figure 4.19. Aniline modified VFs detect electrical activity in iPSC-CMs and neurons.
a,c,e) Epifluorescence images of VF2.1.Cl, ^{i}PrVF, and IndoVF loaded at 300 nM in iPSC-CM monolayers. Image size matches recording area used for functional imaging. Scale bar represents 50 µm. b,d,f) ΔF/F of averaged spontaneous action potentials in iPSC-CM monolayers, recorded with VF2.1.Cl, ^{i}PrVF, and IndoVF, respectively. g) SNR for AP detection in iPSC-CMs. Each point represents a recording from a field of view. Data are shown as mean ± SEM. h,j,l) Epifluorescence images of VF2.1.Cl, ^{i}PrVF, and IndoVF loaded at 300 nM in dissociated rat hippocampal neurons. Scale bar represents 40 µm; image size matches recording area used for functional imaging. i,k,m) Unfiltered %ΔF/F traces from a series of three evoked action potentials. n) SNR for AP detection in neurons. Each point represents the first action potential measured from a field of view. Data are shown as mean ± SEM.

VoltageFluor	HEK293T SNR	Cardio SNR	Neuron SNR
JuloVF	26 ± 1.8[b]	-	-
IndoVF	87 ± 6.5	141 ± 4.4	5.6 ± 0.3
^{i}PrVF	125 ± 1.7	451 ± 11	9.7 ± 0.5
VF2.1.Cl	103 ± 4.6[a] 197 ± 12	130 ± 5.3[a] 441 ± 14	7.8 ± 0.6[a] 13 ± 1
NN26VF	8.6 ± 0.2	-	-
VF2.0.Cl	1.8 ± 0.06[a] 2.4 ± 1.4	-	-

Table 4.2. Signal-to-noise ratio (SNR) in detection of cellular V_{mem} changes.
Data are shown as mean ± SEM. All data were measured at 300 nM unless otherwise indicated. [a]100 nM; [b]500nM.

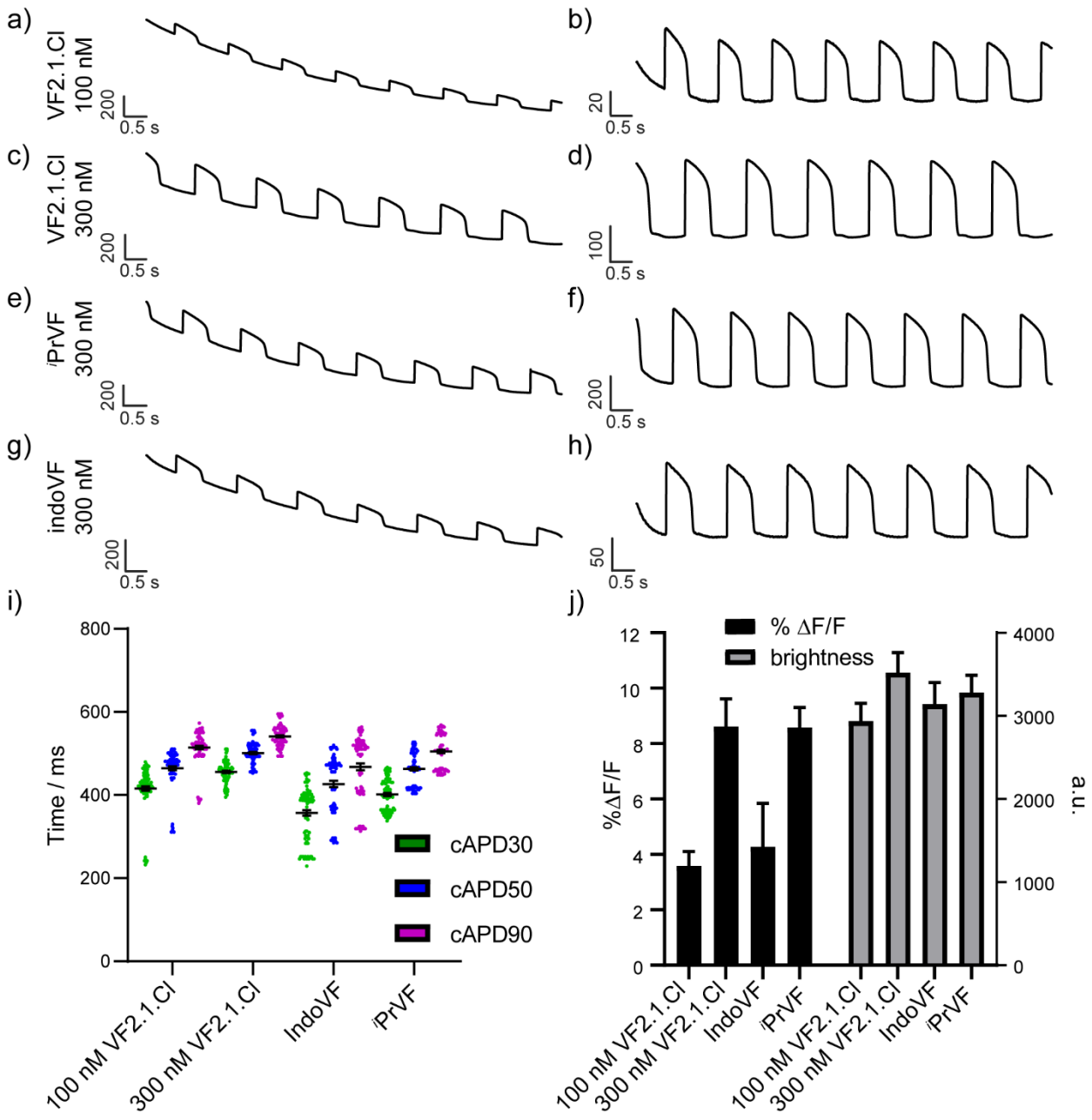

Figure 4.20. Functional comparison of VoltageFluor indicators in hiPSC-CMs.
Representative uncorrected (a,c,e,g) and bleach-corrected (b,d,f,h) functional recordings of spontaneous activity in hiPSC-CMs. Recordings were made for 10 seconds, bleach correction was made by subtracting the exponential decay calculated by an asymmetric least-squares fit to the raw trace. Of the VoltageFluors tested, each has a similar photobleach decay (**Figure 4.21**). i) Scatter plot of corrected action potential duration (cAPD) values at 30, 50, and 90% of the repolarization recorded with VoltageFluors. cAPD, and action potential morphology, was not affected by the identity of VoltageFluor used in these studies. Bars represent mean ± SEM. Samples were taken from 3 wells per condition, with 5 fields of view per well for a total of 15 recordings per condition. Sample size (number of individual action potentials recorded): 100 nM – VF2.1.Cl 100, 300 nM

– VF.2.1.Cl 103, indoVF 89, ^{i}PrVF 102. j) Bar plot of mean %ΔF/F (left y-axis, black bars), and mean brightness (right y-axis, grey bars). Brightness was calculated as the average pixel intensity of the baseline of the fluorescence trace. IndoVF and ^{i}PrVF were loaded at a concentration of 300 nM. As with SNR (**Figure 4.19**), IndoVF performs similarly in %ΔF/F and has a similar brightness to VF2.1.Cl loaded at 100 nM, and ^{i}PrVF performs similarly to VF2.1.Cl loaded at 300 nM.

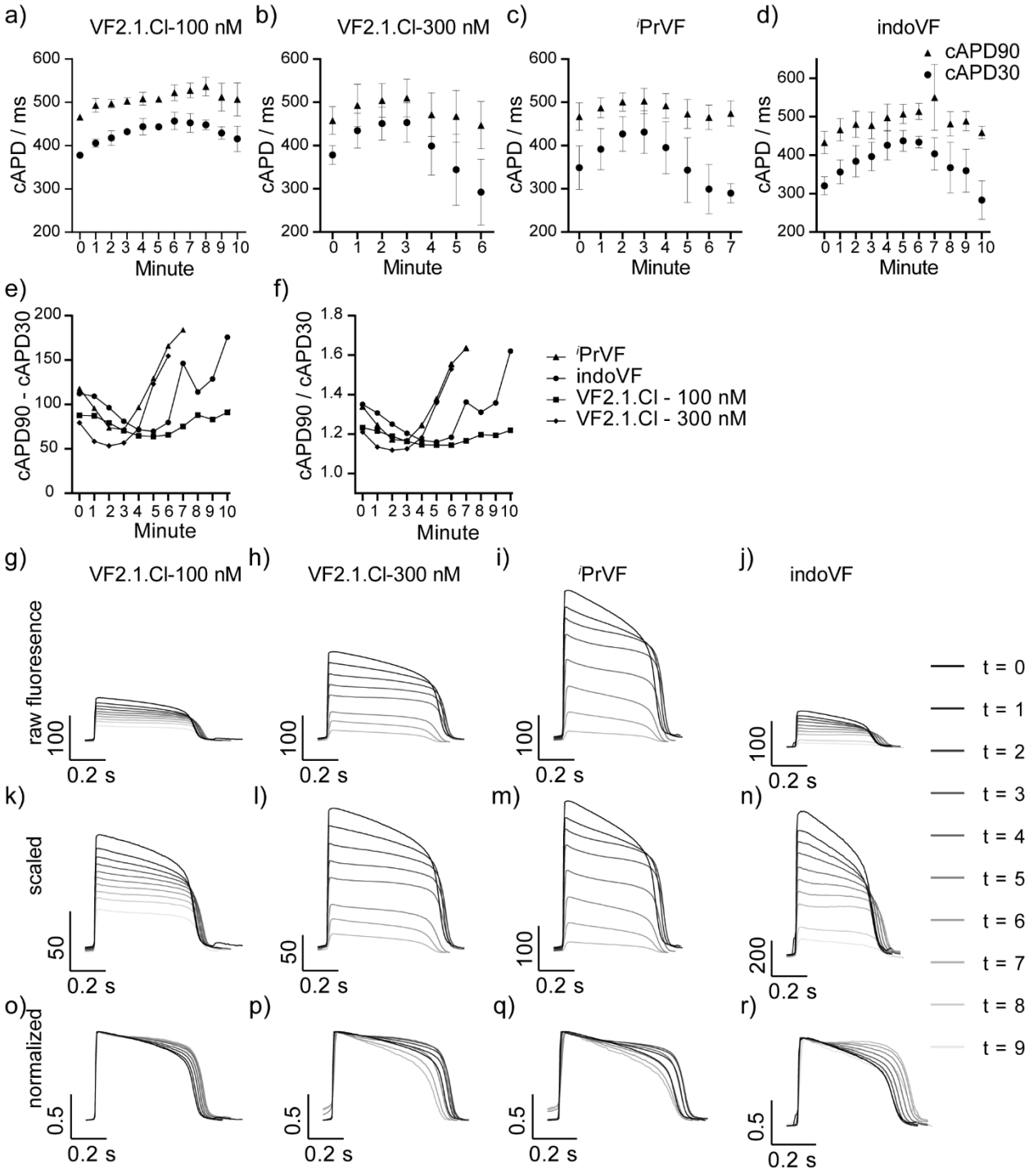

Figure 4.21. Cardiotoxicity with prolonged illumination of VoltageFluors
The phototoxicity of VoltageFluors was examined in hiPSC-CMs by prolonged, continuous exposure to the excitation LED. Action potential morphology was monitored through 10 second recordings made each minute (a-d) and quantified using cAPD. Deviations in cAPD from starting values (recording made at 0 minutes) can be interpreted as an action potential morphology change, which is indicative of potential phototoxic effects. As previously observed,[15] decreasing the

concentration of VF2.1.Cl to 100 nM (a) from 300 nM (b) permits recordings over extended times with minimal change to action potential morphology. ^{i}PrVF (c, 300 nM) performs similarly to VF2.1.Cl loaded at 300 nM (b), permitting recordings for 3 minutes of constant illumination before AP morphology changes are seen. indoVF (d, 300 nM) resembles VF2.1.Cl loaded at a lower concentration (a, 100 nM), as AP morphology changes are not observed until extended illumination periods. AP morphology changes were also quantifies the difference (e) and ratio (f) of cAPD90 and cAPD30. Deviations from initial values indicate changes to AP morphology. In the case of the VoltageFluors tested, both the difference and ratio of cAPD90 and cAPD30 increases over prolonged exposure to excitation light, indicating a prolongation of phase 2 in the cardiac AP and an overall increase in duration. (g-j) Representative fluorescence traces from a single trial, each action potential is the mean trace from a single 10 second recording. As time progresses (purple to cream), the amplitude of the cardiac action potential decreases regardless of VoltageFluor used due to photobleaching. (k-n) Scaled fluorescence traces more clearly show the decrease in amplitude for each VoltageFluor. (o-r) Normalized fluorescence traces show the change in action potential morphology with increased illumination.

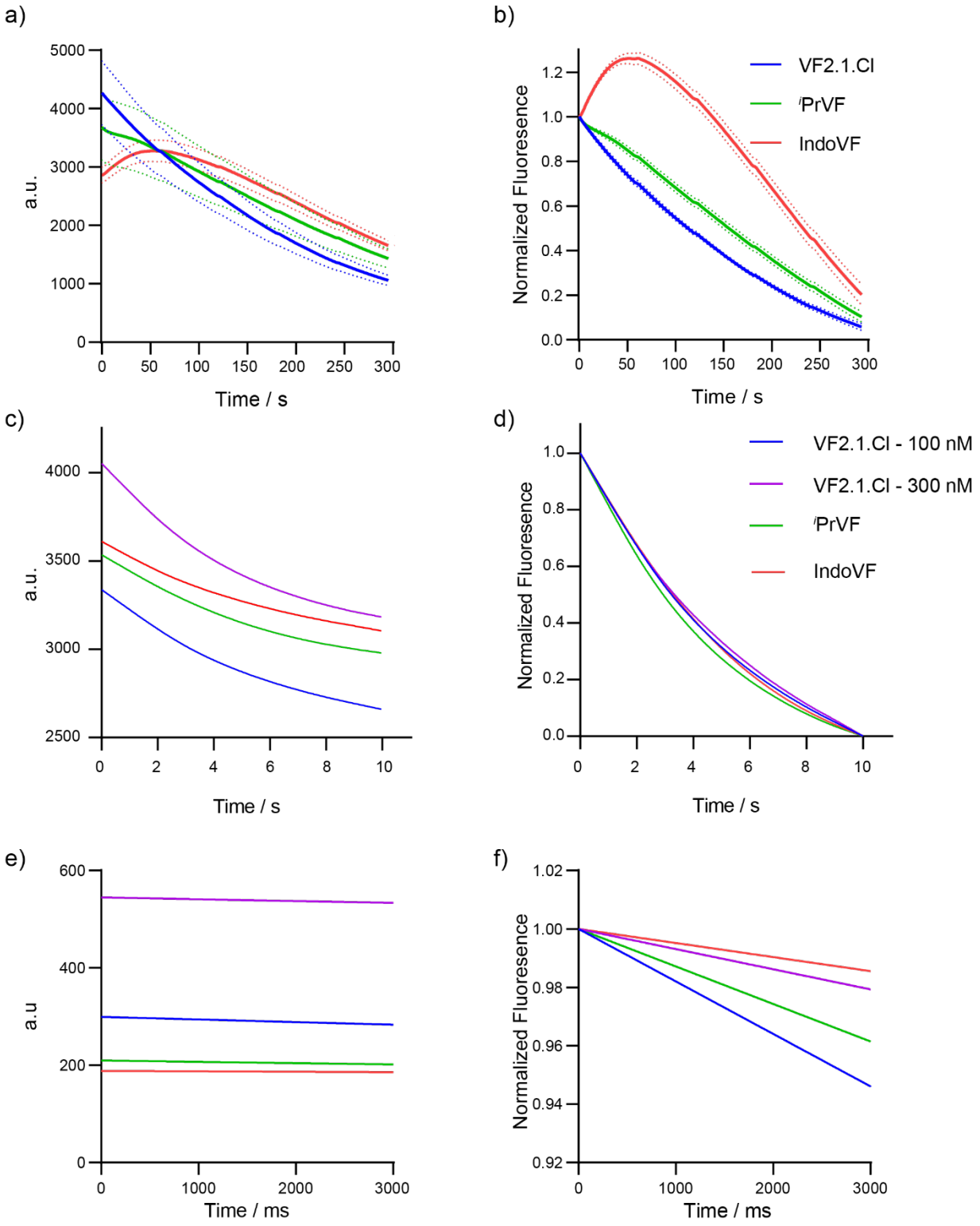

Figure 4.22. Comparison of VF bleach rate in HEK293T, iCMs, and rat hippocampal neurons.

a) Mean fluorescence and b) mean normalized fluorescence signal over time under high light illumination in HEK293T. Dotted lines reflect ± SEM for 3 recordings. c) Fluorescence and d) normalized fluorescence of the background correction spline used for cardiomyocyte functional imaging, reflecting the average bleaching rate of the sensor. e) Average bleaching traces for evoked activity experiments in neurons. The y-intercept is the average fluorescence value of the first frame of the background-subtracted traces for each dye. The slope is the average slope of the regression lines which were fit to the background-corrected traces for each dye and used to correct for bleaching. f) Each trace from (e) normalized.

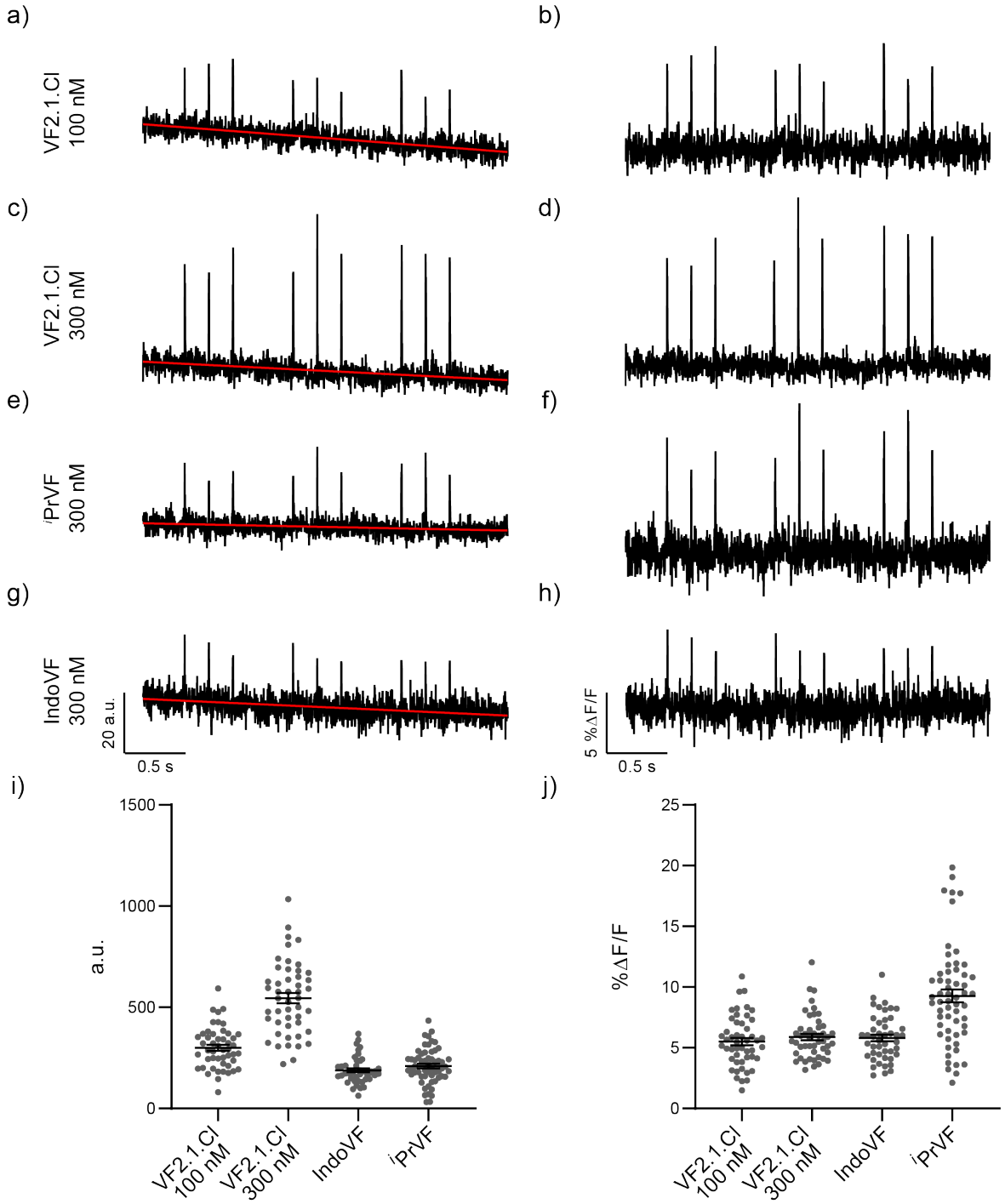

Figure 4.23. Functional comparison of VoltageFluor indicators in rat hippocampal neurons. a,c,e,g) Representative background-corrected traces (black) of evoked activity in rat hippocampal neurons and regression lines (red) fit to the respective traces for VF2.1.Cl 100 nM (a), VF2.1.Cl 300 nM (c), ^{i}PrVF 300 nM (e), and IndoVF 300 nM (g). b,d,f,h) %ΔF/F traces (black) of evoked activity in rat hippocampal neurons for VF2.1.Cl 100 nM (b), VF2.1.Cl 300 nM (d), ^{i}PrVF 300 nM (f), and IndoVF 300 nM (h). i) Plot of the raw fluorescence values of each dye in rat

hippocampal neurons. Each grey dot represents a background-corrected first frame fluorescence value for one measurement of evoked activity; bars represent mean ± SEM. j) Plot of the %ΔF/F values for evoked activity in rat hippocampal neurons. Each grey dot represents the %ΔF/F value of the first action potential in one measurement of evoked activity; bars represent mean ± SEM.

Predictors of VF Performance in Functional Imaging

From the τ_{fl} electrophysiology data, we noticed a tradeoff between the absolute sensitivity and 0 mV τ_{fl} of the VFs (**Figure 4.24a**). Because all of the VFs are based on the dichlorofluorescein chromophore and have the same extinction coefficient, 0 mV τ_{fl} should reflect the inherent brightness of the VFs. Dimmer VFs such as JuloVF and IndoVF have a high relative V_{mem} sensitivity (%ΔF/F or %Δτ/τ, **Figure 4.6**, **Figure 4.18**), but a lower absolute change in τ per mV. We observe the highest absolute sensitivity for VF2.1.Cl, which has an intermediate 0 mV lifetime. Very long lifetimes, such as those in NN26VF, are associated with both low %ΔF/F and low absolute sensitivity. Taken together, these data suggest that the performance of VFs hinges on a balance between fluorescence and PeT, and that the intermediate levels of both PeT and fluorescence produce the largest sensitivities.

We found that fluorescence intensity of the VFs in HEK293T cells did not correlate strongly with the fluorescence lifetime (**Figure 4.24b**), suggesting that VF loading into membranes plays a major role in dictating fluorescence intensity. The differences we observed in the onset of concentration quenching of τ_{fl} are consistent with this notion (**Figure 4.7**). Although the aniline modified VFs are structurally similar, changes in the basicity of the aniline could lead to protonation in buffer, forming a charged, quaternary nitrogen that could disfavor incorporation into the membrane. Taken together, the substantial differences between fluorescence intensity and fluorescence lifetime suggest that caution should be used in interpreting probe brightness in cells in terms of fundamental photophysics. On the other hand, the τ_{fl} in POPC (**Figure 4.1**, **Table 4.1**) matched the trends observed in 0 mV lifetime in HEK293T cell membranes qualitatively, suggesting that characterization in POPC vesicles is a reasonable strategy for predicting VF 0 mV lifetime and baseline levels of PeT.

From this multidimensional characterization, we sought to identify a property that would predict performance (signal-to-noise ratio, SNR) in V_{mem} event detection. We observed strong correlation between the absolute sensitivity (Δτ/mV) and the SNR of a 100 mV step in HEK293T in epifluorescence imaging (**Figure 4.24c).** It stands to reason that the total change in the probe fluorescence lifetime reflects how much V_{mem}-sensitive PeT is modulating the fluorescence. To evaluate whether SNR in HEK293T translates to applications in excitable cell culture, we analyzed the relationship between the SNR for a V_{mem} step in HEK293T and the SNR for per action potential (AP) in cardiomyocytes and neurons (**Figure 4.24d**). We observed strong correlation between the SNR in HEK293T and neurons, with slightly weaker correlation between results in HEK293T and iPSC-CMs. Therefore, the absolute sensitivity of τ_{fl} to Vmem is a good predictor of probe SNR in diverse contexts.

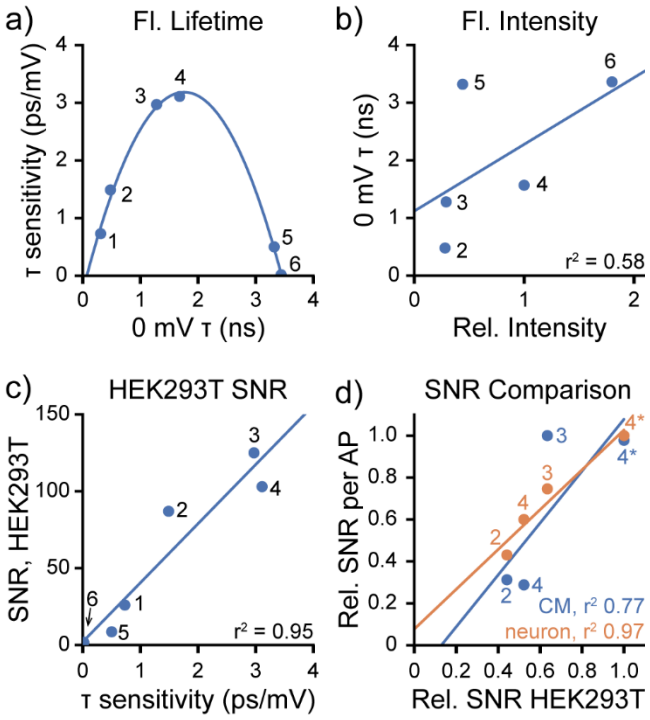

Figure 4.24. Fluorescence lifetime change dictates VF performance.
Data shown here are aggregated from **Figures 4.6, 4.8**, and **4.19** to highlight properties of the VF library. Numbers correspond to aniline-modified VFs: 1 JuloVF (500 nM), 2 IndoVF (300 nM), 3 ^{i}PrVF (300 nM), 4 VF2.1.Cl (100 nM), 4* VF2.1.Cl (300 nM), 5 NN26VF (300 nM), 6 VF2.0.Cl (100 nM). a) The sensitivity (ps/mV) and 0 mV lifetime (ns) of VF fluorescence lifetimes in HEK293T exhibit a parabolic relationship. b) The relative fluorescence intensity of VFs does not display the same trend as τ_{fl}. Fluorescence intensity of VFs at 300 nM in HEK293T is shown here; JuloVF is omitted because no lifetime data were taken at 300 nM. c) Correlation between the signal to noise ratio (SNR) of a 100 mV V_{mem} step (-60 to +40 mV) in HEK293T and the sensitivity of τ_{fl} to V_{mem}. d) Correlation between the SNR in HEK293T (as in c) with the SNR for detection spontaneous action potentials (APs) in cardiomyocytes (CM, blue) or evoked APs in neurons (orange). The SNR for each probe in each system (**Table 4.2**) was normalized to the maximum SNR seen in that system for ease of comparison. Data are represented as the mean; error bars are omitted for clarity.

In summary, we present the design and synthesis of a library of PeT-based voltage-sensitive dyes with conformationally modified electron donating moieties. We performed extensive characterization of VF properties in vitro, in a model cell culture system, and in excitable cells. The large range of brightness and sensitivity observed in our library suggests that synthetic modification of the aniline electron donor is an effective way to tune PeT-based V_{mem} sensing domains across a wide variety of electron donor strengths. We identify that τ_{fl} and the magnitude of V_{mem} induced changes in τ_{fl}, give a more accurate picture of VF photophysics than fluorescence intensity alone. We anticipate that similar τ_{fl} information would be useful for many novel probe libraries, not limited to those designed for V_{mem} sensing.

Materials and Methods

Chemical Synthesis and Characterization

Detailed information regarding the chemical synthesis and characterization is available in Steven Boggess's Ph.D. dissertation.

Spectroscopic Studies

Stock solutions of VoltageFluors were prepared in DMSO (500 μM-1 mM) by comparing the absorbance of the chloro-fluorescein peak of each VoltageFluor with the known extinction coefficient for this dye head.[16] These stock solutions were then diluted (1:1000) in the indicated solvent for each spectroscopic analysis. UV-Vis absorbance and fluorescence spectra were recorded using a Shimadzu 2501 Spectrophotometer (Shimadzu) and a Quantamaster Master 4 L-format scanning spectrofluorometer (Photon Technologies International). The fluorometer is equipped with an LPS-220B 75-W xenon lamp and power supply, A-1010B lamp housing with integrated igniter, switchable 814 photon-counting/analog photomultiplier detection unit, and MD5020 motor driver. Samples were measured in 1-cm path length quartz cuvettes (Starna Cells).

Relative quantum yields (Φ_{Fl}) were calculated by comparison to fluorescein (Φ_{Fl} = 0.93 in 0.1 M NaOH, Φ_{Fl} = 0.92 in Ethanol w/ 0.1 M KOH)[21,22] and rhodamine 6G (Φ_{Fl} = 0.95 in ethanol)[23] as references.[24] Stock solutions of standards were prepared in DMSO (0.25-1.25 mM) and diluted with appropriate solvent (1:1000 dilution). Absorption and emission (excitation = 485 nm) were taken at 5 concentrations. The absorption value at the excitation wavelength (485 nM) was plotted against the integration of the area of fluorescence curve (495-675 nm). For fluorescein, the integration of the area of the fluorescence curve was also taken with an excitation at 450 nm. The area from 460-675 nm and 495-675 nm was used to extrapolate the area of the fluorescence curve with an excitation at 485 nm. This ensured the full fluorescence area of fluorescein excited at 485 nm was used for Φ_{Fl} calculations. The slope of the linear best fit of the data was used to calculate the relative Φ_{Fl} by the equation $\Phi_{Fl(X)} = \Phi_{Fl(R)}(S_X/S_R)(\eta_X/\eta_R)^2$, where S_R and S_X are the slopes of the reference compound and unknown, respectively, and η is the refractive index of the solution. This method was validated by cross-referencing the reported Φ_{Fl} values of fluorescein and rhodamine 6G to the calculated Φ_{Fl} using the one standard as a reference for the other and vice versa. Calculated Φ_{Fl} within 10% of the reported value for both standards ensured that Φ_{Fl} calculated for fluorene VoltageFluors was reliable within 10% error.

Preparation of POPC Vesicles

1-palmitoyl-2-oleoyl-glycero-3-phosphocholine (16:0-18:1 PC, POPC) was purchased as $CHCl_3$ solution from Avanti Polar Lipids (Alabaster, AL). Stocks were aliquoted and stored at -80°C; all lipid solutions were handled in glassware cleaned with copious amounts of $CHCl_3$. For preparation of vesicles, 1-15 mg of POPC (at 4 mg/mL in $CHCl_3$) was dried down on a rotary evaporator at 45°C and 35 RPM to produce a film. The film was dried under vacuum at room temperature overnight and then rehydrated for 30-60 minutes with slow rotation (10-15 RPM) at room temperature in 1x Dulbecco's Phosphate Buffered Saline (dPBS, Gibco, composition in mM: 138 NaCl, 8 NaH_2PO4, 2.7 KCl, 1.5 KH_2PO_4, pH approx. 7.1). Unilamellar vesicles were formed by extrusion through a 0.1 μm pore size polycarbonate membrane with the Mini Extruder Set at room temperature (Avanti) as per the manufacturer's protocol. Vesicles were kept at room temperature and used within a few hours of formation.

Vesicle formation was verified by dynamic light scattering (DLS) with a Zetasizer Nano ZS (Malvern Instruments). Vesicle diameters ranged from 125.9-160.3 nm between batches; all batches were monodisperse, with one primary size peak. For DLS measurements, vesicle suspensions were used directly or diluted 1:1 in dPBS before measurement. 100-200 uL of vesicle suspension was placed into a Zen 0040 cuvette. Refractive indices of 1.450 (material) and 1.332 (dispersant) were used in the Zetasizer software to obtain size distributions. Vesicle size distributions were measured in both naïve POPC vesicles and in POPC vesicles incubated with VoltageFluor; results were indistinguishable.

Cell Culture

All animal procedures were approved by the UC Berkeley Animal Care and Use Committees and conformed to the NIH Guide for the Care and Use and Laboratory Animals and the Public Health Policy.

Human embryonic kidney (HEK) 293T cells

HEK293T cells were acquired from the UC Berkeley Cell Culture Facility and were verified by STR (short tandem repeat) profiling. Cells were routinely checked for mycoplasma contamination. HEK293T cells were maintained in Dulbecco's modified eagle medium (DMEM, Gibco) supplemented with 4.5 g/L D-glucose, 10% fetal bovine serum (FBS, Seradigm), and 2 mM GlutaMAX (Gibco). Cells were passaged every few days into fresh media following dissociation with 0.05% Trypsin-EDTA (Gibco). All cells were discarded after 30 passages. For imaging experiments, 25 mm glass coverslips (Electron Microscopy Sciences) were prepared by acid washing (1 M HCl, approx. 5 hours), followed by three overnight washes in ethanol and three overnight washes in water. Coverslips were sterilized by heating at 150°C for 2-4 hours. To facilitate cell attachment, sterilized coverslips were coated with Poly-D-Lysine (PDL; 1 mg/mL; Sigma-Aldrich) for 1-24 hours at 37°C, followed by two washes with water and two washes with phosphate-buffered saline. For general imaging, cells were seeded onto prepared coverslips in complete DMEM at a 42,000 cells/cm^2 and used approximately 24 hours after plating. For electrophysiology, cells were seeded at a density of 21,000 cells/cm^2 in low glucose DMEM (1 g/L glucose, 10% FBS, 1 mM pyruvate, 2 mM GlutaMAX) and used approximately 16 hours after plating.

Rat hippocampal neurons

Hippocampi were dissected from embryonic day 18 Sprague Dawley rats (Charles River Laboratory) in cold sterile HBSS (zero Ca^{2+}, zero Mg^{2+}). All dissection products were supplied by Invitrogen, unless otherwise stated. Hippocampal tissue was treated with trypsin (2.5%) for 15 min at 37 °C. The tissue was triturated using fire polished Pasteur pipettes, in minimum essential media (MEM) supplemented with 5% fetal bovine serum (FBS; Thermo Scientific), 2% B-27, 2% 1M D-glucose (Fisher Scientific) and 1% glutamax. The dissociated cells were plated onto 12 mm diameter coverslips (Electron Microscopy Sciences, prepared as above) at a density of 27,000 cells per coverslip in MEM supplemented media. Neurons were maintained at 37 °C in a humidified incubator with 5 % CO_2. At 1 day in vitro (DIV) half of the MEM supplemented media was removed and replaced with Neurobasal media containing 2% B-27 supplement and 1% glutamax. Functional imaging was performed on 14-17 DIV neurons.

Differentiation of hiPSC into cardiomyocytes and culture

hiPSCs (WTC11)[25] were cultured on Matrigel (1:100 dilution; Corning)-coated 12 well-plates in StemFlex medium (Gibco). When the cell confluency reached 80–90%, which is referred as day 0, the medium was switched to RPMI 1640 medium (Life Technologies) containing B27 minus insulin supplement (Life Technologies) and 10 μM CHIR99021 GSK3 inhibitor (Peprotech). At day 1, the medium was changed to RPMI 1640 medium containing B27 minus insulin supplement only. At day 3, medium was replaced to RPMI 1640 medium containing B27 supplement without insulin, and 5 μM IWP4 (Peprotech) for 2 days without medium change. On day 5, medium was replaced to RPMI 1640 medium containing B27 minus insulin supplement for 2 days without medium change. On day 7, medium was replaced with RPMI 1640 containing B27 with insulin supplement. After day 7, the medium was changed every two days. Confluent contracting sheets of beating cells appear between days 7 to 15.[26]

Beating sheets were treated with collagenase II for 60-75 minutes. The collagenase solution was carefully transferred to cold DMEM, making sure cardiac sheets were not disturbed. Trypsin (0.25%) was added to dissociated sheets for 4-8 minutes and plated onto 6 well-plates coated with Matrigel (1:100 dilution) in RPMI 1640 medium containing B27 supplement plus ROCK inhibitor Y-27632. 24 hours later, the medium was replaced with fresh RMPI/B27 without ROCK inhibitor. Cardiomyocytes were maintained for 7 days, replacing media every other day, and then were switched to RPMI 1640 medium (-glucose) supplemented with 4 mM sodium lactate (Sigma Aldrich). Cells were maintained in this media for 7 days, replacing every other day, then switched back to RPMI/B27 containing glucose.[27] These purified cardiomyocytes were then used for imaging.

Lactate purified sheets were dissociated with 0.25% trypsin-EDTA (4-8 minutes, depending on density and quality of tissue) and plated onto Matrigel (1:100)-coated Ibidi ® 24 well μ-plates (cat no. 82406**)** in RPMI 1640 medium containing B27 supplement (containing insulin). Medium was changed every 3 days until imaging. For loading hiPSC cardiomyocytes, voltage dyes were diluted 1 in 1000 in RPMI 1640 with B27 supplement minus Phenol Red to the desired final concentration. Cardiomyocytes were incubated in this solution for 20 minutes at 37 °C, then exchanged with dye-free RPMI 1640 with B27 supplement minus Phenol Red.

VoltageFluor Stocks and Cellular Loading

VoltageFluors were stored as 0.5-1 mM DMSO stocks at -20°C or as a solid at room temperature. For cellular loading in HEK293T, DMSO stocks were diluted to the indicated concentration in imaging buffer (IB; composition in mM: 139.5 NaCl, 10 HEPES, 5.6 D-glucose, 5.3 KCl, 1.3 $CaCl_2$, 0.49 $MgCl_2$, 0.44 KH_2PO_4, 0.41 $MgSO_4$, 0.34 Na_2HPO_4; 290 mOsm/kg, pH 7.25). HEK293T cells were incubated in the VF-IB solution for 20-25 minutes in a humidified incubator at 37°C. Cells were washed once in IB and transferred to fresh IB for imaging. Hippocampal neurons were loaded with VoltageFluor at the indicated concentration in HBSS and incubated in the VF-HBSS solution for 20 minutes in a humidified incubator at 37°C. For imaging evoked activity, the hippocampal neurons were then transferred to a HBSS solution containing the synaptic blockers 10 μM 2,3-Dioxo-6-nitro-1,2,3,4-tetrahydrobenzo[f]quinoxaline-7-sulfonamide (NBQX; Santa Cruz Biotechnology) and 25 μM DL-2-Amino-5-phosphonopentanoic acid (APV; Sigma-Aldrich) to prevent recurrent activity. Cardiomyocytes were loaded with VoltageFluor in RPMI-B27 with no phenol red (instead of IB). The loading solution was exchanged for fresh RPMI-B27

without phenol red (and without VF) before imaging. All imaging was conducted under ambient atmosphere; no imaging samples were used for longer than an hour.

For assessment of the concentration dependence of fluorescence lifetime, the indicated concentration of VoltageFluor was used (**Fig. 4.17**). From these data, an optimal working concentration that minimized concentration quenching but retained adequate signal was selected. This concentration was used for all other experiments in HEK293T unless indicated. Optimal concentrations for VF2.1.Cl and VF2.0.Cl were previously determined;[9] where indicated, we also include some data at 300 nM (3x higher concentration) for comparison. Working concentration values are tabulated below (**Table 4.3**):

VoltageFluor	Optimized Concentration
JuloVF	500 nM
IndoVF	300 nM
^{i}PrVF	300 nM
VF2.1.Cl	100 nM
NN26VF	300 nM
VF2.0.Cl	100 nM

Table 4.3. Optimized cellular working concentrations.

Epifluorescence ("fluorescence intensity") imaging

For all experiments, excitation light for epifluorescence intensity image was generated by Spectra-X Light engine LED (Lumencor) using the cyan LED (475/34 nm bandpass filter). Light was collected with an emission filter (bandpass 540/50 nm) after passing through a dichroic mirror (510 nm LP). Images were captured with an OrcaFlash4.0 sCMOS camera (Hamamatsu). More detailed imaging information for each fluorescence intensity application is expanded below.

Membrane staining and photostability in HEK293T cells

HEK293T cells were imaged on an inverted Zeiss AxioObserver Z-1. Fluorescence was collected with a 40x oil immersion objective (EC-Plan-NEOFLUAR 40/1.3; Zeiss). For membrane staining, images (2048x2048 px^2, pixel size 0.16 x 0.16 μm^2) . For voltage sensitivity experiments, images (100x100 px^2, pixel size 0.64 x 0.64 μm^2) were collected continuously with constant LED illumination (9.53 mW/mm^2) and a sampling rate of 0.5 kHz. For photostability experiments, images (2048 x 2048 px^2, pixel size 0.16 x 0.16 μm^2) were taken every 1 second for 5 minutes with constant illumination of LED (30.4 mW/mm^2; 100 ms exposure time).

Evoked activity in rat hippocampal neurons

Evoked activity imaging was performed on an upright AxioExaminer Z-1 (Zeiss), equipped with a Spectra-X light engine LED light (Lumencor), and controlled with µManager (V1.4, open-source, Open Imaging).[10] Images were acquired using a W-Plan-Apo/1.0 NA 20x water immersion objective (Zeiss). Images (2048x400 px^2, pixel size: 0.325 x 0.325 µm) were collected continuously on an OrcaFlash4.0 sCMOS camera (sCMOS; Hamamatsu) at a sampling rate of 0.5 kHz with 4x4 binning and cyan excitation light power of 13.22 mW/mm^2. Extracellular field stimulation was delivered by a Grass Stimulator connected to a recording chamber containing two

platinum electrodes (Warner), with triggering provided through a Digidata 1440A digitizer and pCLAMP 10 software (Molecular Devices). Action potentials were triggered by 1 ms 80 V field potentials delivered at 5 Hz.

Spontaneous activity in hiPSC-derived cardiomyocytes

Functional recordings of VoltageFluors were performed on an inverted AxioObserver Z-1 (Zeiss), equipped with a Spectra-X Light engine LED light (Lumencor), controlled with μManager (V1.4, open-source, Open Imaging).[10] Images were acquired using a Plan-Apochromat 20/0.8 air objective (20x, Zeiss). Images were focused onto an OrcaFlash4.0 sCMOS camera (sCMOS; Hamamatsu). Images (512 x 125 px^2, pixel size 0.64 x 0.64 μm) were taken continuously at 0.2 kHz for ten seconds with constant LED illumination (11.1 mW/mm^2).

Phototoxicity of VoltageFluor dyes was assessed in cardiomyocyte monolayers exposed to constant illumination from the excitation LED (9.53 mW/mm^2) for up to ten minutes (or until automaticity was lost), while typical ten second fluorescence recordings were made at the beginning of each minute.

Epifluorescence ("fluorescence intensity") Image Analysis

Voltage sensitivity in HEK293T cells (%ΔF/F)

Analysis of voltage sensitivity in HEK293T cells was performed using ImageJ (FIJI). Briefly, a region of interest (ROI) encompassing the cell body was selected and average fluorescence intensity was calculated for each frame. For background subtraction, a ROI encompassing a region without cells was selected and the average pixel intensity was calculated for each frame. A linear fit to the background trace was calculated and applied to the background, and this was used to subtract background signal from the fluorescence intensity trace. F/F_o values were calculated by dividing the background subtracted trace by the median value of fluorescence when the cell is held at -60 mV. ΔF/F values were calculated by plotting the change in fluorescence (ΔF) vs the applied voltage step and finding the slope of a linear best-fit.

Spontaneous activity in iPSC-CMs

Analysis of action potential (AP) data from hiPSC cardiomyocytes was performed using in-house MATLAB scripts based on previously developed software by the Efimov lab (Washington University, St. Louis, MO).[11,12] Scripts are available upon request. Briefly, raw OME-tiffs recorded in μManager was read directly into MATLAB for batch-processing of large datasets (>30 Gb per experiment). The mean pixel intensity of the entire image was calculated for each frame and a mean fluorescence trace was extracted for the entire stack. Photobleach correction was performed by subtracting an asymmetric least-squares fit of the data from the mean trace.[13] This spline was used to estimate and compare the rate of photobleaching of VoltageFluors in cardiomyocytes (**Figure 4.21**). No subtraction of background was possible due to staining of the entire monolayer. Individual AP events were identified through threshold detection based on a Schmidtt trigger. Action potential duration (APD) values were calculated for each AP by finding the activation time (time of the maximum derivative of the AP upstroke) and the time the signal returns to 70 and 10% of the maximum depolarization (APD30 and APD90, respectively). APD values were corrected for variation due to spontaneous beat rate by Fridericia's formula (Eq. 4.1). CL is the cycle length, calculated as the time period from the beginning of one beat to the beginning of the succeeding beat.[14]

$$\text{cAPD} = \frac{APD}{\sqrt[3]{CL}} \quad [4\text{-}1]$$

Evoked activity in rat hippocampal neurons

For analysis of evoked voltage responses in neurons, regions of interest encompassing cell bodies were drawn in ImageJ and the mean fluorescence intensities for each frame were extracted. ΔF/F values were calculated in the following manner. First, a mean background value was subtracted from all raw fluorescence frames, bypassing the noise amplification which arises from subtracting background for each frame, to give a background subtracted trace. A least squares regression was then fit to the background subtracted trace. A bleaching curve, derived from the slope of the regression, was then subtracted from the background subtracted trace to correct for photobleaching and yield a bleach-corrected trace. The median of the bleach-corrected trace was subtracted from each timepoint of the bleach-corrected trace to yield a ΔF trace. The ΔF trace was then divided by the median of the bleach-corrected trace to give a ΔF/F trace. No averaging has been applied to any voltage traces. Signal-to-noise ratios were calculated by dividing the ΔF/F value for the frame containing the first spike of evoked activity by the standard deviation of the previous 10 frames in the ΔF/F trace.

Photobleaching studies

For photostability experiments HEK293T cells were loaded the same as above. Images (pixel size 0.16 μm × 0.16 μm) were taken every 1 second for 5 minutes with constant illumination of LED (30.4 mW/mm^2; 50 ms exposure). The obtained fluorescence curves were normalized with the fluorescence intensity at t = 0 and averaged (three different cell rafts for each dye). Phototoxicity of VoltageFluor dyes was assessed in cardiomyocyte monolayers incubated with 0.3 μM of indicator (and 0.1 μM for VF2.1.Cl). These were exposed to constant illumination from the excitation LED (475/34; bandpass) for up to 10 minutes, while typical ten second fluorescence recordings were made at the beginning of each minute. Initial photobleach was compared using splines calculated from asymmetric least squares fit of the baseline. Bleach rate of VoltageFluors in neurons was assessed according to the analysis above.

Fluorescence Lifetime Data Acquisition

Microscopy configuration

Fluorescence lifetime data were obtained as described previously.[9] Briefly, fluorescence lifetime data were acquired on an inverted LSM 510 (Zeiss) scanning confocal microscope equipped with a Becker and Hickl SPC-150N photon counting card. Pulsed excitation light was supplied by a MaiTai HP Ti:Sapphire laser (SpectraPhysics) tuned to 958 nm and frequency doubled to 479 nm. Average power at the sample ranged from 5-25 μW. Photons were collected with a 40x oil immersion objective (1.3 NA Plan-Neofluar, Zeiss) and detected with an HPM-100-40 hybrid detector (Becker and Hickl) after passing through a 488 nm long pass dichroic (Zeiss) and a 550/49 nm bandpass emission filter (Semrock, Rochester, NY). Fluorescence lifetime data were acquired using SPCM software (Becker and Hickl). To maximize photon signal but retain some optical sectioning, the confocal pinhole was set to 2.5-3.5 AU (~2.5 μm optical section). Proper functioning of the fluorescence lifetime imaging system was routinely measured with the standards

erythrosin B and fluorescein in 0.1 N NaOH. The instrument response function (IRF) was recorded at least hourly during data acquisition from a solution of quenched fluorescein (500 μM fluorescein, 12 M NaI, 0.1 N NaOH).[15]

Data acquisition – solution phase measurements

POPC vesicles in 1x dPBS were incubated with VoltageFluor at the indicated concentration at room temperature for 20-30 minutes. The final concentration of DMSO was kept at or below 0.2%. After incubation, vesicle suspensions with dye were transferred to a clean 25 mm coverslip in an Attofluor imaging chamber (Thermo Fisher Scientific). Fluorescence lifetime images were acquired for 60 seconds and generally contained $>10^6$ photons per recording. Data from the image were combined into a global decay with 256 time channels in the fluorescence decay before analysis (see below).

Data acquisition – cellular measurements

HEK293T loaded with VF were transferred to an Attofluor imaging chamber containing imaging buffer. Fluorescence lifetime images were recorded with 256x256 px^2 of spatial resolution (112 x 112 μm^2 image size; see below for binning during lifetime fitting) and 256 time channels. Images for evaluating concentration dependence were acquired for 75-90 seconds; results are the sum of approximately 12 scans across the field of view. For tandem electrophysiology and fluorescence lifetime imaging, data were recorded with 64x64 px^2 of spatial resolution (56.3 x 56.3 μm^2 image size) and 256 time channels. Images with concurrent electrophysiology were acquired for 30 seconds, summing multiple frames recorded from the same field of view.

Fluorescence Lifetime Data Analysis

Time-resolved fluorescence decays I(t) of VoltageFluors were fit to a single exponential decay or to a sum of two or three exponential decays (eqn. 4-2, n=1, 2, or 3). Fits were optimized in custom Matlab code (MathWorks, Natick, MA) using the weighted least squares method to minimize the reduced chi squared χ^2 (eqn. 4-3). The interior-point algorithm from the built-in Matlab optimization routine fmincon was used for optimization. Code is described further in **Appendix 1** and is available upon request.

$$I(t) = \sum_{i=1}^{n} a_i e^{-t/\tau_i} \qquad [4\text{-}2]$$

To calculate χ^2, the difference between the observed value y_m and the calculated value z_m for each time channel m was determined, with Poisson weighting based on the square root of the calculated number of counts in each channel. χ^2 was adjusted for the total number of time channels N included in the fit, as well as the number of parameters p in the model (coefficients a_i and decay constants τ_i).

$$\chi^2 = \sum_{m=1}^{N} \frac{(y_m - z_m)^2}{z_m(N-p)} \quad [4\text{-}3]$$

Where only one fluorescence decay term was used, the reported τ_{fl} is simply the decay constant τ. Where more than one exponential decay term was used, τ_{fl} data are presented as the amplitude weighted average of the two (eqn. 4-4) or three (eqn. 4-5) coefficients a_i and decay constants τ_i.

$$\tau_{fl} = \frac{a_1\tau_1 + a_2\tau_2}{a_1 + a_2} \quad [4\text{-}4]$$

$$\tau_{fl} = \frac{a_1\tau_1 + a_2\tau_2 + a_3\tau_3}{a_1 + a_2 + a_3} \quad [4\text{-}5]$$

The number of fluorescence decay terms was chosen to balance the reduction in χ^2 against the need to minimize fit noise (**Fig. 4.15, 4.16**). The number of terms selected for each probe is indicated below (**Table 4.4**).

VoltageFluor	# exponential decay terms
JuloVF	3
IndoVF	3
^{i}PrVF	2
VF2.1.Cl	2
NN26VF	1
VF2.0.Cl	1

Table 4.4. Number of exponential terms selected to describe VF time-resolved fluorescence decays.

Electrophysiology

For electrophysiological experiments in HEK293T, pipettes were pulled from borosilicate glass with filament (Sutter Instruments, BF150-86-10) with a P-97 pipette puller (Sutter Instruments) to a resistance of 4-7 MΩ. Pipettes were filled with an internal solution (composition, in mM): 125 potassium gluconate, 10 HEPES, 10 KCl, 5 NaCl, 2 ATP disodium salt, 1 EGTA, 0.3 GTP sodium salt (pH 7.25, 285 mOsm). Pipettes were positioned with an MP-225 micromanipulator (Sutter Instruments). Electrophysiological recordings were obtained with an Axopatch 200B amplifier (Molecular Devices) at room temperature. The signals were digitized with a Digidata 1550B sampled at 50 kHz, filtered at 5 kHz and recorded with pCLAMP 10 software (Molecular Devices).

Electrophysiology was performed in the whole cell voltage clamp configuration. After gigaseal formation and break-in, recordings were only pursued if series resistance in voltage clamp was less than 30 MΩ and the recording maintained a 30:1 ratio of membrane resistance to access

resistance throughout all voltage steps. No series resistance compensation was applied. Fast capacitance was compensated in the cell attached configuration. All voltage clamp protocols were corrected for the calculated liquid junction (-14 mV, Liquid Junction Potential Calculator in pClamp).[16] For tandem electrophysiology and fluorescence intensity recordings, cells were held at -60 mV and de- and hyper- polarizing steps were applied from +100 to -100 mV in 20 mV increments, with each step lasting 100 ms. For tandem electrophysiology and fluorescence lifetime recordings, the potentials -80, -40, 0, and +40 mV were randomly applied in four sequential 30 second recordings, followed by a 30 second recording at +80 mV. Cells were only included if the aforementioned patch quality criteria were retained throughout the first 4 steps; the 5th step to +80 mV was included if it also met the quality criteria (true for ~3/4 of cells).

References

(1) Armstrong, C. M.; Gilly, W. F. Access Resistance and Space Clamp Problems Associated with Whole-Cell Patch Clamping. *Methods Enzymol.* **1992**, *207*, 100–122. https://doi.org/10.1016/0076-6879(92)07007-B.

(2) Williams, S. R.; Mitchell, S. J. Direct Measurement of Somatic Voltage Clamp Errors in Central Neurons. *Nat. Neurosci.* **2008**, *11* (7), 790–798. https://doi.org/10.1038/nn.2137.

(3) Knöpfel, T.; Song, C. Optical Voltage Imaging in Neurons: Moving from Technology Development to Practical Tool. *Nat. Rev. Neurosci.* **2019**, *20* (12), 719–727. https://doi.org/10.1038/s41583-019-0231-4.

(4) Miller, E. W. Small Molecule Fluorescent Voltage Indicators for Studying Membrane Potential. *Curr. Opin. Chem. Biol.* **2016**, *33*, 74–80. https://doi.org/10.1016/j.cbpa.2016.06.003.

(5) Tsien, R. Y. New Calcium Indicators and Buffers with High Selectivity Against Magnesium and Protons: Design, Synthesis, and Properties of Prototype Structures. *Biochemistry* **1980**, *19* (11), 2396–2404. https://doi.org/10.1021/bi00552a018.

(6) Paredes, R. M.; Etzler, J. C.; Watts, L. T.; Zheng, W.; Lechleiter, J. D. Chemical Calcium Indicators. *Methods* **2008**, *46* (3), 143–151. https://doi.org/10.1016/j.ymeth.2008.09.025.

(7) Grimm, J. B.; Muthusamy, A. K.; Liang, Y.; Brown, T. A.; Lemon, W. C.; Patel, R.; Lu, R.; Macklin, J. J.; Keller, P. J.; Ji, N.; et al. A General Method to Fine-Tune Fluorophores for Live-Cell and in Vivo Imaging. *Nat. Methods* **2017**, *14* (10), 987–994. https://doi.org/10.1038/nmeth.4403.

(8) Uno, S. N.; Kamiya, M.; Yoshihara, T.; Sugawara, K.; Okabe, K.; Tarhan, M. C.; Fujita, H.; Funatsu, T.; Okada, Y.; Tobita, S.; et al. A Spontaneously Blinking Fluorophore Based on Intramolecular Spirocyclization for Live-Cell Super-Resolution Imaging. *Nat. Chem.* **2014**, *6* (8), 681–689. https://doi.org/10.1038/nchem.2002.

(9) Kulkarni, R. U.; Kramer, D. J.; Pourmandi, N.; Karbasi, K.; Bateup, H. S.; Miller, E. W. Voltage-Sensitive Rhodol with Enhanced Two-Photon Brightness. *Proc. Natl. Acad. Sci.* **2017**, 201610791. https://doi.org/10.1073/pnas.1610791114.

(10) Woodford, C. R.; Frady, E. P.; Smith, R. S.; Morey, B.; Canzi, G.; Palida, S. F.; Araneda, R. C.; Kristan, W. B.; Kubiak, C. P.; Miller, E. W.; et al. Improved PeT Molecules for Optically Sensing Voltage in Neurons. *J. Am. Chem. Soc.* **2015**, *137* (5), 1817–1824. https://doi.org/10.1021/ja510602z.

(11) Fluhler, E.; Burnham, V. G.; Loew, L. M. Spectra, Membrane Binding, and Potentiometric Reponses of New Charge Shift Probes†. *Biochemistry* **1985**, *24* (21), 5749–5755. https://doi.org/10.1021/bi00342a010.

(12) Deal, P. E.; Kulkarni, R. U.; Al-Abdullatif, S. H.; Miller, E. W. Isomerically Pure Tetramethylrhodamine Voltage Reporters. *J. Am. Chem. Soc.* **2016**, *138* (29), 9085–9088. https://doi.org/10.1021/jacs.6b05672.

(13) Huang, Y. L.; Walker, A. S.; Miller, E. W. A Photostable Silicon Rhodamine Platform for Optical Voltage Sensing. *J. Am. Chem. Soc.* **2015**, *137* (33), 10767–10776. https://doi.org/10.1021/jacs.5b06644.

(14) Ortiz, G.; Liu, P.; Naing, S. H. H.; Muller, V. R.; Miller, E. W. Synthesis of Sulfonated Carbofluoresceins for Voltage Imaging. *J. Am. Chem. Soc.* **2019**, *141* (16), 6631–6638. https://doi.org/10.1021/jacs.9b01261.

(15) Boggess, S. C.; Gandhi, S. S.; Siemons, B. A.; Huebsch, N.; Healy, K. E.; Miller, E. W. New Molecular Scaffolds for Fluorescent Voltage Indicators. *ACS Chem. Biol.* **2019**, *14* (3), 390–396. https://doi.org/10.1021/acschembio.8b00978.

(16) Miller, E. W.; Lin, J. Y.; Frady, E. P.; Steinbach, P. A.; Kristan, W. B.; Tsien, R. Y. Optically Monitoring Voltage in Neurons by Photo-Induced Electron Transfer through Molecular Wires. *Proc. Natl. Acad. Sci. U. S. A.* **2012**, *109* (6), 2114–2119. https://doi.org/10.1073/pnas.1120694109.

(17) Rehm, D.; Albert, W. Kinetics of Fluorescence Quenching by Electron and H-Atom Transfer. *Isr. J. Chem.* **1970**, *8* (2), 259–271.

(18) Ahlbrecht, H.; Düber, E. O.; Epsztajn, J.; Marcinkowski, R. M. K. Delocalisation, Conformation and Basicity of Anilines. *Tetrahedron* **1984**, *40* (7), 1157–1165. https://doi.org/10.1016/S0040-4020(01)99321-4.

(19) Lazzari-Dean, J. R.; Gest, A. M. M.; Miller, E. W. Optical Estimation of Absolute Membrane Potential Using Fluorescence Lifetime Imaging. *Elife* **2019**, *8*, e44522. https://doi.org/10.7554/elife.44522.

(20) Chen, R. F.; Knutson, J. R. Mechanism of Fluorescence Concentration Quenching of Carboxyfluorescein in Liposomes: Energy Transfer to Nonfluorescent Dimers. *Anal. Biochem.* **1988**, *172* (1), 61–77. https://doi.org/10.1016/0003-2697(88)90412-5.

(21) Magde, D.; Wong, R.; Seybold, P. G. Fluorescence Quantum Yields and Their Relation to Lifetimes of Rhodamine 6G and Fluorescein in Nine Solvents: Improved Absolute Standards for Quantum Yields¶. *Photochem. Photobiol.* **2002**, *75* (4), 327. https://doi.org/10.1562/0031-8655(2002)075<0327:fqyatr>2.0.co;2.

(22) Zhang, X. F.; Zhang, J.; Liu, L. Fluorescence Properties of Twenty Fluorescein Derivatives: Lifetime, Quantum Yield, Absorption and Emission Spectra. *J. Fluoresc.* **2014**, *24* (3), 819–826. https://doi.org/10.1007/s10895-014-1356-5.

(23) Fischer, M.; Georges, J. Fluorescence Quantum Yield of Rhodamine 6G in Ethanol as a Function of Concentration Using Thermal Lens Spectrometry. *Chem. Phys. Lett.* **1996**, *260*, 115–118.

(24) Wall, K. P.; Dillon, R.; Knowles, M. K. Fluorescence Quantum Yield Measurements of Fluorescent Proteins: A Laboratory Experiment for a Biochemistry or Molecular Biophysics Laboratory Course. *Biochem. Mol. Biol. Educ.* **2015**, *43* (1), 52–59. https://doi.org/10.1002/bmb.20837.

(25) Kreitzer, F. R.; Salomonis, N.; Sheehan, A.; Huang, M.; Park, J. S.; Spindler, M. J.;

Lizarraga, P.; Weiss, W. A.; So, P.; Conklin, B. R. A Robust Method to Derive Functional Neural Crest Cells from Human Pluripotent Stem Cells. *Am. J. Stem Cell* **2013**, *2* (2), 119–131.

(26) Lian, X.; Zhang, J.; Azarin, S. M.; Zhu, K.; Hazeltine, L. B.; Bao, X.; Hsiao, C.; Kamp, T. J.; Palecek, S. P. Directed Cardiomyocyte Differentiation from Human Pluripotent Stem Cells by Modulating Wnt/β-Catenin Signaling under Fully Defined Conditions. *Nat. Protoc.* **2013**, *8* (1), 162–175. https://doi.org/10.1038/nprot.2012.150.

(27) Tohyama, S.; Hattori, F.; Sano, M.; Hishiki, T.; Nagahata, Y.; Matsuura, T.; Hashimoto, H.; Suzuki, T.; Yamashita, H.; Satoh, Y.; et al. Distinct Metabolic Flow Enables Large-Scale Purification of Mouse and Human Pluripotent Stem Cell-Derived Cardiomyocytes. *Cell Stem Cell* **2013**, *12*, 127–137.

Chapter 5

Fast, Stable, Absolute Voltage Recordings with the Red-Shifted Indicator TMCRh.OMe

This work was conducted in collaboration with the following individuals:

Synthesis and characterization (fluorescence intensity) of carborhodamine VoltageFluors were performed by Gloria Ortiz.

A portion of the fluorescence lifetime data in serum-starved A431 cells was collected by Anneliese Gest.

Abstract

Transmembrane potential (V_{mem}) is a ubiquitous biophysical signal, with implications ranging from signal transmission in excitable cells to regulation of cell cycle progression. Optical strategies for accessing V_{mem} across diverse time and length scales have been developed, but they generally do not provide a fully electrophysiological profile of the cell, including the absolute value of V_{mem} in millivolts and the magnitude of V_{mem} changes that occurred. To fill this need, we designed and synthesized five red-shifted voltage dyes based on a photoinduced electron transfer V_{mem} sensing trigger and the carborhodamine chromophore. Using the best of these dyes, we develop a red-shifted platform for optical absolute V_{mem} recordings using fluorescence lifetime. We apply this platform to both extended (hundreds of measurements from the same cells over minutes) and to rapid (20 Hz) absolute V_{mem} measurements. With this system, we track spontaneous activity in excitable cells, recording the absolute V_{mem} waveform of beating cardiomyocytes in real time.

Introduction

Transmembrane potential (V_{mem}) arises from differences in ionic concentration across the plasma membrane of all cells. V_{mem} signals occur across timescales and may be either cell-autonomous or delocalized. Action potentials in cardiomyocytes and neurons last milliseconds,[1] but growth-related V_{mem} signals continue over hours to days.[2–4] With respect to spatial reach, V_{mem} may be localized within micron-scale structures such as organelles[5–7] or dendritic spines,[8] but it also can extend across tissues.[9,10] A complete understanding of V_{mem} signaling requires mapping of V_{mem} across these diverse time and length scales.

Electrode-based recording forms the basis of most of our knowledge about V_{mem}, but these techniques cannot report V_{mem} across all time and length scales of interest (**Chapter 1**). By physically contacting the cell of interest with a small electrode, patch clamp electrophysiology enables precise and rapid recording of V_{mem} from the cell body.[11] However, electrode-based V_{mem} recordings are damaging to the cell of interest and challenging to sustain on timescales longer than minutes. Washout of the cytosol by the pipette solution may affect the cellular property of interest,[12] and the electrode only reports V_{mem} at a single point of contact (space clamp error).[13,14] Furthermore, electrode recordings are low throughput and difficult to multiplex *in situ*, so V_{mem} patterning across many cells in a neuronal circuit or an electrically coupled tissue is impossible to interrogate.

To access multiplexed V_{mem} recordings in varied samples, significant progress has been made in optical detection of V_{mem} events such as action potentials. An array of tools, both genetically encoded (GEVIs) and small molecule, have been developed,[15,16] and recently these sensors have demonstrated the ability to record electrophysiological signatures from individual cells in awake, behaving animals.[17–19] In particular, the development of red-shifted voltage sensors has been transformative. Red-shifted sensors generally exhibit improved signal to noise, reduced phototoxicity, and access to deeper tissue regions.[20]

Despite these improvements, most optical V_{mem} recording strategies are based on fluorescence intensity, meaning that they can detect relative changes in V_{mem} but not assign a value to V_{mem} directly.[21] We refer to this value of V_{mem} in millivolts as the "absolute V_{mem}." Fluorescence intensity depends on probe concentration and illumination intensity, and it is sensitive to artifacts

arising from sample motion, focal plane drift, and region of interest selection. As a result, the fluorescence intensity is generally normalized into a relative change (ΔF/F), which reports the presence of V_{mem} changes but cannot report either absolute V_{mem} or the magnitude of absolute V_{mem} changes.

To fully characterize electrical signaling, the absolute resting membrane potential and the magnitude of any V_{mem} changes must be known. In order to do this optically, an additional fluorescence property beyond single-color intensity must be recorded. One successful approach is to use the fluorescence lifetime (τ), which is a measure of how long the dye remains in the fluorescent excited state.[22] τ is an intrinsic property of the sensor, so it does not depend on the probe concentration or illumination intensity. Although τ, like intensity, may depend on temperature, solvent, and ionic strength, it has been used to make absolute measurements of a wide range of cellular properties.[23]

For absolute V_{mem}, fluorescence lifetime imaging (FLIM) based V_{mem} recordings were first demonstrated with GEVIs, albeit with poor V_{mem} resolution.[24] We recently demonstrated that the use of small-molecule VoltageFluors as lifetime-based V_{mem} reporters improves the V_{mem} resolution 19-fold versus the GEVI CAESR (**Chapter 2**).[25] VoltageFluor (VF) probes, which report V_{mem} via changes in photoinduced electron transfer (PeT),[26,27] display a rapid, linear response to V_{mem} that translates favorably into fluorescence lifetime readings. Ratiometric fluorescence measurements from electrochromic stryl dyes can also be used for absolute V_{mem} recording,[28,29] although these measurements display lower V_{mem} resolution than VF lifetime-based recordings (**Chapter 2**).[25]

In FLIM, the use of red-shifted chromophores is particularly valuable, but no red-shifted FLIM system for absolute V_{mem} recording has been reported. To fit fluorescence lifetime decays with high accuracy, large numbers of photons per pixel are required (generally, 1000s). The use of a red-shifted V_{mem} sensor would allow larger photon flux from the sample without photodamage, enabling both higher frame rates and longer time series in FLIM. We have previously demonstrated that the VoltageFluor scaffold is compatible with chromophores across the visible spectrum, including those in the red and far-red.[30–33]

To this end, we combined the advantages of red-shifted VF indicators with the absolute quantitation of FLIM. Here, we report the design and synthesis of five novel red voltage dyes based on the carborhodamine fluorophore. From these five dyes, we selected TMCRh.OMe for characterization of its absolute V_{mem} sensing capabilities via fluorescence lifetime. Using TMCRh.OMe, we develop the first red-shifted system for lifetime-based absolute V_{mem} recordings. TMCRh.OMe displays higher V_{mem} sensitivity and a longer fluorescence lifetime than VF2.1.Cl, the VF used in VF-FLIM (**Chapter 2**). With this platform, we are able to record the V_{mem} response to EGF stimulation in A431 with 15 minutes of continuous illumination, opening up the possibility for extended absolute V_{mem} recordings with hundreds of time points in the same field of view. We also improve upon the temporal resolution of absolute V_{mem} recordings, accessing recording speeds up to 20 Hz. With these fast FLIM recordings, we track V_{mem} of spontaneously beating cardiomyocytes in real time and extract a complete electrophysiological profile from these cells.

Results

Synthesis and epifluorescence characterization of carborhodamine voltage dyes

We synthesized three carborhodamine fluorophores and five carborhodamine voltage indicators (**Scheme 5.1**). Further synthetic details are available in Gloria Ortiz's PhD dissertation. The voltage dyes exhibited red fluorescence absorption and emission from the carborhodamine chromophore (λ_{abs} 622 nm, λ_{em} 641 nm), consistently with previously reported properties of carborhodamine fluorophores.[34,35] Voltage dyes also displayed characteristic blue absorption from the molecular wire (**Figures 5.1, 5.2; Table 5.1**).[27] We measured the fluorescence quantum yield of all five voltage dyes (**Table 5.1**). We observed the largest quantum yield (0.62) for TMCRhZero (**13**), consistent with its lack of a dimethyl aniline electron donor that could quench the fluorescence. The quantum yields of all other voltage dyes were approximately 6 to 18 fold lower than the TMCRhZero derivative.

All voltage dyes stained HEK293T cell membranes with minimal internalization. isoTMCRh.OMe (**17**) produced the highest fluorescence intensity at the membrane (~5x higher than TMCRhZero), a somewhat surprising result given its low quantum yield. All derivatives displayed visible V_{mem} sensitivity in HEK293T. We observed the highest voltage sensitivity in TMCRh.OMe **15** (18 ± 2% ΔF/F per 100 mV) and the lowest voltage sensitivity in TMCRhZero **13** (0.3 ± 0.1%). These trends are similar to V_{mem} sensitivity patterns seen with other VoltageFluors, where we hypothesize that the added electron density of the methoxy-substituted molecular wire increases the dynamic range of PeT accessible to the molecule.[27] Because of its superior signal-to-noise, we selected TMCRh.OMe for further investigation in fluorescence lifetime imaging studies, along with TMCRhZero as a voltage-insensitive control compound.

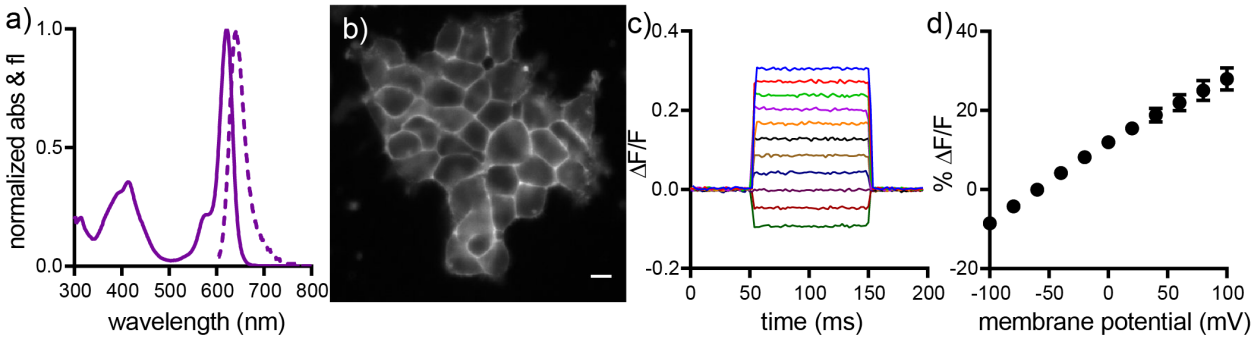

Figure 5.1. Characterization of TMCRh.OMe (15) voltage sensitivity in HEK293T.
a) Absorption (solid line) and emission (dashed line) spectra of TMCRh.OMe (**15**) in PBS, pH 7.4, 0.1% SDS. b) Epifluorescence image of a group of HEK293T cells stained with 500 nM TMCRh.OMe. Scale bar is 10 µm. c) Change in fluorescence for a single HEK293T cell under whole cell voltage clamp conditions in which the membrane potential was stepped from +100 to -100 mV in 20 mV increments. d) Average fluorescence intensity change (%ΔF/F) observed across multiple voltage-clamped HEK293T cells.

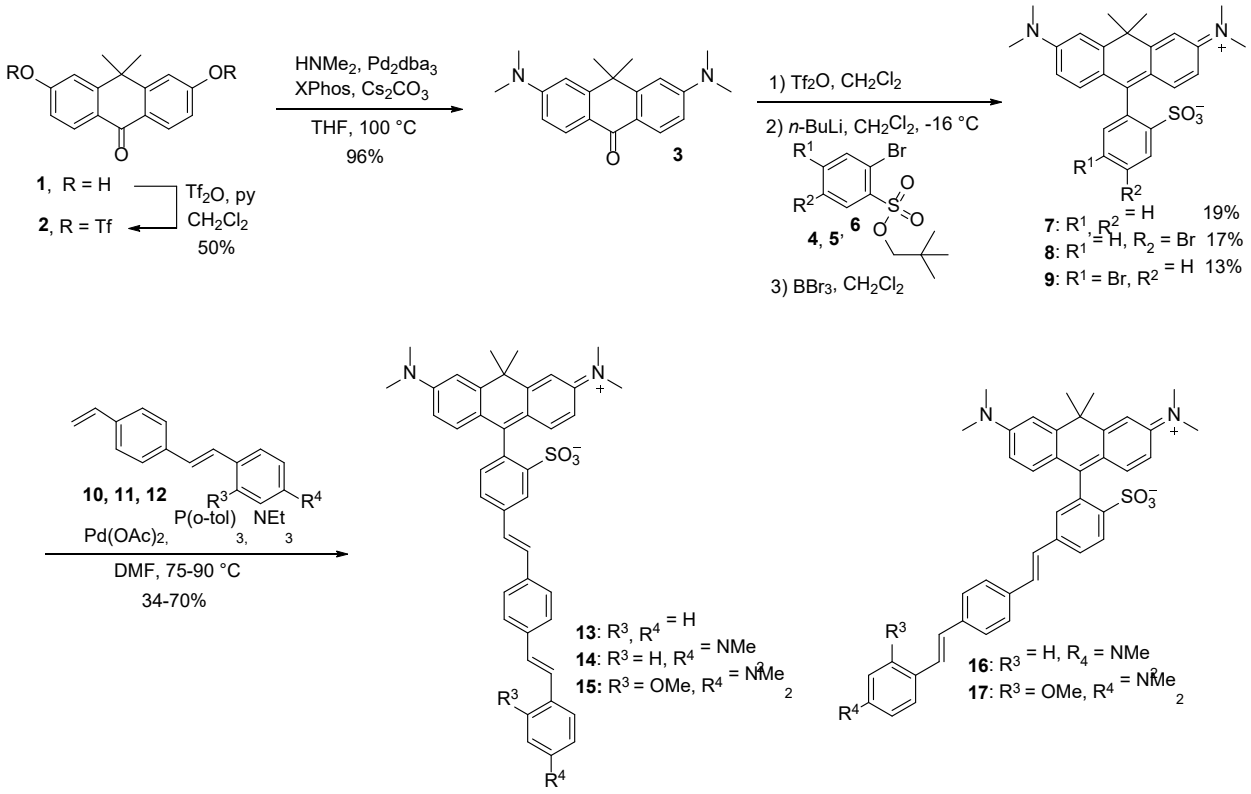

Scheme 5.1. Synthesis of carborhodamine fluorophores (7-9) and voltage dyes (13-17).

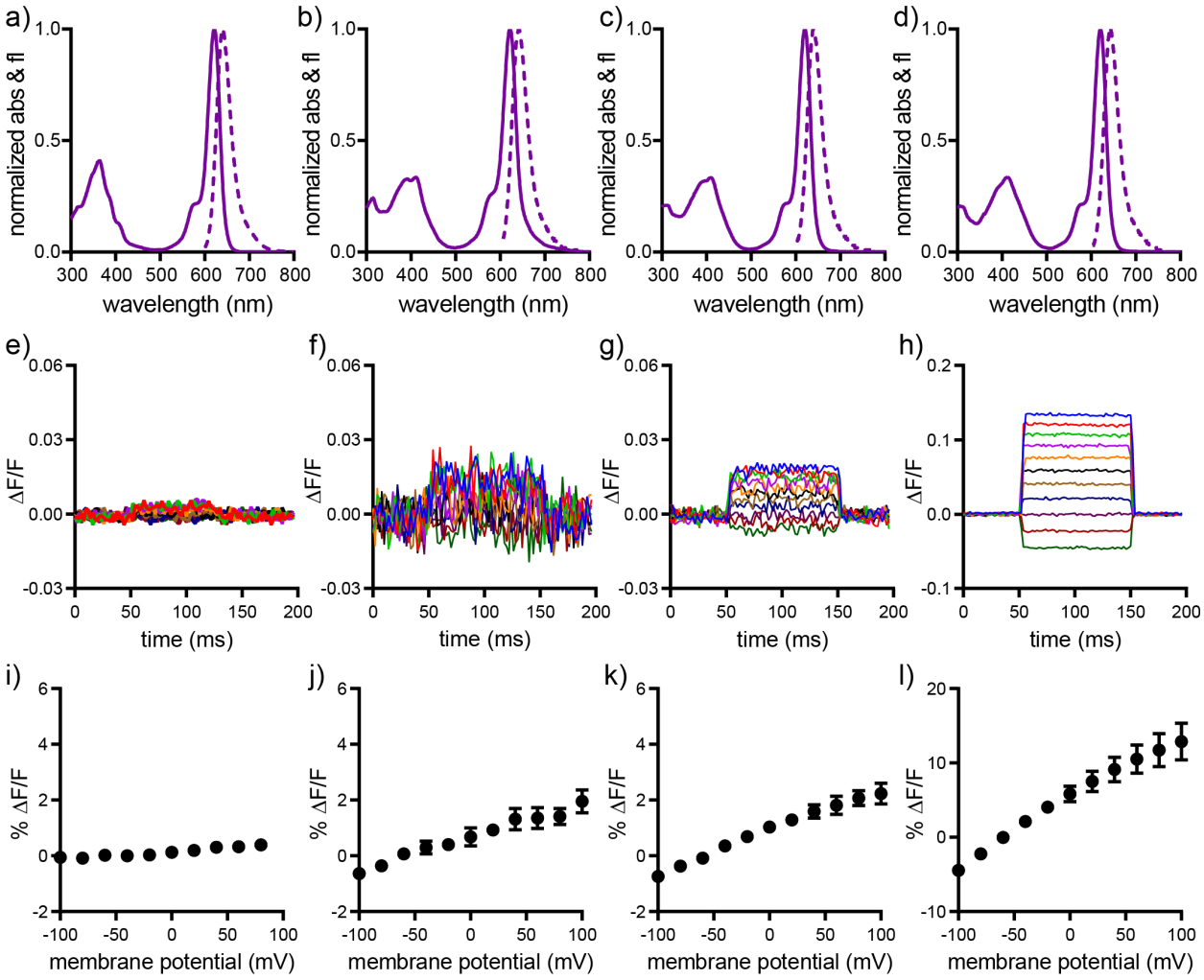

Figure 5.2. Characterization of voltage sensitivities of other carborhodamine voltage dyes. Voltage sensitivity of TMCRh dyes. a,e) **13**; b,f) **14**; c,g) **16**; and d,h) **17**. Upper row: Plots of fractional change in fluorescence (ΔF/F) vs time for HEK cells held at -60 mV and stepped to 100 ms hyper- and depolarizing steps in 20 mV increments (±100 mV) under whole-cell voltage-clamp conditions. Lower row: Plots of % ΔF/F vs. final membrane potential (mV) for n = 4-7 cells for each TMCRh dye. Error bars are ± S.D.

Compound	R^3	R^4	λ_{max} / nm[a]	λ_{em} / nm[a]	$\Phi^{a/b}$	$\Delta F/F$ / 100 mV[c]	Relative brightness[d]
TMCRhZero **13**	H	H	622	641	0.62/0.61	0.3% ± 0.1%	3.9 ± 0.12
TMCRh.H **14**	H	NMe_2	622	642	0.096/0.087	1.2% ± 0.4%	1.0 ± 0.04
TMCRh.OMe **15**	OMe	NMe_2	622	642	0.038/0.027	18% ± 2%	3.8 ± 0.13
isoTMCRh.H **16**	H	NMe_2	621	641	0.050/0.057	1.5% ± 0.2%	5.4 ± 0.22
isoTMCRh.OMe **17**	OMe	NMe_2	621	641	0.058/0.054	9% ± 2%	17 ± 0.84

Table 5.1. Photophysical properties of carborhodamine voltage dyes.
[a] Determined in PBS, pH 7.4, 0.1% SDS. [b] Determined in MeOH. [c] Voltage-clamped HEK cells. Error is ± S.D. for n = 4-7 cells. [d] Determined in HEK cells. Error is ± S.E.M for n = 4 coverslips (>100 cells per coverslip) for relative brightness.

Calibration of fluorescence lifetime in cells

We recorded the time resolved fluorescence decay of the TMCRh fluorophore **7** at 1 μM in water with time correlated single photon counting (TCSPC) FLIM on a line scanning confocal microscope (Zeiss LSM 880). Excitation at 637 nm was provided by a pulsed diode laser. The time-resolved fluorescence decay was well described by a single exponential model and exhibited a lifetime of 3.06 ± 0.02 ns (mean ± SEM of 16 measurements). We then measured the fluorescence lifetime of TMCRh.OMe in HEK293T cells at rest (**Figure 5.3**), which was also best described by a single exponential decay. We observed a mean lifetime of 2.52 ± 0.07 ns (mean ± SD of 103 cell groups). In serum-starved A431 cells, the lifetime of TMCRh.OMe was similar (2.6 ± 0.1 ns, mean ± SD of 18 cell groups). For the voltage-insensitive control compound TMCRhZero in HEK293T (**Figure 5.4**), we again observed a single exponential decay with a lifetime of 3.70 ± 0.01 (mean ± SD of 103 cell groups). We measured lifetimes across a range a range of dye loading concentrations to look for concentration quenching (**Figure 5.5**), which we observed with green VoltageFluors (**Chapters 2 and 4**). All subsequent experiments were conducted at concentrations below the point where concentration quenching was observed (approximately 500 nM in HEK293T culture).

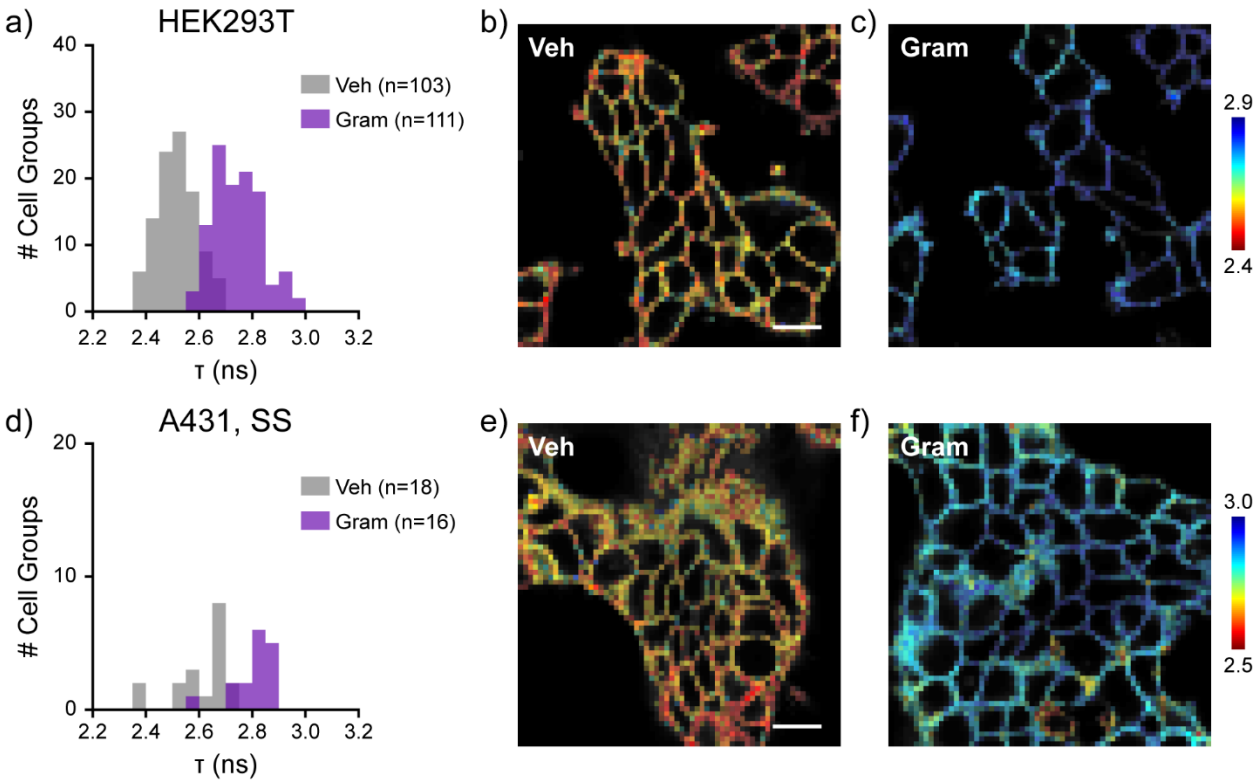

Figure 5.3. Lifetime of TMCRh.OMe in cells at rest and depolarized with gramicidin.
a) Histogram of lifetimes observed for 300 nM TMCRh.OMe in groups of HEK293T at rest (vehicle, Veh, 0.05-0.1% DMSO) and treated with 500 ng/mL gramicidin (Gram). b) Lifetime-photon count overlay image of HEK293T at rest and c) treated with 500 ng/mL gramicidin. d) Histogram of TMCRh.OMe lifetimes observed in groups of serum starved (SS) A431 cells at rest and depolarized with gramicidin. e-f). Lifetime images of SS A431 at rest and gramicidin-treated, as in (b)-(c). Bin sizes were determined by the Freedman-Diaconis rule. Scale bars represent 20 µm. Photon counts of lifetime-photon count overlay images are not scaled to each other.

We were unable to perform patch-clamp electrophysiology on this FLIM microscope to record the lifetime-V_{mem} calibration curve directly, so we turned to the Na^+/K^+ ionophore gramicidin[36] (**Figure 5.3**). Because it increases the permeability to both Na^+ and K^+, we expect that gramicidin will depolarize cellular V_{mem} to approximately 0 mV. In HEK293T cells treated with 500 ng/mL gramicidin, the fluorescence lifetime of TMCRh.OMe rose to 2.74 ± 0.09 ns (mean ± SD of 111 cell groups). When we increased the gramicidin concentration to 1 µg/mL, there was no further increase in the fluorescence lifetime (2.75 ± 0.04 ns, mean ± SD of 50 cell groups). We observed a similar increase in fluorescence lifetime in serum-starved A431 cells treated with gramicidin. This total change of 225 ps between vehicle and gramicidin treated cells is larger than the change seen for VF2.1.Cl treated similarly (**Appendix 3**). These results suggest that TMCRh.OMe has a sensitivity (slope) for its lifetime-V_{mem} calibration around 4 or 4.5 ps/mV and a 0 mV lifetime (y-intercept) near 2.7 ns.

Surprisingly, the spread in the lifetimes observed with and without 500 ng/mL gramicidin was similar. We would expect that a compound that moves all cells to 0 mV would decrease the variability in the measured lifetime. We did observe a slight decrease in the standard deviation at

1 µg/mL gramicidin, but we used 500 ng/mL gramicidin for further experiments to minimize nonspecific effects on the membrane and cell health.

We also recorded the fluorescence lifetime of TMCRhZero in HEK293T at rest and after incubation with 0.5 or 1 µg/mL of gramicidin (**Figure 5.4**). We observed a slight change in the lifetime at 1 µg/mL gramicidin. However, the effect was much smaller than that observed with the voltage-sensitive compound TMCRh.OMe, suggesting that gramicidin does not directly modulate the fluorescence of the carborhodamine chromophore.

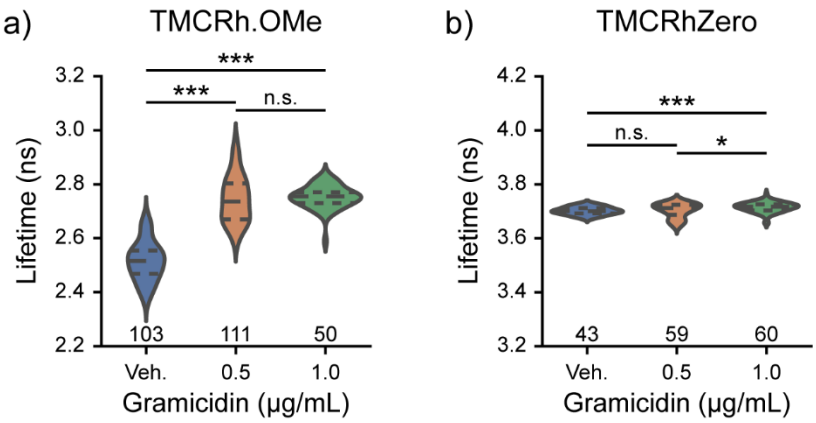

Figure 5.4. Gramicidin effects on TMCRh.OMe and TMCRhZero lifetimes.
a) Violin plots of the fluorescence lifetime of TMCRh.OMe in HEK293T incubated with varying concentrations of gramicidin or DMSO vehicle. Dashed lines within plots indicate the first quartile, median, and third quartile of the data. Significant differences between groups were observed (Welch's one-way ANOVA, $F(2, 166.3) = 352.86$, $p<0.001$). Data for vehicle and 500 ng/mL are reproduced from **Figure 5.3**. b) Fluorescence lifetime of TMCRhZero in HEK293T plotted as in (a). Significant differences between groups were observed (Welch's one-way ANOVA, $F(2,104.5) = 8.70$, $p<0.001$). Asterisks indicate the results of Games-Howell post hoc tests (n.s. $p>0.05$, * $p<0.05$, ** $p<0.01$, *** $p<0.001$). Sample sizes (number of cell groups) are indicated on the plot for each category. Veh. = 0.05-0.1% DMSO.

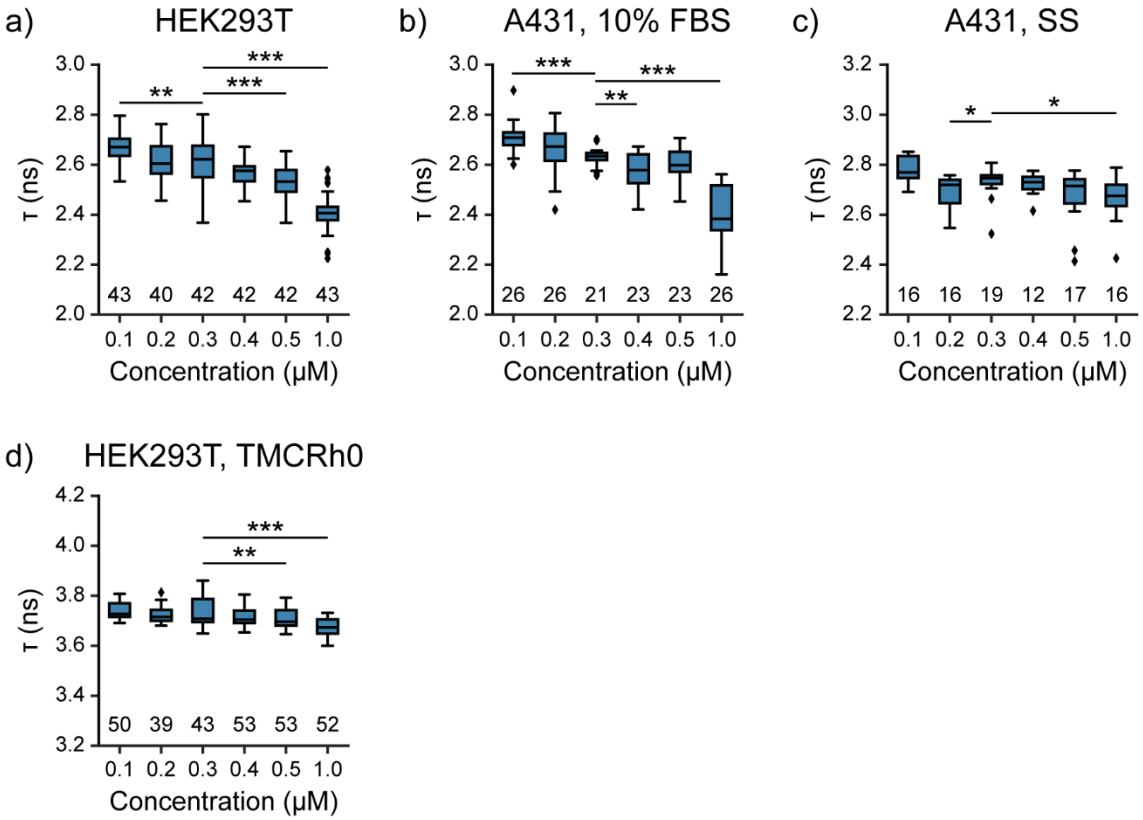

Figure 5.5. Effect of dye concentration on lifetime in cultured cell lines.
a) Box plot of the fluorescence lifetime of TMCRh.OMe at varying concentrations in HEK293T. Significant differences were observed between groups (Welch's ANOVA, $F(5,113.8)=76.6$, $p<0.001$). b) The fluorescence lifetime of TMCRh.OMe at varying concentrations in A431 cultured in complete media (10% FBS). Significant differences were observed between groups (Welch's ANOVA, $F(5,64.3) = 33.36$, $p<0.001$). c) Concentration dependence of TMCRh.OMe fluorescence lifetime in serum starved A431 cells (SS). Significant differences were observed between groups (Kruskal-Wallis test, $H(5) = 23.1$, $p<0.001$). d) Concentration dependence of TMCRhZero (voltage-insensitive compound) fluorescence lifetime in HEK293T. Significant differences were observed between groups (Kruskal-Wallis Test, $H(5) = 70.8$, $p<0.001$). Asterisks represent the results of Games-Howell or Dunn's pairwise post hoc tests, as appropriate (n.s. $p>0.05$, * $p<0.05$, ** $p<0.01$, *** $p<0.001$). For clarity, only the result of post hoc tests with the 300 nM concentration are shown, as it was the concentration used for further studies. Whiskers represent the range of data or 1.5 times the interquartile range; diamonds represent outliers determined by the Tukey method.

TMCRh.OMe lifetime enables extended absolute V_{mem} recordings

A key advantage of red-shifted voltage sensors is the ability to record for long periods of time with low phototoxicity. To evaluate TMCRh.OMe FLIM in this context, we recorded the response of serum-starved A431 cells to re-introduction of EGF (500 ng/mL) for 15 minutes. We previously performed this experiment with the green VoltageFluor VF2.1.Cl (**Chapter 2**).[25] Using that system and an LSM 510 scanning confocal microscope, we were able to make six, intermittent V_{mem} measurements within a 15 minute time window, with each measurement lasting 30 seconds.

With TMCRh.OMe as a voltage indicator and an improved confocal microscope (LSM 880), we were able to record continuously for 15 minutes, with each measurement lasting 5 seconds across a field of view 1.5 fold larger than the VF2.1.Cl study (**Figure 5.6**, total of ~180 V_{mem} measurements). Samples treated with imaging buffer vehicle displayed consistent lifetimes, although some showed a steady downward trend of 20-40 ps in total (**Figure 5.7**), likely the result of temperature equilibration (see below). The control TMCRhZero displayed a steady, slight shortening of the lifetime, although of lesser magnitude than TMCRh.OMe.

In EGF-treated samples, we observed an immediate lifetime decrease of 75 ps on average with a steady return to baseline that did not complete within 15 minutes (**Figure 5.8**), consistent with the expected hyperpolarization. The magnitude of this change is again larger than that seen with VF-FLIM, where a lifetime shortening of 40-50 ps upon EGF addition was typical. We did not observe signs of phototoxicity in these recordings (increasing lifetime or changing cell morphology in the vehicle control).

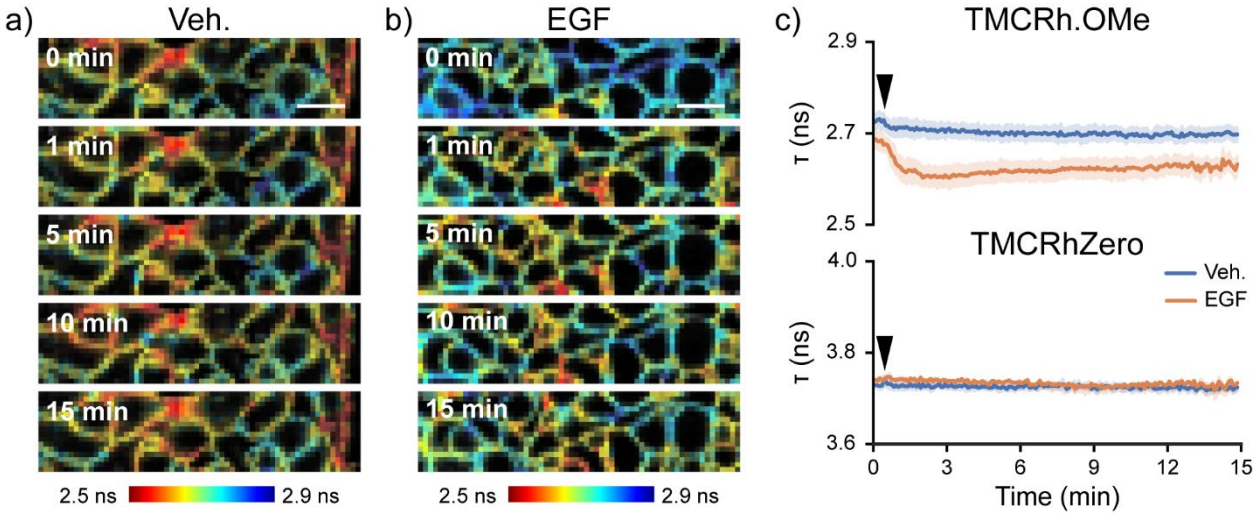

Figure 5.6. Continuous, 15 minute recordings of A431 response to EGF treatment.
a) Snapshots from a τ time series of serum-starved A431 cells treated with imaging buffer (IB) vehicle to illustrate baseline changes in lifetime during the recording session. b) Snapshots of serum-starved A431 cells treated with EGF 20 seconds into the recording period. c) Mean lifetime of TMCRh.OMe (top) and TMCRhZero (bottom) across the full recording. Shading represents standard error of the mean. Vehicle or 500 ng/mL EGF was added at the black arrow. Sample sizes: TMCRh.OMe Veh 5, EGF 5; TMCRhZero Veh 3, EGF 3.

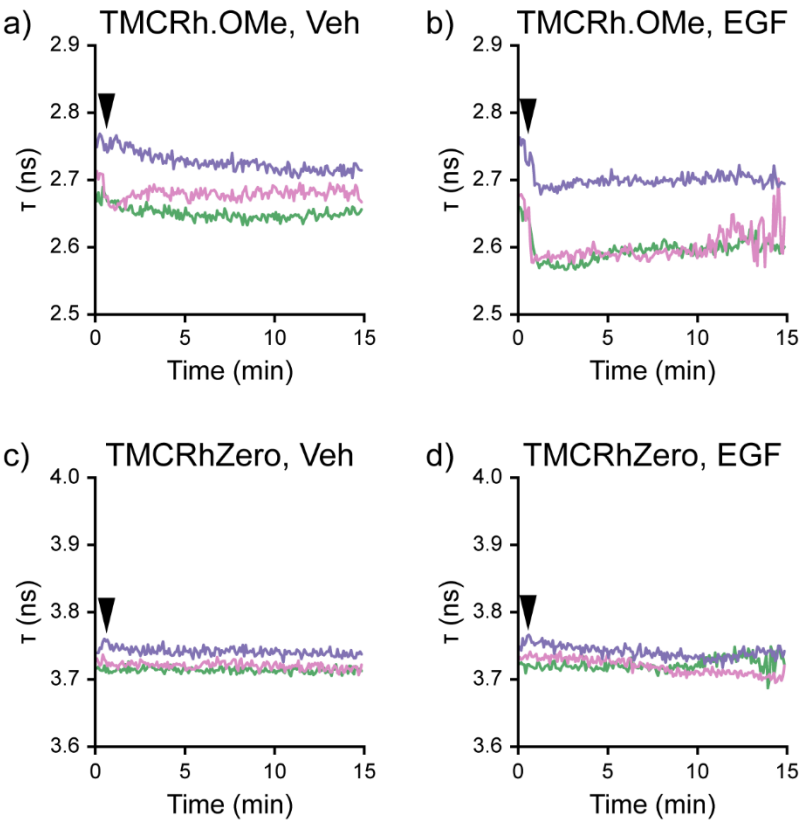

Figure 5.7. Individual recordings of the A431 V_{mem} response to EGF treatment.
Representative individual trials for TMCRh.OMe stained A431 treated with a) vehicle (Veh) or b) 500 ng/mL EGF. Representative individual trials for TMCRhZero stained A431 treated with c) vehicle (Veh) or d) 500 ng/mL EGF. Vehicle or EGF was added at the black arrow. Recordings are quantified as the average lifetime per frame for all contiguous cells in the field of view. Colors represent distinct recordings; there is no relationship for colors between panels.

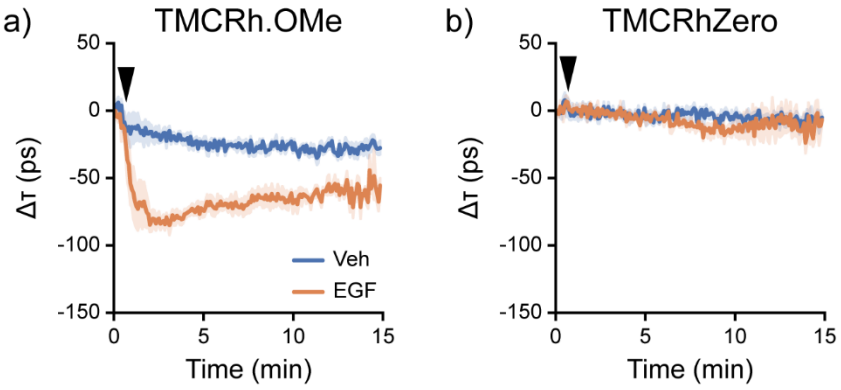

Figure 5.8. Average τ change for TMCRh.OMe, TMCRhZero in EGF-stimulated A431 cells. Data are reproduced from **Figure 5.6** as the mean change in τ relative to the first frame of each recording. Data for vehicle (Veh) or 500 ng/mL EGF treatment are shown for a) TMCRh.OMe and b) TMCRhZero. Veh or EGF was added at the black arrow. Shading represents SEM.

Absolute V_{mem} recordings of cardiomyocyte spontaneous action potentials in real time

To demonstrate the improved temporal resolution and stability to motion of our absolute V_{mem} sensing platform, we monitored the absolute V_{mem} of spontaneously beating human induced pluripotent stem cell derived cardiomyocytes (iCMs). Upon loading TMCRh.OMe or TMCRhZero into iCM monolayers, we observed membrane localized fluorescence, with a minimal amount of punctate, intracellular staining (**Figure 5.9A, 5.10**). Because we are using a confocal pinhole larger than 1 airy unit to maximize photon count, some regions of the membrane appear as flat sheets where they traverse the optical section at a near-horizontal angle.

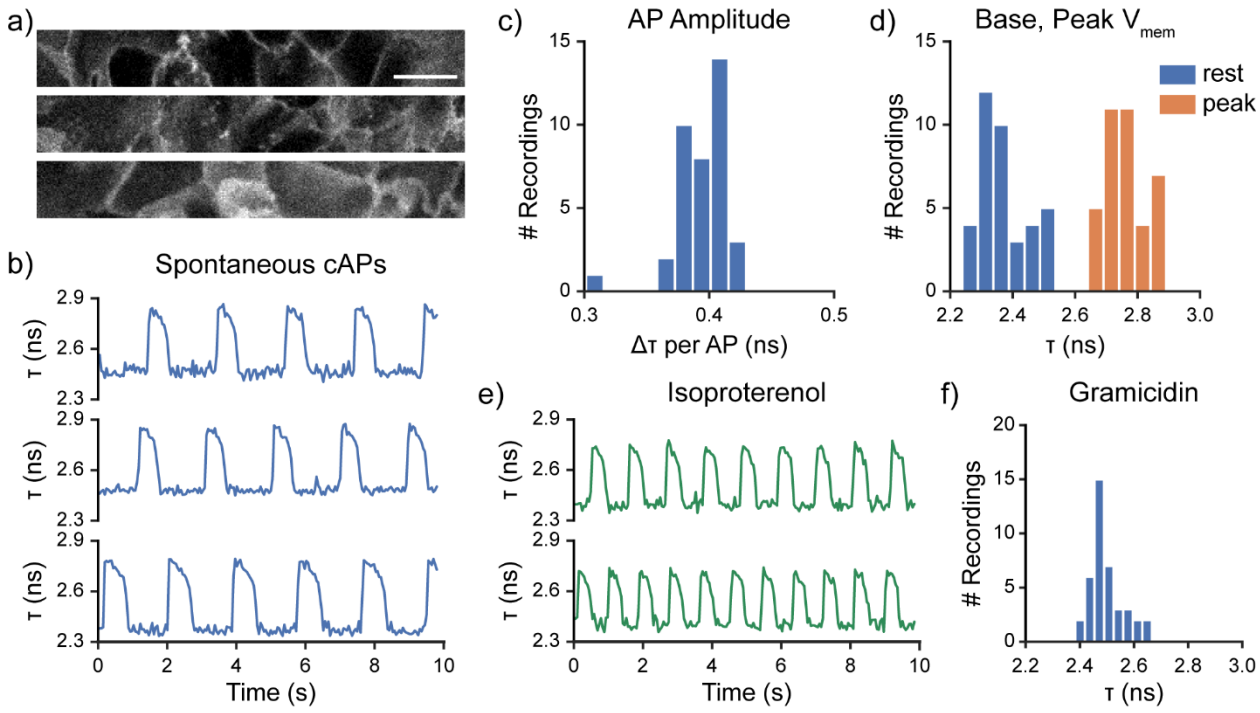

Figure 5.9. TMCRh.OMe lifetime reports absolute V_{mem} during cardiac action potentials. a) Representative confocal images of regions of iCMs used for 20 Hz lifetime imaging. Images here are fluorescence intensity only and were acquired for 400 ms (line averaged) to improve contrast. iCMs were stained with 500 nM TMCRh.OMe. Scale bar is 20 µm. b) Fluorescence lifetime of TMCRh.OMe, quantified from the fields of view in (a). c) Amplitude of iCM action potentials, as measured by the change in τ of TMCRh.OMe. Data represent 38 recordings from 8 iCM wells. d) Fluorescence lifetime at the rest (between APs, blue) or at the action potential peak (orange) from the iCM recordings in (c). e) Representative recordings of TMCRh.OMe absolute V_{mem} imaging of iCMs treated with 1 µM isoproterenol, which accelerates beat rate. f) Histogram of TMCRh.OMe lifetimes in cardiomyocytes treated with 500 ng/mL gramicidin (n=40 recordings from 8 wells). Lifetime reported here is the average τ across the 10 second recording. Bin size for all histograms was determined by the Freedman-Diaconis rule.

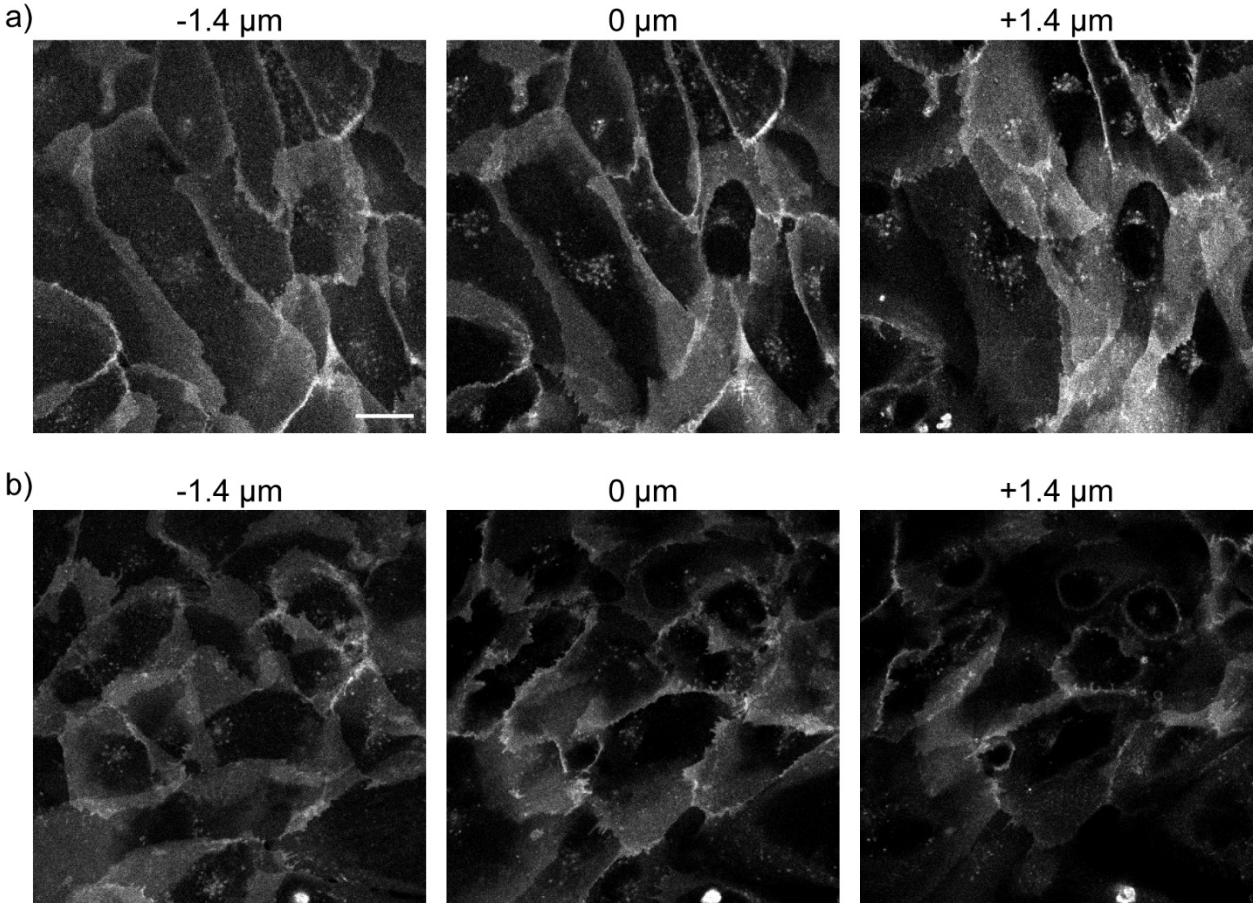

Figure 5.10. TMCRh.OMe staining in iCMs is membrane-localized.
Confocal z stack images of two fields of view (a) and (b) of iCMs stained with 500 nM TMCRh.OMe. Slices were recorded every 0.7 µm; only a representative set are shown. Data were taken with the confocal pinhole set to the same settings as for FLIM (4.5 AU, 3.8 µm section). Scale bar is 20 µm.

The action potential (AP) in iCMs is typically on the order of 500 ms in duration. Intensity-based V_{mem} imaging techniques in cardiomyocytes generally use sampling rates between 50 and 500 Hz,[37–39] but fluorescence lifetime imaging studies in other systems rarely exceed frame rates of 0.1 Hz. Using TCSPC FLIM, we acquired a raw lifetime data stream at 40 Hz (25 ms acquisition per frame). We opted to bin successive pairs of frames to produce a final recording with 20 Hz frame rates and dramatically reduced noise in lifetime from the increase in photon count (**Figure 5.9D, Figure 5.11**). The limiting factor in the achievable frame rate was the speed at which the TCSPC electronics could process photons (i.e. the pile-up limit). We did not observe phototoxicity to the sample or drift in the lifetime; this is consistent with our ability to acquire continuously for 15 minutes in A431 cells (**Figure 5.6**).

We observed a very stable lifetime baseline and consistent action potential morphology throughout all 10 second, 20 Hz frame rate recordings (**Figure 5.11A**). We used TMCRhZero to further verify that lifetime is insensitive to motion artifacts from the iCM contraction. Recordings with this

voltage-insensitive derivative are stable throughout the 10 second acquisition, despite normal contraction of the iPSCs (**Figure 5.12**).

In contrast, the photon count (fluorescence intensity) showed both a variable baseline and a variable AP waveform (**Figure 5.11B**), presumably attributable to motion artifacts as the cardiomyocytes contract. Even though all wells and fields of view were loaded with the same concentration of dye (500 nM), the baseline intensity varied widely between recordings. Differences in the amount of membrane in the field of view (**Figure 5.9A**), as well as differences in focal plane, are likely responsible for this. Normalizing the photon count into relative fluorescence units (**Figure 5.11C**), as is common with fluorescence intensity imaging, did not fully resolve these artifacts. Although the baseline was generally more consistent, gradual drifting was still visible. Furthermore, artifacts in the action potential morphology from cellular contraction (motion) were not resolved by this normalization.

Using TMCRh.OMe as a proxy for absolute V_{mem}, we catalogued the action potential amplitude, resting τ, and peak τ across 40 iCM recordings (**Figure 5.9B,C**). We observed a consistent lifetime change of 0.394 ± 0.004 ns (mean ± SEM of 40 recordings across two differentiations). iCM action potentials are typically 100 mV in amplitude, although they may range from 80-100 mV depending on differentiation conditions.[40–42] The observed AP height therefore suggests that TMCRh.OMe has an absolute V_{mem} sensitivity of approximately 4 ps/mV (perhaps up to 4.9 ps/mV if AP amplitude is 80 mV). Resting τ (2.37 ± 0.01 ns) and peak τ (2.76 ± 0.01 ns) were somewhat more variable than the AP amplitude for these cells. We tested for concentration quenching by determining these AP parameters at TMCRh.OMe concentrations of 300 nM, 500 nM, and 1 μM (**Figure 5.13**). Minimal differences between concentrations were observed.

Because we are not able to perform simultaneous electrophysiology and lifetime imaging on this microscope, we again turned to gramicidin to approximate 0 mV in the iCM culture (**Figure 5.9F, Figure 5.12C**). iCMs incubated with 500 ng/mL gramicidin displayed a lifetime of 2.50 ± 0.01 ns (mean ± SEM of 40 recordings). The change in lifetime between baseline and gramicidin suggests a depolarized resting V_{mem} around -30 mV, which is inconsistent with reported resting V_{mem} of iCMs between -45 and -70 mV.[40–42] Furthermore, our iCMs were able to fire APs of approximately 100 mV, which would require them to achieve the unlikely peak V_{mem} of +70 mV from a starting V_{mem} of -30 mV. Taken together, these data suggest that this dose of gramicidin may have incompletely depolarized the iCMs. A more detailed dose response study, as well as concurrent electrophysiology, could help resolve this discrepancy.

To push the temporal resolution of TMCRh.OMe FLIM further, we treated iCMs with the β adrenoreceptor agonist isoproterenol, which increases beat rate (**Figure 5.9E**). Under these conditions, we observed spontaneous APs at approximately twice the frequency (~1.2 Hz versus ~0.6 Hz). Even with this more rapid activity, we were able to record the full AP waveform and a consistent baseline τ. As expected with an increase in beat rate, AP duration shortened in isoproterenol treated cells. AP amplitude appeared slightly smaller than in treated cells, and baseline τ remained unchanged.

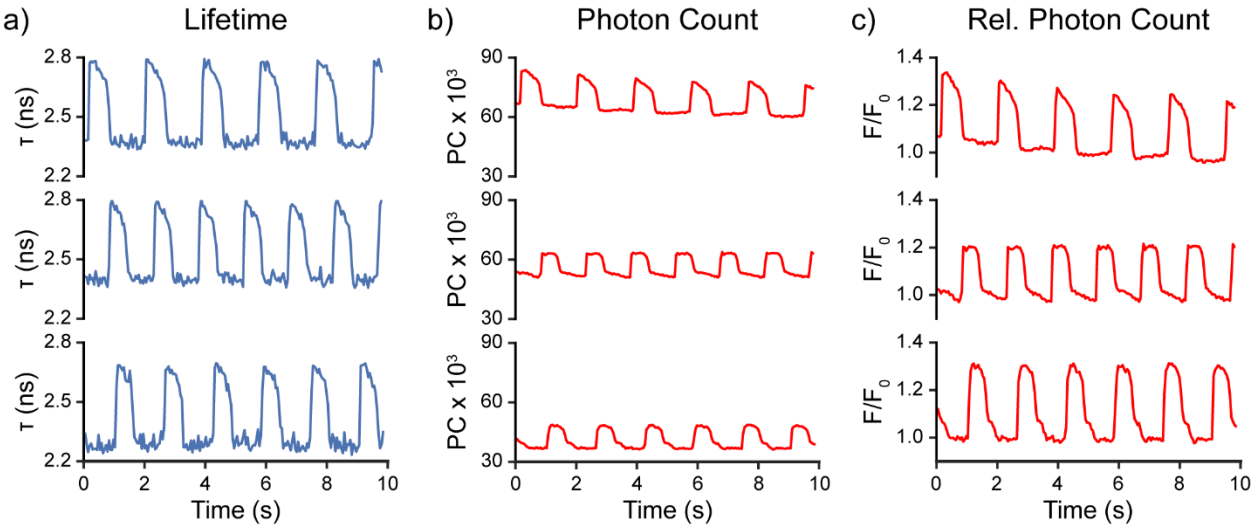

Figure 5.11. Comparison between lifetime, photon count, and relative photon count.
a) Fluorescence lifetime recordings from 3 representative fields of view. Data are not filtered or processed in any way after fitting. b) Photon count recordings from the same fields of view as in (a). c) Relative photon count (photon count divided by the average photon count baseline) for the same fields of view as in (a).

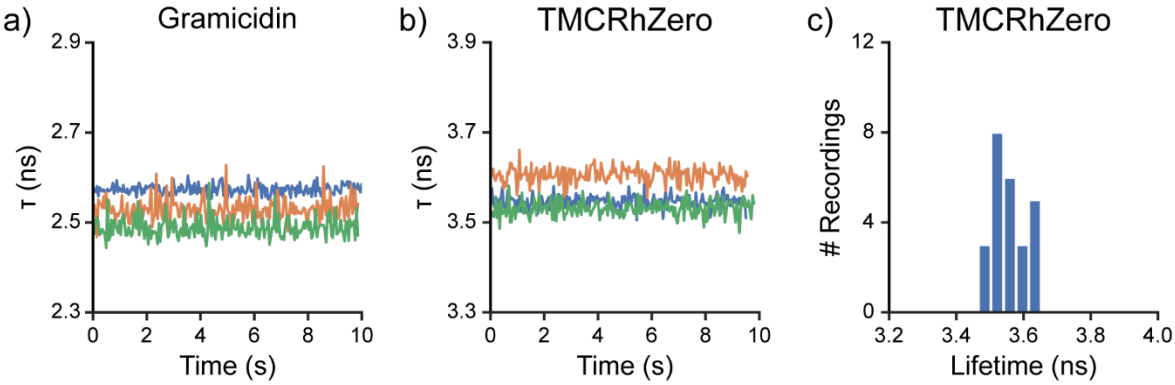

Figure 5.12. Stability of τ during gramicidin and TMCRhZero recordings.
a) Three representative single-trial recordings of TMCRh.OMe fluorescence lifetime in iCMs incubated with 500 ng/mL gramicidin. Gramicidin incubation arrested beating in these samples. b) TMCRhZero fluorescence lifetime in spontaneously beating iCMs. c) Histogram of TMCRhZero lifetimes observed in iCMs (n=25 recordings from 5 wells). Bin size was determined by the Freedman-Diaconis rule.

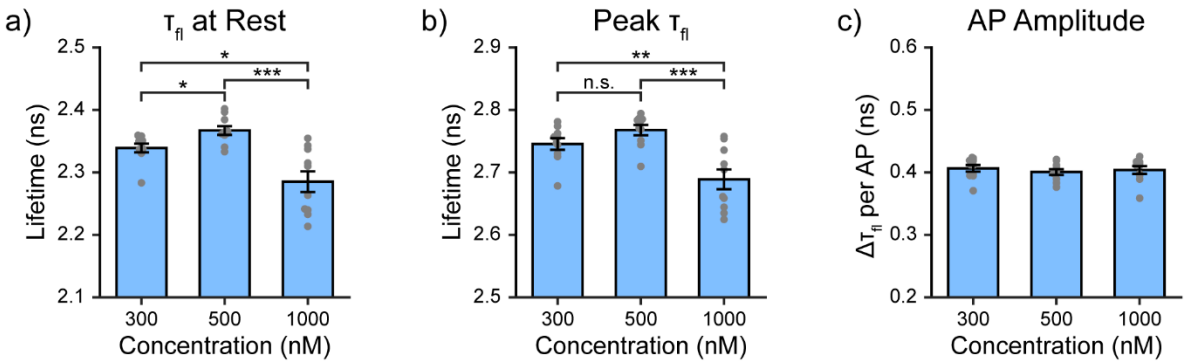

Figure 5.13. Effects of TMCRh.OMe concentration on recorded iCM APs.
a) Resting lifetime of TMCRh.OMe iCMs at different probe concentrations. Significant differences between concentrations were observed (Welch's ANOVA, $F(2,16.80) = 11.35$, $p=0.0008$). b) Lifetime at the peak of iCM action potential (AP) at different TMCRh.OMe concentrations. Significant differences between conditions were observed (Welch's ANOVA, $F(2, 17.13)=9.48$, $p=0.0017$). c) Action potential height (difference between resting and peak lifetime) at 300, 500, and 1000 nM TMCRh.OMe. No significant differences between concentrations were observed (Fisher's ANOVA, $F(2,27)=0.291$, $p=0.75$). Data are shown as mean ± SEM of 10 recordings from two wells for each concentration. Asterisks reflect the significance level of Games-Howell post hoc tests (n.s. $p>0.05$, *$p<0.05$, **$p<0.01$, *** $p<0.001$). The 500 nM data shown here is a subset of the data shown in **Figure 5.9**.

Discussion

We synthesized five new voltage dyes based on the tetramethylcarborhodamine chromophore and compared their brightness and sensitivity in fluorescence intensity. We took the most promising candidate in the series, TMCRh.OMe, and used it as a probe of absolute V_{mem} with fluorescence lifetime imaging. With TMCRh.OMe FLIM, we achieved improved temporal resolution, reduced phototoxicity, and improved V_{mem} sensitivity over FLIM approaches with green VFs. Below, we compare trends seen in fluorescence intensity and fluorescence lifetime and discuss how TMCRh.OMe expands the reach of optical absolute V_{mem} recordings.

Relating fluorescence intensity, quantum yield, and lifetime

The time-resolved fluorescence decays of TMCRh.OMe and TMCRhZero can be modeled by a single exponential decay in cells. This result is in contrast to VF2.1.Cl and its V_{mem}-insensitive counterpart VF2.0.Cl, which were modeled by a biexponential model and a single exponential model, respectively (**Chapter 2**).[25] Single exponential decay models are convenient for data analysis, especially in biological samples with limited photon counts. Because the single exponential model contains fewer free parameters than the biexponential model, data can be processed effectively with lower photon count.[43] Because total photon count limits the resolution of lifetime maps, this reduction in model complexity translates into improved spatial and/or temporal resolution in FLIM images.

Differences in trends seen with fluorescence lifetime and intensity are most likely attributable to probe loading. Fluorescence lifetime is related to the intrinsic brightness of a fluorophore, or, in

our case, a readout of how much PeT is occurring in a V_{mem} sensor. As we would expect, the lifetime of the voltage-insensitive compound TMCRhZero is over 1 ns longer than the lifetime of the voltage sensitive compound TMCRh.OMe (**Figure 5.4**). However, they have similar fluorescence intensity in cells (**Table 5.1**). The most likely explanation for this is that there are actually fewer TMCRhZero molecules in the membrane than TMCRh.OMe molecules when the two dyes are loaded at the same nominal concentration. The concentration dependence of the fluorescence lifetime is consistent with this hypothesis (**Figure 5.5**). Concentration quenching does not appear in the TMCRhZero compound until 1 μM probe is loaded, whereas concentration quenching is visible for TMCRh.OMe around 500 nM in HEK293T cells. Of course, we cannot rule out that structural differences between TMCRh.OMe and TMCRhZero alter the favorability of concentration quenching, even at the same actual probe concentration in the membrane. To better validate this, and to discriminate between PeT modulation and probe delivery, it would be informative to investigate the lifetimes of other carborhodamine-based voltage dyes in this series.

The difference between in vitro quantum yield (**Table 5.1**) and lifetime in cells suggests that the fluorescence properties of the carborhodamine voltage dyes are strongly solvent dependent. The fluorescence lifetime of TMCRhZero is 1.5 fold longer than the fluorescence lifetime of TMCRh.OMe in HEK293T, but the quantum yield of TMCRhZero is 16 fold higher. With the same core fluorophore, quantum yield and lifetime should be highly correlated; this difference suggests that the dyes behave differently in aqueous or MeOH solution than they do in the plasma membrane. In further evidence of solvent dependence, the lifetime of the carborhodamine fluorophore alone is 3.1 ns in water, but the TMCRhZero compound displays a lifetime of 3.7 ns in HEK293T cell membranes. Taken together, these data highlight the importance of measuring VoltageFluor properties in a lipophilic environment; similar trends were observed with aniline modified fluorescein-based VFs (**Chapter 4**).

Comparing the V_{mem} sensitivity and brightness of TMCRh.OMe and VF2.1.Cl

Functional imaging data suggest that TMCRh.OMe has improved brightness and absolute sensitivity versus VF2.1.Cl. The magnitude of the lifetime changes associated with gramicidin treatment in HEK293T (**Figure 5.3**), EGF treatment of A431 cells (**Figure 5.8**), and spontaneous iCM action potentials (**Figure 5.9**) all point to an absolute sensitivity at or above 4 ps/mV. The 0 mV lifetime appears to be approximately 2.7 ns. This value is a full nanosecond longer than VF2.1.Cl in cell membranes, and combined with its higher extinction coefficient, it indicates that TMCRh.OMe is fundamentally brighter than VF2.1.Cl. Electrode-based calibration is required to confirm this and to determine the absolute V_{mem} resolution of TMCRh.OMe; such studies are a priority for future investigations.

Interestingly, the relative sensitivity of the fluorescence intensity (%ΔF/F per 100 mV) of VF2.1.Cl is higher than that of TMCRh.OMe, highlighting essential differences between relative (intensity based) and absolute (lifetime based) sensitivity. %ΔF/F depends on the starting fluorescence intensity of the sensor, as well as how much the signal changes with V_{mem}. As we observed with aniline-modified VoltageFluors (**Chapter 4**), very dim probes such as JuloVF may have a large percent turn-on but a low absolute sensitivity to V_{mem}. The sensitivity in lifetime ($\Delta\tau$/mV) measures only the V_{mem}-dependent change in lifetime and is not relative to the starting lifetime or brightness. The lifetime change is a better predictor of signal-to-noise (**Chapter 4**), highlighting the power of fluorescence lifetime in understanding dye performance.

Synthesis of a voltage dye that is both brighter and more sensitive is difficult to achieve. We have observed this brightness-sensitivity tradeoff with fluorescein-based VFs (**Chapter 4**). The improvement in both regimes seen with TMCRh.OMe makes it an interesting candidate for additional synthetic modification. Specifically, TMCRh.OMe has a relatively long lifetime, despite incorporating one of the more electron donating molecular wires used in VoltageFluor studies.[27,30,31] Incorporation of an even more electron rich molecular wire could further improve the balance between PeT and fluorescence. produce even higher absolute V_{mem} sensitivity.

TMCRh.OMe FLIM improves the temporal resolution and reach of absolute V_{mem} imaging

In this study, we perform functional absolute V_{mem} imaging at 20 Hz, which is a 300-fold improvement in temporal resolution over VF-FLIM.[25] Reduced phototoxicity, simpler lifetime decay, and strong absorption of common pulsed laser lines all contribute to the excellent performance of TMCRh.OMe. FLIM frame rates are limited by photon counts; enough photons must be obtained to fit the selected decay model to the data. Because of its red-shifted spectrum and reduced phototoxicity, we are able to obtain higher photon count rates from TMCRh.OMe. With VF-FLIM, light power (and therefore emitted photo counts) had to be kept low to reduce phototoxicity and photobleaching of the sensor. The TMCRh.OMe fluorescence decay can be modeled with a single fit component, enabling analysis with fewer photons than VF2.1.Cl (biexponential decay model). Furthermore, TMCRh.OMe's peak absorption is close to the peak of our pulsed laser line, and the chromophore itself has a higher extinction coefficient than dichlorofluorescein.[26,34]

Our current acquisition speeds are limited by how many photons can be processed by the photon counting electronics (photon pile-up limit).[43] Splitting of the emitted photon stream between multiple photon counting cards or use of a laser with a faster repetition rate could increase the pile-up limit and further improve temporal resolution.

Some factors improving the properties of TMCRh.OMe in this study could be related to improvements to the microscope as well as the voltage dye. TCSPC FLIM data for TMCRh.OMe was taken on a substantially upgraded confocal microscope with a faster scan head and better photon collection efficiency (Zeiss LSM 880 versus a Zeiss LSM 510 for VF-FLIM). However, investigation of VF2.1.Cl lifetime on an LSM-880 did not produce a dramatic change in its lifetime properties (**Appendix 2**), suggesting that the majority of the observed improvement here lies with properties of TMCRh.OMe.

TMCRh.OMe FLIM also enables the acquisition of longer absolute V_{mem} time series, which is critical for the study of slower V_{mem} events. In studying the A431 EGF response, we were able to acquire at least 180 separate 5 second exposures without notable phototoxicity (**Figure 5.6**), which is 30 times more images than could be acquired with the VF-FLIM system. Although the stability of TMCRh.OMe localization to the plasma membrane would have to be evaluated, long term absolute V_{mem} imaging, such as over the course of cell division or migration, is a promising future application of this technology.

Gramicidin as a potential alternative to electrode-based calibrations

Although optical techniques can make V_{mem} recordings in samples inaccessible to electrodes, these strategies still require some sort of calibration, often with an electrode. Here, we investigated gramicidin as a pharmacological means to clamp cellular V_{mem} at 0 mV. Because the sensitivity

(slope) of VF2.1.Cl in different contexts appeared relatively consistent, it is possible that a single point measurement to determine the y-intercept is all that is needed to translate the lifetime-V_{mem} calibrations between systems.

Nevertheless, caution is warranted in interpretation of gramicidin as an exact 0 mV point. The amount of gramicidin to reach 0 mV may differ between systems; in cardiomyocytes, the depolarization with gramicidin appears incomplete (**Figure 5.9**). Furthermore, we observed aberrant results with ionophores and VF2.1.Cl (**Appendix 3**), and similar artifacts were previously reported with other V_{mem} sensitive dyes.[44] Rigorous comparison between an electrode-based 0 mV point and a gramicidin 0 mV point for TMCRh.OMe is the best way to determine the value of gramicidin-based calibration. Such work is ongoing in our laboratory.

Extended recordings of EGF-induced hyperpolarization in A431 cells

We recorded the V_{mem} response to EGF in A431 cells with superior time resolution than in previous studies.[25] Previous work examining this response with high temporal resolution was conducted in heterologous model systems, such as 3T3 cells expressing EGFR.[45,46] When hyperpolarization was detected in these model systems, it was often accompanied by oscillations in V_{mem} on the timescale of seconds to minutes. With TMCRh.OMe FLIM, we did not detect oscillatory V_{mem} behavior in A431 cells, suggesting that the dynamics of the V_{mem} response may be different in A431 and the systems studied previously. We cannot rule out the alternative explanation that the isolated cells used for electrophysiology experience V_{mem} oscillations, but these oscillations are somehow buffered via electrical coupling with the surrounding cells or obscured by our analysis. Although different regions of the cell group have different starting lifetimes, all regions exhibit shorter lifetimes following EGF treatment (**Figure 5.6B**), suggesting that the hyperpolarizing response is shared across the field of view. Separation of the V_{mem} response in adjacent cells is challenging, as the membranes of adjacent cells are both stained with TMCRh.OMe and cannot be resolved with standard confocal microscopy. Expansion of VF-FLIM to include covalently targeted VFs could produce sparser labeling and afford an elegant strategy to shed light on heterogeneity in the V_{mem} response with cellular resolution.[47–49]

Although 15 minutes of continuous illumination was well tolerated by the sample, there was slight to moderate baseline drift in the vehicle recordings. Our current experimental set-up for EGF addition does not allow for precise temperature control during the recordings, and we hypothesize that this drift is due to heating of the samples near the microscope. The source of the heat appears to be the microscope body itself, rather than heat transfer from laser illumination, as the drift occurs even across multiple fields of view that were not illuminated (data not shown). Improved temperature regulation and equilibration, as well as heated perfusion, would likely result in more stable lifetime recordings and could perhaps improve absolute V_{mem} resolution by eliminating a source of voltage-independent variability.

Fast, absolute V_{mem} imaging in excitable cells

We recorded the absolute V_{mem} waveform of spontaneous cardiac action potentials in real time, both at their natural beat rate and with accelerated beating from isoproterenol treatment. Because cardiomyocyte electrical activity is accompanied by motion (contraction), lifetime is a particularly attractive strategy for recording V_{mem}. Unlike the intensity (photon count) data, lifetime recordings were free of motion artifacts and consistently reported normal AP waveforms (**Figure 5.11**). We

observed very consistent action potential amplitudes (400 ps), with slightly more variable resting (diastolic) V_{mem} and peak V_{mem}.

Resting membrane potential and AP amplitude change over the course of differentiation and maturation. Adult cardiomyocytes have a resting V_{mem} of approximately -80 mV,[50,51] whereas iPSC-derived cardiomyocytes tend to display immature electrical phenotypes and depolarized resting V_{mem} (-70 to -45 mV).[40–42] We envision that TMCRh.OMe FLIM will be highly useful in characterizing the electrical properties of iCMs and mature cardiomyocytes, towards the development of improved differentiation protocols. Optical recordings can be made in intact monolayers without dissociation to single cells, avoiding space clamp artifacts associated with electrode-based recordings.[13,14] Furthermore, electrical coupling within the tissue could be assessed via the homogeneity (or inhomogeneity) of resting V_{mem} in various regions. To our knowledge, such a tool does not currently exist in the cardiomyocyte field.

With VF2.1.Cl lifetime-V_{mem} calibrations, we saw slight differences between different cell lines used. It remains to be seen whether iCMs of varying maturities or differentiation stage would show differences in their lifetime-V_{mem} calibrations. Direct interrogation of this with electrode-based calibration would be required for rigorous interpretation of lifetime results in terms of absolute V_{mem}. Despite this, we believe that the greatly improved ease and non-invasiveness of optical absolute V_{mem} recordings makes them a promising technology.

It is important to note the tradeoff between spatial and temporal resolution in FLIM. In achieving 20 Hz absolute V_{mem} imaging, we completely eliminated spatial resolution in the images; this was only possible because the iCM AP occurs as a large, concerted V_{mem} event. To retain cellular resolution, as with the A431 EGF studies, we reduced the frame rate to 0.2 Hz. Therefore, expansion of TMCRh.OMe to other excitable activity, such as recording of action potentials in neurons, poses a continued challenge, as neuronal APs are ~100 fold faster than cardiac APs and are not delocalized across many cells. To access sufficient frame rates and signal levels to study such events, investigation of other strategies for fast lifetime recordings is warranted.[52,53]

Conclusion

We synthesized five carborhodamine voltage-dyes with red excitation and emission profiles. One of these dyes, TMCRh.OMe, displayed favorable performance for absolute V_{mem} via fluorescence lifetime imaging. With TMCRh.OMe, we achieved real-time, absolute V_{mem} recordings in excitable tissue, improving the temporal resolution of VoltageFluor FLIM absolute V_{mem} recordings 300-fold. The improved photostability also enables extended absolute V_{mem} recordings, with hundreds of FLIM measurements in the same field of view without damage to the sample. TMCRh.OMe FLIM technology will facilitate optical recordings of absolute V_{mem} both at high speeds and over the course of longer cellular events such as cell division or differentiation.

Materials and Methods

Materials

Synthetic information and chemical characterization are available in Gloria Ortiz's Ph.D. dissertation. Dyes were stored either as solids at room temperature or as 1 mM stock solutions in DMSO at -20°C. All stock concentrations were determined via the absorbance of the carborhodamine chromophore using a 2501 Spectrophotometer (Shimadzu).

Epidermal growth factor (Peprotech) was made up as a 1 mg/mL stock solution in water and stored at -80°C. Gramicidin (Sigma-Aldrich) was purchased as a mixture of A, B, C, and D from *Bacillus brevis*. 1 µg/mL stocks of gramicidin were made up in DMSO and stored at -20°C. Isoproterenol was a gift from the Healy lab at UC Berkeley and was stored as a 10 mM stock in DMSO at -20°C.

Cell line maintenance and microscopy sample preparation

HEK293T and A431 cells were obtained from the UC Berkeley Cell Culture Facility. Both cell lines were verified by STR profiling (short tandem repeat) and were tested routinely for mycoplasma. Cell lines were discarded after 25 passages. Cells were maintained in complete DMEM (Gibco, Thermo Fisher Scientific) supplemented with 4.5 g/L glucose, 2 mM GlutaMAX (Gibco), and 10% FBS (Seradigm) in a 37°C humidified incubator at 5% CO_2. Cells were passaged into fresh complete media every few days following dissociation with trypsin-EDTA (Gibco, 0.05% for HEK293T, 0.25% for A431). Residual trypsin was removed from A431 cells by centrifugation for 5 minutes at 300xg.

For imaging experiments, cells were plated onto prepared poly-D-lysine (PDL)-coated coverslips. Coverslips (#1.5, either 12 mm of 25 mm diameter, Electron Microscopy Sciences) were acid washed for 2-5 hours in 1 M HCl. Coverslips were then washed three times overnight in 100% ethanol, followed by three times overnight in MilliQ (Millipore) purified water. Coverslips were sterilized by heating for 2-3 hours in a glassware oven to 150°C. Prior to seeding of cells, coverslips were incubated in 1x PDL (Sigma-Aldrich, made as a 0.1 mg/mL solution in phosphate-buffered saline with 10 mM Na_3BO_4) for 1-10 hours and then washed twice with sterile water and twice with 1x Dulbecco's Phosphate Buffered Saline (dPBS, Gibco).

For probe loading and gramicidin treatment experiments, HEK293T were seeded onto prepared coverslips in complete DMEM at a density of 42-52 $x10^3$ cells per cm^2 (in a 6 well or 24 well tissue culture plate, Corning) and imaged approximately 24 hours after plating. For electrophysiology experiments, HEK293T were seeded at 26,000 cells/cm^2 in low glucose DMEM (Gibco; 1 g/L glucose, 1 mM sodium pyruvate, 2 mM GlutaMAX, 10% FBS) and used 12-24 hours after plating.

A431 cells were serum deprived prior to use (**Chapter 2**).[25] Briefly, cells were seeded onto PDL-coated glass coverslips at a density of 83,000 cells/cm^2 in low serum DMEM (4.5 g/L glucose, 2 mM GlutaMAX, 2% FBS) two days prior to imaging experiments. 3.5-5.5 hours prior to imaging, media was exchanged for serum-free DMEM (4.5 g/L glucose, 2 mM GlutaMAX).

Culture of human induced pluripotent stem cell (hiPSC) derived cardiomyocytes

Cardiomyocyte culture and differentiation were performed as described in **Chapter 4**. Imaging experiments were performed approximately two weeks after cells were seeded onto Matrigel-coated 24 well plates.

Epifluorescence microscopy

Imaging was performed on an AxioExaminer Z-1 (Zeiss) equipped with a Spectra-X Light engine LED light (Lumencor), controlled with Slidebook (v6, Intelligent Imaging Innovations). Images were acquired with a W-Plan-Apo 20x/1.0 water objective (20x; Zeiss). Images were focused onto either an OrcaFlash4.0 sCMOS camera (sCMOS; Hamamatsu) or an eVolve 128 EMCCD camera (EMCCD; Photometrix). For TMCRh images, the excitation light was delivered from a LED (4.5 W/cm^2; 20 ms exposure time) at 631/28 (bandpass) nm and emission was collected with a quadruple emission filter (430/32, 508/14, 586/30, 708/98 nm) after passing through a quadruple dichroic mirror (432/38, 509/22, 586/40, 654 nm LP).

For epifluorescence imaging experiments, carborhodamine voltage dyes were loaded at 500 nM in HEK293T HBSS (Gibco) for 20 minutes at 37°C in a humidified incubator with 5% CO_2. Coverslips were washed once with HBSS and transferred to fresh HBSS for imaging. All epifluorescence imaging was conducted under ambient atmosphere.

Whole cell patch clamp electrophysiology

Pipettes were pulled from borosilicate glass with filament (Sutter Instruments, Novato, CA) with resistances ranging from 4 to 7 MΩ with a P97 pipette puller (Sutter Instruments). Internal solution composition, in mM (pH 7.25, 285 mOsmol/L): 125 potassium gluconate, 10 KCl, 5 NaCl, 1 EGTA, 10 HEPES, 2 ATP sodium salt, 0.3 GTP sodium salt. EGTA (tetraacid form) was prepared as a stock solution in 1 M KOH before addition to the internal solution. Pipettes were positioned with an MP-225 micromanipulator (Sutter Instruments). Voltage clamp protocols for epifluorescence experiments were not corrected for liquid junction potential.

Electrophysiology recordings were made with an Axopatch 200B amplifier and digitized with a Digidata 1440A (Molecular Devices). Cells were held at -60 mV and potentials from +100 to -100 mV were applied in descending order with 20 mV steps. Signals were sampled at 50 kHz and filtered with a 5 kHz low-pass Bessel filter. Correction for pipette capacitance was performed in the cell attached configuration. Recordings were only included if they maintained a 30:1 ratio of membrane resistance (R_m) to access resistance (R_a) and an R_a value below 30 MΩ throughout the recording.

Spectroscopic studies

UV-Vis absorbance and fluorescence spectra were recorded using a 2501 Spectrophotometer (Shimadzu) and a Quantamaster Master 4 L-format scanning spectrofluorometer (Photon Technologies International). The fluorometer is equipped with an LPS-220B 75-W xenon lamp and power supply, A-1010B lamp housing with integrated igniter, switchable 814 photon-counting/analog photomultiplier detection unit, and MD5020 motor driver. Samples were measured in 1-cm path length quartz cuvettes (Starna Cells).

Sample preparation and treatment for fluorescence lifetime imaging

For all experiments following concentration optimization (conc curve supplement) in HEK293T or A431, TMCRh.OMe and TMCRhZero were used at 300 nM, directly from a 1 mM (3333x) DMSO stock (final DMSO concentration in loading solution, 0.03). 1x loading solutions were prepared in imaging buffer (IB, made in-house; composition in mM: 139.5 NaCl, 10 HEPES, 5.6 D-glucose, 5.33 KCl, 1.26 $CaCl_2$, 0.49 $MgCl_2$, 0.44 KH_2PO_4, 0.41 $MgSO_4$, 0.34 NaH_2PO_4; 290 mOsm/L; pH 7.25). Osmolarity was determined with a μOsmette (Precision Instruments). Cells were incubated at 37°C for 20-25 minutes in loading solution, washed once in IB, and transferred to fresh IB in an Attofluor cell imaging chamber (Invitrogen).

iCMs were loaded in RPMI with B27 supplement without phenol red containing 500 nM of TMCRh.OMe or TMCRh Zero (0.05% final concentration of DMSO). Media was exchanged for fresh RPMI-B27 without phenol red before imaging.

Gramicidin solutions were prepared at either 0.5 μg/mL or 1 μg/mL in IB immediately before use. Immediately after dye loading, HEK293T and A431 were incubated for 5 minutes at room temperature IB containing either gramicidin or DMSO vehicle. Coverslips were then transferred to fresh IB with gramicidin or vehicle and imaged. To minimize media changes and time at room temperature for iCMs, iCMs were incubated for 5 minutes at 37°C in RPMI-B27 containing 0.5 μg/mL gramicidin and then imaged in the same media.

A431 EGF treatment was performed as described previously (**Chapter 2**).[25] On the day of the experiment, 2x EGF (1 μg/mL) solutions were prepared in IB. Approximately twenty seconds into the recording, 500 μL of IB or IB containing 2x EGF was gently pipetted into the imaging chamber (which contained 500 μL IB). IB control recordings were made prior to EGF treatment recordings from a different field of view on the same sample.

Most imaging experiments except for those involving serum starved A431 cells were conducted under ambient atmosphere and at room temperature (18-22°C). To improve cell viability, some of the cardiomyocyte experiments were conducted with the XL incubation chamber on the LSM 880 set to 25°C. To minimize temperature fluctuations during extended recordings with serum-starved A431 cells, all work with these cells was conducted with the system incubation chamber set to 25°C and solutions pre-warmed to approximately 25°C. Samples were generally kept on the microscope for under 20 minutes; longer term EGF studies required samples to be kept on the microscope for up to 45 minutes.

Time Correlated Single Photon Counting (TCSPC)

Fluorescence lifetime imaging (FLIM) data were determined by TCSPC. Data were acquired on an inverted LSM 880 confocal microsope (Carl Zeiss AG, Oberkochen, Germany) equipped with a FLIM upgrade kit (PicoQuant GmbH, Berlin, Germany). The LSM 880 was controlled with Zen Black software (Zeiss); the TCSPC unit was controlled with SymPhoTime 64 software (PicoQuant). Pulsed excitation at 40 MHz was supplied with a 640 nm diode laser (PicoQuant LDH-P-C-640B with a ZET635/20x cleanup filter, AHF/Chroma; average output wavelength 637 nm) controlled by a PDL-800-D laser controller (PicoQuant). Laser intensity from the PDL-800-D was kept at 24% to optimize instrument response function (IRF) shape; excitation power at the

sample was controlled with a micrometer in the laser combining unit (PicoQuant). Power at the sample was adjusted to maximize count rate without exceeding the pile-up limit (a count rate of 4e6 photons/s at any individual pixel, 10% of the laser repetition rate). Because the dye was localized to membranes, large regions of the field of view were relatively dark, so average count rates varied from 1e5-2e6 counts per second depending on the sample and field of view. Average power at the sample ranged from 1-5 µW.

Excitation light was coupled to the microscope with a polarization-maintaining single mode fiber and passed through a line pass dichroic (MBS 405/488/560/640) before reaching the sample. Emitted photons were collected with a 63x oil/1.4 NA Apochromat objective (Zeiss) immersed in Immersol 518F (Zeiss). The confocal pinhole was set to 300 (4.5 AU, optical slice thickness of approximately 3.9 µm), increasing the size of the optical section but improving photon count rates for TCSPC. A 690/70 nm bandpass emission filter (AHF) was used. Single photons were detected with a PMA-Hybrid 40 detector (PicoQuant) and processed with a TH260 Pico Dual TCSPC Unit (T3 TCSPC mode). The detector parameters used were the following: constant fraction discriminator (CFD) -100 mV, zero cross -10 mV, offset -47000 ps. Sync parameters used were the following: CFD -150 mV, zero cross -10 mV, offset 0 ps, sync divider 8. Data were acquired with 1000 TCSPC time channels (0.025 ns/channel). The IRF was measured each day from a sample of 1 mg/mL erythrosin B through the same imaging substrate (#1.5 coverglass or ibidi 24 well plate). 1 µM TMCRh (small molecule dye head) in water was recorded daily as an additional standard to verify correct instrument function.

Monodirectional scanning was used for all applications except iCM spontaneous activity, where bidirectional scanning was used. Bidirectional scan correction is not possible in SymPhoTime, so the images of cardiomyocyte field of view (FOV) were acquired in Zen (same acquisition settings as FLIM, with the addition of 16x line averaging). Spatial and temporal resolution of the data acquisition for specific applications is enumerated in the table below.

Application	Raw Frame Acquisition Time (s)	Binned Frame Acquisition Time (s)	Number of Time Points (Total Time Series Duration)	Image Size (width x height, μm^2)	Pixel Size of Lifetime Image (binned, μm^2)
Single Image	0.94	75-90	1 (75-90 s)	135 x 135	2.1 x 2.1
EGF Treatment	0.63	5	36 (180 s), 177 (900 s)	135 x 33.7	6.3 x 6.3 *
iCM Spontaneous Activity	0.025	0.050	200 (10 s)	135 x 18	N/A (global analysis)

Table 5.2. Spatiotemporal resolution of fluorescence lifetime imaging data.
"Single image" data includes concentration curve loading tests and gramicidin treatment in cell lines (**Figures 5.3-5.5**). EGF time series are shown in **Figures 5.6-5.8**. iCM spontaneous activity data are shown in **Figures 5.9 and 5.10-5.13**. Raw frame acquisition time reflects the frame rate at which data were captured; successive frames were combined for later analysis to obtain good photon statistics. The number of time points is the number of analyzed, binned frames. *For EGF

treatment, pixel size after standard binning is the same as single images (2.1 x 2.1 μm^2). To improve photon statistics for pixelwise fitting, moving average binning was performed during analysis, as is common for Becker & Hickl FLIM products (e.g. SPCImage). Therefore, the lifetimes at each pixel were determined by photons from a 6.3 x 6.3 μm^2 area centered on the displayed pixel. The photon count image is displayed at the native resolution (2.1 μm per side of pixel).

Fluorescence lifetime data analysis

Time resolved fluorescence decays I(t) were modeled as a monoexponential decay (equation 5.1) in custom Matlab code via a weighted least-squares approach. A represents the amplitude of the photon count signal and τ represents the fluorescence lifetime. TMCRhZero was well-modeled by a single exponential decay; TMCRh.OMe contained slight structure in the residuals but two component decays resulted in overfitting.

$$I(t) = Ae^{-t/\tau} \quad [5.1]$$

Minimization of the reduced chi squared (χ^2, equation 5.2) was used to determine the final parameter values, where n is the number of free parameters (number of fit time channels – number of free parameters in model), st is the first fit time channel, fi is the final fit time channel, z is the value of the fit model, and x is the value of the experimentally measured decay. Poisson weighting of the time channels was used.

$$\chi^2 = \frac{1}{n}\sum_{i=st}^{fi}\frac{(z_i - x_i)^2}{|z|} \quad [5.2]$$

The built-in minimization function fmincon with the interior-point algorithm was used, with the following settings: StepTolerance 1e-4, OptimalityTolerance 1e-4, ConstraintTolerance 1e-6. All fits converged in fewer than the maximum number of function evaluations (1e5). The fluorescence lifetime τ was constrained between 0 and 10 ns.

The experimentally measured instrument response function (IRF, erythrosin B fluorescence decay) was cropped time channels 40-60 out of 1000 channels (25 ns) and reconvolved with the decay model before the reduced chi squared was determined. The time resolved signal was binned by a factor of 4 in time (to 250 channels representing 25 ns) before fitting was performed to reduce fit noise with low photon counts. Time channels 20 through 980 (st through fi) of the unbinned signal were used in the fit where photon counts were sufficient. Otherwise, the final time bin used was the first instance of zero photon counts in a time channel. The shift between the IRF and the measured time resolved decays was fixed to 0. The offset (time-independent background) was also fixed to 0; dark counts were generally negligible (20-40 counts per second during experiments). A threshold of 5000 total photons was used in pixelwise analysis. Pixels with photon counts below this threshold were excluded from analysis and appear black in images. Spatial binning was performed before fitting for pixel by pixel analysis (**Table 5.2**). For global analysis of cardiomyocyte data, all photons in the field of view were used to fit one decay per time point.

Analysis of cardiomyocyte spontaneous action potential recordings

For action potential detection, lifetime recordings were transformed into a series of differences between successive frames ("difference trace"). This difference trace was filtered with a 6^{th} order low pass Butterworth filter with the signal processing toolkit in SciPy (scipy.signal). A threshold that differentiated between action potentials and baseline was selected manually. The peak lifetime was defined as the value of the lifetime at the index identified by the above process. For each recording, the peak is reported as the mean of peaks of all action potentials in the recording. No filtering was used on lifetime traces shown or on lifetime data used for analysis; filtering was used exclusively in peak identification.

The baseline was defined from a series of 15 frames (750 ms) before the peak of each action potential (AP), beginning 20 frames before the peak and ending 5 frames before the peak. While this omits some areas of the baseline, it allows automatic processing at a variety of beat rates. The baseline reported for each recording is the average lifetime in all of these 15 frame windows except the first, which was often cut off by the start of the recording. For example, if a recording contained 6 APs, the baseline τ would represent the average of 75 frames of lifetime data (15 frames per AP from 5 APs).

The peak height was calculated as the average baseline subtracted from the average peak for each trace. For recordings containing gramicidin or made with TMCRhZero, no APs were visible, so the lifetime reported is the average across all frames in the 10 second recording.

For analysis of the photon count data (**Figure 5.11**), photon count data were taken from the same indices as defined by the lifetime trace (see above). The relative fluorescence intensity (F/F_0) was calculated by dividing each value in the photon count trace by the average photon count baseline.

Statistical analysis

Data are reported as either mean ± standard deviation (SD) or mean ± standard error of the mean (SEM) throughout the text (as indicated). All aggregated data were acquired across at least two independent experimental days.

For analysis of differences between groups, all datasets were tested for normality (Shapiro-Wilk test) and homoscedasticity (Levene's test on the median) before ANOVA was applied. For data that were both normal and homoscedastic, Fisher's one-way ANOVA with Tukey-Kramer post hoc tests was used ($p>0.05$ on both the Shapiro-Wilk test and Levene's test). For data that were non-normally distributed and homoscedastic, the Kruskal-Wallis test with Dunn's test for pairwise post hoc tests was used. For data that were heteroscedastic ($p<0.05$ on Levene's test), Welch's one-way ANOVA with Games-Howell post hoc tests was used, even if the data were significantly non-normal by Shapiro-Wilk. All statistical analysis was performed in Python using the SciPy, Scikit-Posthocs and Pingouin[54] statistical packages.

References

(1) Bean, B. P. The Action Potential in Mammalian Central Neurons. *Nat. Rev. Neurosci.* **2007**, *8* (6), 451–465. https://doi.org/10.1038/nrn2148.

(2) Wonderlin, W. F.; Woodfork, K. A.; Strobl, J. S. Changes in Membrane Potential during the Progression of MCF-7 Human Mammary Tumor Cells through the Cell Cycle. *J. Cell. Physiol.* **1995**, *165* (1), 177–185. https://doi.org/10.1002/jcp.1041650121.

(3) Wang, S. Y.; Melkoumian, Z.; Woodfork, K. A.; Cather, C.; Davidson, A. G.; Wonderlin, W. F.; Strobl, J. S. Evidence for an Early G1 Ionic Event Necessary for Cell Cycle Progression and Survival in the MCF-7 Human Breast Carcinoma Cell Line. *J. Cell. Physiol.* **1998**, *176* (3), 456–464. https://doi.org/10.1002/(sici)1097-4652(199809)176:3<456::aid-jcp2>3.0.co;2-n.

(4) Urrego, D.; Movsisyan, N.; Ufartes, R.; Pardo, L. A.; Urrego, D.; Movsisyan, N. Periodic Expression of Kv10 . 1 Driven by PRb / E2F1 Contributes to G2 / M Progression of Cancer And. *Cell Cycle* **2016**, *15* (6), 799–811. https://doi.org/10.1080/15384101.2016.1138187.

(5) Zorova, L. D.; Popkov, V. A.; Plotnikov, E. Y.; Silachev, D. N.; Pevzner, I. B.; Jankauskas, S. S.; Babenko, V. A.; Zorov, S. D.; Balakireva, A. V.; Juhaszova, M.; et al. Mitochondrial Membrane Potential. *Anal. Biochem.* **2018**, *552*, 50–59. https://doi.org/10.1016/j.ab.2017.07.009.

(6) Rad, M. S.; Cohen, L. B.; Braubach, O.; Baker, B. J. Monitoring Voltage Fluctuations of Intracellular Membranes. *Sci. Rep.* **2018**, *8* (1), 1–9. https://doi.org/10.1038/s41598-018-25083-7.

(7) Xu, H.; Ren, D. Lysosomal Physiology. *Annu. Rev. Physiol.* **2015**, *77* (1), 57–80. https://doi.org/10.1146/annurev-physiol-021014-071649.

(8) Yuste, R. Electrical Compartmentalization in Dendritic Spines. *Annu. Rev. Neurosci.* **2013**, *36* (1), 429–449. https://doi.org/10.1146/annurev-neuro-062111-150455.

(9) Durant, F.; Bischof, J.; Fields, C.; Morokuma, J.; LaPalme, J.; Hoi, A.; Levin, M. The Role of Early Bioelectric Signals in the Regeneration of Planarian Anterior/Posterior Polarity. *Biophys. J.* **2019**, *116* (5), 948–961. https://doi.org/10.1016/j.bpj.2019.01.029.

(10) Cervera, J.; Alcaraz, A.; Mafe, S. Bioelectrical Signals and Ion Channels in the Modeling of Multicellular Patterns and Cancer Biophysics. *Sci. Rep.* **2016**, *6* (January), 1–14. https://doi.org/10.1038/srep20403.

(11) Hamill, O. P.; Marty, A.; Neher, E.; Sakmann, B.; Sigworth, F. J. Improved Patch-Clamp Techniques for High-Resolution Current Recording from Cells and Cell-Free Membrane Patches. *Pflügers Arch. Eur. J. Physiol.* **1981**, *391* (2), 85–100. https://doi.org/10.1007/BF00656997.

(12) Spruston, N.; Johnston, D. Perforated Patch-Clamp Analysis of the Passive Membrane Properties of Three Classes of Hippocampal Neurons. *J. Neurophysiol.* **1992**, *67* (3), 508–529. https://doi.org/10.1152/jn.1992.67.3.508.

(13) Armstrong, C. M.; Gilly, W. F. Access Resistance and Space Clamp Problems Associated with Whole-Cell Patch Clamping. *Methods Enzymol.* **1992**, *207*, 100–122. https://doi.org/10.1016/0076-6879(92)07007-B.

(14) Williams, S. R.; Mitchell, S. J. Direct Measurement of Somatic Voltage Clamp Errors in Central Neurons. *Nat. Neurosci.* **2008**, *11* (7), 790–798. https://doi.org/10.1038/nn.2137.

(15) Knöpfel, T.; Song, C. Optical Voltage Imaging in Neurons: Moving from Technology Development to Practical Tool. *Nat. Rev. Neurosci.* **2019**, *20* (12), 719–727. https://doi.org/10.1038/s41583-019-0231-4.

(16) Miller, E. W. Small Molecule Fluorescent Voltage Indicators for Studying Membrane Potential. *Curr. Opin. Chem. Biol.* **2016**, *33*, 74–80. https://doi.org/10.1016/j.cbpa.2016.06.003.

(17) Abdelfattah, A. S.; Kawashima, T.; Singh, A.; Novak, O.; Liu, H.; Shuai, Y.; Huang, Y.-C.; Campagnola, L.; Seeman, S. C.; Yu, J.; et al. Bright and Photostable Chemigenetic Indicators for Extended in Vivo Voltage Imaging. *Science (80-.).* **2019**, No. August, eaav6416. https://doi.org/10.1126/science.aav6416.

(18) Piatkevich, K. D.; Jung, E. E.; Straub, C.; Linghu, C.; Park, D.; Suk, H. J.; Hochbaum, D. R.; Goodwin, D.; Pnevmatikakis, E.; Pak, N.; et al. A Robotic Multidimensional Directed Evolution Approach Applied to Fluorescent Voltage Reporters Article. *Nat. Chem. Biol.* **2018**, *14* (4), 352–360. https://doi.org/10.1038/s41589-018-0004-9.

(19) Adam, Y.; Kim, J. J.; Lou, S.; Zhao, Y.; Xie, M. E.; Brinks, D.; Wu, H.; Mostajo-radji, M. A.; Kheifets, S.; Parot, V.; et al. Voltage Imaging and Optogenetics Reveal Behaviour-Dependent Changes in Hippocampal Dynamics. *Nature* **2019**, *569*, 413–417. https://doi.org/10.1038/s41586-019-1166-7.

(20) Weissleder, R. A Clearer Vision for in Vivo Imaging. *Nat. Biotechnol.* **2001**, *19*, 316–317.

(21) Peterka, D. S.; Takahashi, H.; Yuste, R. Imaging Voltage in Neurons. *Neuron* **2011**, *69* (1), 9–21. https://doi.org/10.1016/j.neuron.2010.12.010.

(22) Berezin, M. Y.; Achilefu, S. Fluorescence Lifetime Measurements and Biological Imaging. *Chem. Rev.* **2010**, *110* (5), 2641–2684. https://doi.org/10.1021/cr900343z.

(23) Yellen, G.; Mongeon, R. Quantitative Two-Photon Imaging of Fluorescent Biosensors. *Curr. Opin. Chem. Biol.* **2015**, *27*, 24–30. https://doi.org/10.1016/J.CBPA.2015.05.024.

(24) Brinks, D.; Klein, A. J.; Cohen, A. E. Two-Photon Lifetime Imaging of Voltage Indicating Proteins as a Probe of Absolute Membrane Voltage. *Biophys. J.* **2015**, *109* (5), 914–921. https://doi.org/10.1016/j.bpj.2015.07.038.

(25) Lazzari-Dean, J. R.; Gest, A. M. M.; Miller, E. W. Optical Estimation of Absolute Membrane Potential Using Fluorescence Lifetime Imaging. *Elife* **2019**, *8*, e44522. https://doi.org/10.7554/elife.44522.

(26) Miller, E. W.; Lin, J. Y.; Frady, E. P.; Steinbach, P. A.; Kristan, W. B.; Tsien, R. Y. Optically Monitoring Voltage in Neurons by Photo-Induced Electron Transfer through

Molecular Wires. *Proc. Natl. Acad. Sci. U. S. A.* **2012**, *109* (6), 2114–2119. https://doi.org/10.1073/pnas.1120694109.

(27) Woodford, C. R.; Frady, E. P.; Smith, R. S.; Morey, B.; Canzi, G.; Palida, S. F.; Araneda, R. C.; Kristan, W. B.; Kubiak, C. P.; Miller, E. W.; et al. Improved PeT Molecules for Optically Sensing Voltage in Neurons. *J. Am. Chem. Soc.* **2015**, *137* (5), 1817–1824. https://doi.org/10.1021/ja510602z.

(28) Zhang, J.; Davidson, R. M.; Wei, M. De; Loew, L. M. Membrane Electric Properties by Combined Patch Clamp and Fluorescence Ratio Imaging in Single Neurons. *Biophys. J.* **1998**, *74* (1), 48–53. https://doi.org/10.1016/S0006-3495(98)77765-3.

(29) Bullen, A.; Saggau, P. High-Speed, Random-Access Fluorescence Microscopy: II. Fast Quantitative Measurements with Voltage-Sensitive Dyes. *Biophys. J.* **1999**, *76* (4), 2272–2287. https://doi.org/10.1016/S0006-3495(99)77383-2.

(30) Huang, Y. L.; Walker, A. S.; Miller, E. W. A Photostable Silicon Rhodamine Platform for Optical Voltage Sensing. *J. Am. Chem. Soc.* **2015**, *137* (33), 10767–10776. https://doi.org/10.1021/jacs.5b06644.

(31) Deal, P. E.; Kulkarni, R. U.; Al-Abdullatif, S. H.; Miller, E. W. Isomerically Pure Tetramethylrhodamine Voltage Reporters. *J. Am. Chem. Soc.* **2016**, *138* (29), 9085–9088. https://doi.org/10.1021/jacs.6b05672.

(32) Kulkarni, R. U.; Vandenberghe, M.; Thunemann, M.; James, F.; Andreassen, O. A.; Djurovic, S.; Devor, A.; Miller, E. W. *In Vivo* Two-Photon Voltage Imaging with Sulfonated Rhodamine Dyes. *ACS Cent. Sci.* **2018**, acscentsci.8b00422. https://doi.org/10.1021/acscentsci.8b00422.

(33) Ortiz, G.; Liu, P.; Naing, S. H. H.; Muller, V. R.; Miller, E. W. Synthesis of Sulfonated Carbofluoresceins for Voltage Imaging. *J. Am. Chem. Soc.* **2019**, *141* (16), 6631–6638. https://doi.org/10.1021/jacs.9b01261.

(34) Grimm, J. B.; Sung, A. J.; Legant, W. R.; Hulamm, P.; Matlosz, S. M.; Betzig, E.; Lavis, L. D. Carbofluoresceins and Carborhodamines as Scaffolds for High-Contrast Fluorogenic Probes. *ACS Chem. Biol.* **2013**, *8*, 1303–1310.

(35) Grimm, J. B.; Muthusamy, A. K.; Liang, Y.; Brown, T. A.; Lemon, W. C.; Patel, R.; Lu, R.; Macklin, J. J.; Keller, P. J.; Ji, N.; et al. A General Method to Fine-Tune Fluorophores for Live-Cell and in Vivo Imaging. *Nat. Methods* **2017**, *14* (10), 987–994. https://doi.org/10.1038/nmeth.4403.

(36) Kelkar, D. A.; Chattopadhyay, A. The Gramicidin Ion Channel: A Model Membrane Protein. *Biochim. Biophys. Acta - Biomembr.* **2007**, *1768* (9), 2011–2025. https://doi.org/10.1016/j.bbamem.2007.05.011.

(37) Bedut, S.; Seminatore-Nole, C.; Lamamy, V.; Caignard, S.; Boutin, J. A.; Nosjean, O.; Stephan, J. P.; Coge, F. High-Throughput Drug Profiling with Voltage-and Calcium-Sensitive Fluorescent Probes in Human IPSC-Derived Cardiomyocytes. *Am. J. Physiol. - Hear. Circ. Physiol.* **2016**, *311* (1), H44–H53. https://doi.org/10.1152/ajpheart.00793.2015.

(38) Shaheen, N.; Shiti, A.; Huber, I.; Shinnawi, R.; Arbel, G.; Gepstein, A.; Setter, N.; Goldfracht, I.; Gruber, A.; Chorna, S. V.; et al. Human Induced Pluripotent Stem Cell-Derived Cardiac Cell Sheets Expressing Genetically Encoded Voltage Indicator for Pharmacological and Arrhythmia Studies. *Stem Cell Reports* **2018**, *10* (6), 1879–1894. https://doi.org/10.1016/j.stemcr.2018.04.006.

(39) Boggess, S. C.; Gandhi, S. S.; Siemons, B. A.; Huebsch, N.; Healy, K. E.; Miller, E. W. New Molecular Scaffolds for Fluorescent Voltage Indicators. *ACS Chem. Biol.* **2019**, *14* (3), 390–396. https://doi.org/10.1021/acschembio.8b00978.

(40) Ma, J.; Guo, L.; Fiene, S. J.; Anson, B. D.; Thomson, J. A.; Kamp, T. J.; Kolaja, K. L.; Swanson, B. J.; January, C. T. High Purity Human-Induced Pluripotent Stem Cell-Derived Cardiomyocytes: Electrophysiological Properties of Action Potentials and Ionic Currents. *Am. J. Physiol. - Hear. Circ. Physiol.* **2011**, *301* (5), 2006–2017. https://doi.org/10.1152/ajpheart.00694.2011.

(41) López-Redondo, F.; Kurokawa, J.; Nomura, F.; Kaneko, T.; Hamada, T.; Furukawa, T.; Yasuda, K. A Distribution Analysis of Action Potential Parameters Obtained from Patch-Clamped Human Stem Cell-Derived Cardiomyocytes. *J. Pharmacol. Sci.* **2016**, *131* (2), 141–145. https://doi.org/10.1016/j.jphs.2016.04.015.

(42) Verkerk, A. O.; Veerman, C. C.; Zegers, J. G.; Mengarelli, I.; Bezzina, C. R.; Wilders, R. Patch-Clamp Recording from Human Induced Pluripotent Stemcell-Derived Cardiomyocytes: Improving Action Potential Characteristics Throughdynamic Clamp. *Int. J. Mol. Sci.* **2017**, *18* (9). https://doi.org/10.3390/ijms18091873.

(43) Becker, W. *The Bh TCSPC Handbook*, 5th edn.; Becker & Hickl, 2012.

(44) Montana, V.; Farkas, D. L.; Loew, L. M. Dual-Wavelength Ratiometric Fluorescence Measurements of Membrane Potential. *Biochemistry* **1989**, *28* (11), 4536–4539. https://doi.org/10.1021/bi00437a003.

(45) Magni, M.; Meldolesi, J.; Pandiella, A. Ionic Events Induced by Epidermal Growth Factor: Evidence That Hyperpolarization and Stimulated Cation Influx Play a Role in the Stimulation of Cell Growth. *J. Biol. Chem.* **1991**, *266* (10), 6329–6335.

(46) Pandiella, A.; Magni, M.; Lovisolo, D.; Meldolesi, J. The Effects of Epidermal Growth Factor on Membrane Potential. *J. Biol. Chem.* **1989**, *264* (22), 12914–12921.

(47) Deal, P. E.; Liu, P.; Al-Abdullatif, S. H.; Muller, V. R.; Shamardani, K.; Adesnik, H.; Miller, E. W. Covalently Tethered Rhodamine Voltage Reporters for High Speed Functional Imaging in Brain Tissue. *chemRxiv* **2019**, Preprint.

(48) Liu, P.; Grenier, V.; Hong, W.; Muller, V. R.; Miller, E. W. Fluorogenic Targeting of Voltage-Sensitive Dyes to Neurons. *J. Am. Chem. Soc.* **2017**, *139* (48), 17334–17340. https://doi.org/10.1021/jacs.7b07047.

(49) Grenier, V.; Daws, B. R.; Liu, P.; Miller, E. W. Spying on Neuronal Membrane Potential with Genetically Targetable Voltage Indicators. *J. Am. Chem. Soc.* **2019**, *141*, 1349–1358. https://doi.org/10.1021/jacs.8b11997.

(50) Vaidyanathan, R.; Markandeya, Y. S.; Kamp, T. J.; Makielski, J. C.; January, C. T.; Eckhardt, L. L. IK1-Enhanced Human-Induced Pluripotent Stem Cell-Derived Cardiomyocytes: An Improved Cardiomyocyte Model to Investigate Inherited Arrhythmia Syndromes. *Am. J. Physiol. - Hear. Circ. Physiol.* **2016**, *310* (11), H1611–H1621. https://doi.org/10.1152/ajpheart.00481.2015.

(51) Horváth, A.; Lemoine, M. D.; Löser, A.; Mannhardt, I.; Flenner, F.; Uzun, A. U.; Neuber, C.; Breckwoldt, K.; Hansen, A.; Girdauskas, E.; et al. Low Resting Membrane Potential and Low Inward Rectifier Potassium Currents Are Not Inherent Features of HiPSC-Derived Cardiomyocytes. *Stem Cell Reports* **2018**, *10* (3), 822–833. https://doi.org/10.1016/j.stemcr.2018.01.012.

(52) Gao, L.; Liang, J.; Li, C.; Wang, L. V. Single-Shot Compressed Ultrafast Photography at One Hundred Billion Frames per Second. *Nature* **2014**, *516* (729), 74–77. https://doi.org/10.1038/nature14005.

(53) Raspe, M.; Kedziora, K. M.; van den Broek, B.; Zhao, Q.; de Jong, S.; Herz, J.; Mastop, M.; Goedhart, J.; Gadella, T. W. J.; Young, I. T.; et al. SiFLIM: Single-Image Frequency-Domain FLIM Provides Fast and Photon-Efficient Lifetime Data. *Nat. Methods* **2016**, No. October 2015, 1–6. https://doi.org/10.1038/nmeth.3836.

(54) Vallat, R. Pingouin: Statistics in Python. *J. Open Source Softw.* **2018**, *3* (31), 1026. https://doi.org/10.21105/joss.01026.

Chapter 6

Two Photon Absolute Voltage Imaging with VoltageFluor Fluorescence Lifetime

Portions of this work were done in collaboration with the following people:

Some of the two photon FLIM data were collected with Anneliese Gest.

Abstract

The role of transmembrane potential (V_{mem}) in tissue patterning has recently attracted attention; more broadly, the distributions and patterning of V_{mem} in vivo are largely uncharacterized. Optical strategies for recording V_{mem} are attractive in this arena, as they have the ability to record from many cells simultaneously and noninvasively. However, the blue excitation light used for VF-FLIM with VF2.1.Cl is largely incompatible with fluorescence lifetime imaging in thick tissue. To this end, we explored two photon (2p) excitation with fluorescence lifetime imaging of VoltageFluors to enable translation of VF-FLIM to thick tissue. We documented the 2p-excited lifetimes of five VoltageFluors and assess their V_{mem} sensitivity. We find that VF dyes in multiple colors yield V_{mem}-sensitive fluorescence lifetimes under two-photon excitation. In doing so, we observe and discuss discrepancies between the fluorescence lifetimes seen under one and two photon excitation conditions.

Introduction

Two-photon (2p) excitation microscopy has transformed *in vivo* imaging by enabling fluorescence microscopy deep (up to ~1 mm) into thick, scattering tissue.[1] Two-photon imaging relies on the ability of certain chromophores to efficiently absorb two photons, each individually with lower energy, to access a fluorescent excited state. This lower energy excitation light then falls within the "near infrared window," where scattering and autofluorescence in biological samples is greatly reduced.

For voltage imaging in particular, there is a pressing need for optical strategies to record V_{mem} in tissue. Rapid changes in V_{mem} within the brain transmit information throughout complex, spatially organized neural circuits. To capture the information within these circuits, it is imperative that they be studied *in situ*.[1] Furthermore, 'non-excitable' cells that may undergo V_{mem} changes during growth must do so as part of an electrically coupled tissue.[2] Reporting the pattern of V_{mem} in such a system requires simultaneous recording from hundreds of cells, a feat that is not possible with patch-clamp electrophysiology.

To measure absolute Vmem from many cells simultaneously in thick tissue, we sought to translate the VF-FLIM system (**Chapter 2**) from one photon (1p) to 2p illumination. We first report the fluorescence lifetime of VF2.1.Cl under two photon illumination and then expand to other VoltageFluors with more favorable two photon cross sections. Specifically, our lab has shown that VoltageFluors based on a rhodamine or rhodol fluorophore exhibit large two photon cross sections and V_{mem}-sensitive fluorescence.[3,4] To this end, we evaluated the 2p fluorescence lifetime of these red-shifted VoltageFluors in cultured HEK293T cells and identify promising candidates for future studies in tissue. With some of the sensors, we observe differences in the 1p and 2p excited fluorescence lifetimes; reasons for this are discussed. Taken together, these data demonstrate that VF-FLIM can be translated from one photon to two photon illumination in cultured cell lines.

Results and Discussion

VF2.1.Cl Fluorescence Lifetime under Two Photon Excitation

We measured the fluorescence lifetime of the VoltageFluor VF2.1.Cl under two photon excitation at 820 nm in HEK293T. Due to the relatively poor two photon cross section of VF2.1.Cl,[3] high light power was required to obtain sufficient photon output; photobleaching appeared more rapid

under these conditions than under 1p excitation with similar photon output. Excellent membrane staining and optical sectioning was observed (**Figure 6.1**).

Using simultaneous fluorescence lifetime imaging and whole cell patch clamp electrophysiology, we determined that the τ_{fl} of VF2.1.Cl under these excitation conditions is sensitive to V_{mem}. With 820 nm 2p excitation, we observe a sensitivity of 3.86 ± 0.04 ps/mV with a 0 mV lifetime (y-intercept) of 1.95 ± 0.01 ns (n=16 cells, **Figure 6.1**) when employing the same fitting model (weighted average τ_{fl} of a two-component decay) from 1P illumination (**Chapter 2**, **Chapter 6 Methods**). Under otherwise identical 1p excitation conditions, the linear lifetime-V_{mem} relationship for VF2.1.Cl displayed a slope of 3.50 ± 0.08 ps/mV and a y-intercept of 1.77 ± 0.02 ns.[5] In this 2p calibration, we observed slightly improved V_{mem} resolution over the 1p calibration (14 mV inter-cell RMSD and 4.4 ± 0.6 mV intra-cell RMSD, calculated as in Chapter 2).

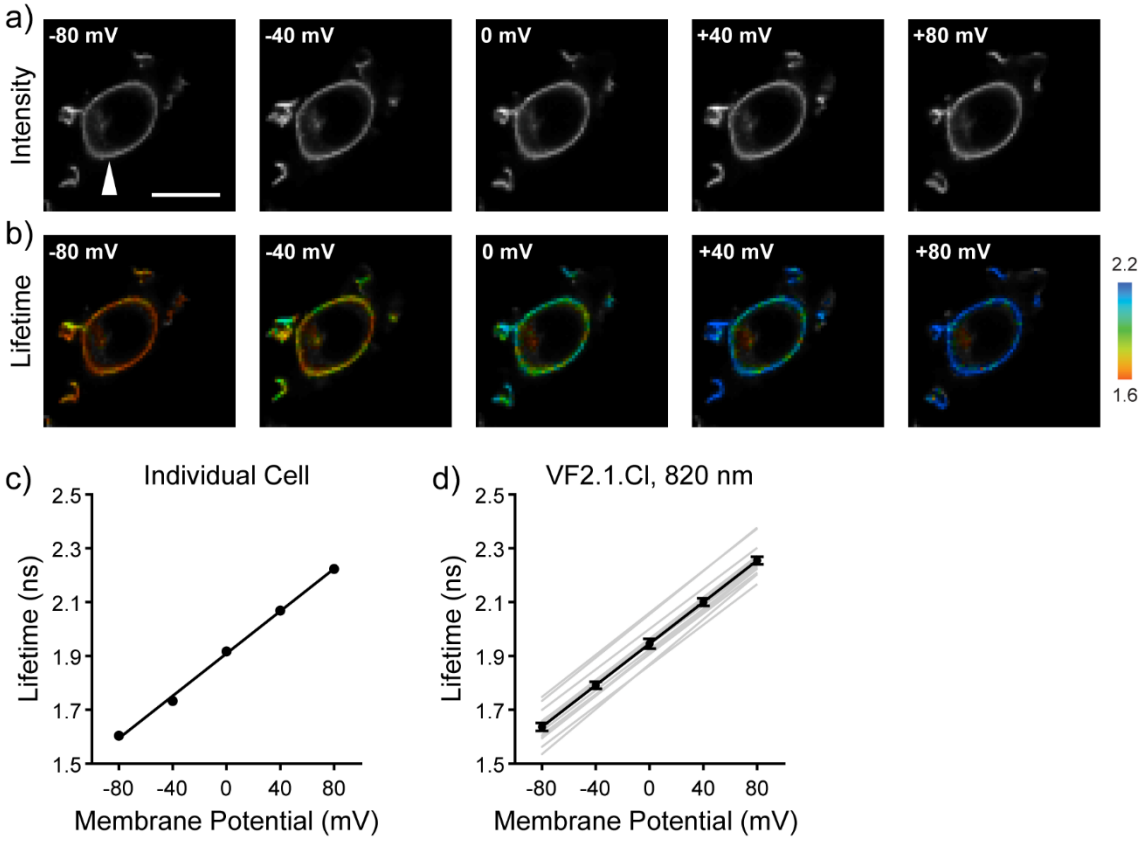

Figure 6.1. VF2.1.Cl fluorescence lifetime reports absolute V_{mem} under 2p excitation. Simultaneous whole cell patch clamp electrophysiology and two photon FLIM (820 nm excitation) of VF2.1.Cl in HEK293T reveals a V_{mem} sensitive τ_{fl}. a) Photon count images of 100 nM VF2.1.Cl in a HEK293T cell held at the indicated V_{mem}. White arrow indicates the patch pipette; scale bar is 20 µm. b) Lifetime-intensity overlay of the same HEK293T. c) Quantification of the lifetime images in (b), revealing a clear linear relationship between τ_{fl} and V_{mem}. Points indicate average lifetime for the individual cell in (b) within a membrane localized region of interest at each potential. Black line indicates the line of best fit. d) Aggregated lifetime-V_{mem} calibration for VF2.1.Cl, where individual cells are represented by gray lines. Black line represents the average slope and y-intercept for n=16 HEK293T cells. Data are shown as mean ± SEM.

The fluorescence lifetime of VF2.1.Cl under 2p excitation could be a useful method for measuring absolute V_{mem}, as it displays excellent V_{mem} sensitivity and resolution. The slight increase in 2p lifetime versus the 1p lifetime for VF2.1.Cl is most likely attributable to reduced autofluorescence presence at 820 nm versus the blue 479 nm excitation light. This hypothesis is consistent with the slightly increased sensitivity under two photon illumination, as autofluorescence will contribute a V_{mem}-insensitive background to the lifetime recording. This reduction in autofluorescence could also produce the observed resolution improvement for Vmem recordings. Nevertheless, these data were collected over the course of a much smaller time window than the 1p data in Chapter 2 (1 month versus 1.5 years). Slight differences in instrument performance over time may also contribute to this 1p versus 2p resolution difference.

TMCRh.OMe Fluorescence Lifetime Under 2p Excitation Differs from 1p Excitation

Despite the favorable sensitivity and V_{mem} resolution of VF2.1.Cl, its poor two photon cross section and high excitation light power render it suboptimal for absolute V_{mem} imaging in tissue. In search of a VoltageFluor with better performance in 2p-FLIM, we recorded lifetime-V_{mem} calibrations for a variety of red-shifted VoltageFluors with improved two photon cross sections. The VoltageFluor TMCRh.OMe exhibits favorable properties in 1p FLIM (**Chapter 5**).

Although their 1p absorption maximum is around 625 nm, carborhodamines exhibit strong two photon absorbance in the low 800 nm region, as well as around 1100 nm.[6] Due to limitations of our excitation source, we opted to excite TMCRh.OMe at 820 nm in two photon, where we observed bright, membrane localized signal. Under continuous illumination, we again observed much faster photobleaching under these 2p illumination conditions than we did under 1p illumination. Photobleaching was often accompanied by an upward drift in the fluorescence lifetime.

We observe different fluorescent lifetimes for TMCRh.OMe under 2p illumination than we saw under 1p illumination (Chapter 5). Whereas the 1p time resolved fluorescence signal can be modeled by a single exponential decay, the 2p signal contains three decay components, with an average lifetime of ~1.7 ns at rest in HEK293T cells (approximately 0.8 ns shorter than the 1p signal). Using simultaneous 2p FLIM and whole cell voltage clamp electrophysiology, we measured the voltage sensitivity of 2p lifetime of TMCRh.OMe. In doing so, we noticed that only the third component of the lifetime (τ_3) was voltage sensitive, so we fixed the lifetimes of τ_1 and τ_3 to the values that minimized the reduced χ^2 (0.1 and 0.9 ns, respectively). For τ_3, we obtain a sensitivity of 2.60 ± 0.04 ps/mV and a y-intercept of 2.83 ± 0.01 ns (mean ± SEM of n=16 HEK293T cells, **Figure 6.2**).

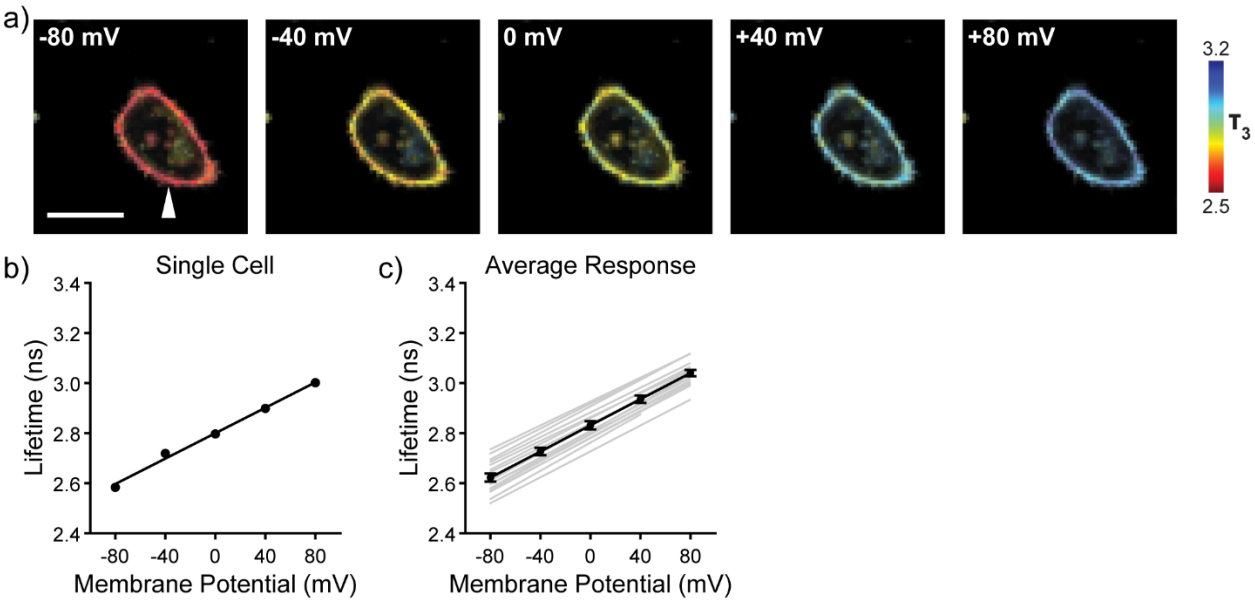

Figure 6.2. Components of TMCRh.OMe 2p Fluorescence Lifetime are V_{mem} Sensitive.
a) Overlay of the photon count and the third component of the fluorescence lifetime (τ_3) of 300 nM TMCRh.OMe in a HEK293T cell under two photon illumination (820 nm). The cell was held at the indicated V_{mem} with whole cell voltage clamp electrophysiology (white arrow). Scale bar indicates 20 µm. b) Quantification of the data in (a), along with the line of best fit for the individual cell's τ_3-V_{mem} relationship. c) The average τ_3-V_{mem} relationship from 16 individual HEK293T cells (lines of best fit shown in gray). The line of best fit with the average slope and y-intercept is shown in black; data points are represented as mean ± SEM.

We were surprised by the discrepancy between the one photon and two photon excited fluorescence lifetimes of TMCRh.OMe. We considered the possibility that the molecular wire of TMCRh.OMe can be excited directly in 2p at 820 nm, which perhaps was resulting in aberrant results. The addition of a methoxy group to the molecular wire of TMCRh.OMe (versus that of VF2.1.Cl) red-shifts the wire absorption, perhaps enabling 2p excitation under our conditions. However, we saw no change in the fluorescence lifetime resulting from excitation in the range 750 nm to 950 nm (**Figure 6.3**); wavelengths above 900 nm would likely not directly excite the molecular wire.

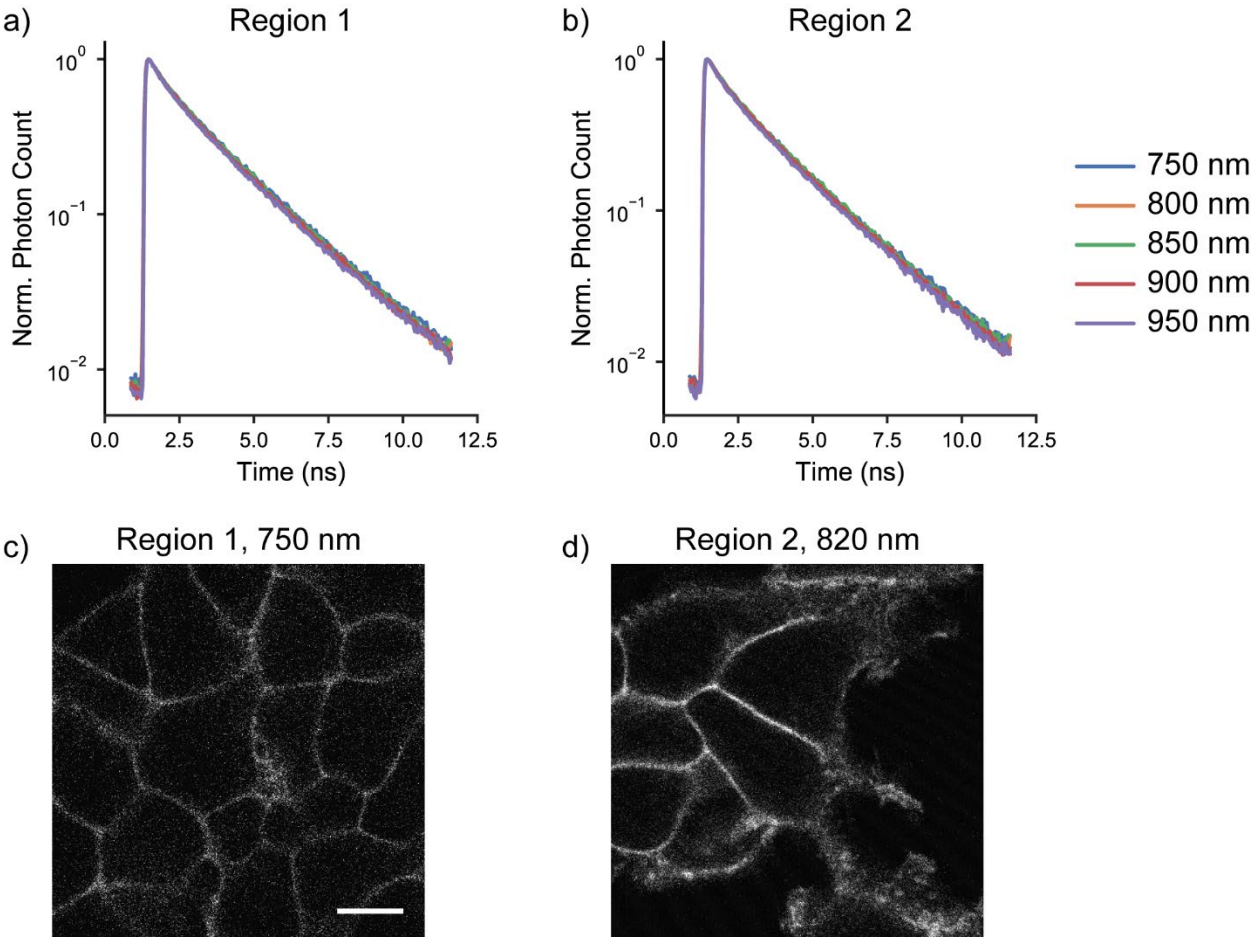

Figure 6.3. TMCRh.OMe 2p fluorescence lifetime is not dependent on the excitation wavelength.
a) Time resolved fluorescence of 300 nM TMCRh.OMe in HEK293T as the excitation wavelength was increased from 750 nm to 950 nm. Where traces are not visible, they overlap with other data. b) Time resolved fluorescence of TMCRh.OMe as the excitation wavelength was decreased from 950 to 750 nm to compensate for potential light exposure artifacts. Measurements were not corrected for the input power at the sample, which varied substantially across this range; lifetimes presented in (a) and (b) were normalized to the peak photon count. Decays correspond to the sum of all photons present in the fields of view shown in (c) and (d). c-d) Representative two photon fluorescence images of the HEK293T cell groups at 750 nm and 820 nm excitation. Scale bar is 10 μm.

Thus, the origin of these voltage-insensitive shorter components to the 2p-FLIM signal for TMCRh.OMe is unclear, as is the reason for the discrepancy between 1p and 2p FLIM results. Although we have yet to calibrate the 1p lifetime-V_{mem} relationship for TMCRh.OMe with electrophysiology, our initial data indicated a sensitivity of approximately 4 ps/mV and a 0 mV lifetime of approximately 2.7 ns in HEK293T (**Chapter 5**). Therefore, the 1p 0 mV lifetime is similar to the 0 mV lifetime for τ_3 alone in 2p, but the V_{mem} sensitivities differ considerably. Furthermore, one would expect to see the same number of decay components in the time-resolved fluorescence for the same fluorophore under 1p and 2p illumination. Systematic comparison of

additional VFs under one- and two-photon illumination may provide further insight into this apparent paradox.

Nevertheless, using τ_3 for TMCRh.OMe in 2p FLIM is a viable option for absolute V_{mem} imaging with comparable V_{mem} resolution to VF-FLIM (intra cell RMSD of 5.0 ± 0.6 mV, inter cell RMSD of 22 mV). Preliminary work with this sensor in thick tissue is described elsewhere in this dissertation (**Appendix 4**), and additional studies with TMCRh.OMe are underway in our laboratory.

carboVF 2p Fluorescence Lifetime is Somewhat V_{mem} Sensitive

We also explored the fluorescence lifetime of the carbofluorescein-based voltage sensitive dye carboVF, which has a reported sensitivity of 30% ΔF/F per 100 mV and the ability to be enzymatically targeted to cells of interest in complex samples.[7] Under two photon illumination at 740 nm, we observed strong, membrane-localized signal from carboVF, although there was unexpectedly variability in the lifetime across the membrane of an individual cell (**Figure 6.4**). We attribute this to fit noise, as the lifetime data from carboVF appeared contaminated by a small amount of laser bleedthrough (see Methods). For the cell shown in **Figure 6.4**, we observed a slope of 3.0 ps/mV and a y-intercept of 1.80 ns, although individual points deviated somewhat from the line of best fit. This sensitivity corresponds to a 19% Δτ/τ per 100 mV, which is a smaller fractional change than expected from the fluorescence intensity data. Further characterization of carboVF in 2p was impractical because of contaminating excitation bleedthrough at 740 nm. Nevertheless, the absolute sensitivity of carboVF under 2p illumination was only slightly less than the sensitivity of VF-FLIM, rendering it a potentially useful absolute V_{mem} probe. Future investigation of the properties of carboVF lifetime under 1 photon illumination would likely be fruitful.

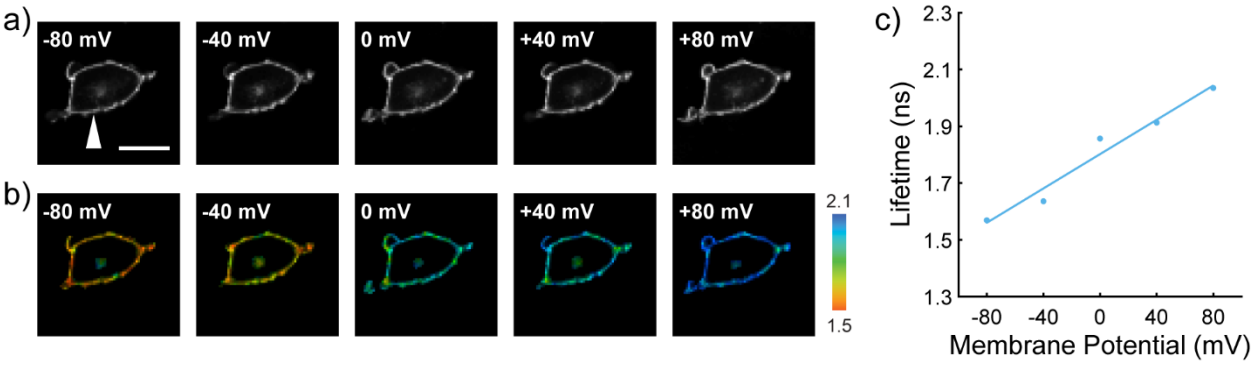

Figure 6.4. V_{mem} Dependence of carboVF fluorescence lifetime at 740 nm.
a) Photon count and b) lifetime images of a HEK293T loaded with 200 nM carboVF and held at the indicated potential with whole cell voltage clamp electrophysiology. c) Quantification of the fluorescence lifetime data shown in (b). Individual points represent the average lifetime in a membrane ROI; the blue line is the line of best fit (slope of 3.0 ps/mV, 0 mV lifetime of 1.80 ns). Scale bar is 20 µm. White arrow indicates patch pipette.

RhoVR 2p-FLIM is V_{mem}-sensitive but Complicated by Excitation Photoselection

To evaluate the two photon fluorescence lifetime signal from RhoVR dyes under 2p illumination (820 nm), we loaded 500 nM of RhoVR1 or RhoVR(Me) into HEK293T and measured the fluorescence lifetime. To our surprise, we observed differences in both fluorescence intensity and

fluorescence lifetime between membranes with different orientations (horizontal vs. vertical, **Figure 6.5**). The phenomenon was rotated by 90° with the addition of a half-wave plate to the beampath, which rotates the polarization of the excitation light by 90°.

The differences in RhoVR brightness with excitation polarization can be explained by excitation photoselection, as chromophores are most efficiently excited when the excitation dipole of the transition the fluorescent excited state (S_1) is aligned with the electric field of the incident light.[8] Because VoltageFluors are oriented in the plasma membrane, the molecules on the "horizontal" and "vertical" membranes will be excited with different propensities by a polarized excitation source, such as the Ti:Sapphire laser used in this experiment. Excitation photoselection is stronger under two photon illumination because two photons must be absorbed by the same molecule within a very short span of time.[8]

The effect of incoming light polarization on fluorescence lifetime is more complex, as the fluorescence lifetime should be independent of the number of chromophores that reach the fluorescent excited state. In addition, we see the polarization effect on 2p lifetime most strongly in RhoVR1, with weak effects in RhoVR(Me) and no obvious effect in other probes studied (**Figure 6.1, 6.2, 6.4**). One way that the time-resolved fluorescence signal can be affected by polarization is through fluorescence anisotropy, as the fluorescence emission is also polarized. If the RhoVR1 molecules are rotating on a similar timescale to the fluorescence emission, this can there will be interchange between emission polarized parallel to and perpendicular to the excitation light. Because our setup does not collect the full fluorescence emission in all directions, this can lead to the appearance of two populations of fluorescence lifetime, which populate or depopulate as the molecule rotates.[8] This hypothesis could be further evaluated by the placement of a magic angle polarizer on the emission beampath, which should remove this effect but would result in a large loss of signal.

Despite this polarization-induced artifact, we tested the V_{mem} dependence of the 2p lifetime of RhoVR1 and RhoVR(Me) (**Figure 6.6**). For RhoVR1, we struggled to adequately describe the time-resolved fluorescence decay as a sum of three exponential components. With this three exponential fit, we observed a lot of apparently random deviation from the linear fit, which is in stark contrast to the intensity-based %ΔF/F response.[9] Furthermore, the observed change in lifetime is much less than 47% per 100 mV, which is what we expect from the fluorescence intensity response of this probe.

In contrast, the fluorescence lifetime of RhoVR(Me) under 2p illumination matches reasonably well with expectations for a PeT-based voltage sensitive dye. RhoVR(Me) has a reported sensitivity of 14% ΔF/F per 100 mV and is brighter than RhoVR1 in fluorescence intensity. These characteristics are consistent with a reduced rate of PeT in RhoVR(Me), as the methyl substituent on the molecular wire is less electron donating than the methoxy substituent on the RhoVR1 molecular wire. In 2p-FLIM, we observe a sensitivity of 2.09 ± 0.04 ps/mV and a 0 mV lifetime of 1.75 ± 0.03 ns (mean ± SEM of n=7 HEK293T cells). This lifetime-V_{mem} calibration corresponds to a 13% change in lifetime per 100 mV, in good agreement with the fluorescence intensity data. For absolute V_{mem} determinations, RhoVR(Me) under 2p illumination exhibits an intra cell RMSD of 6.3 ± 0.5 mV and an inter cell RMSD of 36 mV (calculated as described in **Chapter 2**).

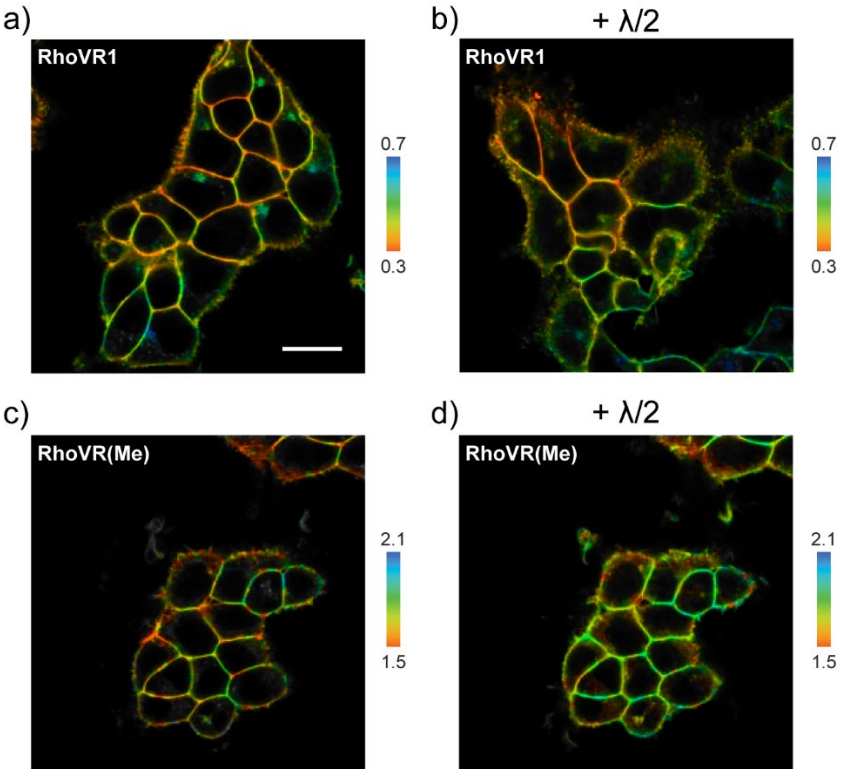

Figure 6.5. RhoVR lifetimes depend on the polarization of the excitation light.
a) 2p-FLIM image at 820 nm excitation of 500 nM RhoVR1 in HEK293T. b) 2p-FLIM image of 500 nM RhoVR1 in HEK293T with addition of half-wave plate to the beam path to rotate the polarization of the excitation light by 90°. Different fields of view are shown in (a) and (b). c) 2p-FLIM image of 500 nM RhoVR(Me) in HEK293T. d) 2p-FLIM image of the same group of HEK293T in (c), with the polarization of the excitation light rotated by 90°. Scale bar is 20 μm.

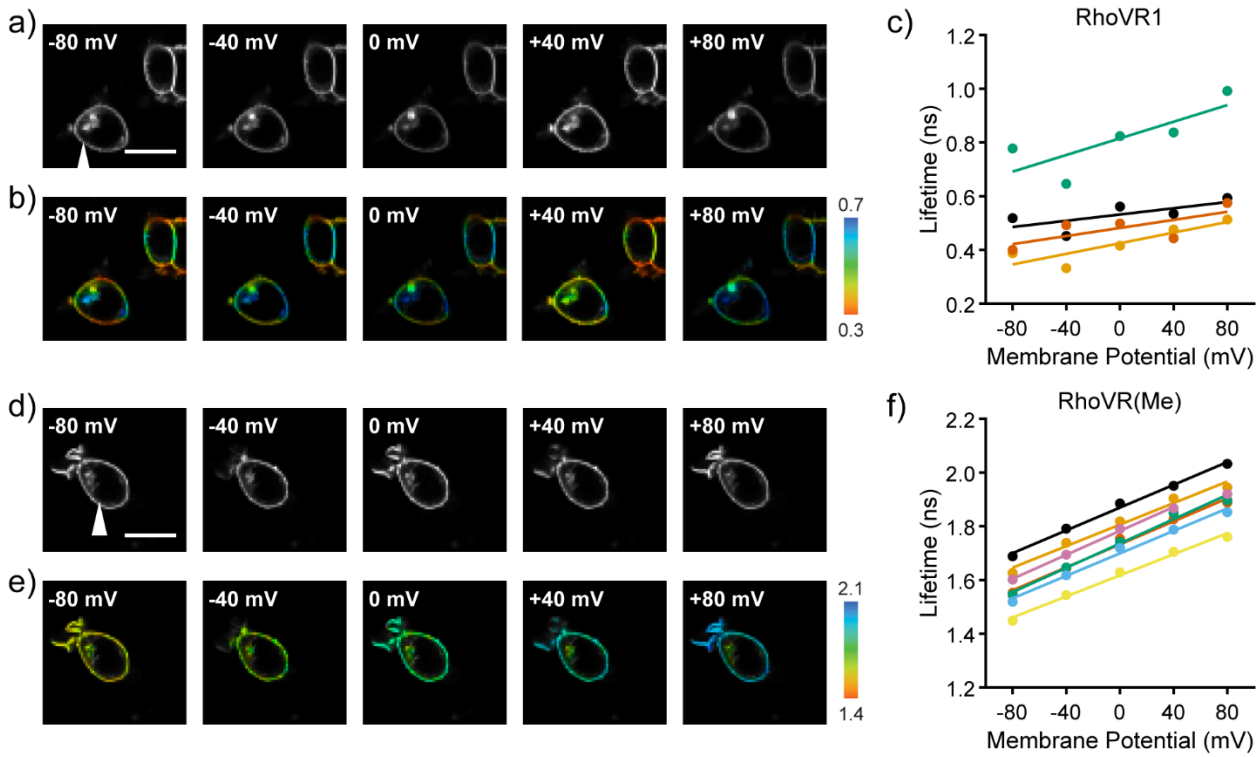

Figure 6.6. RhoVR1 and RhoVR(Me) show V_{mem} sensitive fluorescence lifetimes.
a) Photon count (fluorescence intensity) and b) lifetime-intensity overlay images of an individual HEK293T cell loaded with 500 nM RhoVR1. V_{mem} was held to the indicated value with whole cell voltage clamp electrophysiology. c) Quantification of the 2p fluorescence lifetime for RhoVR1 in 4 HEK293T cells subjected to the same protocol, along with the line of best fit for the lifetime-V_{mem} relationship. The cell shown in (a)-(b) is shown in red-orange in (c). d) Photon count and e) fluorescence lifetime images of a HEK293T loaded with 500 nM RhoVR(Me) and held at the indicated V_{mem} electrophysiologically. f) Quantification of the 2p fluorescence lifetime-V_{mem} relationship for RhoVR(Me) in 7 individual HEK293T cells. The cell from (d)-(e) is shown in purple in (f). The patch electrode is indicated by the white arrow; scale bars represent 20 μm.

In summary, we determined the relationship between fluorescence lifetime and V_{mem} for five VoltageFluors under two photon illumination. TMCRh.OMe, RhoVR1, and carboVF all show V_{mem} sensitive fluorescence lifetimes but have currently unexplained differences between their performance under 1p and 2p illumination. Going forward, it will be informative to measure the 1p lifetime of RhoVR1, but we unfortunately did not have a FLIM instrument with these capabilities. Both RhoVR(Me) and VF2.1.Cl do not exhibit such discrepancies, and they could both be useful voltage sensors for absolute V_{mem} determinations under 2p illumination. RhoVR(Me) is a particularly attractive target for future studies, as the sarcosine membrane anchor provides a synthetic handle for targeting of the sensor to cells of interest in complex tissue.[10]

Materials and Methods

VoltageFluor Stocks and Synthesis

VF2.1.Cl, carboVF, and RhoVR1 were synthesized in house according to the published syntheses.[7,9,11] TMCRh.OMe was synthesized in-house by Gloria Ortiz; these methods are described in her Ph.D. dissertation. RhoVR(Me) was synthesized in-house by Parker Deal.[10]

VF2.1.Cl, carboVF, and TMCRh.OMe were stored either as solids at room temperature or as 1000-5000x DMSO stocks at -20°C. RhoVR1 and RhoVR(Me) were stored as dried solid aliquots at -20°C or -80°C and reconstituted in DMSO prior to use. The concentration of dye stocks was determined from the absorption maximum of the chromophore via UV-Vis spectroscopy with a Shimadzu 2501 Spectrophotometer. Measurements were performed in 1 cm path length quartz cuvettes (Starna cells).

HEK293T Cell Culture, Dye Loading, and Electrophysiology

HEK293T cell culture and whole cell patch clamp electrophysiology was performed as described in detail in **Chapter 2**. The VF dyes mentioned here were used at the following concentrations: 100 nM VF2.1.Cl, 200 nM carboVF, 300 nM TMCRh.OMe, 500 nM RhoVR1, 500 nM RhoVR(Me). All dye loading was performed in Hank's Balanced Salt Solution (HBSS, with Ca^{2+} and Mg^{2+}) for 20 minutes in a humidified 37°C incubator.

For VF2.1.Cl and TMCRh.OMe, loading concentrations were selected to avoid concentration based quenching seen in the fluorescence lifetime (**Chapter 2**, **Chapter 5**); for other sensors, the concentration used was approximate and should be refined by systematic testing for concentration quenching.

Two-Photon Fluorescence Lifetime Imaging

2p-FLIM was performed on an inverted Zeiss LSM 510 equipped with a Becker and Hickl SPC-150N photon counting card. Excitation was provided by a MaiTai HP Ti:Sapphire laser tuned to the indicated wavelength. Excitation power was controlled by a polarizer followed by a polarizing beamsplitter, as well as an acousto-optic modulator (AOM) controlled by the Zen software (Zeiss). Light was directed into the microscope from a series of silver mirrors (Thorlabs or Newport Corporation).

For all probes, emitted photons were collected with a 40x/1.3 NA EC Plan-Neofluoar oil immersion objective (Zeiss) and detected with an HPM-100-40 single photon counting detector (Becker and Hickl). Photons were detected from the non-descanned side port of the LSM 510 after being reflected off of a 680 nm long pass dichroic mirror and passing through an IR-blocking filter. The following Semrock emission filters were used (all bandpass, in nm): VF2.1.Cl 550/49; carboVF, RhoVR1, RhoVRMe 593/40; TMCRh.OMe 650/60. Reference pulses for time correlated single photon timing were sampled from the excitation beam and detected with PHD-400-N high speed photodiode (Becker and Hickl).

Analysis of VF2.1.Cl, RhoVR1, RhoVRMe and carboVF 2p FLIM Data

2p-FLIM data for VF2.1.Cl were fit to an incomplete biexponential decay model in SPCImage (Becker and Hickl) as described in **Chapter 2**. An experimentally measured instrument response

function (IRF) was obtained from a solution of 0.5 mM fluorescein and saturating (12.2 M) NaI in 0.1 N NaOH. The IRF was measured frequently (at a minimum daily) during imaging. Using the same standard solutions of 2 μM fluorescein in 0.1 NaOH and 1 mg/mL erythrosin B, the optimal value for the color shift between the IRF and the measured decay was determined to be 0.7 (out of 256 time channels on the analog-to-digital converter). The photon count threshold for fitting was set to 200 instead of 300 counts in the brightest time channel. Other fitting parameters and binning were as described for the one photon signal (**Chapter 2**). Lifetime images in lifetime-intensity overlays are scaled as indicated; underlying photon count images are scaled to maximize contrast.

RhoVR1 was fit to an incomplete decay model as the sum of three exponential decay terms; RhoVR(Me) was fit to an incomplete decay model as the sum of two exponential decay terms. Peak photon thresholds of 300 were used for all probes other than VF2.1.Cl, as much larger photon counts were achievable. All other fit parameters were the same as for VF2.1.Cl.

carboVF lifetimes were measured at 740 nm and modeled as a sum of two exponential decay components. Data analysis was complicated by the presence of slight laser bleedthrough. The scatter parameter in SPCImage was set to an empirically determined value of 0.006 in an attempt to compensate for this. Shift was fixed to 0.9 based on fitting of the lifetime standard erythrosin B.

Analysis of TMCRh.OMe 2p FLIM Data

The fluorescence lifetime of TMCRh.OMe was first fit to a sum of three exponential decay components using custom Matlab code (described in **Appendix 1**) with all decay components and coefficients as free parameters. In doing so, we observed that τ_1 and τ_2 were V_{mem}-invariant, so we fit these parameters to the values that minimized the average χ^2 across all patches in the dataset (0.1 and 0.9 ns, respectively). Using the fluorescein-based IRF, a color shift of 0 was found to describe the lifetime standards best, so this value was used for all fitting. Offset was fixed to zero. A threshold of 300 peak photon counts in the brightest ADC time channel was used. Images were binned standard 2x2 upon export (in contrast to the SPCImage moving average binning used for other probes).

References

(1) Svoboda, K.; Yasuda, R. Principles of Two-Photon Excitation Microscopy and Its Applications to Neuroscience. *Neuron* **2006**, *50* (6), 823–839. https://doi.org/10.1016/j.neuron.2006.05.019.

(2) Cervera, J.; Alcaraz, A.; Mafe, S. Bioelectrical Signals and Ion Channels in the Modeling of Multicellular Patterns and Cancer Biophysics. *Sci. Rep.* **2016**, *6* (January), 1–14. https://doi.org/10.1038/srep20403.

(3) Kulkarni, R. U.; Kramer, D. J.; Pourmandi, N.; Karbasi, K.; Bateup, H. S.; Miller, E. W. Voltage-Sensitive Rhodol with Enhanced Two-Photon Brightness. *Proc. Natl. Acad. Sci.* **2017**, 201610791. https://doi.org/10.1073/pnas.1610791114.

(4) Kulkarni, R. U.; Vandenberghe, M.; Thunemann, M.; James, F.; Andreassen, O. A.; Djurovic, S.; Devor, A.; Miller, E. W. *In Vivo* Two-Photon Voltage Imaging with Sulfonated Rhodamine Dyes. *ACS Cent. Sci.* **2018**, acscentsci.8b00422. https://doi.org/10.1021/acscentsci.8b00422.

(5) Lazzari-Dean, J. R.; Gest, A. M. M.; Miller, E. W. Optical Estimation of Absolute Membrane Potential Using Fluorescence Lifetime Imaging. *Elife* **2019**, *8*, e44522. https://doi.org/10.7554/elife.44522.

(6) Grimm, J. B.; Muthusamy, A. K.; Liang, Y.; Brown, T. A.; Lemon, W. C.; Patel, R.; Lu, R.; Macklin, J. J.; Keller, P. J.; Ji, N.; et al. A General Method to Fine-Tune Fluorophores for Live-Cell and in Vivo Imaging. *Nat. Methods* **2017**, *14* (10), 987–994. https://doi.org/10.1038/nmeth.4403.

(7) Ortiz, G.; Liu, P.; Naing, S. H. H.; Muller, V. R.; Miller, E. W. Synthesis of Sulfonated Carbofluoresceins for Voltage Imaging. *J. Am. Chem. Soc.* **2019**, *141* (16), 6631–6638. https://doi.org/10.1021/jacs.9b01261.

(8) Lakowicz, J. R. *Principles of Fluorescence Spectroscopy*, 3rd ed.; Springer, 2011. https://doi.org/10.1007/978-0-387-46312-4.

(9) Deal, P. E.; Kulkarni, R. U.; Al-Abdullatif, S. H.; Miller, E. W. Isomerically Pure Tetramethylrhodamine Voltage Reporters. *J. Am. Chem. Soc.* **2016**, *138* (29), 9085–9088. https://doi.org/10.1021/jacs.6b05672.

(10) Deal, P. E.; Liu, P.; Al-Abdullatif, S. H.; Muller, V. R.; Shamardani, K.; Adesnik, H.; Miller, E. W. Covalently Tethered Rhodamine Voltage Reporters for High Speed Functional Imaging in Brain Tissue. *chemRxiv* **2019**, Preprint.

(11) Miller, E. W.; Lin, J. Y.; Frady, E. P.; Steinbach, P. A.; Kristan, W. B.; Tsien, R. Y. Optically Monitoring Voltage in Neurons by Photo-Induced Electron Transfer through Molecular Wires. *Proc. Natl. Acad. Sci. U. S. A.* **2012**, *109* (6), 2114–2119. https://doi.org/10.1073/pnas.1120694109.

Chapter 7
Investigation of Alternative Exponential Decay Models for VoltageFluor FLIM

Abstract

Fluorescence lifetime imaging (FLIM) can quantitatively report on a variety of features of the cell by measurement of the fluorescence decay of a fluorophore on the nanosecond timescale. Interpretation of FLIM data requires fitting to a decay model, selection of which can dramatically alter the quality of FLIM results. Both the value and the reproducibility of the fluorescence lifetime of VoltageFluor (VF) probes also depends on the fit model selected, making fit model a critical consideration in analysis of such data. Here, we explore and discuss different fit models for lifetimes of a library of VFs. We conclude that discrete exponential models are reasonable for the VFs studied here, although we cannot fully rule out the use of distribution fit models.

Introduction

FLIM is a powerful tool for quantitatively and optically measuring various parameters inside cells.[1] Because fluorescence lifetime (τ_{fl}) is an intrinsic property of a sensor, such measurements avoid artifacts in fluorescence intensity that arise from variable probe concentration or movement. Importantly, τ_{fl} can be altered by temperature, viscosity, solvent, or the presence of quenchers,[2] all of which can complicate the application of FLIM in biological settings.

In this dissertation, we explore FLIM of the small-molecule voltage dyes VoltageFluors as a strategy to measure the cellular transmembrane potential (V_{mem}). We demonstrated that VF FLIM can report absolute V_{mem} throughout both the gradual changes associated with EGF stimulation (**Chapter 2**) and fast spontaneous activity in cardiomyocytes (**Chapter 5**). We also use FLIM as a tool to inform indicator design, investigating structure-activity relationships across a panel of conformationally restricted VFs (**Chapter 4**). In all of these studies, we observed that the model selected in such fluorescence lifetime imaging studies has a major impact on the reproducibility and noise in the resultant fluorescence lifetimes. Optimization of the fit model is therefore an essential step in the use of FLIM to study V_{mem} (or any cellular parameter).

The time-resolved fluorescence decay I as a function of time t measured by time correlated single photon counting (TCSPC) FLIM is commonly modeled as a sum of n equals one, two, or three exponential terms (eqn 7-1), where a_i is the amplitude of each term and τ_i is the decay constant (lifetime).

$$I(t) = \sum_{i=1}^{n} a_i e^{-t/\tau_i} \qquad [7\text{-}1]$$

In theory, each decay constant represents a population of fluorophores at a particular temperature, viscosity, solvation state, etc. This framework is commonly used in the interpretation of binding ratios of sensors with two distinct states. For example, we expect that photoinduced electron transfer (PeT) based Ca^{2+} sensors would display two primary states, Ca^{2+} bound and Ca^{2+} free, each represented by a distinct lifetime term.[3–5] In simple systems, the amplitudes can be interpreted as the fractions of each state present in the sample.

When fluorophores and fluorescent indicators are delivered into a biological specimen, the true profile of distinct emitting populations often becomes complicated. Autofluorescence, sensor aggregation or misfolding, and inhomogeneous viscosities/solvents/temperatures introduce additional fluorescent decay components.[2] Explicit modeling of these factors is impractical, as the

number of photons required to obtain a reasonable fit increases with the number of fluorescent decay terms.[6] In practice, the number of decay components appropriate to model time resolved fluorescence data is often determined empirically from the reduction in the fit residuals as more components are added (e.g. **Chapter 4**, **Figures 4.15**, **4.16**). A useful parameter to describe the goodness-of-fit in such analyses is the reduced chi squared (χ^2), which assesses deviation between the experimental data y and the fit model z at each recorded time channel. N is the total number of time channels used in the fitting, and p is the number of free parameters in the fit.

$$\chi^2 = \frac{1}{N-p}\sum_{i=1}^{N}\frac{(y_i - z_i)^2}{z_i} \qquad [7\text{-}2]$$

We frequently observe multiple fluorescent decay components in the lifetime of membrane-localized voltage (V_{mem})-sensitive dyes (VoltageFluors, VFs). For example, we generally model the fluorescence decay of the voltage sensitive dye VF2.1.Cl as a biexponential decay (n=2 in eqn. 7-1). From this biexponential decay, we analyze only the weighted average (τ_m, eqn 7-3), as we found that it could be consistently measured with fewer photons than any individual component of the biexponential model. However, the use of a biexponential decay model for VF2.1.Cl is not fully satisfying, as the origin of these two populations of fluorophore is unclear. Furthermore, when we explored the fluorescence lifetimes of other VF dyes, we found that a biexponential model frequently either under- or over-fit the data (**Chapter 4**, **Chapter 6**).

$$\tau_m = \frac{a_1\tau_1 + a_2\tau_2}{a_1 + a_2} \qquad [7\text{-}3]$$

As an alternative to discrete exponential models, distribution fit models (eqn 7-4) can be employed to describe the time-resolved fluorescence decay of fluorophores in complex mixtures.[7–9] If a range of states are accessible to the fluorophore, the exponential decay is often best described by a distribution of lifetimes rather than single discrete values. For instance, fluorophores in a solvent mixture (e.g. the plasma membrane) may experience a range of solvation states, each with a slightly different lifetime.[10] Similarly, a FRET system accessing a variety of donor-acceptor distances rather than distinct ligand bound or free states may also be modeled in this manner.

$$I(t) = \int_0^\infty \alpha(\tau)e^{-t/\tau}d\tau \qquad [7\text{-}4]$$

$$\alpha(\tau) = \frac{1}{\sigma\sqrt{2\pi}}exp\left\{-\frac{1}{2}\left(\frac{\tau-\bar{\tau}}{\sigma}\right)^2\right\} \qquad [7\text{-}5]$$

$$\alpha(\tau) = \frac{1}{\tau}\frac{1}{\sigma\sqrt{2\pi}} exp\left\{-\frac{1}{2}\left(\frac{(ln\tau) - \bar{\tau}}{\sigma}\right)^2\right\} \quad [7\text{-}6]$$

In a distribution fit model, the amplitudes a_i are replaced by a probability distribution function (PDF) of decay constants $\alpha(\tau)$. The sum of the contribution from each τ in this PDF makes up the fluorescence decay I over time t. Two common PDFs used in this analysis are the Gaussian PDF (eqn 7-5) and the log-normal PDF (eqn 7-6). Gamma distributions have also been successful in FLIM analysis.[8]

Gaussian PDFs (eqn 7-5) are convenient to work with and can be described by two summary parameters, the mean $\bar{\tau}$ and standard deviation σ (or the variance, σ^2) of the distribution. However, Gaussian functions are not constrained to $\tau > 0$, but zero or negative lifetimes are non-physical and can pose problems in fitting.[8] The log-normal distribution (PDF in eqn 7-6) avoids this issue, because it is defined by exponentiation of a normally distributed variable, the log-normal distribution is most conveniently described by the geometric mean and geometric standard deviation of these summary parameters. This geometric mean (τ_{GM}) is the median of the distribution and can be obtained by exponentiating $\bar{\tau}$ (eqn 7-7). A form of the geometric standard deviation (σ_g) can be used to quantify spread in the distribution and is obtained by exponentiating σ (eqn 7-8).

$$\tau_{GM} = e^{\bar{\tau}} \quad [7\text{-}7]$$

$$\sigma_G = e^{\sigma} \quad [7\text{-}8]$$

When the theoretical justification for selection of an exponential decay model is unclear, a few model-agnostic strategies exist. The exponential series method (ESM) allows for discrimination between lifetime distributions and discrete lifetime decays by fitting to many fixed τ_i with the amplitudes a_i as free parameters (eqn. 7-9).[11] Fluorescence distributions can theoretically be observed in plots of a versus τ with many similar a_i for a series of τ_i. On the other hand, discrete exponential decays would appear as isolated high a_i at a particular τ_i. "Incorrect" τ that are not present in the dataset should have low amplitudes. However, the ESM contains many free parameters, so very high photon counts (greater than 1 million total per fit) must be obtained for the ESM model to give accurate results.[11]

$$I(t) = \sum_{i=1}^{n} a_i e^{-t/\tau_i} \text{ , where } \tau_i \equiv 0.05, 0.10, 0.15 \ldots ns \quad [7\text{-}9]$$

Exponential fits without *a priori* knowledge of the number of exponential terms can be accessed more elegantly through the Padé approximant of the Laplace transform of the data.[12] This approach is relatively recent and is not commonly employed in the context of fluorescence lifetime decays, although preliminary studies to this end have been reported.[13]

Here, we document the V_{mem} sensitivity of individual components of the VF2.1.Cl biexponential decay and explore the use of distribution fit models to describe the fluorescence decays of a library of conformationally restricted VFs (**Chapter 4**). Where sufficient photons could be collected, we performed exponential series analysis of the fluorescence decay of our probe library. With these analyses, we show that both discrete exponential models and distribution models are reasonable strategies to describe VF fluorescence decays. Exponential series analysis of VF exponential decays suggests that discrete exponential models may be more appropriate, although further investigation across larger libraries of VFs is required.

Results and Discussion

Voltage Dependence of Individual Components of VF2.1.Cl Biexponential Fit

Using whole cell patch clamp electrophysiology, we recorded the V_{mem} dependence of VF2.1.Cl lifetime in HEK293T cells (raw data are originally presented in Chapter 4 and re-analyzed here). We employed global analysis in the fitting instead of the pixelwise analyses presented previously to increase the number of photons in each fit and improve the ability to resolve individual components of the fit model (**Appendix 1**). In addition to the weighted average lifetime τ_m, we analyzed the V_{mem} dependence of the individual amplitudes and lifetimes in the biexponential fit model for VF2.1.Cl (**Figure 7.1**, **Table 7.1**). We observe individual decay components of 0.7 ns and 2.5 ns of approximately equal amplitude. Both decay components exhibit V_{mem} sensitivity that is lower in magnitude to the V_{mem} sensitivity of τ_m. τ_2 appeared more sensitive than τ_1. The relatively large amplitudes of these components, as well as their V_{mem} sensitivity suggests that they are not from cellular autofluorescence. The physical origin of these two components in the fluorescence lifetime is somewhat unclear, although it may be related to the interaction between VF2.1.Cl and the complex membrane environment.[10,14]

In addition, we analyzed V_{mem} sensitivity in the reduced chi squared χ^2. The quality of the fit would ideally be independent of the V_{mem} condition studied, but we observe poorer fits under hyperpolarized conditions. The origin of this effect is unclear, although it perhaps suggests that the biexponential model does not fully describe the V_{mem} sensitivity of VF2.1.Cl. In other words, if the V_{mem} sensitivity seen in the fit quality were instead actually described by the model, we might observe a slight increase in the nominal V_{mem} sensitivity of τ_m.

Somewhat surprisingly, we observed V_{mem} sensitivity in the amplitudes of fluorescence lifetime components. One explanation for this is that the larger V_{mem} sensitivity of τ_2 increases its amplitude at depolarized potentials (i.e. population 2 gets brighter). Another explanation is that there is some interconversion between the two populations in a V_{mem} dependent manner, perhaps attributable to V_{mem} dependent membrane reorganization.[15] These hypotheses are difficult to test experimentally, although future studies of the relationship between τ_{fl} and lipid composition in a defined environment such as synthetic vesicles could prove informative.

Taken together, these analyses support the use of τ_m as the primary parameter in reporting V_{mem} with VF2.1.Cl, as it shows the largest V_{mem} sensitivity. The underlying physical explanation for the behavior seen in other aspects of the model remains unclear. It is also possible that a biexponential model is not the best way to represent VF2.1.Cl lifetimes, as the choice between

discrete exponential decay models and lifetime distribution models is difficult to make statistically with photon counts typical of FLIM experiments in biological systems.[11]

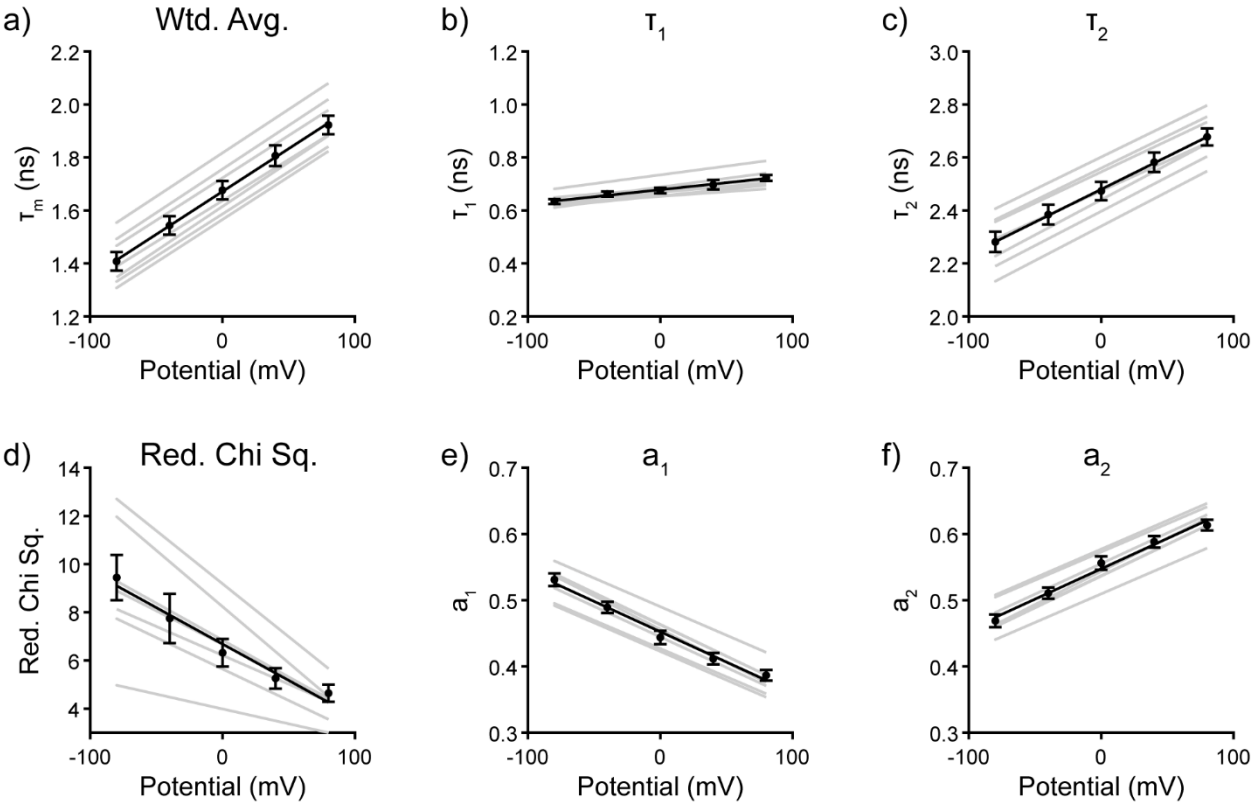

Figure 7.1. Response of VF2.1.Cl fit components to V_{mem}.
HEK293T cells incubated with 100 nM VF2.1.Cl were held at the indicated Vmem with whole cell voltage clamp electrophysiology while fluorescence lifetime was recorded. Fluorescence lifetime data were fit to a biexponential decay model. The relationship between a) weighted average lifetime τ_m, b) first decay component τ_1 c) second decay component τ_2 d) reduced chi squared (red. chi sq.) e) first amplitude a_1 f) first amplitude a_2 and V_{mem}. Gray lines are lines of best fit for individual measurements, and black line is the average line of best fir for the combined dataset. Data are shown as mean ± SEM across n=7 HEK293T cells.

Parameter	Sensitivity	Value at 0 mV
Weighted Avg τ_m	3.20 ± 0.08 ps/mV	1.67 ± 0.04 ns
First Lifetime τ_1	0.5 ± 0.1 ps/mV	0.68 ± 0.01 ns
Second Lifetime τ_2	2.5 ± 0.1 ps/mV	2.48 ± 0.04 ns
First Amplitude a_1	-9.2 ± 0.6 x 10^{-4} Δa/mV	0.45 ± 0.01
Second Amplitude a_2	9.2 ± 0.6 x 10^{-4} Δa/mV	0.55 ± 0.01

Table 7.1. Summary of VF2.1.Cl fit components' sensitivity to V_{mem}.
Data are mean ± SEM of n=7 cells. Raw dataset was re-analyzed from **Chapter 4**.

Log-Normal Distribution Fitting in Aniline-Modified VFs

To investigate distribution models more directly, we modeled the time-resolved fluorescence decay of VF2.1.Cl a single Gaussian or log-normal distribution of lifetimes (eqn 7-3, 7-4, 7-5). With Gaussian models (data not shown), we did not obtain satisfactory results, with frequent issues arising from negative or zero values of τ in VFs with short fluorescence lifetimes. With log-normal models, we obtained reasonable lifetimes and sensitivities for VF2.1.Cl (**Figure 7.2**, **Table 7.2**). We observe a V_{mem} sensitivity of τ_{GM} of 3.60 ± 0.08, which is similar to sensitivities seen with biexponential models (3.2-3.5 ps/mV, **Chapter 2**, **Chapter 4**). The 0 mV value of τ_{GM} was slightly shorter than the 0 mV value seen with biexponential models, but overall the results were strikingly similar. We observe a slight negative V_{mem} sensitivity in the spread of the log-normal distribution at higher V_{mem}. The physical explanation for this is not obvious, although it perhaps could arise from V_{mem}-dependent membrane reorganization.[15]

The reduced chi squared χ^2 for a log-normal distribution model was on average higher than the χ^2 obtained from a biexponential fit. Both χ^2 show some V_{mem} dependence, although the slope was greater for the χ^2 from a biexponential model. It is difficult to directly compare χ^2 from these two models, as the biexponential model involves four free parameters and the log-normal distribution model only employs two free parameters. One would expect a reduction in χ^2 based on the addition of more parameters, regardless of the model validity.

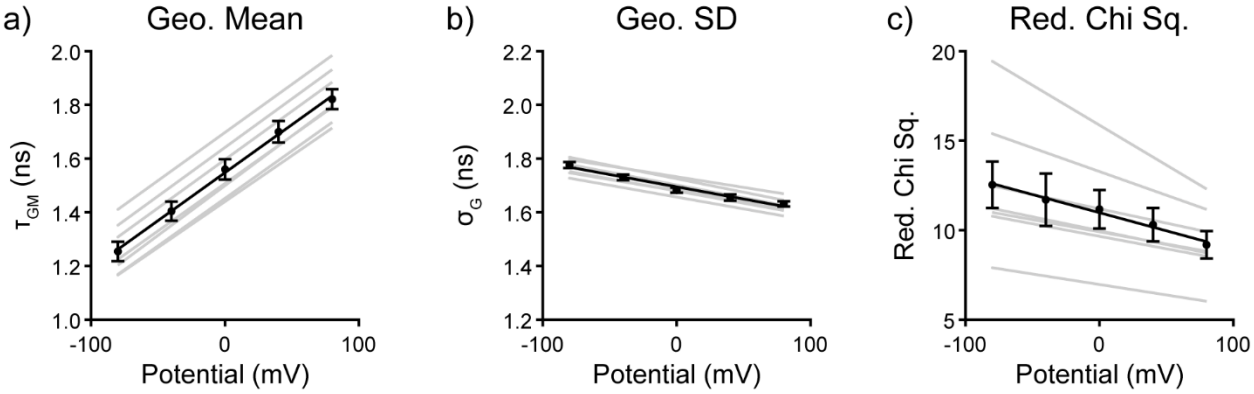

Figure 7.2. Log-normal distribution model for VF2.1.Cl.
Data are re-analyzed from the raw dataset described in **Chapter 4** and **Figure 7.1**. HEK293T were loaded with 100 nM VF2.1.Cl and held at fixed V_{mem} with whole cell patch clamp electrophysiology, and the measured fluorescence lifetime decays were modeled as log-normal distributions of lifetimes. The a) geometric mean, b) "geometric standard deviation," or a measure of scatter, and c) reduced chi squared (red. chi sq.) were analyzed for their dependence on V_{mem}. Gray lines represent lines of best fit from individual cells, and black line is the average line of best fit across all cells. Data are shown as mean ± SEM of n=7 cells.

We further explored the use of log-normal distribution models in VFs with modifications to the aniline conformation (**Chapter 4**). We had observed that the six VFs in our library could not all be fit with the same number of discrete exponential decay components, so we were curious as to whether a single log-normal distribution model would adequately reflect the observed lifetime decays for all probes. Using a log-normal distribution model and focusing only on τ_{GM}, we observe a similar overall trend in the absolute sensitivities and 0 mV lifetimes to that seen in **Chapter 4**, with intermediate levels of PeT and fluorescence producing the highest absolute sensitivities (**Figure 7.3**, **Table 7.2**). The lifetimes of iPrVF, IndoVF and JuloVF at 0 mV were all about 300 ps shorter in the log-normal distribution model fits, with JuloVF showing a τ_{GM} below 100 ps. Most VFs appeared slightly more sensitive to V_{mem} (larger slope of τ_{GM} vs. V_{mem} than τ_{fl} vs. V_{mem}).

The fluorescence decays were generally described adequately by the log-normal distribution model, although higher χ^2 values were observed for log-normal distributions in probes that were fit to 2 or 3 discrete exponential terms. An individual point appears poorly described in ^{i}PrVF, leading to deviation from the trend by one cell. Again, direct comparison between the χ^2 values across these models is not valid, as the models contain different numbers of parameters (2 for log-normal, 1 for 1 exponential decay, 4 for 2 exponential discrete, and 6 for 3 exponential discrete). Indeed, the main trends in χ^2 seem to track with the number of terms in the model rather than the identity of the model itself (**Table 7.2**).

Ideally, one would be able to justify the selection of a probability distribution model based on knowledge of the physical system at hand. However, our understanding of VF interactions within the plasma membrane environment is limited. Simulations suggest that VF2.1.Cl samples a variety of conformations and tilt angles within the plasma membrane,[16] which certainly could produce a distribution of lifetimes. Based on a Marcus model of electron transfer in the membrane, this angular dependence appears in an exponent in its effect on the rate of PeT,[17] potentially justifying a log-normal probability distribution. Nevertheless, we acknowledge that a fully satisfactory physical explanation for model selection in VFs is lacking.

Overall, the differences we observed between the optimized discrete component models and a log-normal distribution model were relatively minor. Larger differences were seen in the addition or removal of discrete exponential components (**Chapter 4**, **Figure 4.15**, **Figure 4.16**). We did not explore models involving a sum of two distributions due to the complexity of implementation and analysis. On the basis of the comparisons made here, we cannot rule out the use of a log-normal distribution model instead of a discrete exponential model. However, since the log-normal model did not improve results noticeably, we opted to continue with the more widely-used discrete exponential models.

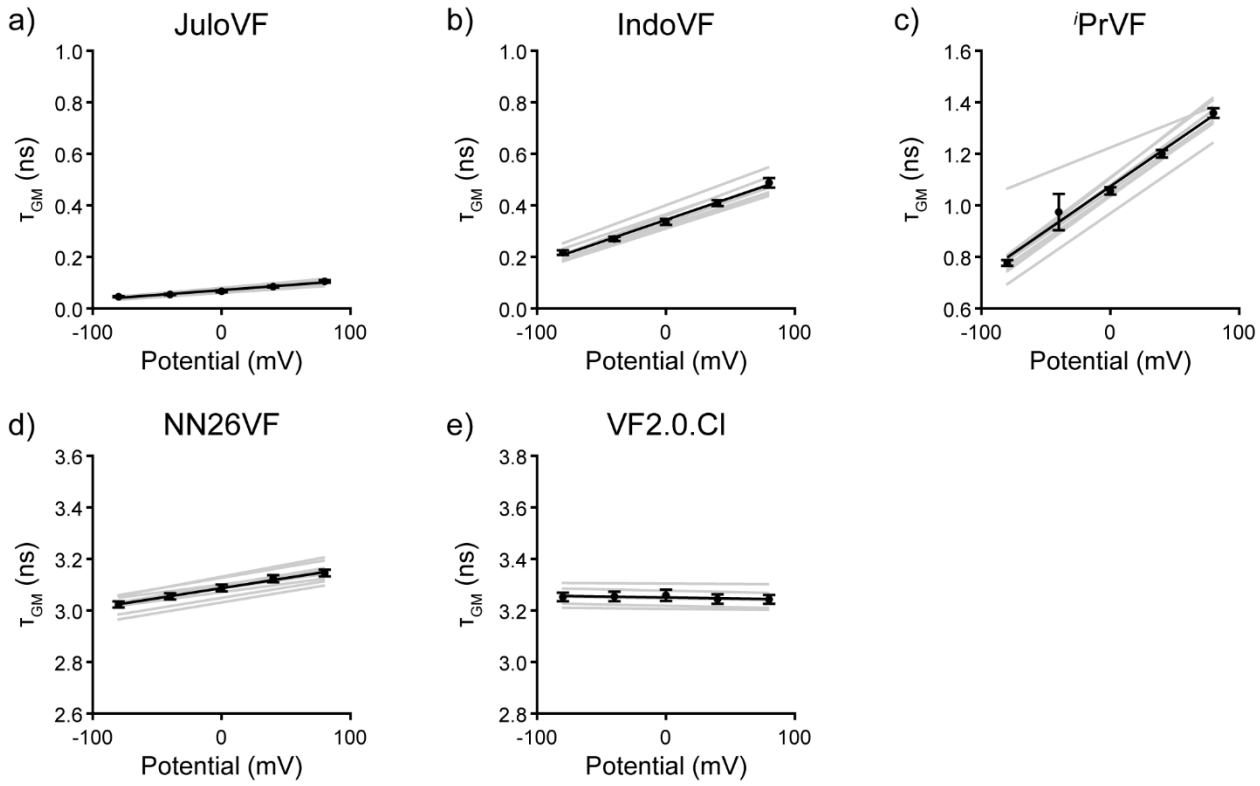

Figure 7.3. Log-normal distribution models for aniline-modified VFs.
Data are re-analyzed from the raw dataset described in **Chapter 4**. HEK293T were loaded with VF held at fixed V_{mem} with whole cell patch clamp electrophysiology, and the measured fluorescence lifetime decays were modeled as log-normal distributions of lifetimes. The dependence of the geometric mean on V_{mem} for a) 500 nM JuloVF, b) 300 nM IndoVF, c) 300 nM ^{i}PrVF, d) 300 nM NN26VF, and e) 100 nM VF2.0.Cl was analyzed. Gray lines indicate lines of best fit for individual cells, and black line represents the overall line of best fit. Data are shown as mean ± SEM for the following numbers of patched HEK293T cells: JuloVF 6, IndoVF 8, ^{i}PrVF 10, NN26VF 8, VF2.0.Cl 5.

VoltageFluor	τ_{GM}, slope, ps/mV	τ_{GM}, 0 mV lifetime, ns	Log-Normal χ^2	Exp. χ^2 (# Terms)
JuloVF	0.37 ± 0.04	0.071 ± 0.003	7.51	5.23 (3)
IndoVF	1.7 ± 0.1	0.34 ± 0.01	15.52	10.30 (3)
^{i}PrVF	3.4 ± 0.1	1.07 ± 0.02	12.70	11.26 (2)
VF2.1.Cl	3.60 ± 0.08	1.55 ± 0.03	10.98	6.68 (2)
NN26VF	0.8 ± 0.1	3.09 ± 0.01	2.17	4.56 (1)
VF2.0.Cl	-0.07 ± 0.02	3.25 ± 0.02	1.73	2.93 (1)

Table 7.2. Summary of V_{mem} sensitivity with log-normal distribution analysis.
Summary of data presented in **Figure 7.3**. Data are presented as mean ± SEM. χ^2 was determined from global analysis; values are larger than typical for pixel by pixel analysis because of the increased photon counts in each fit. χ^2 is shown as the average of all potentials accessed for all cells (4 or 5 potentials per cell). χ^2 for global analysis using the discrete exponential model selected in **Chapter 4** is shown for comparison, along with the number of exponential decay terms used.

Exponential Series Models – An 'Unbiased' Approach to Fitting

In cases where the correct model is not known, it would be ideal to fit data in such a way as to reveal the underlying distribution of the fluorescence lifetimes. To this end, we investigated the exponential series model (ESM) for analysis of VF2.0.Cl, NN26VF, VF2.1.Cl, and ^{i}PrVF lifetimes (eqn. 7-9).[18] Because many photons are required for accurate results with ESM, we used whole cell patch clamp electrophysiology in HEK293T to clamp cellular V_{mem} at -80 mV or 0 mV for 2.5-5 minutes while fluorescence lifetime data were collected (**Figure 7.4-7.7**). Both potentials were applied on every cell studied, although the order was randomized. We observed some photobleaching during this time period, especially for ^{i}PrVF, which was sometimes accompanied by moderate drifting in the lifetime (changes of approximately 50 ps). However, lifetimes were generally stable throughout this extended recording period.

We modeled the resulting fluorescence decays with a series of amplitudes for 120 fixed, equally spaced lifetimes ranging from 50 ps to 6 ns. We note that this is a large number of free parameters to model a function of 220 time channels (usable time channels of the FLIM apparatus across the 12.5 ns laser period). Nevertheless, in the VF2.0.Cl lifetime (**Figure 7.4**), we observe a single, V_{mem}-independent peak with high amplitude around 3.3 ns, with a few much smaller peaks at lower τ. One recording showed a more distribution-like form (**Figure 7.4**, bottom panel), but this result did not repeat on any other patched cells. The presence of a single peak is consistent with observations that VF2.0.Cl shows a single decay component that does not change with V_{mem} (**Chapter 2**, **Chapter 4**). The lower amplitude peaks at shorter τ are likely fit noise arising from the large numbers of components in the model, although they also could represent cellular autofluorescence. We observe similar results for NN26VF (**Figure 7.5**), which also showed a single exponential decay component and low V_{mem} sensitivity (**Chapter 4**).

For VF2.1.Cl (**Figure 7.6**), we observe three amplitude peaks in the τ distribution at both 0 mV and -80 mV. There is a clear shift to longer lifetimes for the peak around 2 ns upon cellular depolarization; V_{mem} dependence of the other peaks is less clear. This shift in lifetime, as opposed to a change in amplitude or disappearance of a peak, is consistent with a PeT-based V_{mem} sensing mechanism.[19] For ^{i}PrVF, we also observe multiple peaks, although they appear less well resolved and more inconsistent between trials (**Figure 7.7**). Shifts towards longer τ with depolarization are evident in some of the peaks but not all.

For all VFs studied with ESM analysis, we observe lifetime histograms that most closely resemble discrete exponential terms, rather than continuous lifetime distributions. However, the large numbers of parameters involved in ESM models, as well as the potential for photobleaching or photodamage across extended recordings with high light power, makes them suboptimal for our application and impractical as part of a standard VF-FLIM analysis.

In summary, discrete exponential models are adequate for describing VoltageFluor fluorescence lifetime in membranes. The number of exponential terms included in the model affects fit results considerably, but surprisingly, the switch to a log-normal distribution model yielded qualitatively similar results as the optimized discrete exponential models. Use of ESM analysis supports discrete exponential models, but ESM results should be interpreted cautiously. Future fluorescence lifetime studies of more VF derivatives will build further understanding of the optimal methods for describing these time-resolved fluorescence decays.

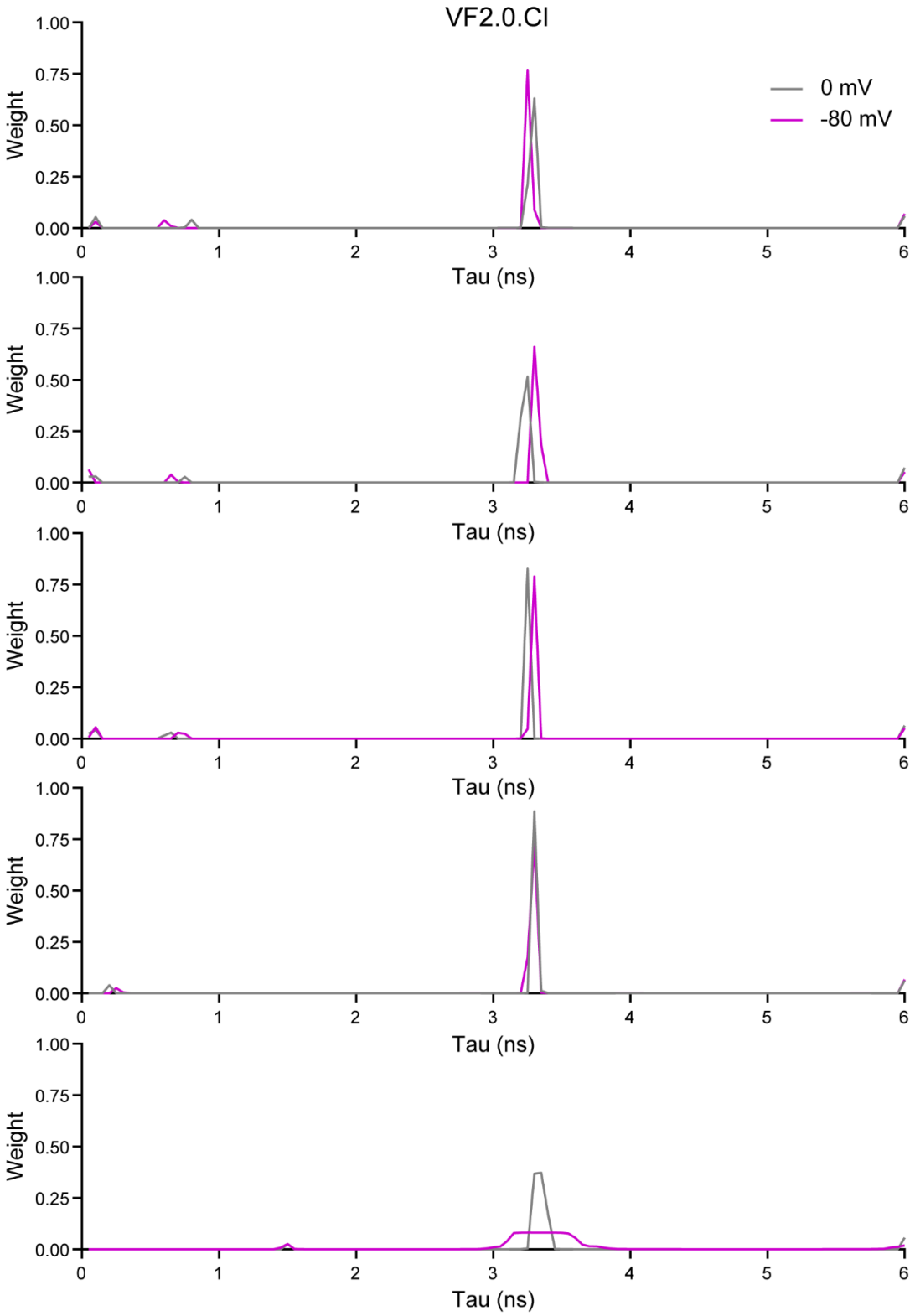

Figure 7.4. Exponential series analysis of VF2.0.Cl lifetime at -80 mV and 0 mV.
Recordings from five HEK293T cells stained with 100 nM VF2.0.Cl and held at either 0 mV or -80 mV. Data were fit with an exponential series model (eqn 7-9).

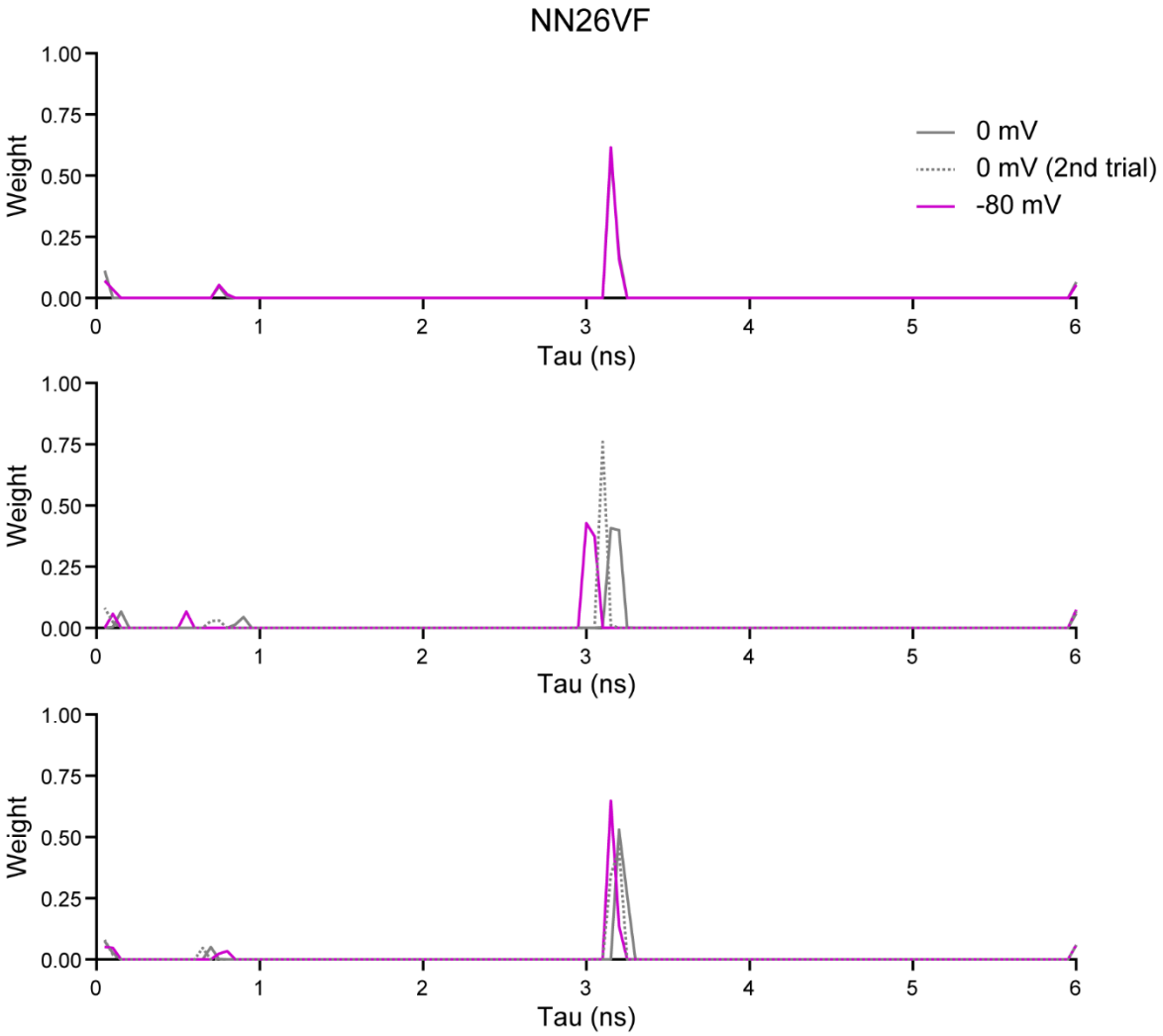

Figure 7.5. Exponential series analysis of NN26VF lifetime at -80 mV and 0 mV.
Recordings from three HEK293T cells stained with 300 nM NN26VF and held at either 0 mV or -80 mV. Data were fit with an exponential series model (eqn 7-9).

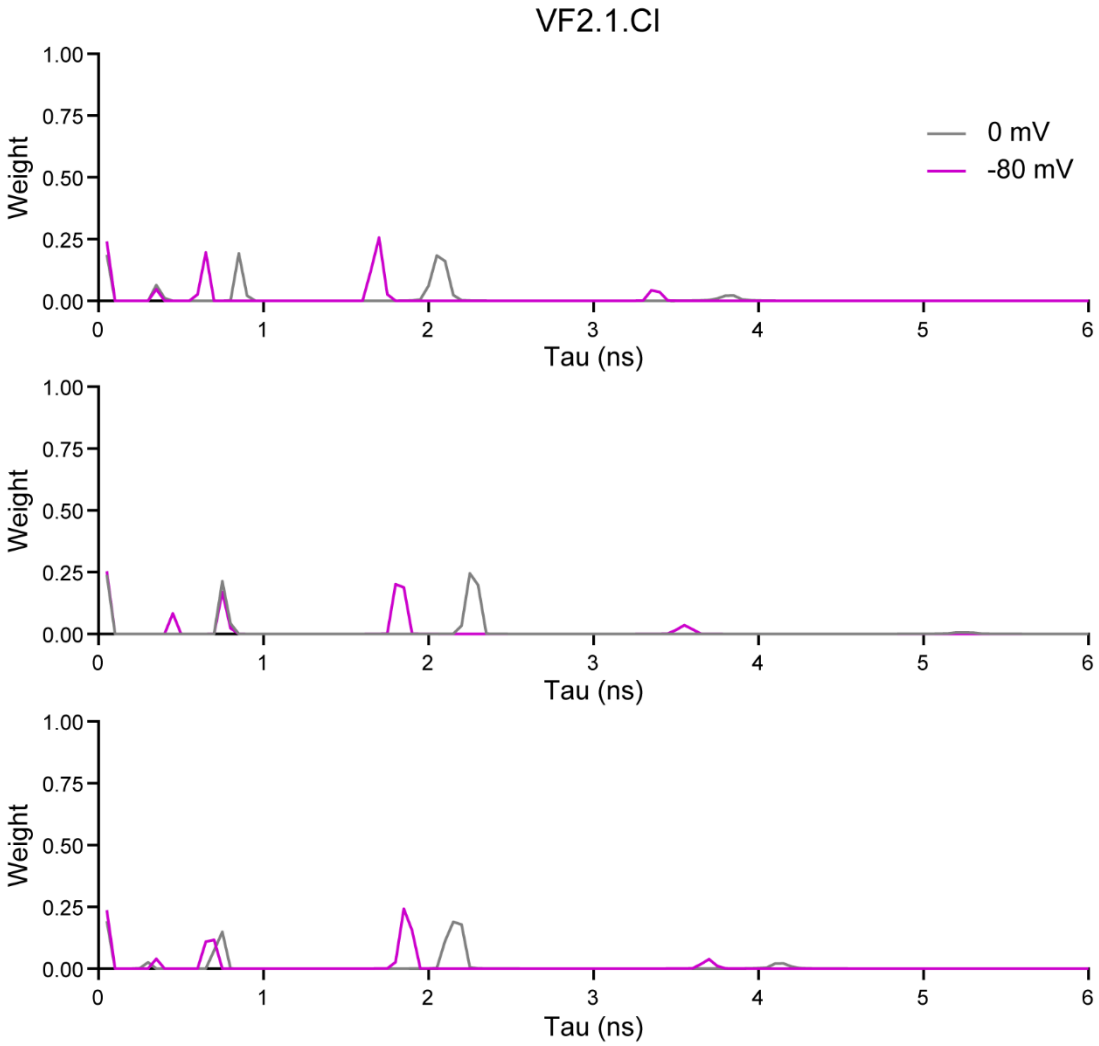

Figure 7.6. Exponential series analysis of VF2.1.Cl lifetime at -80 mV and 0 mV.
Recordings from three HEK293T cells stained with 100 nM VF2.1.Cl and held at either 0 mV or -80 mV for approximately 5 minutes per potential. Data were fit with an exponential series model (eqn 7-9).

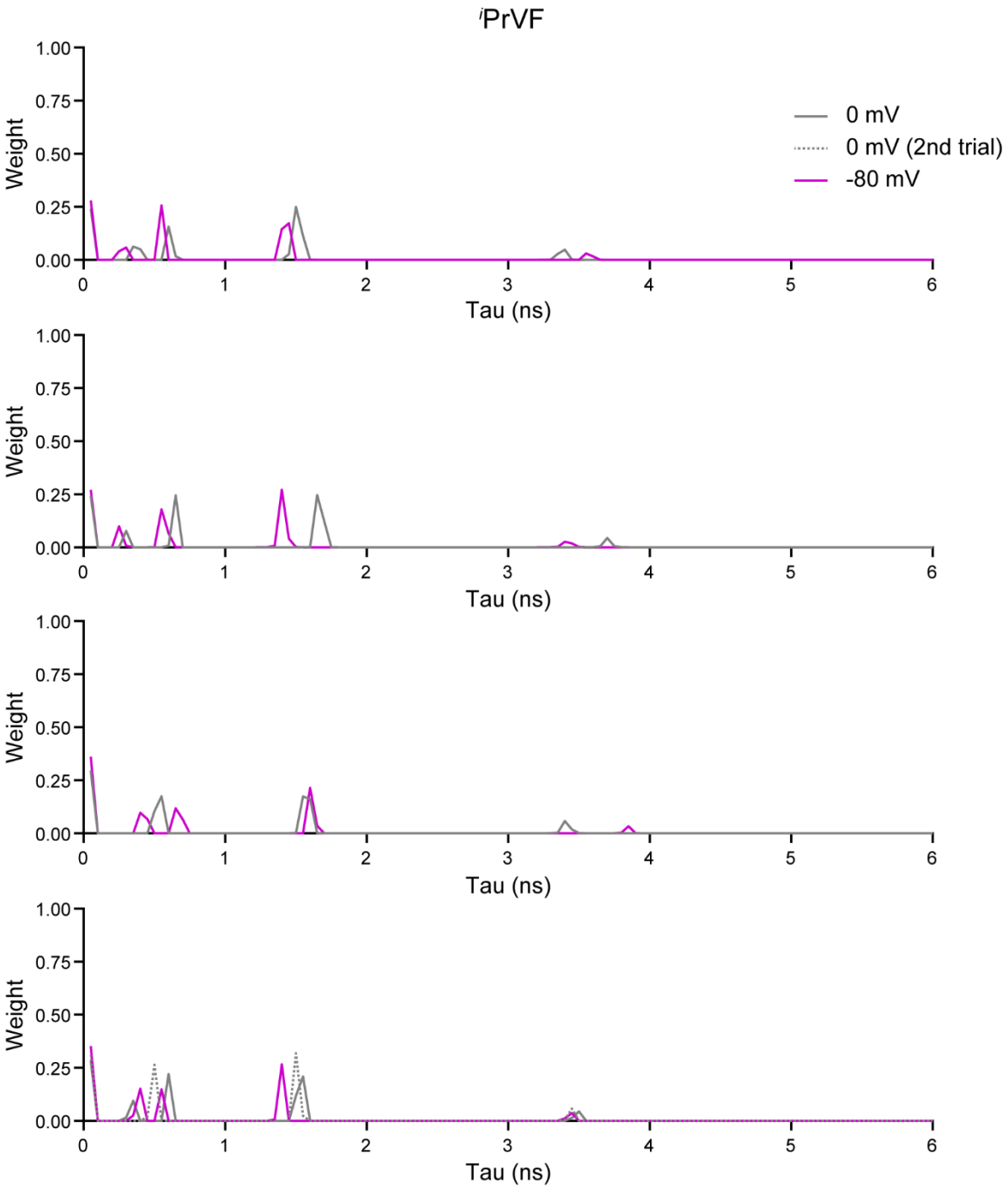

Figure 7.7. Exponential series analysis of ^{i}PrVF lifetime at -80 mV and 0 mV.
Recordings from four HEK293T cells stained with 300 nM ^{i}PrVF and held at either 0 mV or -80 mV. Data were fit with an exponential series model (eqn 7-9).

Materials and Methods

Collection of Fluorescence Lifetime Datasets

Data explored with biexponential and log-normal analyses was re-analyzed from **Chapter 4**; details of its acquisition are described there.

For exponential series model (ESM) analysis, more photons than are typically contained within a single V_{mem} step image were required. Using the same lifetime and electrophysiology acquisition settings described in **Chapter 4**, cells were held at either 0 mV or -80 mV for 5 or 10 successive 30 second exposures, and all membrane-localized signal from these images was combined into a single decay for analysis (generally 1e6-5e6 total photons per potential). Cells were only included if electrophysiology quality thresholds were maintained throughout a minimum of 10 recordings (5 at each potential). In some cells, the 0 mV steps were applied first, and in others, the -80 mV steps were applied first; this was designed to avoid potential systematic errors from photobleaching or photodamage to the molecular wire during these extended exposures.

Implementation of Fluorescence Decay Models

Fluorescence decay models used are described in the Introduction. Parameters were optimized via weighted least squares analysis in custom Matlab code (MathWorks, as described in **Appendix 1**). The built-in fmincon optimization function with the interior-point algorithm was used for optimization. Code is available upon request.

All fitting was done with global analysis rather than the pixelwise analysis used in **Chapter 4**. Membrane-localized ROIs were manually identified in FIJI.[20] Time-resolved fluorescence decays were extracted from the raw .sdt files in FIJI and imported into Matlab for further analysis. An experimentally measured instrument response function (IRF) of quenched fluorescein in NaI was used for analysis.[21] The shift and offset were fixed to 0 for all fitting.

To speed up optimization run times, log-normal integrals were evaluated numerically for a range of 1000 equally spaced data points in τ ranging from 0.001 to 10 ns. For ESM analysis, data were fit to a series of amplitudes for 120 fixed, equally spaced lifetime components ranging from 50 ps to 6 ns.

References

(1) Yellen, G.; Mongeon, R. Quantitative Two-Photon Imaging of Fluorescent Biosensors. *Curr. Opin. Chem. Biol.* **2015**, *27*, 24–30. https://doi.org/10.1016/J.CBPA.2015.05.024.

(2) Berezin, M. Y.; Achilefu, S. Fluorescence Lifetime Measurements and Biological Imaging. *Chem. Rev.* **2010**, *110* (5), 2641–2684. https://doi.org/10.1021/cr900343z.

(3) Lakowicz, J. R.; Szmacinski, H.; Johnson, M. L. Calcium Imaging Using Fluorescence Lifetimes and Long-Wavelength Probes. *J. Fluoresc.* **1992**, *2* (1), 47–62. https://doi.org/10.1007/BF00866388.

(4) Zheng, K.; Jensen, T. P.; Rusakov, D. A. Monitoring Intracellular Nanomolar Calcium Using Fluorescence Lifetime Imaging. *Nat. Protoc.* **2018**, *13* (3), 581–597. https://doi.org/10.1038/nprot.2017.154.

(5) Gersbach, M.; Boiko, D. L.; Niclass, C.; Petersen, C. C. H.; Charbon, E. Fast-Fluorescence Dynamics in Nonratiometric Calcium Indicators. *Opt. Lett.* **2009**, *34* (3), 362–364. https://doi.org/10.1364/OL.34.000362.

(6) Becker, W. *The Bh TCSPC Handbook*, 5th edn.; Becker & Hickl, 2012.

(7) Bajzer, Ž.; Therneau, T. M.; Sharp, J. C.; Prendergast, F. G. Maximum Likelihood Method for the Analysis of Time-Resolved Fluorescence Decay Curves. *Eur. Biophys. J.* **1991**, *20* (5), 247–262. https://doi.org/10.1007/BF00450560.

(8) Fogarty, A. C.; Jones, A. C.; Camp, P. J. Extraction of Lifetime Distributions from Fluorescence Decays with Application to DNA-Base Analogues. *Phys. Chem. Chem. Phys.* **2011**, *13* (9), 3819–3830. https://doi.org/10.1039/c0cp01779e.

(9) Libertini, L. J.; Small, E. W. Application of Method of Moments Analysis to Fluorescence Decay Lifetime Distributions. *Biophys. Chem.* **1989**, *34* (3), 269–282. https://doi.org/10.1016/0301-4622(89)80064-X.

(10) Williams, B. W.; Stubbs, C. D. Properties Influencing Fluorophore Lifetime Distributions in Lipid Bilayers. *Biochemistry* **1988**, *27* (21), 7994–7999. https://doi.org/10.1021/bi00421a004.

(11) James, D. R.; Ware, W. R. Recovery of Underlying Distributions of Lifetimes from Fluorescence Decay Data. *Chem. Phys. Lett.* **1986**, *126* (1), 7–11. https://doi.org/10.1016/0009-2614(86)85107-7.

(12) Yeramian, E.; Claverie, P. Analysis of Multiexponential Functions without a Hypothesis as to the Number of Components. *Nature* **1987**, *326* (6109), 169–174. https://doi.org/10.1038/326169a0.

(13) Bajzer, Z.; Sharp, J. C.; Sedarous, S. S.; Prendergast, F. G. Padé-Laplace Method for the Analysis of Time-Resolved Fluorescence Decay Curves. *Eur. Biophys. J.* **1990**, *18* (2), 101–115. https://doi.org/10.1007/BF00183269.

(14) Gross, E.; Bedlack, R. S.; Loew, L. M. Dual-Wavelength Ratiometric Fluorescence Measurement of the Membrane Dipole Potential. *Biophys. J.* **1994**, *67* (1), 208–216.

https://doi.org/10.1016/S0006-3495(94)80471-0.

(15) Zhou, Y.; Wong, C.; Cho, K.; van der Hoeven, D.; Liang, H.; Thakur, D. P.; Luo, J.; Babic, M.; Zinsmaier, K. E.; Zhu, M. X.; et al. Membrane Potential Modulates Plasma Membrane Phospholipid Dynamics and K-Ras Signaling. *Science (80-.).* **2015**, *349* (6250), 873–876. https://doi.org/10.1126/science.aaa5619.

(16) Kulkarni, R. U.; Yin, H.; Pourmandi, N.; James, F.; Adil, M. M.; Schaffer, D. V.; Wang, Y.; Miller, E. W. A Rationally Designed, General Strategy for Membrane Orientation of Photoinduced Electron Transfer-Based Voltage-Sensitive Dyes. *ACS Chem. Biol.* **2017**, *12* (2), 407–413. https://doi.org/10.1021/acschembio.6b00981.

(17) Li, L. S. Fluorescence Probes for Membrane Potentials Based on Mesoscopic Electron Transfer. *Nano Lett.* **2007**, *7* (10), 2981–2986. https://doi.org/10.1021/nl071163p.

(18) James, D. R.; Ware, W. R. Recovery of Underlying Distributions of Lifetimes from Fluorescence Decay Data. *Chem. Phys. Lett.* **1986**, *126* (1), 7–11. https://doi.org/10.1016/0009-2614(86)85107-7.

(19) Miller, E. W.; Lin, J. Y.; Frady, E. P.; Steinbach, P. A.; Kristan, W. B.; Tsien, R. Y. Optically Monitoring Voltage in Neurons by Photo-Induced Electron Transfer through Molecular Wires. *Proc. Natl. Acad. Sci. U. S. A.* **2012**, *109* (6), 2114–2119. https://doi.org/10.1073/pnas.1120694109.

(20) Schindelin, J.; Arganda-Carreras, I.; Frise, E.; Kaynig, V.; Longair, M.; Pietzsch, T.; Preibisch, S.; Rueden, C.; Saalfeld, S.; Schmid, B.; et al. Fiji: An Open-Source Platform for Biological-Image Analysis. *Nat. Methods* **2012**, *9* (7), 676–682. https://doi.org/10.1038/nmeth.2019.

(21) Liu, M.; Jia, M.; Pan, H.; Li, L.; Chang, M.; Ren, H.; Argoul, F.; Zhang, S.; Xu, J. Instrument Response Standard in Time-Resolved Fluorescence Spectroscopy at Visible Wavelength: Quenched Fluorescein Sodium. *Appl. Spectrosc.* **2014**, *68* (5), 577–583. https://doi.org/10.1366/13-07236.

Appendix 1
Implementation of Fluorescence Lifetime Analysis Suite

Synopsis

For fluorescence lifetime imaging to be easily digestible, the time-resolved decays collected must be described by summary parameters, most commonly an exponential decay constant τ. While both commercially available and open source software for this purpose exist, we found that no individual package implemented all or even most of our required functionalities. To remedy this, we developed a MATLAB pipeline capable of processing fluorescence lifetime imaging data in an automated fashion. This improvement to the analysis workflow was essential both for development of reproducible fitting models and for the advancements in throughput made by VF-FLIM.

The purpose of this code package is to process, analyze and visualize fluorescence lifetime imaging data. The specifics of this workflow were optimized towards membrane-localized fluorescence signal in mammalian cultured cell lines, but much of the package is generalizable to any application.

1. Process: Identify the regions of interest for fitting of time resolved fluorescence decays and extract these decays.
2. Analyze: Fit the fluorescence decays to the specified model, generally a sum of exponential decays.
3. Visualize: Rebuild the fluorescence lifetime data into image format or summarize it by time point and region of interest for plotting of summarized results.

Use of the FLIM-FLAM Analysis Suite

Selection of an Exponential Decay Model

The simplest fluorescence decay model is a single exponential decay, reflecting a uniform population of molecules emitting with a decay constant τ. In practice, many fluorescence decays are not well described by a single fluorescence decay model. Multiple populations of emitters exist in most biological samples, resulting from heterogeneous probe environments and the fluorescence of endogenous chromophores. These multiple populations of emitters appear as a sum of n exponential decays in the fluorescence intensity (I) as it decays over time (t) (eqn. A1-1).

$$I(t) = \sum_{i=1}^{n} a_i e^{-t/\tau_i} \qquad \text{[A1-1]}$$

In equation A1.1, a_i represents the amplitude of each exponential term, and τ_i represents the time constant for that term (fluorescence lifetime). Selection of the most appropriate number of decay components is a statistically challenging problem. With VoltageFluors, a naïve expectation would be that the decays would show a single exponential form, arising from fluorophore uniformly localized to the interface between the plasma membrane and the extracellular space. However, most VoltageFluor probes tested exhibit biexponential or triexponential fluorescence decays in cells (**Chapters 2, 4, 5, 6**).

For fluorophores delivered to biological systems, a practical decay model is often selected by iteratively fitting additional terms and monitoring the concomitant decrease in the reduced chi squared. This model selection process is best performed on a standardized dataset. Ideally, the standards would be close to the system of interest (e.g. voltage-clamped HEK293T cells to develop standard fitting for non-voltage clamped cells), but if that is not possible, lifetime standards characterized by other researchers can be used.[1] The addition of terms must also be appropriate for the photon statistics acquired, as fit noise increases and nonsensical values can emerge if the fluorescence decay is modeled with more terms than can be consistently described by the data (**Chapter 4**).

Where multiple exponential terms are included in the model, it is often convenient to represent the lifetime as a weighted average of all exponential terms (τ_m) instead of analyzing each component individually. The software will automatically calculate τ_m for these models. In our hands, we found that this analysis has the added benefit of requiring fewer photons to obtain consistent results (versus modeling each term individually). The weighted average lifetime τ_m for two component (eqn. A1-2) and three component (eqn. A1-3) exponential decay models is shown below.

$$\tau_m = \frac{a_1\tau_1 + a_2\tau_2}{a_1 + a_2} \qquad \text{[A1-2]}$$

$$\tau_m = \frac{a_1\tau_1 + a_2\tau_2 + a_3\tau_3}{a_1 + a_2 + a_3} \qquad \text{[A1-3]}$$

As in eqn. A1-1 above, the amplitudes of each exponential term are represented as a_i and the decay constants (lifetimes) are represented as τ_i.

Optimization of Model Parameters to Reflect Experimental Data

Regardless of the model selected, the software uses weighted least squares minimization to determine a set of optimal parameters to model the experimental data. This optimization is performed using Matlab's built-in fmincon function, which uses the interior-point algorithm. The scoring function is a reduced chi squared (χ^2) that describes the deviation between the modeled data and the experimental data, with higher weight placed on time channels containing more photons (eqn A1-4).

$$\chi^2 = \frac{1}{N-p}\sum_{i=1}^{N}\frac{(y_i - z_i)^2}{|z_i|} \qquad \text{[A1-4]}$$

where N is the number of free parameters in the fit (number of time channels included), p is the number of fit parameters, z is the value of the fit model at a particular time channel, and y is the value if the decay at a particular time channel.

Selection of Global versus Pixelwise Analysis

Fluorescence lifetime analysis in the context of *images* can be broken down into two major classes: pixelwise and global (**Scheme A1.1**). In pixelwise analysis, the fluorescence decay constants τ are determined at each pixel and a heatmap of τ is generated. For summaries of results, the average of these τ values in the region of interest is often obtained. On the other hand, global analysis involves consolidation of photon histograms for an entire region of interest (ROI) *before fitting*; decay constants are then determined per region of interest from the selected exponential model.

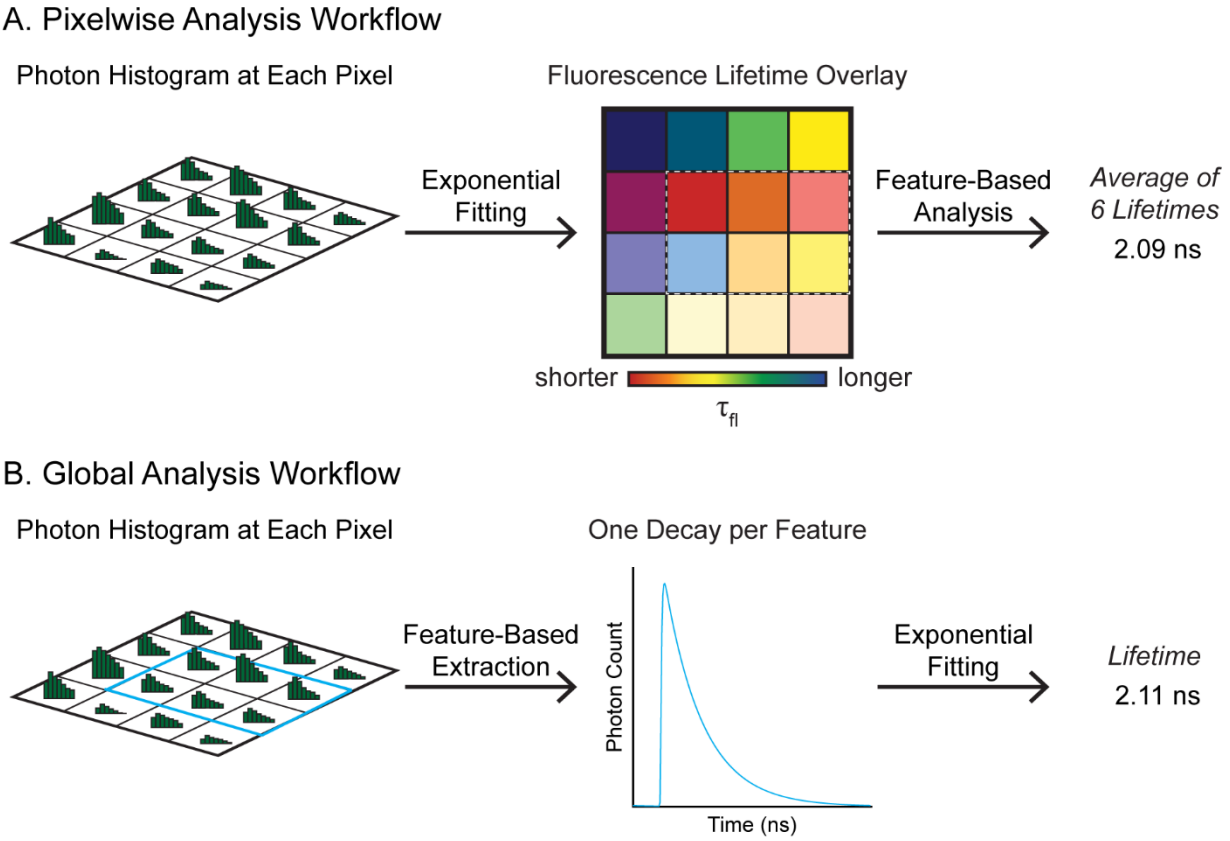

Scheme A1.1. Workflows for analysis of fluorescence decays.
(A) Analysis at each pixel involves fitting an exponential decay model to each position in the image. Often, images must be binned dramatically to obtain quality photon statistics and manageable fit noise. (B) Global analysis involves combination of photon histograms from multiple pixels in the region of interest (usually determined by the nature of the experiment.)

The selection of pixelwise versus global analysis methods depends largely on the application at hand, and there is no general rule. We have used both pixelwise and global analysis with

VoltageFluor FLIM data. Indeed, an advantage of the FLIM-FLAM suite is that it enables facile global and pixelwise analysis on the same dataset. Below, we outline some considerations in selecting an analysis mode.

Pixelwise analysis is often the most satisfying, when using VF-FLIM to map V_{mem} in a biological specimen. Pixelwise analysis also provides an easier interface to discover unexpected relationships in the data, as the regions with interesting features do not need to be known a priori. However, care must be taken in the generation of images fit at each pixel, as many photons are required to accurately fit exponential decays, so acquiring enough photons to resolve the lifetime at each pixel limits the temporal resolution of the experiment. Most pixel by pixel fitting with VoltageFluors shows only the weighted average decay, as the individual parameters (taus and coefficients) displayed more variability.

If detailed information is desired about individual components of multiexponential fluorescence decays, global analysis is usually the best option. Sufficient photons to determine a fluorescence decay can be obtained much more easily on sensitive specimens, and often enough photons may be collected to resolve individual parameters of the decay model. Global analysis can also be used to extract information from carefully constructed regions of interest on the raw photon image, which may be useful for identifying fluorescence decays from fine structures such as neuronal processes.

The wrapper code for the file parsers (importData.m) accepts four different import modes, which determine how the data are broken down. The below descriptions depict how an image of X pixels by Y pixels by N time channels would be handled by the software.

1. “single”: Combines all of the pixels X by Y into a single N by 1 decay for each image.
2. “pxwise”: Retains the native spatial resolution and returns an X by Y by N array.
3. “global_fiji”: Parses ROIs provided by the user as binary exports from ImageJ (FIJI). This mode uses these masks to define regions of interest for global analysis.
4. “global_btm”: Uses thresholding code optimized for finding membranes in confocal images of cultured cells to identify ROIs for global analysis. The user has an opportunity to modify and verify ROIs generated by this “batch trace membranes” (BTM) routine.

Once the data have been imported, there are two exponential fitting functions easily available to the user. For global analysis, fitDataStruct.m will process the output of a global import and return a structure with the exponential decay fit results as well as any metadata. For pixelwise analysis, pxwiseAnalysis.m will fit the output of a “pxwise” import and render images of the components of interest, as well as overlays of these components on the photon count image. Feature-based results can be identified (batchTraceFromStruct.m) by taking the average lifetime of the fit image within the BTM-identified ROI.

Selection of Other Fit Parameters

After the model is selected, the most important additional parameter in the model is the shift in time between the instrument response function (IRF) and the fluorescence decay (sometimes called the color shift), as well as whether this parameter is fixed or allowed to vary during fitting (specified in the input configuration file). We follow the common convention of working with shift in units of bins in the lifetime decay time (determined by the analog to digital converter (ADC)

resolution). A measured IRF at the same wavelength as the sample should have a shift very close to 0, but a measured IRF at a different wavelength may show a shift in time, especially on older detectors.[2] The best way to optimize the shift is to fit a monoexponential lifetime standard with the same emission spectrum as your fluorophore and then fix the shift to the shift obtained for that standard. Synthetic IRFs determined from the rising edge of the fluorescence decay are not implemented in FLIM-FLAM. Although they are common in commercial FLIM packages, we found a dramatic increase in the noise in VoltageFluor lifetimes determined from calculated IRFs, likely attributable to poor modeling of the short τ components present in certain VoltageFluor fluorescence decays.

The offset of the lifetime decay is the amount of non-time-resolved signal in the decay, arising most commonly from dark counts on the photon counting detector or from stray light in the room. If acquisitions were carefully performed in a cool, dark room, this parameter can generally be fixed to zero.

The start and end time bin of the IRF should be selected to include the main IRF pulse but avoid other noise in the baseline. The start and end time of the decay should be a few bins in from either end of the signal region to avoid artifacts from the time to amplitude converter (TAC). Setting the IRF mode to paired can correct for variability in an individual measured IRF but is generally not required. The threshold in number of photons for fitting a decay depends on the number of parameters in your model; more photons are required to model more decay parameters. Threshold 5000 is probably a good starting point for monoexponential and biexponential models, but the consistency of the lifetimes obtained must be evaluated for each system under study.

Region of Interest Identification

The scripts adapt the routines we developed previously in batchTraceMembranes2 to enable automated identification of contiguous membrane regions. These regions can be applied either before the fitting (global analysis) or after the fitting (pixelwise analysis). The user has the opportunity to remove debris, merge ROIs that were erroneously split, and approve the final ROIs within the batch tracing script. This processing mode works best if the thresholding is tweaked slightly to reflect the morphology and characteristics of the cell line, so the function takes the cell type as an input parameter. Currently supported cell lines are A431, CHO, HEK293T, MCF-7, and MDA-MB-231. If the cell line name is not recognized, the defaults for HEK293T are used.

If no spatial resolution is desired, the global decay for the entire photon histogram can also be selected. More complex ROIs should be generated as TIFF masks (e.g. in FIJI). These can then be imported and applied as masks to the data (0 is background and values >1 are kept).

Function Usage Overview

The most useful sequence of function calls (all MATLAB code files) for typical workflows is listed here for reference. Additional documentation on usage is available within each individual function file (*.m).

1. Pixelwise fitting and rendering of FLIM images: importData, pxwiseAnalysis
2. Pixelwise fitting of FLIM images, followed by averaging across automatically identified membrane regions of interest: importData, pxwiseAnalysis, batchTraceFromStruct

3. Global fitting, in any mode (single decay per image or decays defined by regions of interest): importData, fitDataStruct
4. Rendering TIFF photon count images for defining ROIs on data without processing in any other way: renderPhotonsImg
5. Rendering of TIFF images of parameters that were not previously processed from a pixelwise analysis (e.g. if you only rendered images of τ_m when you fit the data but would like to see the spatial localization of, say, χ^2 or τ_1 without refitting OR you would like to render the same parameter across a different scale - for VF-FLIM this might be rendering across a range of τ_m that matches convenient membrane voltages): renderImage

Formatting of Input FLIM Data Files and Metadata Files

Filename Formats for Data Records

FLIM records should be imported as photon histograms generated either by the binary export in SymPhoTime (*.bin) or as the raw acquisition format in SPCM (*.sdt). Opening of sdt files relies on the BioFormats package for MATLAB. Data records can be uniquely identified by a combination of the following parameters:

1. Date recorded, generally YYYY-MM-DD
2. Coverslip or sample identifier (abbreviated 'cID', CC).
3. Image identifier (abbreviated as 'imageID', II). This is a unique field of view within the sample.
4. Replicate identifier (abbreviated 'repID', RR). This is the number of times a FLIM images was recorded from a particular field of view. It is almost always 1, but this parameter is included to allow for re-acquisition of images if technical difficulties arose or for comparisons of signal stability.
5. Frame identifier (abbreviated 'frameID', XX). This is the slice of a time series (in experiment time) that the image corresponds to. It is more generally used than replicate ID. For instance, if I recorded two time series of ten images each from the same field of view. they would have the (repID, frameID) combinations of (1,1-10) and (2,1-10).

We save our FLIM files to a regularized format so that the file name strings can be parsed to obtain information about the various IDs in the recordings. If filenames are not in the format below, they will need to be renamed for proper functioning of the multilevel ID system.

General format of data filename string, before the .bin or .sdt file extension:

YYYY-MM-DD_CC-II-RR_anything_else_you_wantXXX

	Parsing Results				
Input name	**Date**	**cID (CC)**	**imageID (II)**	**repID (RR)**	**frameID (XX)**
2019-10-12_01-1_bob.bin	2019-10-12	1	1	1	N/A
2019-10-12_5-06-3_awesome.bin	2019-10-12	5	6	3	N/A
2019-10-12_5-06-3_ralph011.bin	2019-10-12	5	6	3	11
2019-10-12_010-02_ralph_1.bin	2019-10-12	10	2	1	1

Table A1-1: Sample parsing results for various filename strings.

This is not an exhaustive list of acceptable strings, but it is intended to give the user a sense of parser requirements. The software is flexible regarding the number of digits in CC, II, and RR as long as they are separated by dashes. 02-03-02 and 2-3-2 will give the same result. The RR is frequently not present; it will be assigned to 1 if it is missing. The XXX frameID is only processed if nFrames is set in the metadata (see below). The character before the start of the frameID does not matter as long as it is not another number. Not applicable (N/A) means that the field will not exist in the output data.

Configuration and Metadata File Formats

In general, these files should be saved in a comma separated values (csv) format in which the first row is the categories and each subsequent row corresponds to a unique record. The analysis suite looks for exact matches for certain categories/fields in the input metadata to properly complete the analysis. Sample functional metadata is available within the software, and the fields required are enumerated here:

The configuration file indicates standard fit settings and instrument properties. Most, if not all, of the metadata about acquisition settings is lost upon exporting to a histogrammed photon images (especially in the SymPhoTime software package from PicoQuant), so it needs to be re-entered here. Expected fields are below; order of the columns in the input file does not matter.

1. model: string or character array for the number of exponential components. Accepted values are 1exp, 2exp, 3exp, and 4exp.
2. fixedParam_X: A boolean indicating which parameters (taus and term weights) should be fixed to their starting values (fixedParam_X = 0) and which parameters should be allowed to vary (fixedParam_X = 1) during the fitting. The number _X at the end of the name specifies the parameter, with all of the coefficients numbered before all of the lifetimes. For example, for a biexponential fit, X = [1 2 3 4] for [a1 a2 tau1 tau2]. For a monoexponential fit, fixedParam is set to -1 by default in the software.
3. startParam_X: Floating point fields determining the starting value for each parameter, numbered as for fixedParam_X. If the parameter is fixed, it will be fixed to the input value of startParam_X. floating-point fields for each coefficient and tau to be fit. X is the index of the parameter. For a monoexponential fit, only provide the starting lifetime as startParam_1.
4. offFixed: boolean indicating whether the offset (dark counts) should be fixed to zero or allowed to vary in the fitting.

5. cShift: floating-point number corresponding to the shift between the IRF and the decay to be fit, in units of ADC time bins.
6. shiftFixed: boolean indicating whether the shift should be fixed to the starting value or used as a free parameter in the fit.
7. period_ns: The period of the laser cycle during the acquisition in nanoseconds. For 80 MHz laser repetition rate, the period_ns is 12.5.
8. irf_start: The beginning of the IRF (in ADC time bins). This enables cropping of a measured IRF to just the segment corresponding to the laser pulse.
9. irf_end: The end of the IRF (in ADC time bins).
10. fit_start: The first ADC time bin to be used in the fit.
11. fit_end: The final ADC time bin to be used in the fit.
12. threshold: number of photons minimum in a decay to be processed (sum across all time, not the peak value). This value is only used in pixelwise analysis; global analysis will be performed regardless of the number of photons.
13. IRFmode: Accepted values are "single" or "paired." This parameter indicates whether each IRF file will correspond to an IRF index or if the average of sequential IRF files should be used to generate an IRF for each IRF index.
14. ADCres: The expected number of time channels from the analog to digital converter (N in X by Y by N photon histograms). This value should be constant across all data and IRFs analyzed. It is provided as a fail safe check in the configuration file to verify that nothing strange happened to the data upon exporting.

The metadata file provides information about the data being analyzed. It is intended to be a useful way to track categorical data and later bring output data with this information into any plotting software. Each file (defined by cID-imageID-repID) must map to a single, unique value in the metadata. The required files are below; again order does not matter:

6. irf_index: The number of the IRF to be used in processing the data. If IRFs are imported as an average of a pair of two, this should count the pairs as a group, not as two individual files.
7. cID: The coverslip or sample ID of the record. If no other IDs are provided, all images

Certain special fields in the metadata file are not required, but their presence will change how the data are processed. Any fields beyond the required and special fields will be carried forward and assigned to the appropriate records, but they will not affect the analysis. Special fields are below:

8. imageID: If an imageID is provided, then all imageIDs in the input data must have a match in the metadata, and records will be matched to metadata based on both cID and imageID.
9. repID: Similar to imageID. It is only used for matching records with metadata if it is provided.
10. nFrames: The number of frames in the record. If this is specified, the file name parser will look for and assign the frameID based on the end of the filename.
11. cellType: This field must be provided if the user would like to access the automated membrane tracing in "BTM" modes either before or after fitting exponential decays. Supported values are "A431", "CHO", "HEK293T", "MCF-7" and "MDA-MB-231," which threshold the image slightly differently to best capture membrane given the

typical morphology of that cell line. If cellType does not match one of these values, the code will use the settings for HEK293T cells as a default.

12. smallestObject: This field must be provided if the user would like to access the automated membrane tracing in "BTM." The units are in pixel areas. The script will assume that regions smaller than smallestObject are debris and will remove them automatically.

If the user is importing ROIs as TIFF masks (e.g. those generated in FIJI, see Materials and Methods), there are two options for matching the ROIs to the relevant images. This option is determined by a command prompt to the user, and it is specified within the function as the mode string (either "csv" or "parse").

13. parse: Use the structure of the ROI name to determine which image the apply the ROI to. The ROI must be named in the format CC-II-RR_NN, where NN is the numerical identifier of that ROI (the number of ROIs for that image). CC, II, and RR are the cID, imageID, and repID as described above. Names in the format CC-II, CC-II-RR_NN, and CC-II_NN also are accepted. Missing fields are assumed to be equal to 1. Parse mode can be used for time series but the same ROIs will be applied to every frame of the time series. If changing ROIs are desired for a time series, they must be specified in the csv mode.
14. csv: Uses a separate ROI metadata file (*.csv) that contains the cID, imageID, repID, and frameID of the image as well as the exact name of the ROI (minus the file extension). cID and imageID must be present; if repID or frameID is missing, it will be filled in with the value 1.

Materials and Methods

This software was written in MATLAB version 2019b (MathWorks, Natick, MA). Code is available upon request. The reconvolution of the instrument response function with the exponential decay "guess" function was performed by open source code from Enderlein and Erdmann.[3] Output files from Becker Hickl FLIM systems (SPCM software, extension .sdt) are opened with the BioFormats plugin for MATLAB,[4] which is developed by Open Microscopy Environment and is freely available under a GNU public license. Successful running of the software requires that BioFormats be added to the user's MATLAB path.

This code does not support hand-drawing of ROIs within MATLAB. Hand-drawn ROIs used with this software were generated in FIJI[5] and saved to a TIFF file. A sample IJM macro file to perform this transformation is available within the code package.

Fluorescence lifetime data taken on both the Zeiss LSM510-Becker Hickl instrument and Zeiss LSM880-PicoQuant described in other sections can be processed by this software. Details of the experimental setup to acquire this data are described elsewhere (**Chapters 2, 4, 5, 6**)

References

(1) Boens, N. N.; Qin, W.; Basarić, N.; Hofkens, J.; Ameloot, M.; Pouget, J.; Lefèvre, J.-P.; Valeur, B.; Gratton, E.; vandeVen, M.; et al. Fluorescence Lifetime Standards for Time and Frequency Domain Fluorescence Spectroscopy. *Anal. Chem.* **2007**, *79* (5), 2137–2149. https://doi.org/10.1021/ac062160k.

(2) Becker, W. *The Bh TCSPC Handbook*, 5th edn.; Becker & Hickl, 2012.

(3) Enderlein, J.; Erdmann, R. Fast Fitting of Multi-Exponential Decay Curves. *Opt. Commun.* **1997**, *134*, 371–378.

(4) Linkert, M.; Rueden, C. T.; Allan, C.; Burel, J. M.; Moore, W.; Patterson, A.; Loranger, B.; Moore, J.; Neves, C.; MacDonald, D.; et al. Metadata Matters: Access to Image Data in the Real World. *J. Cell Biol.* **2010**, *189* (5), 777–782. https://doi.org/10.1083/jcb.201004104.

(5) Schindelin, J.; Arganda-Carreras, I.; Frise, E.; Kaynig, V.; Longair, M.; Pietzsch, T.; Preibisch, S.; Rueden, C.; Saalfeld, S.; Schmid, B.; et al. Fiji: An Open-Source Platform for Biological-Image Analysis. *Nat. Methods* **2012**, *9* (7), 676–682. https://doi.org/10.1038/nmeth.2019.

Appendix 2

Reproducibility of VF-FLIM across Photon Counting Instruments

Synopsis

By measuring the fluorescence lifetime of voltage sensitive fluorophores, one hopes to access a consistent, absolute value. However, the fluorescence lifetimes measured can vary between instruments and preparations, even for well characterized fluorescence lifetime standards.[1] To assess the reproducibility of V_{mem}-τ_{fl} calibration results from the VF-FLIM technique, we measured the V_{mem}-τ_{fl} relationship for VF2.1.Cl in HEK293T cells on two additional time-correlated single photon counting (TCSPC) instruments that we had available during demonstration periods. The lifetimes obtained for VF2.1.Cl on these systems are very similar to the data collected on the Zeiss LSM 510 instrument with Becker & Hickl FLIM hardware used in **Chapter 2**.[2] These results indicate that VF-FLIM is translatable between acquisition systems, although validation of the τ_{fl}-V_{mem} calibration is generally beneficial when starting a new or sensitive set of experiments.

Results

We measured the lifetime-V_{mem} relationship for VF2.1.Cl on two independent TCSPC instruments and found that the results were nearly identical (**Figure A2.1**, **Table A2.1**). This observation is consistent with the intrinsic nature of fluorescence lifetime and suggests that a calibration obtained on one TCSPC FLIM system could be used on a different system with minimal recalibration. Nevertheless, there were slight differences between the results, so the most accurate V_{mem} determinations would require electrode-based calibration on the system to be used for data collection.

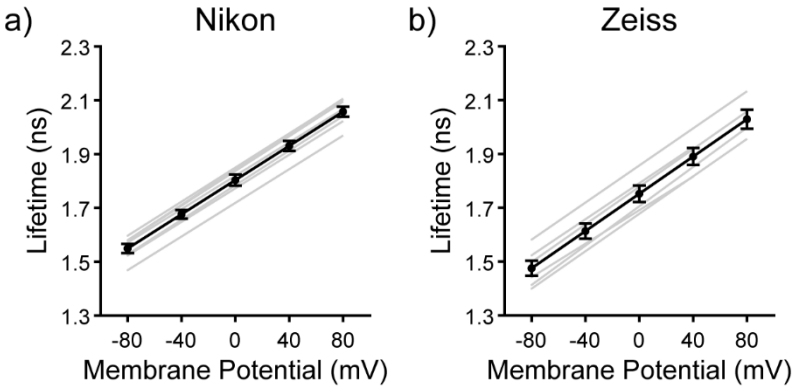

Figure A2.1. Lifetime-V_{mem} calibrations for VF2.1.Cl on different TCSPC systems.
HEK293T cells were held at specified Vmem with whole-cell voltage clamp electrophysiology while lifetime was measured on a) a Nikon confocal equipped with a Becker&Hickl FLIM system and b) a Zeiss LSM 880 confocal equipped with a PicoQuant FLIM system. Gray lines indicate lines of best fit for individual cells; black line indicates the average line of best fit. Data are shown as mean ± SEM.

System	Slope (ps/mV)	Y-Intercept (ps)
VF-FLIM[2]	3.50 ± 0.08	1.77 ± 0.02
Zeiss/PQ	3.43 ± 0.08	1.75 ± 0.03
Nikon/BH	3.20 ± 0.03	1.80 ± 0.02

Table A2.1. Summarized Lifetime-V_{mem} Calibration for VF2.1.Cl in HEK293T on Different TCSPC Systems.
Summary of data presented in **Figure A2.1**. Slope and y-intercept values were averaged across all cells measured on a particular instrument and are presented as mean ± SEM. Data represent the following numbers of cells: VF-FLIM 17 (**Chapter 2**), Zeiss/PQ 6, Nikon/BH 7.

Materials and Methods

Materials

VF2.1.Cl was synthesized in-house according to the published synthesis.[3] VF2.1.Cl was stored as a 1000x stock in DMSO at -20°C, and stocks were checked every few months to confirm no decomposition had occurred. All chemicals were obtained from either Sigma-Aldrich or Thermo Fisher Scientific.

Cell Culture

HEK293T cells were obtained from the UC Berkeley Cell Culture Facility and were verified by STR profiling. Cells were maintained in a humidified 37°C incubator with 5% CO_2 and were discarded after thirty passages. Cells were maintained in Dulbecco's Modified Eagle Medium (DMEM) supplemented with 4.5 g/L glucose, 2 mM GlutaMAX, and 10% fetal bovine serum (FBS). Cells were dissociated with 0.05% trypsin-EDTA for passaging and preparation of microscopy samples. FBS was purchased from Seradigm; all other media and supplements were purchased from Gibco (Thermo Fisher Scientific).

14 to 24 hours before electrophysiology recordings, HEK293T cells were dissociated and plated at a density of 21,000 cells/cm^2 in low glucose DMEM (1 g/L glucose, 2 mM GlutaMAX, 10% FBS, 1 mM sodium pyruvate) on poly-D-lysine coated 25 mm coverslips (Electron Microscopy Sciences) in a 6 well tissue culture plate (Corning). Coverslips were prepared by acid wash in 1 M HCl for 2-5 hours, followed by three overnight washes in 100% ethanol and three overnight washes in MilliQ purified water. Coverslips were sterilized by heating to 150°C for 2-5 hours. Before addition of cells, coverslips were incubated with poly-D-lysine (Sigma-Aldrich, made as a 0.1 mg/mL solution in phosphate-buffered saline with 10 mM Na_3BO_4) for 1-24 hours in a humidified 37°C incubator and washed twice with sterile MilliQ purified water and twice with dPBS.

Microscopy Sample Preparation

Cells were loaded with 100 nM VF2.1.Cl for 20 minutes in a humidified 37°C incubator with 5% CO_2 in imaging buffer (IB; pH 7.25; 290 mOsmol/L; composition in mM: NaCl 139.5, KCl 5.33, $CaCl_2$ 1.26, $MgCl_2$ 0.49, KH_2PO_4 0.44, $MgSO_4$ 0.41, Na_2HPO_4 0.34, HEPES 10, D-glucose 5.56). Cells were washed once in IB and transferred to fresh IB for electrophysiology.

Whole Cell Patch Clamp Electrophysiology

Electrodes were pulled from glass capillaries with filament (Sutter Instruments) with a P-97 pipette puller (Sutter Instruments) to resistances of 4-7 MΩ. Electrodes were filled with a K-gluconate internal solution (pH 7.25; 285 mOsmol/L, composition in mM: 125 potassium gluconate, 10 KCl, 5 NaCl, 1 EGTA, 10 HEPES, 2 ATP sodium salt, 0.3 GTP sodium salt). EGTA (tetraacid form) was prepared as a stock solution in 1 M KOH before addition to the internal solution. Voltage steps were corrected for the calculated liquid junction (pClamp software package, Molecular Devices) between IB and the K-gluconate internal.[4]

Electrodes were position with an MP-225 micromanipulator (Sutter Instruments) to obtain a gigaseal prior to breaking into the whole cell configuration. Recordings were sampled at a rate of > 10 kHz using an Axopatch 200B amplifier, filtered with a 5 kHz low-pass Bessel filter, and digitized with a DigiData 1440A (Molecular Devices). Only recordings that maintained a 30:1 ratio of membrane resistance R_m to access resistance R_a were used for analysis. Pipette capacitance was corrected with the fast magnitude knob only; series resistance compensation was not performed. Voltage steps of -80, -40, 0, and +40 mV were applied in random order, followed by a voltage step to +80 mV.

Nikon A1R-HD25 on Ti2E with Becker & Hickl FLIM

Excitation was provided by a 480 nm pulsed diode laser (repetition rate 50 MHz) and directed to the sample with a line pass dichroic. Individual photons were detected with a hybrid detector (HPM-100-40, Becker and Hickl) and converted to photon arrival times with an SPC-150 photon counting card (Becker and Hickl). Acquisition times of 30 seconds were used at each V_{mem} step. Fluorescence lifetime images were acquired in Nikon Elements and transferred to SPCImage for fitting of exponential decays. VF2.1.Cl fluorescence lifetime was modeled as a biexponential decay at each pixel of the resulting FLIM image. Data were processed with the following fit parameters fixed: shift 0, offset 0. Images were binned by a factor of 1 prior to analysis (as supported by SPCImage software, moving average of adjacent pixels). A measured IRF from a solution of quenched fluorescein (500 μM fluorescein, 0.1 N NaOH, 12 M sodium iodide)[5] was used for all fitting. Regions of interest were identified in FIJI;[6] lifetime is reported as the average of the weighted average τ_m over a region.

Zeiss LSM 880 with PicoQuant FLIM

A 480 nm diode laser operating at a repetition rate of 20 MHz was used to provide pulsed excitation for FLIM. The hardware configuration for a Zeiss LSM 880 equipped with PicoQuant FLIM is described in **Chapter 5**. Data presented here were taken on a demo version of that instrument. Data were acquired at an approximate frame rate of 1 Hz; successive frames were binned before analysis to obtain a total acquisition of 5 seconds (5-6 frames per V_{mem} step).

Fluorescence lifetime analysis was performed with global analysis in SymPhoTime (PicoQuant). All photons from a defined ROI per frame were combined for a global fit. An experimentally measured IRF was used for fitting (same as Nikon data above). Shift was fixed to 0, and offset was determined by the software from the baseline. Lifetimes of successive frames at the same V_{mem} were similar. Data presented here were averaged across all frames at a given potential for each cell before lines of best fit were determined.

Fluorescence Lifetime Biexponential Model

Fluorescence lifetimes obtained on both systems were modeled as biexponential decays (eqn.A2-1) before convolution with the experimentally measured IRF. Lifetimes are reported as the weighted average τ_m (eqn. A2-2), consistent with the reported analysis for VF-FLIM (**Chapter 2**).[2]

$$I(t) = a_1 e^{-t/\tau_1} + a_2 e^{-t/\tau_2} \quad \text{[A2-1]}$$

$$\tau_m = \frac{a_1\tau_1 + a_2\tau_2}{a_1 + a_2} \quad \text{[A2-2]}$$

where I is the time resolved fluorescence intensity as a function of time t, a_i is the amplitude of each exponential component, and τ_i is the decay constant (lifetime) of each exponential component.

References

(1) Boens, N.; Qin, W.; Basaric, N.; Hofkens, J.; Ameloot, M.; Pouget, J.; Lefevre, J.-P.; Valeur, B.; Gratton, E.; VandeVen, M.; et al. Fluorescence Lifetime Standards for Time and Frequency Domain Fluorescence Spectroscopy. *Anal. Chem.* **2007**, *79* (5), 2137–2149. https://doi.org/10.1021/ac062160k.

(2) Lazzari-Dean, J. R.; Gest, A. M. M.; Miller, E. W. Optical Estimation of Absolute Membrane Potential Using Fluorescence Lifetime Imaging. *Elife* **2019**, *8*, e44522. https://doi.org/10.7554/elife.44522.

(3) Miller, E. W.; Lin, J. Y.; Frady, E. P.; Steinbach, P. A.; Kristan, W. B.; Tsien, R. Y. Optically Monitoring Voltage in Neurons by Photo-Induced Electron Transfer through Molecular Wires. *Proc. Natl. Acad. Sci. U. S. A.* **2012**, *109* (6), 2114–2119. https://doi.org/10.1073/pnas.1120694109.

(4) Barry, P. H. JPCalc, a Software Package for Calculating Liquid Junction Potential Corrections in Patch-Clamp, Intracellular, Epithelial and Bilayer Measurements and for Correcting Junction Potential Measurements. *J. Neurosci. Methods* **1994**, *51* (1), 107–116. https://doi.org/10.1016/0165-0270(94)90031-0.

(5) Liu, M.; Jia, M.; Pan, H.; Li, L.; Chang, M.; Ren, H.; Argoul, F.; Zhang, S.; Xu, J. Instrument Response Standard in Time-Resolved Fluorescence Spectroscopy at Visible Wavelength: Quenched Fluorescein Sodium. *Appl. Spectrosc.* **2014**, *68* (5), 577–583. https://doi.org/10.1366/13-07236.

(6) Schindelin, J.; Arganda-Carreras, I.; Frise, E.; Kaynig, V.; Longair, M.; Pietzsch, T.; Preibisch, S.; Rueden, C.; Saalfeld, S.; Schmid, B.; et al. Fiji: An Open-Source Platform for Biological-Image Analysis. *Nat. Methods* **2012**, *9* (7), 676–682. https://doi.org/10.1038/nmeth.2019.

Appendix 3
Pharmacological Voltage Calibrations for VF-FLIM

Synopsis

Optical determination of absolute V_{mem} is a powerful tool that can expand the reach of V_{mem} recordings. However, all strategies for optical absolute V_{mem} recording require an initial calibration step, in which the optical readout is performed at a known value of V_{mem}. The gold standard for this calibration is voltage-clamp electrophysiology, but electrodes cannot access all systems of interest for V_{mem} studies (**Chapter 1**). To obviate the need for the electrode-based calibration in VF-FLIM, we investigated the Na^+/K^+ ionophore gramicidin and the K^+ ionophore valinomycin as a potential strategy to set cellular V_{mem} to 0 mV. We observed similar lifetimes in gramicidin treatment and at 0 mV by electrode, although the lifetimes in gramicidin were on average slightly higher than the electrode-based 0 mV lifetimes. Valinomycin treatment did not produce shorter lifetimes (hyperpolarization) as expected, leading to concern about artefactual interactions between VF2.1.Cl and ionophores.

Results

HEK293T cells loaded with 100 nM VF2.1.Cl were treated with either 500 ng/mL gramicidin or vehicle control. As it increases the permeability of both Na^+ and K^+,[1] we expect that gramicidin would depolarize the membrane potential to approximately 0 mV. Gramicidin-based calibrations have been used previously for V_{mem} sensors (see **Chapter 1**). Consistent with this, we observe a large (~175 ps) increase in lifetime upon gramicidin treatment, indicating depolarization (**Figure A3.1**). The lifetime in gramicidin treated cells was 1.79 ± 0.01 ns (mean ± SEM of n=66 cell groups) when data were processed with custom Matlab code.

This gramicidin-treated lifetime is consistent with the 0 mV lifetime reported from SPCImage analysis for VF-FLIM (1.77 ns, **Chapter 2**), but it is somewhat longer than the more analogous 0 mV lifetimes fit with Matlab code (1.68 ns, **Chapter 4**). The total change in the fluorescence lifetime between DMSO and gramicidin corresponds to approximately 50 mV (using the slopes obtained by electrophysiology), which is consistent with expected resting membrane potentials for HEK293T (**Chapter 2**).[2]

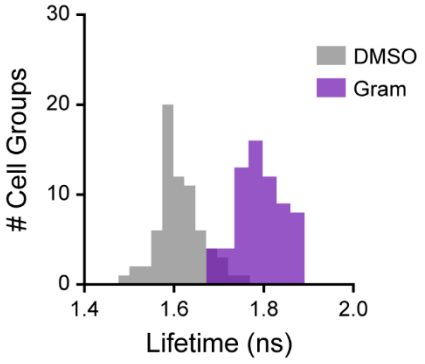

Figure A3.1. Effects of Gramicidin Treatment on VF2.1.Cl Lifetime in HEK293T.
The fluorescence lifetime of VF2.1.Cl was recorded in HEK293T cells treated with DMSO vehicle or with 500 ng/mL gramicidin (Gram). Data represent 69 cell groups for DMSO and 66 cell groups for 500 ng/mL gramicidin. Histogram bins were determined with the Freedman-Diaconis rule.

In order to obtain a second point in the calibration, we attempted to hyperpolarize HEK293T with the K^+ ionophore valinomycin (**Figure A3.2**). By increasing the K^+ permeability and allowing K_+ to flow out of the cell, we would expect that valinomycin would produce hyperpolarization.[3] However, we did not see any change in lifetime upon treatment with either 100 nM or 1 µM valinomycin. We explored higher concentrations and other treatment conditions, but we observed noticeable cytotoxicity without a change in lifetime (data not shown).

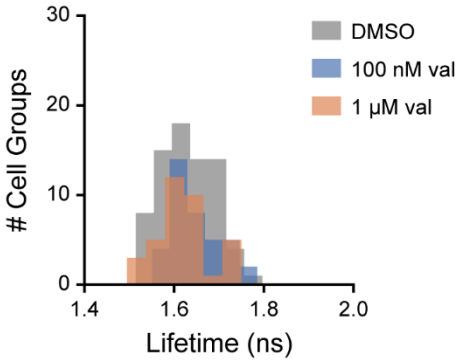

Figure A3.2. Effects of Valinomycin Treatment on VF2.1.Cl Lifetime in HEK293T.
The fluorescence lifetime of VF2.1.Cl was recorded in HEK293T cells treated with DMSO vehicle or valinomycin (val) at 100 nM or 1 µM. No significant difference was observed between groups (Fisher's one-way ANOVA, $F(2, 145) = 1.9$, $p=0.15$). Sample sizes (number of cell groups): DMSO 74, 100 nM valinomycin 38, 1 µM valinomycin 36. Histogram bins were determined with the Freedman-Diaconis rule.

Artifacts arising from treatment with valinomycin have been observed with other voltage sensitive dyes;[4] we speculate that such an interaction may be occurring between valinomycin and VF2.1.Cl. If this is the case, then there is perhaps a cancellation of effects, where an artefactual slight increase in lifetime obscures the slight decrease in lifetime from hyperpolarization. To validate this, we attempted to measure the membrane potential of cells treated with valinomycin with whole cell patch clamp electrophysiology, but cell health was too poor for stable recordings. Taken together, these results do not fully explain what is occurring in valinomycin treated cells, but they definitely suggest that valinomycin alone is not a good avenue for FLIM calibration, although valinomycin in conjunction with varied extracellular K^+ may merit future investigation.

Gramicidin may also have unwanted effects on the membrane that change the VF-FLIM response, as it is known to change membrane height locally where it forms a channel.[1] For these reasons, we believe that, if possible, electrode-based calibration is the best approach for optical absolute V_{mem} recordings. In cases where electrophysiology is impossible, gramicidin may be a reasonable avenue for calibration. Preliminary results with gramicidin and TMCRh.OMe appear promising, although electrode-based calibration is still required (**Chapter 5**). Nevertheless, gramicidin treatment only produces a single point value, not a slope for the calibration, and additional validation of its off-target effects should be performed.

Methods

Cell Culture and Drug Treatment

HEK293T cells were maintained as described above (**Chapter 2**). Prior to imaging experiments, cells were seeded at a density of 42,000 cells/cm^2 on poly-D-lysine treated glass coverslips. Cells were loaded with 100 nM VF2.1.Cl (from 1000x DMSO stock) in imaging buffer (IB) for 20 minutes in a humidified 37°C incubator at 5% CO_2. For gramicidin treatment, coverslips were then transferred to room temperature IB containing either 500 ng/mL gramicidin or 0.05% DMSO vehicle and incubated for 5 minutes. Coverslips were transferred to fresh IB containing drug or vehicle and were imaged at room temperature in an Attofluor chamber (Thermo Fisher Scientific).

For valinomycin treatment, coverslips were then incubated in HBSS (Thermo Fisher Scientific) containing either valinomycin or 0.1% DMSO vehicle for 10 minutes at 37°C. Coverslips were transferred to fresh HBSS containing vehicle or drug and were imaged under ambient conditions. Data for valinomycin treatment were acquired from cells loaded with 200 nM VF2.1.Cl; while this is suboptimal, it is unlikely to be the cause of the aberrant results observed with valinomycin.

Gramicidin A, B, C, D was purchased from Sigma-Aldrich and was stored as a 1 mg/mL (2000x) DMSO stock at -20°C. Imaging buffer composition, in mM: 139.5 NaCl, 10 HEPES, 5.6 D-glucose, 5.3 KCl, 1.3 $CaCl_2$, 0.49 $MgCl_2$, 0.44 KH_2PO_4, 0.41 $MgSO_4$, 0.34 Na_2HPO_4; 290 mOsm/kg, pH 7.25).

Valinomycin was purchased from Sigma-Aldrich and stored as a DMSO stock at -20°C.

Fluorescence Lifetime Data Acquisition

Fluorescence lifetime data were acquired as described above for VF-FLIM (**Chapter 2**).

Fluorescence Lifetime Data Analysis

Time correlated single photon counting data were fit to a biexponential model using custom MATLAB (Mathworks) code as described in **Chapter 4**. Data were binned 4x4 to produce a 64x64 pixel image from the acquired 256x256 pixel image. HEK293T membrane regions of interest (ROIs) were automatically identified by thresholding, and each value presented here represents the mean of each ROI. ROIs represent cell groups (contiguous sets of cells).

References

(1) Kelkar, D. A.; Chattopadhyay, A. The Gramicidin Ion Channel: A Model Membrane Protein. *Biochim. Biophys. Acta - Biomembr.* **2007**, *1768* (9), 2011–2025. https://doi.org/10.1016/j.bbamem.2007.05.011.

(2) Lazzari-Dean, J. R.; Gest, A. M. M.; Miller, E. W. Optical Estimation of Absolute Membrane Potential Using Fluorescence Lifetime Imaging. *Elife* **2019**, *8*, e44522. https://doi.org/10.7554/elife.44522.

(3) Novo, D.; Perlmutter, N. G.; Hunt, R. H.; Shapiro, H. M. Accurate Flow Cytometric Membrane Potential Measurement in Bacteria Using Diethyloxacarbocyanine and a Ratiometric Technique. *Cytometry* **1999**, *35* (1), 55–63. https://doi.org/10.1002/(SICI)1097-0320(19990101)35:1<55::AID-CYTO8>3.0.CO;2-2.

(4) Montana, V.; Farkas, D. L.; Loew, L. M. Dual-Wavelength Ratiometric Fluorescence Measurements of Membrane Potential. *Biochemistry* **1989**, *28* (11), 4536–4539. https://doi.org/10.1021/bi00437a003.

Appendix 4

VF-FLIM in Drosophila Imaginal Wing Disc

This work was conducted in collaboration with Maya Emmons-Bell.

Synopsis

The role of V_{mem} in tissue patterning has been a topic of recent inquiry.[1,2] A complete understanding of V_{mem} signaling in development is hampered by a lack of methods for recording V_{mem} in this context. We thought that VF-FLIM would be well suited to map V_{mem} across tissue, as it enables simultaneous recording from many cells with minimal invasiveness. We applied fluorescence lifetime imaging with TMCRh.OMe under two photon illumination in the imaginal wing disc of developing Drosophila larvae. The wing imaginal disc consists of two layers of cells separated by a lumen: an exterior squamous epithelium and an internal columnar layer.[3] Because of the small cell size and presence of a lumen, the columnar layer of this tissue is inaccessible to patch clamp electrophysiology. We measured fluorescence lifetimes in a positive control system expressing a depolarizing sodium channel on the anterior side of the wing disc, but technical limitations in the staining of the dye prevented clear interpretation of the lifetime results.

Results

In order to perform two photon FLIM and record absolute V_{mem}, we stained Drosophila imaginal wing discs with the voltage indicator TMCRh.OMe. We sought to measure V_{mem} in the interior columnar layer, but obtaining adequate signal in this layer proved challenging. We consistently observed bright staining in the exterior squamous epithelium and much dimmer staining in the interior columnar layer. Given the lipophilicity of VoltageFluors, this result is not entirely surprising – once the probe is localized to the exterior cell layer, it would need to leave the membrane, dissolve in the lumen, and re-enter membrane on the far side – a very unfavorable process. Increasing dye concentration to 3 μM improved staining in the columnar layer but also produced concentration quenching (shorter lifetimes) in the exterior squamous epithelium (**Figure A4.1A).** By increasing the concentration of the surfactant pluronic F-127 up to 0.04%, we were able to further improve staining in the columnar layer without observing cytotoxicity in the tissue. We did observe increasing brightness during imaging at room temperature, suggesting that dye was continuing to diffuse into the columnar layer from the lumen.

Using 3 μM TMCRh.OMe and 0.04% pluronic F-127, we observed consistent membrane staining in the wing disc, so we sought to record fluorescence lifetimes. We tested a positive control line, which expressed the depolarizing sodium channel NaChBac in their anterior compartment along with a GFP label (**Figure A4.1C**). NaChBac expression is frequently used to depolarize Drosophila tissue,[4] although the magnitude of the depolarization is difficult to assess without knowledge of resting V_{mem}. Under two photon illumination, we observed variable τ_3 for TMCRh.OMe between imaginal discs, with values ranging from 3.3 to 3.5 ns (**Figure A4.1D**). On average, fluorescence lifetime decreased slightly across the disc, and no clear drop in lifetime was visible at the compartment boundary (i.e. between NaChBac positive and negative cells, **Figure A4.1E-F**). If the cells across the compartment boundary are electrically coupled, it is possible that such a slow drop-off in V_{mem} could occur. The average 40 ps change in lifetime across the disc would correspond to approximately 15 mV difference in V_{mem} (using the calibration of 2.6 ps/mV from **Chapter 6**). While this value is biologically reasonable, it should not be interpreted strongly given the amount of baseline variability in the lifetime recordings.

We successfully recorded the fluorescence lifetime of VoltageFluors in complex tissue under two photon illumination, but we were unable to reproduce a strong, consistent response to the positive control condition. Future work using TMCRh.OMe under one photon illumination could be more straightforward, as the sensor exhibited improved V_{mem} sensitivity and a simpler time resolved decay under those conditions (**Chapter 5**). However, the presence of a lumen and the inability to incubate the samples warmer than 25°C pose fundamental issues for delivering TMCRh.OMe to the cells of interest. Samples without such constraints will likely be more promising arenas for VF-FLIM recordings in tissue.

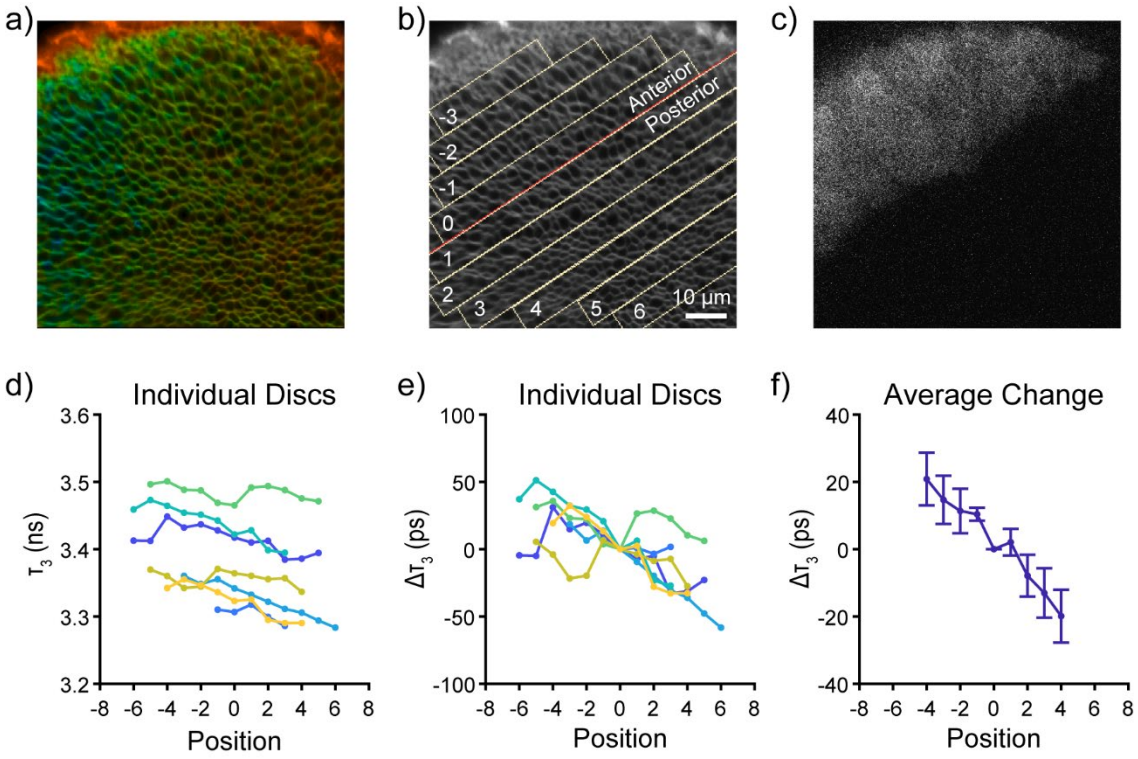

Figure A4.1. Lifetime changes across Drosophila imaginal wing discs expressing NaChBac. Two photon fluorescence lifetime imaging was performed using the voltage sensor TMCRh.OMe. a) Overlay of the weighted average lifetime (τ_m, not τ_3) and the photon count for a representative disc. This image is for display purposes only; a global fit of τ_3 was used for analysis. The lifetime is scaled from 1.8 to 2.5 ns. Shorter lifetime at the upper edge corresponds to the exterior squamous epithelium. b) Regions of interest used for analysis, shown as an overlay on the photon count image. Position 0 is defined as a rectangular region of interest immediately on the anterior side of the compartment boundary. c) Confocal image of the GFP marker from the same field of view in (a) and (b). The GFP marker was used to define the location of the compartment boundary. d) Fluorescence lifetimes from global analysis of individual discs (n=8, each color represents one disc). Only visible positions were used (i.e. each disc did not have all positions -6 to +6 in view). e) Fluorescence lifetimes across wing discs, shown as the change from position 0. f) The average change in lifetime with position for all 8 discs studied.

Methods

Drosophila Sample Preparation

Wing imaginal discs were obtained from *Drosophila melanogaster* larvae in the third instar phase (L3) and early L3 (eL3). Larvae expressed the sodium channel NaChBac fused to GFP in the anterior compartment of the wing disc (*ci*>NaChBac, driving NaChBac under GAL4/UAS).

Imaginal discs were loaded with 3 μM TMCRh.OMe and 0.04% Pluronic F-127 (Life Technologies) for 15 minutes at 25°C in Schneider's Drosophila Medium (Thermo Fisher Scientific). Discs were briefly transferred into a fresh Schneider's media and then placed onto a 25 mm glass coverslip in an Attofluor cell imaging chamber (Thermo Fisher Scientific). An 18 mm glass coverslip was gently placed on top to maintain all discs in the correct focal plane. All samples were used within twenty minutes of the start of imaging; reduced viability was observed after that point.

Two Photon Fluorescence Lifetime Imaging

All fluorescence was collected on an LSM 510 laser scanning confocal microscope (Zeiss) with a 40x/1.3 NA oil objective immersed in Immersol 518F (Zeiss). Two photon fluorescence lifetime imaging of TMCRh.OMe with excitation at 820 nm was performed as described above (**Chapter 6**). Average power at the sample was approximately 1-2 mW. GFP fluorescence was obtained via one photon illumination with an Argon laser (488 nm, 10-40% transmittance). A 488 nm long pass dichroic and a 505 nm long pass emission filter were used to collect the GFP fluorescence. GFP images were formed on the built-in detectors of the Zeiss LSM 510.

Rectangular regions of interest (ROIs) were defined parallel to the compartment boundary as indicated by the GFP marker. ROIs were drawn by hand in FIJI.[5] Time-resolved fluorescence decays were obtained from the entire region of interest (global analysis). Decays were fit to a sum of three exponential components in custom Matlab code (**Appendix 1**), and the third exponential component was used for all analysis (as described in **Chapter 6**).

References

(1) McLaughlin, K. A.; Levin, M. Bioelectric Signaling in Regeneration: Mechanisms of Ionic Controls of Growth and Form. *Dev. Biol.* **2018**, *433* (2), 177–189. https://doi.org/10.1016/j.ydbio.2017.08.032.

(2) Durant, F.; Bischof, J.; Fields, C.; Morokuma, J.; LaPalme, J.; Hoi, A.; Levin, M. The Role of Early Bioelectric Signals in the Regeneration of Planarian Anterior/Posterior Polarity. *Biophys. J.* **2019**, *116* (5), 948–961. https://doi.org/10.1016/j.bpj.2019.01.029.

(3) Beira, J. V; Paro, R. The Legacy of Drosophila Imaginal Discs. *Chromosoma* **2016**, *125* (4), 573–592. https://doi.org/10.1007/s00412-016-0595-4.

(4) Nitabach, M. N.; Wu, Y.; Sheeba, V.; Lemon, W. C.; Strumbos, J.; Zelensky, P. K.; White, B. H.; Holmes, T. C. Electrical Hyperexcitation of Lateral Ventral Pacemaker Neurons Desynchronizes Downstream Circadian Oscillators in the Fly Circadian Circuit and Induces Multiple Behavioral Periods. *J. Neurosci.* **2006**, *26* (2), 479–489. https://doi.org/10.1523/JNEUROSCI.3915-05.2006.

(5) Schindelin, J.; Arganda-Carreras, I.; Frise, E.; Kaynig, V.; Longair, M.; Pietzsch, T.; Preibisch, S.; Rueden, C.; Saalfeld, S.; Schmid, B.; et al. Fiji: An Open-Source Platform for Biological-Image Analysis. *Nat. Methods* **2012**, *9* (7), 676–682. https://doi.org/10.1038/nmeth.2019.